FACULTY OF SCIENCE
UNIVERSITY OF COPENHAGEN
NIELS BOHR INSTITUTE

PhD thesis

Myriam Guillevic

Characterisation of rapid climate changes through isotope analyses of ice and entrapped air in the NEEM ice core

Academic advisors:

Thomas Blunier
Centre for Ice and Climate, Niels Bohr Institute
University of Copenhagen, Denmark

Amaëlle Landais
Valérie Masson-Delmotte
Laboratoire des Sciences du Climat et de l'Environnement,
UMR CEA/CNRS/UVSQ
Gif sur Yvette, France

Laboratoire des Sciences du climat et de l'environnement, UMR CEA/CNRS/UVSQ

Centre for Ice and Climate, Niels Bohr Institute, University of Copenhagen

THESE DE DOCTORAT

DE L'UNIVERSITE DE VERSAILLES SAINT–QUENTIN–EN-YVELINES

DISCIPLINE / SPECIALITE : paleoclimatologie

Présentée par :

Myriam Guillevic

Pour obtenir le grade de **Docteur de l'Université de Versailles Saint-Quentin-en-Yvelines**

Characterization of rapid climate changes through isotope analyses of ice and entrapped air in the NEEM ice core

Soutenance prévue le 20 novembre 2013

Jury

Dr. Todd Sowers, Pennsylvania State University, USA — Rapporteur

Dr. Barbara Stenni, University of Trieste, Italy — Rapporteur

Prof. Markus Jochum, Niels Bohr Institute, University of Copenhagen, Denmark — Examinateur

Prof. Matthieu Roy-Barman, UVSQ, France — Examinateur

Directeurs de thèse

Prof. Thomas Blunier

Centre for ice and Climate, Niels Bohr Institute, University of Copenhagen, Denmark

Dr. Amaëlle Landais

Dr. Valérie Masson-Delmotte

Laboratoire des Sciences du Climat et de l'Environnement, Gif sur Yvette, France

If we don't tell strange stories,
when something strange happens we won't believe it.
Shannon Hale, *The Goose Girl.*

Abstract

Analyses of Greenland ice core samples have revealed the occurrence of rapid climatic instabilities during the last glacial period. These events, commonly known as Dansgaard-Oeschger (DO) events, are characterised by temperature variations of about 8-16°C in a few decades in Greenland. The imprint of DO events is also recorded at mid to low latitudes in different archives of the northern hemisphere. A detailed multi-proxy study of the sequence of these rapid instabilities is essential for understanding the climate mechanisms at play. In this thesis, we combine stable water isotopes (δ^{18}O, d-excess and ^{17}O excess) and air isotopes in Greenland ice cores (δ^{15}N, δ^{18}O$_{\text{atm}}$, and also concentration and isotopic composition of methane) to quantify regional temperature changes in Greenland, to characterise the reorganisation of the hydrological cycle and to better understand the role of the biosphere in climate feedbacks and the sequence of events that lead to major climatic changes during the last glacial period. Most of the new data presented in this thesis were obtained from the NEEM ice core, NW Greenland, drilled in 2008-2011 in the frame of an international project led by the Centre for Ice and Climate (CIC), Denmark.

Recent analytical developments have made it possible to measure new paleoclimate proxies in Greenland ice cores, with increasing accuracy and temporal resolution. We present new measurements performed at LSCE of ^{17}O excess from recent Greenland snow (years 2003-2005) that show seasonal variations with amplitudes of 25 permeg, with a minimum in July leading the d-excess maximum level reached 3 months later. These observations are in agreement with our understanding of ^{17}O excess and d-excess variations in polar regions with minima in ^{17}O excess in phase with maxima in source relative humidity and maxima in d-excess largely influenced by source temperature maxima. Then, at CIC, we contribute to the development of a protocol for absolute referencing of methane gas isotopes, and making full air standard with known concentration and isotopic composition of methane. Such a standard is needed for intercomparison between different laboratories measuring methane isotopes from ice cores, firn air as well as atmospheric air.

The evolution of the isotopic composition of nitrogen trapped in the ice bubbles, δ^{15}N, combined with firn modelling, allows us to reconstruct the past temperature and accumulation rate histories in Greenland. We use new and published δ^{15}N and Δage (ice age - gas age) data from different Greenland ice cores and two different firn models: the Goujon model (Goujon et al., 2003) and the Schwander model (Schwander et al., 1997). We show that these two models, while using different densification equations, produce very similar δ^{15}N and Δage scenarios for climatic conditions covering present and glacial NGRIP conditions. We propose a methodology to estimate the uncertainty assigned to lock-in-depth (the firn depth where air diffusion stops), accumulation and temperature reconstruction linked to the firn modelling method, for periods where δ^{15}N data are available and where

the Δage uncertainty is calculated. Such uncertainty estimation is necessary to compare the firn model-based temperature and accumulation rates with the output of other methods, such as ice flow models.

Focusing on a sequence of Dansgaard-Oeschger events during Marine Isotopic Stage 3, we use δ^{15}N data and firn models to quantitatively reconstruct temperature and accumulation rates at NEEM, NGRIP, GRIP and GISP2. We show that at the onset of DO-8 and DO-10, the temperature and accumulation increases are smaller for the higher latitude sites, while the water isotope increase associated with the warming episode is larger. These observations are in agreement with a study of spatial Greenland response to reduced sea-ice extent in the Nordic seas (Li et al., 2010). Our results therefore suggest that abrupt sea ice retreat in the Nordic Seas at the beginning of a DO event is likely to contribute to the warming and accumulation rate increase in Greenland. Moreover, our new δ^{15}N-based NGRIP temperature reconstruction from the Holocene to the Eemian shows that the amplitude of Greenland warming at the onset of DO events cannot be explained by the see-saw mechanism only and support local Arctic amplification mechanisms. At orbital timescales, our results suggest that the sensitivity of water isotopes to Greenland temperature increase with decreasing obliquity (qualitatively in agreement with the Rayleigh distillation) and with increasing northern hemisphere ice sheet size (possibly through changes in atmospheric circulation, influencing the vapour source location and its trajectory on the way to Greenland).

Finally, we develop a multi-proxy approach to identify fingerprints of Heinrich events in polar ice cores. These events were originally identified by layers of ice rafted debris in North Atlantic marine cores, deposited by melting icebergs. We propose that at 39 400 a b2k according to the GICC05 chronology, 540 a after the onset of GS-9, the ^{17}O excess decrease (attributed to a southward shift and more mixing of Greenland moisture source, without significant source temperature effect) and the methylsulfonic acid decrease (North Atlantic sea ice expansion) correspond to the signature of the H4 icebergs delivery from the Laurentide ice sheet. These variations are accompanied by heavier δ^{18}O$_{atm}$ and δD-CH$_4$ (probably reflecting heavier meteoric water in the northern tropics due to ITCZ southwards shift) and a small abrupt increase in methane (reflecting enhanced emissions in the southern tropics) and CO$_2$ measured in Antarctic ice cores (possibly caused by southwards westerlies shift and subsequent enhanced upwelling in the East coast of South America). All these synchronous changes are interpreted as a polar ice core fingerprint of the climatic impacts associated with H4. Based on a reduced dataset, a similar fingerprint is observed for H5, also mostly due to the Laurentide collapse. Our findings obviously call for systematic investigations of the ice core multi-proxy fingerprints of other Heinrich events, and in particular H3 and H6 that are mainly due to European ice sheets and may have different signatures. The decoupling between the flat Greenland temperature during GS-9 and the climate variability associated with H4 at lower latitudes challenges the use of Greenland ice core temperatures as a single target for benchmarking climate simulations focused on Heinrich events. Our multi-proxy study opens new paths for parallel investigations of different marine, terrestrial and ice core climate archives.

Resumé på dansk

Analyser og studier af iskerner fra Grønlands Indlandsis har afsløret hurtige klimaskift gennem hele den sidste istid. Disse ændringer er karakteriseret ved 8-16°C temperatur skift i løbet af få årtier. Sådanne klimaskift betegnes almindeligvis som Dansgaard-Oeschger (DO) begivenheder, og deres spor kan også registreres i forskellige andre typer af klimaarkiver på lavere breddegrader. Et detaljeret multi-proxy studie af forløbet af disse hurtige klimaskift er essentielt for at forstå de klimamekanismer, der er i spil. I denne afhandling kombineres vandisotoper (δ^{18}O, d-excess samt ^{17}O excess) med luft fra iskerner fra Grønland (δ^{15}N, δ^{18}O$_{\text{atm}}$, samt koncentration og isotopmæssig sammensætning af metan). Formålet med dette er at kvantificere de regionale temperaturændringer i Grønland, at beskrive omlægningen af vandets kredsløb samt forbedre forståelsen af biosfærens rolle i de hurtige klimaskift. De fleste nye data, der præsenteres i nærværende afhandling, stammer fra analyserne af NEEM-iskernen, der blev boret i nordvest Grønland i perioden 2008-2011 i regi af et internationalt forskningsprojekt ledet af Center for Is og Klima.

Den seneste udvikling af analytiske redskaber har muliggjort måling af nye palæo-klima proxier i iskerner fra Grønland. Nærværende afhandling bidrager til denne udvikling med data fra måling af den innovative parameter ^{17}O excess udført ved det franske LSCE (Laboratoire des Sciences du Climat et l'Environnement) og ved etablering af et referencesystem for metanisotoper ved Center for Is og Klima. Først præsenteres data fra de nye målinger af ^{17}O excess fra grønlandsk sne i perioden 2003-2005, der viser årstidsvariationer med udsving på 25 per meg, - med et minimum i juli der fører til et maksimalt d-excess niveau tre måneder senere. Disse observationer er i overensstemmelse med forståelsen af variationer i ^{17}O excess og d-excess i polaregnene, hvor minima i ^{17}O excess er i fase med maksima i relativ fugtighed for kildeområdet samt i d-excess, der hovedsageligt er påvirket af øgning i temperatur ved kildeområdet. Denne afhandling indeholder også en protokol for hvorledes man kan lave en absolut reference for methan isotoper, samt hvordan man kan etablere en luftstandard med kendt methan koncentration og kendt isotopisk sammensætning. En sådan standard er nødvendig for at kunne foretage sammenligninger mellem forskellige laboratoriers målinger af metanisotoper fra iskerner, firn og atmosfærisk luft.

Ændringer i isotop-sammensætningen i kvælstof indespærret i isens luftbobler, δ^{15}N, i kombination med computermodellering af firn muliggør en rekonstruktion af fortidens temperaturer og sneens akkumulationsrate i Grønland. Der anvendes nye samt publicerede data for δ^{15}N og Δalder (isalder - gasalder) fra forskellige grønlandske iskerner samt to firnmodeller: Goujon-modellen (Goujon et al., 2003) og Schwander-modellen (Schwander et al., 1997). Uanset at de to modeller anvender forskellige ligninger til beskrivelse af sne-sammenpresningen (densificeringen) producerer begge meget ens δ^{15}N og Δalder scenarier med hensyn til de nutidige klimaforhold samt dem, der herskede under istiden ved

NGRIP. Det foreslås, hvorledes man kan estimere usikkerheden i beregningen af LID [Lock-in-Depth; dybden hvor firnens luftindhold forsegles i individuelle bobler] samt i rekonstrueringen af sneakkumulation og temperatur i forhold til firnmodellering, når det drejer sig om perioder, hvor δ^{15}N data er tilgængelige og Δalder usikkerheden er beregnet. En sådan usikkerhedsberegning er nødvendig for at kunne sammenligne temperatur og akkumulationsrater baseret på firnmodeller med resultater opnået ved andre metoder, som f.eks. isflydningsmodeller.

Med fokus på en række Dansgaard-Oeschger (DO) begivenheder under MIS 3 (Marine Isotope Stage 3; ca. 60.000 år siden) anvendes δ^{15}N data og firnmodeller til en kvantitativ rekonstruktion af temperaturer og akkumulationsrater ved NEEM, NGRIP, GRIP og GISP2. Ved begyndelsen af DO-8 og DO-10 bliver størrelsen af stigningen i temperatur og akkumulation mindre jo længere nordpå, man går, medens størrelsen af stigningen i vandisotoper stiger. Disse observationer stemmer overens med resultater af, hvorledes Grønland rent rumligt reagerer på en formindsket udbredelse af havis i Nordatlanten (Li et al., 2010). Vi kan derfor antage, at en hurtig forsvinden af havis i Nordatlanten ved begyndelsen af en DO begivenhed sandsynligvis vil bidrage til en øgning i både opvarmning og sneakkumulation i Grønland. Ydermere viser den nye δ^{15}N-baserede rekonstruktion af temperaturen ved NGRIP fra Holocæn til Eem-tiden, at udsvinget af opvarmningen ved DO-begivenheders begyndelsen ikke alene kan forklares ved hjælp af en bipolar vippefunktion [bipolar seesaw] men må understøttes af lokale arktiske forstærkningsmekanismer. På orbital tidsskala foreslår vore resultater at vandisotopernes følsomhed over for Grønlands temperaturstigning øges, når hældningen af Jordens rotationsakse reduceres (i kvalitativ overensstemmelse med Rayleigh's destillationsligning) og når omfanget af den nordlige halvkugles indlandsis stiger (dette foregår muligvis gennem ændringer i den atmosfæriske cirkulation, der påvirker hvor vanddampen dannes og ad hvilke veje, den føres til Grønland).

Endelig har vi også udviklet en multi-proxi metode til at identificere Heinrich- begivenhedernes særlige spor i iskerner. Heinrich events ses som lag i nordatlantiske marine sedimentkerner med istransporteret materiale, tilført af smeltende isbjerge. Baseret på GICC05-kronologien foreslår vi at der for 39.400 år siden, d.v.s. 540 år efter begyndelsen af GS-9 (Greenland Stadial 9), må være sket en reduktion i ^{17}O excess og metansvovlsyre (CH_3SO_3H) samt, i samme periode, en stigning i CH_4, CO_2, $\delta^{18}O_{atm}$ og δD-CH_4. Denne stigning er relateret til afsmeltningen af Laurentide iskappen under Heinrich begivenhed 4 (H4). Det samme "fingeraftryk" er fundet i materiale fra H5, også mestendels forårsaget af Laurentide iskappens kollaps. Disse resultater bør følges op med systematiske undersøgelser af iskerners multi-proxi "fingeraftryk" fra andre Heinrich begivenheder, i særlig grad H3 og H6, der hovedsagelig skyldes afsmeltning af europæiske iskapper, og som derfor kan have andre karakteristika. En adskillelse af Grønlands flade temperaturkurve gennem GS-9 og klimaets variabilitet gennem H4 på lavere breddegrader, udfordrer anvendeligheden af Grønlands iskernetemperatur som et enkeltstående værktøj til benchmarking af klimasimuleringer, der fokuserer på Heinrich begivenheder. Vores multi-proxi arbejde åbner nye veje for sammenligning af forskellige klimaarkiver fra hav, land og iskerner.

Résumé en français

L'analyse de la glace forée sur la calotte groenlandaise a révélé l'occurrence d'instabilités rapides du climat pendant la dernière période glaciaire. Celles-ci sont caractérisées par des variations de température de 8 à 16°C en quelques décades. Ces événements sont communément connus sous le nom d'événements de Dansgaard-Oeschger (DO). L'empreinte des DO est aussi enregistrée aux moyennes et basses latitudes dans différentes archives de l'hémisphère nord. Une étude multi-proxy détaillée de la séquence de ces instabilités rapides est essentielle pour comprendre les mécanismes climatiques en jeu. Dans cette thèse, nous combinons les isotopes de l'eau (δ^{18}O, d-excess et ^{17}O excess) et de l'air des carottes de glace du Groenland (δ^{15}N, δ^{18}O$_{\text{atm}}$, ainsi que la concentration et la composition isotopique du méthane), pour quantifier les changements de température régionaux au Groenland, caractériser la réorganisation du cycle hydrologique et mieux comprendre le rôle de la biosphère et la séquence d'événements climatiques. La plupart des nouvelles données présentées dans cette thèse ont été effectuées sur la carotte de NEEM, forée au nord-ouest du Groenland en 2008-2011 dans le cadre d'un projet international piloté par le Centre for Ice and Climate (CIC, Danemark).

Des développements expérimentaux récents ont rendu possible la mesure de nouveaux proxys paléoclimatiques dans les carottes de glace du Groenland. Nous contribuons à ces développements tout d'abord par de nouvelles mesures au LSCE du nouveau paramètre ^{17}O excess, effectuées sur de la neige récente (années 2003-2005). Ces mesures montrent des variations saisonnières de 25 permeg d'amplitude avec un minimum en Juillet, précédant de 3 mois le maximum de d-excess. Ces observations sont en accord avec notre compréhension du ^{17}O excess et du d-excess en régions polaires: minima de ^{17}O excess en phase avec maxima d'humidité relative à la source et maxima de d-excess largement influencés par les augmentations de température à la source. Ensuite, nous contribuons au développement d'un protocole expérimental pour le référencement absolu des isotopes du méthane, et pour la création d'air synthétique standard de concentration et de composition isotopique en méthane connues. Un tel standard est nécessaire pour l'intercomparaison de résultats effectués dans différents laboratoires mesurant la composition isotopique du méthane dans l'air des carottes de glace, dans l'air des névés ainsi que dans l'air atmosphérique.

L'évolution de la composition isotopique de l'azote piégé dans les bulles d'air, le δ^{15}N, combiné à la modélisation du névé, rend possible de reconstruire des scénarios passés de température et de taux d'accumulation au Groenland. Nous utilisons des données nouvelles et publiées de δ^{15}N et Δage (age de la glace - age du gaz) de différentes carottes de glace et deux modèles de névé différents: le modèle de Goujon (Goujon et al., 2003) et le modèle de Schwander (Schwander et al., 1997). Nous montrons que ces deux modèles, bien qu'utilisant des équations différentes pour la densification, produisent des scé-

narios de δ^{15}N et Δage très similaires pour des conditions climatiques recouvrant les conditions présentes et glaciaires à NGRIP. Nous proposons une estimation des incertitudes dues à cette méthode sur la reconstruction de la profondeur de fermeture des bulles, de l'accumulation et de la température, valides pour les périodes où le δ^{15}N est mesuré et où une estimation de l'incertitude sur le Δage est calculée. Une telle estimation des incertitudes est nécessaire pour comparer les reconstructions de température et de taux d'accumulation basés sur les modèles de névé avec les résultats d'autres méthodes, comme les modèles d'écoulement de la glace.

En se focalisant sur une séquence d'événements de Dansgaard-Oeschger pendant le stade isotopique marin 3, nous utilisons le δ^{15}N et les modèles de névé pour reconstruire quantitativement la température et le taux d'accumulation à NEEM, NGRIP, GRIP et GISP2. Nous montrons qu'au début des DO-8 et DO-10, les augmentations de température et de taux d'accumulation sont plus petites vers le nord, tandis que les augmentations des isotopes de l'eau sont plus grandes. Ces observations sont en accord avec un étude de la réponse spatiale du Groenland à une réduction de la couverture en glace de mer dans les Mers Nordiques (Li et al., 2010). Nos résultats suggèrent ainsi qu'un recul abrupt de la glace de mer dans les Mers Nordiques au début des DO contribue probablement au réchauffement et à l'augmentation du taux d'accumulation au Groenland. De plus, notre nouvelle reconstruction de température pour NGRIP basée sur le δ^{15}N, de l'Holocène à l'Eemien, montrent que les amplitudes de réchauffement au Groenland au début des DO ne peuvent être expliquées uniquement par le mécanisme de bascule bipolaire et suggèrent des mécanismes d'amplification climatique dans l'Arctique. Aux échelles de temps orbitales, nos résultats suggèrent que la sensibilité des isotopes de l'eau à la température du Groenland augmente lorsque l'obliquité décroît (qualitativement en accord avec la distillation de Rayleigh) et lorsque le volume des calottes de glace de l'hémisphère nord augmente (probablement à travers des changements de la circulation atmosphérique, influençant l'origine de la vapeur et sa trajectoire vers le Groenland).

Enfin, nous développons une approche multi-proxy pour identifier dans les carottes polaires l'empreinte des événements de Heinrich. Ces événements ont initialement été mis en évidence par des couches de débris détritiques grossiers dans les carottes marines de l'Atlantique Nord, déposés lors de la fonte d'icebergs. Nous proposons que à 39 400 a b2k selon la chronologie GICC05, 540 a après le début du GS-9, la baisse du ^{17}O excess (attribué à un déplacement vers le sud et plus de mélange de la source de vapeur pour le Groenland, sans changement significatif de la température à la source) et la baisse d'acide méthylsulfonique (expansion de glace de mer dans l'Atlantique Nord) correspondent à la signature de la débâcle d'icebergs de la Laurentide lors de l'événement de Heinrich 4 (H4). Ces variations sont accompagnées d'une augmentation du δ^{18}O$_{\text{atm}}$ et du δD-CH$_4$ (probablement reflétant des précipitations enrichies en isotopes lourds dans les tropiques nord, en raison du déplacement vers le sud de l'ITCZ) et d'une légère augmentation abrupte du méthane (augmentation des émissions dans les tropiques sud) et du CO$_2$ mesuré dans les carottes de glace d'Antarctique (sans doute causé par un déplacement au sud des vents d'ouest causant l'augmentation de l'upwelling sur la côte ouest de l'Amérique du Sud). Tous ces changements synchrones sont interprétés comme la signature dans les glaces polaires de l'impact climatique associé au H4. Se basant sur un jeu de données réduit, une signature similaire est observée pour H5, aussi dû à une débâcle de la Laurentide principalement. Nos résultats appellent à une investigation systématique de la signature multi-proxy des événements de

Heinrich dans les carottes de glace, et en particulier pour H3 et H6 qui sont principalement le fait de calottes européennes et ont peut-être des signatures différentes. Le découplage entre le climat stable au Groenland pendant le GS-9 et la variabilité climatique associée avec H4 à des latitudes plus basses remet en question l'utilisation de la température locale enregistrée dans les glaces du Groenland comme cible unique pour évaluer les simulations climatiques focalisées sur les événements de Heinrich. Notre étude multi-proxy ouvre de nouvelles possibilités pour la comparaison d'archives climatiques terrestres, marines et des glaces polaires.

Contents

Introduction

Motivations

Analyses of Greenland ice core samples have revealed the occurrence of rapid climatic instabilities during the last glacial period, at the millennial time scale (Fig. 1). They are characterized by temperature increases of about 8-16°C in a few decades in Greenland (e.g., Huber et al., 2006; Capron et al., 2010a), followed by a more gradual cooling. These events are commonly known as Dansgaard-Oeschger (DO) events. The imprint of DO events is also recorded at mid to low latitudes in different archives of the northern hemisphere. The last glacial period was also marked by instabilities at the millennial time scale of the northern hemisphere ice sheets, that collapsed and released icebergs in the North Atlantic (the Laurentide in North America, and relatively smaller ice sheets in Scandinavia, Greenland, Iceland, the British Islands, Fig. 2). These ice sheet collapses are identified by layers of ice rafted debris in marine cores from the North Atlantic and known as Heinrich events.
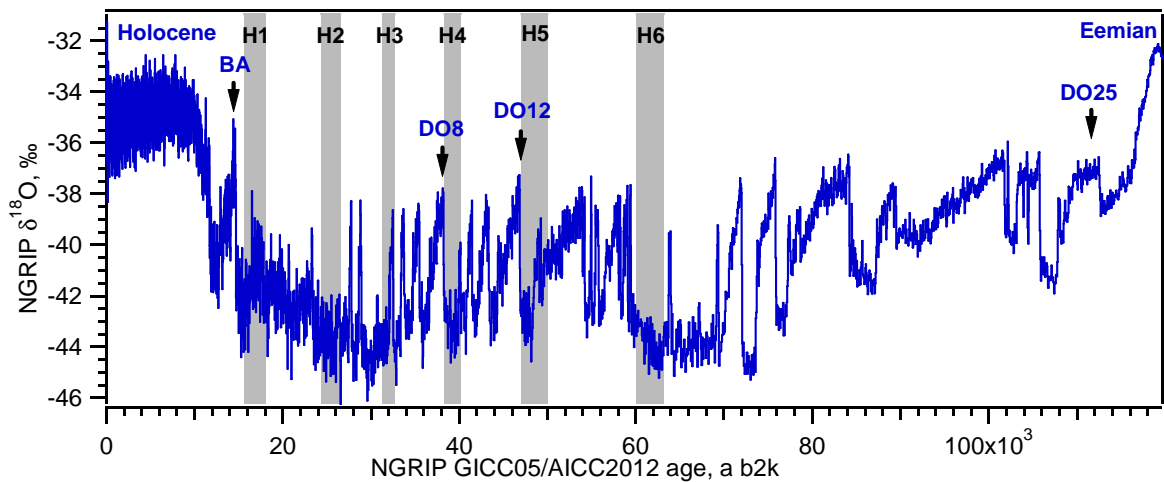
Figure 1: Millennial scale climatic events of the last glacial period: Dansgaard-Oeschger (DO) events and Heinrich events. Blue line: NGRIP δ^{18}O water isotope (NGRIP members, 2004), a proxy for local precipitation-weighted temperature, recording the Dansgaard-Oeschger events. BA: Bølling Allerød. DO events numbered according to Wolff et al. (2010). Gray areas: H1 to H6, major Heinrich events recorded in marine cores from the North Atlantic, with position and duration according to Sánchez Goñi and Harrison (2010). Timescales: GICC05 (Greenland Ice Cores Chronology, Svensson et al., 2008, and references therein) and AICC2012 (Antarctic Ice Cores Chronology, Bazin et al., 2013; Veres et al., 2013), compatible with GICC05 back to 60 ka b2k.

Up to now, the triggers of the Dansgaard-Oeschger events and Heinrich events are still unknown. A detailed multi-proxy study of the sequence of these rapid instabilities is es-

Figure 2: Northern hemisphere ice sheets extend at the last glacial maximum (LGM), ∼20 ka b2k. Picture from D. Freidel, http://www.sonoma.edu/users/ f/freidel/global/372Chapt9.htm.

sential for understanding the climate mechanisms at play. The subject of this project is to combine in an innovative way high-resolution isotopic measurements of water and air trapped in Greenland ice cores, to study the extent, speed, and sequence of key abrupt events during the last glacial period: DO events 8 to 10, iconic of Marine Isotopic Stage 3, and the major Heinrich event 4.

Greenland ice cores are precious archives of the past climate. The centre of the Greenland ice sheet preserves the layers of snow falling each year at the surface. Analysing the ice layers deeper in the ice sheet gives access to the past climate in Greenland. Moreover, the past atmospheric air gets trapped into air bubbles near the surface of the ice sheet in the firn/ice transition region. The surface ice and trapped air are advected through the ice sheet. Vertical ice cores provide the means of reconstructing the chemical composition of the precipitation along with the trapped bubbles of past atmospheres. In Greenland, the longest undisturbed record is so far provided by the NGRIP ice core (North Greenland Ice Core Project), the ice at the bottom being 120 ka b2k old (kilo years before 2000 AD) (Veres et al., 2013).

The following work in this thesis is based on a combination of new and published results from four deep Greenland ice cores, including ^{17}O excess (measured at Laboratoire des Sciences du Climat et de l'Environnement (LSCE)) and methane isotope data (that can now be measured at the Centre for Ice and Climate, CIC, Sperlich et al. (2012, 2013)): GRIP (Greenland Ice core Project), GISP2 (Greenland Ice Sheet Project 2), NGRIP and NEEM (North Greenland Eemian Ice Drilling) (Fig. 3). Most of the new data presented in this thesis were obtained from the NEEM ice core, NW Greenland, drilled in 2008-2011 in the frame of an international project led by the Centre for Ice and Climate (CIC), Denmark, and a host of international collaborators including LSCE. The NEEM site is complementary to previous Greenland deep drilling sites, because the source of water vapour is different, marked by a strong contribution of summer air masses from the Labrador Sea (Steen-Larsen et al., 2011). Sequence comparisons of fast instabilities at NEEM, NGRIP, and GRIP should thus allow detection of regional climate variability in Greenland and its source regions of water vapour.

NEEM ice core
77.45 °N, 51.06 °W
2484 m above sea level
T = -29 °C, δ^{18}O = -33 ‰
Accumulation 0.22 m.i.e.yr^{-1}

NGRIP ice core
75.10 °N, 42.32 °W
2917 m above sea level
T = -31.5 °C, δ^{18}O = - 35.5 ‰
Accumulation 0.19 m.i.e.yr^{-1}

GISP2 ice core
72.58 °N, 38.48 °W
3214 m above sea level
T = -31.4 °C, δ^{18}O = -35.01 ‰
Accumulation 0.248 m.i.e.yr^{-1}

GRIP ice core
72.58 °N, 37.64 °W
3238 m above sea level
T = -31.7 °C, δ^{18}O = - 34.9 ‰
Accumulation 0.23 m.i.e.yr^{-1}
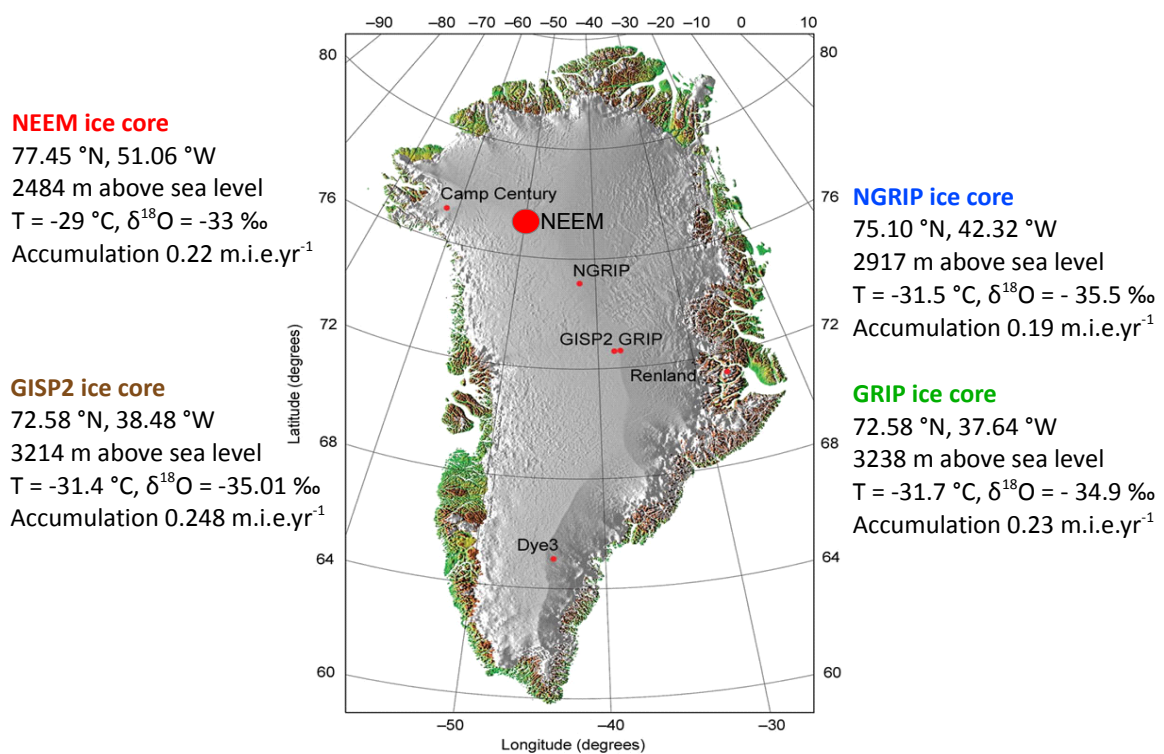
Figure 3: Location of the deep ice core drilling sites in Greenland. Source: http://www.iceandclimate.nbi.ku.dk/

Main scientific questions and organisation of this manuscript

Can we use ^{17}O excess from Greenland ice cores as a tracer for relative humidity at the oceanic vapour source? Chapter 1 presents the new tracer ^{17}O excess recently measured in vapour, snow and ice. We briefly present the theory on water isotopes (δ^{18}O, d-excess, ^{17}O excess) used to reconstruct the water cycle. We then report the article published by Landais et al. (2012b), presenting the first ^{17}O excess data from Greenland, where we contributed to the ^{17}O excess measurements. This article investigates the possibility of using oxygen 17 from Greenland snow and ice as a tracer for the relative humidity of the vapour source. This study paves the way for paleoclimate studies using ^{17}O excess measured in Greenland ice cores.

How to reference methane isotopes vs primary standards for carbon and hydrogen isotopes? Methane mixing ratio and isotopes have been widely used in paleoclimate studies. However, so far there is no universal procedure to reference methane isotopes vs the internationally recognized primary standards, VBDP for carbon isotopes and VSMOW for hydrogen isotopes. In Chapter 2, in collaboration with P. Sperlich from CIC, we develop such a protocol. This work has been published in Sperlich et al. (2012), and this article is reported here. In Chapter 5, published methane mixing ratio and isotopes from ice cores measured in different laboratories, together with other ice core proxies, will be used to reconstruct the response of the biosphere to Heinrich Event 4.

What was the sensitivity of the water isotope δ^{18}O to temperature in Greenland during the last glacial period? The evolution of the isotopic composition of nitrogen trapped in the ice bubbles, δ^{15}N, combined with firn modelling allows us to reconstruct the past

temperature and accumulation rate histories in Greenland. In Chapters 3 and 4, δ^{15}N and Δage (ice age - gas age) data and two different firn models are used to quantitatively reconstruct the past temperature and accumulation rate at different ice core drilling sites in Greenland. We propose a methodology to estimate the uncertainty assigned to accumulation and temperature reconstruction linked to the firn modelling method. The obtained δ^{15}N-based temperature scenarios will be then compared to the water isotope records. This will be done in particular for the NGRIP ice core, from the Holocene to the Eemian, covering the entire last glacial period. Such comparison allows us to study what influenced the water isotopes in the past, and thus to better reconstruct the past hydrological cycle.

What was the spatial expression of the Greenland climate over a sequence of DO events? In chapter 4, we use δ^{15}N data and firn models to quantitatively reconstruct temperature and accumulation rates at NEEM, NGRIP, GRIP and GISP2, focusing on the sequence of Dansgaard-Oeschger events 8 to 10 during Marine Isotopic Stage 3. The different locations of these drilling sites, from 72.58°N to 77.45°N and 37.64°W to 51.06°W, allowed us to reconstruct the spatial gradients of temperature and accumulation rate changes during these abrupt climatic events. These results will be compared to the water isotope spatial gradients as well as to atmospheric general circulation models (AGCM) studies, in order to identify what influenced (e.g., oceanic circulation, sea-ice cover) the Greenland climate during these events.

Can we identify the fingerprint of Heinrich events in ice cores? No consensus exists for robustly identifying the counterparts of Heinrich events in ice cores. This motivates an exploration of Greenland ice cores for proxies sensitive to climate at mid to low latitudes. In this last chapter, we develop a multi-proxy approach by combining water isotopes (δ^{18}O, d-excess, ^{17}O excess), methane concentration and isotopes as well as other ice core proxies, with the aim to assess the sequence of events from low to high latitudes surrounding Heinrich Event 4 ($\sim$39 ka b2k).

Chapter 1

Water stable isotopes from Greenland ice cores: a proxy for the present and past water cycle

1.1 Introduction

Measurements of δD (deuterium) and δ^{18}O (oxygen 18) have been performed on Greenland snow and ice throughout the last six decades (e.g., Dansgaard et al., 1969). Combined with water isotope modelling, these data help to reconstruct the present and past hydrological cycle. More recently, analytical developments have made it possible to measure the oxygen 17 content in the water molecule, giving access to the triple (stable) isotopic composition of water (e.g., Barkan and Luz, 2005). This new tracer is expected to bring complementary information on the relative humidity at the source of vapour that falls as precipitation over Greenland (e.g., Angert et al., 2004; Landais et al., 2008a; Winkler et al., 2012).

In this chapter, we contribute to a better understanding of the oxygen 17 measured in Greenland vapour and recent snow. We first present the theory on water isotopes used to reconstruct the water cycle. We then report the article published by Landais et al. (2012b), where we contributed to the oxygen 17 measurements, investigating the possibility to use oxygen 17 from Greenland snow and ice as a tracer for the relative humidity of the vapour source. This study paves the way for paleoclimate studies using oxygen 17 measured in Greenland ice cores.

1.2 The water cycle and associated isotopic fractionation

1.2.1 Natural abundances of isotopes and isotopologues in the environment

In the environment, numerous atoms have one or several stable isotopes, not subject to radioactive decay. Isotopes are atoms with the same number of protons but a different number of nucleons, and therefore a different atomic mass. For oxygen, the light isotope is ^{16}O and the heavy isotopes ^{17}O and ^{18}O. For hydrogen, ^{1}H is the light isotope (written H hereafter) and ^{2}H the heavy isotope (also called deuterium and written D). Each of these isotopes has a specific abundance in the environment, H and ^{16}O being the most abundant ones (Table 1.1 p. 6).

isotope or isotopologue	relative abundance (%)
^{16}O	99.760
^{17}O	0.035
^{18}O	0.205
H	99.985
D	0.015
H_2^{16}O	99.730
H_2^{17}O	0.035
H_2^{18}O	0.205
HD^{16}O	0.015

Table 1.1: Natural abundances of oxygen and hydrogen isotopes (Mook, 2001, Chapter 7).

Molecules made of the same atomic species but with different isotopes of these atoms are called isotopologues. For the water molecule H_2O, the most abundant ones are: H_2^{16}O, H_2^{18}O, H_2^{17}O, HDO (Table 1.1 p. 6).

1.2.2 Isotopic ratio and δ notation

H.C. Urey and H. Craig are the founding fathers for isotope ratio mass spectrometry (IRMS, see Sect. 1.3.3 p. 17). This experimental technique allows the measurement of the ratio of a given isotopologue compared to another one. Given the very low abundance of the heavy isotopes in general, and because measuring ratio of different isotopologues is much more accurate than measuring their absolute abundance, these quantities are expressed in *isotopic ratios*, the ratio of the rare isotope divided by the abundant isotope:

$$^{18}R \;=\; \frac{^{18}O}{^{16}O} \text{ for isotope } ^{18}\text{O in the isotopologue } H_2^{18}\text{O.} \qquad (1.1)$$

To allow comparison of measurements performed on different mass spectrometers, reference materials have been introduced. These reference materials have an isotopic ratio that has been accurately measured and their value is defined by the IAEA (International Atomic Energy Agency). For water, the absolute reference material is water representing the isotopic composition of the ocean. Its isotopic ratio has been measured by Baertschi (1976): $^{18}R_{VSMOW} = 0.0020052$. At present, this standard is prepared by the IAEA in Vienna and called VSMOW, Vienna Standard Mean Ocean Water.

Isotopic ratios measured on other water samples are expressed vs VSMOW using the δ notation:

$$\delta^{18}O_{sample} \;=\; \frac{^{18}R_{sample}}{^{18}R_{VSMOW}} - 1 \qquad (1.2)$$

By definition, $\delta^{18}O_{VSMOW}$ and δD_{VSMOW} equal zero. δ values have no unit. Usually, their numeric value is so small that a factor 1000 is applied and the factor ‰ (permil) is then written after the value. Another common unit is permeg in which the delta value is multiplied by 10^6.

1.2.3 Equilibrium and kinetic isotopic fractionation

Mass differences in between isotopologues modify their physical and chemical properties (Mook, 2001, Chap. 3), resulting in *isotopic fractionation* (a more complete description can be found in Winkler, 2012):

- the saturation vapour pressure for the heavy isotopologues of water is lower than for the light isotopologues relative to the source water. Conversely, condensed phases (liquid compared to vapour, for example) tend to be enriched in heavy isotopologues. This phenomenon is responsible for *equilibrium fractionation*. A detailed description of

the macroscopic and microscopic processes can be found in Winkler (2012) and Mook (2001);

- heavy isotopologues are less mobile, according to the relation: $k\,T = 1/2\,m\,V^2$, where k is the Boltzmann constant, T the absolute temperature, m the mass and V the average molecular velocity. This effect leads to *kinetic fractionation*.

An equilibrium fractionation can occur between two elements A and B in equilibrium (e.g., liquid water and vapour in a closed chamber). The equilibrium fractionation factor α_{eq} is defined as the ratio of the isotopic compositions of these two elements: $\alpha_{eq} = R_A/R_B$. Its value varies with the temperature.

Between liquid water (l) and vapour (v) for ^{18}O in $H_2^{18}O$, alpha_{eq} is:

$$^{18}\alpha_{eq} = \frac{^{18}R_l}{^{18}R_v} \tag{1.3}$$

so that $^{18}\alpha_{eq}$ is more than one.

The kinetic fractionation factor has a specific expression for each given process. Equilibrium and kinetic fractionation coefficient between vapour–liquid and vapour–ice for the water isotopologues $H_2^{18}O$ and HDO have been determined by theory and laboratory experiments; they are a function of temperature (see Ellehoj, 2011, for an overview). Below are described more in detail the effect of equilibrium and kinetic isotopic fractionation in the water cycle.

1.2.4 From vapour over the ocean to snow in Greenland

Vapour formation

Craig and Gordon (1965) proposed a model for evaporation from a liquid surface and we summarise it here. The water cycle starts with evaporation of the ocean, producing water vapour. First, equilibrium fractionation occurs between the liquid phase and a thin layer of air assumed to be saturated with water vapour (relative humidity = 100%); the vapour formed is relatively depleted in heavy isotopes compared to the ocean, because of the difference of saturation vapour pressure of the various isotopologues. Then, water vapour progressively ascends by (molecular and eddy) diffusion in the atmospheric boundary layer, that is not saturated with vapour (relative humidity less than 100%). Light molecules are faster, creating a kinetic fractionation that is superimposed on the equilibrium fractionation.

For evaporation over the ocean, the kinetic fractionation has been described by Merlivat and Jouzel (1979):

$$\alpha_k = \frac{1 - kh}{1 - k} \tag{1.4}$$

where h is the relative humidity of the air and k is a function of the wind regime in the boundary layer and decreases for more windy regimes. For a subtropical ocean, $k_{18_O}=0.006$ and $k_D = 0.88\,k_{18_O}$. The apparent or effective fractionation coefficient α_{eff} between oceanic water and vapour above the boundary layer is (Merlivat and Jouzel, 1979):

$$\alpha_{eff} = \frac{\alpha_{eq}(1 - kh)}{1 - k} \tag{1.5}$$

An air parcel reaching the free atmosphere has therefore an isotopic composition:

$$\delta_v = \frac{1-k}{\alpha_{eq}(1-kh)} - 1 \tag{1.6}$$

Transport: Rayleigh distillation process, rain and snow formation
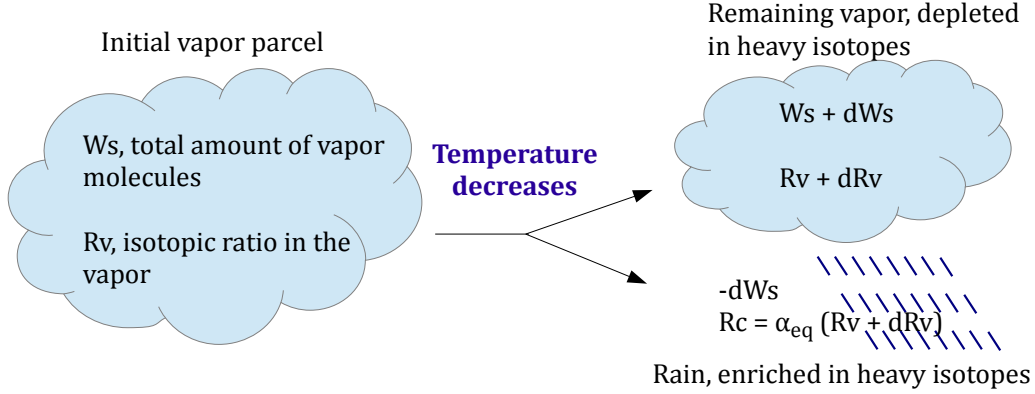
Figure 1.1: Schematic of the Rayleigh distillation process.

The air temperature decreases from the tropics towards the poles. This temperature decrease causes the saturation vapour pressure of the air to decrease, and the vapour parcel (initial amount of vapour: W_{s0}) to progressively condensate and loose vapour ($W_s + dW_s$, dW_s being a negative value). This process can be described by a Rayleigh distillation (Fig. 1.1). The Rayleigh distillation process does not take convection into account.

The first step in the Rayleigh distillation assumes that condensation of vapour occurs only when the parcel is saturated with vapour (relative humidity = 100 %), meaning that only equilibrium fractionation occur between vapour and the formed droplets of water. The cloud is assumed to be an open system: the water droplets produced by vapour condensation are directly removed from the cloud by rain, without further interaction with the remaining water vapour in the cloud. The formed water droplets are enriched in heavy isotopes, the remaining vapour is depleted in heavy isotopes compared to the rain and to the original water vapour in the cloud. Because the remaining vapour is depleted in heavy isotopes, the second rain formed from this vapour will be even more depleted in heavy isotopes compared to the first rain formed, but still enriched in heavy isotopes compared to the second vapour. As the cloud temperature decreases, the subsequent rain events make the amount of water vapor in the cloud to decrease and the water vapor and rain become progressively depleted in the heavy water isotopes. The largest the temperature gradient between the initial vapour parcel and the temperature at the precipitation site in Greenland, the less vapour remains in the parcel, and the more the final rain/snow is depleted in heavy isotopes. The isotopic ratio R_v in the remaining vapour in the vapour parcel can be well approximated by:

$$R_v = R_{v0} \left(\frac{W_s}{W_{s0}} \right)^{\alpha_{eq}-1} \tag{1.7}$$

and for the rain R_c (c for condensate):

$$R_c = \alpha_{eq} R_v = \alpha_{eq} R_{v0} \left(\frac{W_s}{W_{s0}} \right)^{\alpha_{eq}-1} \tag{1.8}$$

These equations really show that the isotopic composition of the precipitation is a function of the isotopic composition of the initial vapour, R_{v0}, and of how much vapour the parcel has already lost (W_s/W_{s0}). Figure 1.2 illustrates the Rayleigh distillation of a vapour parcel, using simplified calculations. Normally, α_{eq} is a function of temperature, and therefore the value of α_{eq} should be updated each time the temperature decreases. For this graph a constant α_{eq} value has been taken (following the approximation from Dansgaard, 1964).
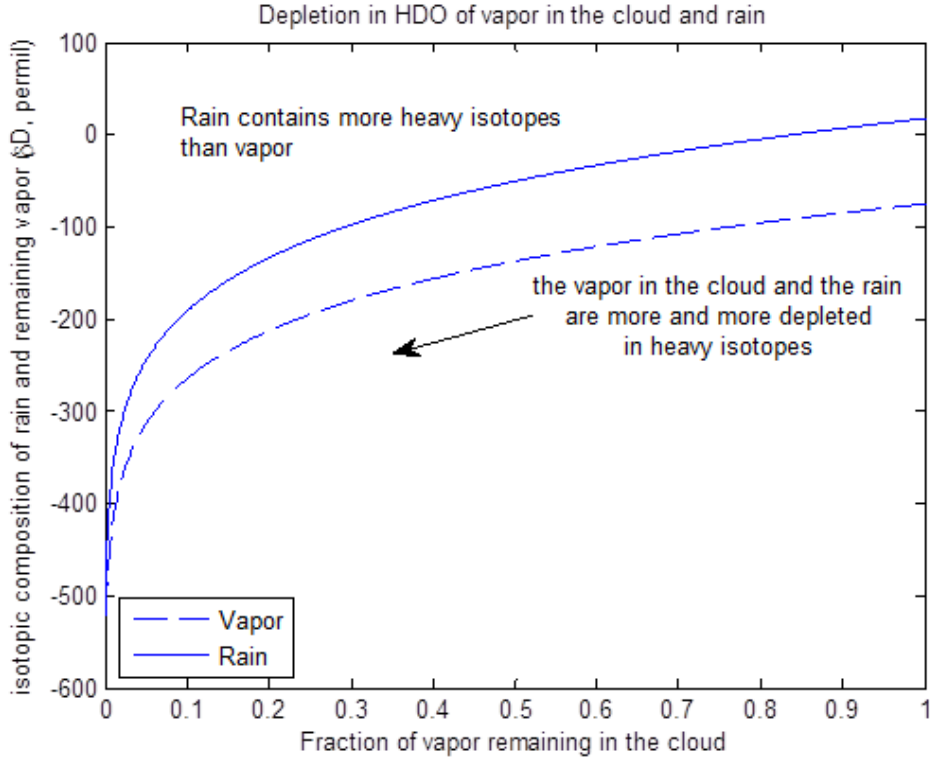
Figure 1.2: Isotopic composition of vapour and rain during a Rayleigh distillation process.

When the vapour parcel reaches a cold enough temperature (generally taken as -5°C, Ciais and Jouzel, 1994), vapour condenses into ice. Unlike condensation into liquid droplets where vapour and liquid are in equilibrium (as long as the droplets are less than 30 μm, Jouzel et al., 1975), condensation into ice crystals occurs without equilibration, because of the low mobility of molecules in the crystal. Therefore, kinetic fractionation is at play. Moreover, condensation into ice starts when the cloud still contains liquid water. A cloud model considering the possibility to contain vapour, liquid and ice has been proposed by Ciais and Jouzel (1994), called Mixed Cloud Isotopic Model (MCIM). In the MCIM, "According to the Bergeron-Findesein hypothesis, the value of the vapour pressure lies between the saturation over liquid water and the saturation over ice" (Ciais and Jouzel, 1994). This is also called "supersaturation". The super-saturation function S_i is not well know. In the MCIM it is parametrised by a linear function of temperature:

$$\alpha_k = \frac{S_i}{\alpha_{eq} \frac{D}{D'}(S_i - 1) + 1} \tag{1.9}$$

$$S_i = \frac{e_w}{e_i^s} = p + q\,T \tag{1.10}$$

with e_w the water vapour partial pressure in the cloud, e_i^s the saturation over ice, T the temperature, p and q chosen constants. This model has already been used to reconstruct the past Greenland temperature and source conditions (e.g., Masson-Delmotte et al., 2005a; Jouzel et al., 2007b), using measured δ^{18}O and d-excess (see Sect. 1.2.4 p. 10). It will be used here in Sect. 1.4 p. 20, applied to present-day δ^{18}O, d-excess and ^{17}O excess seasonal cycles in Greenland.

Meteoric water line and d-excess
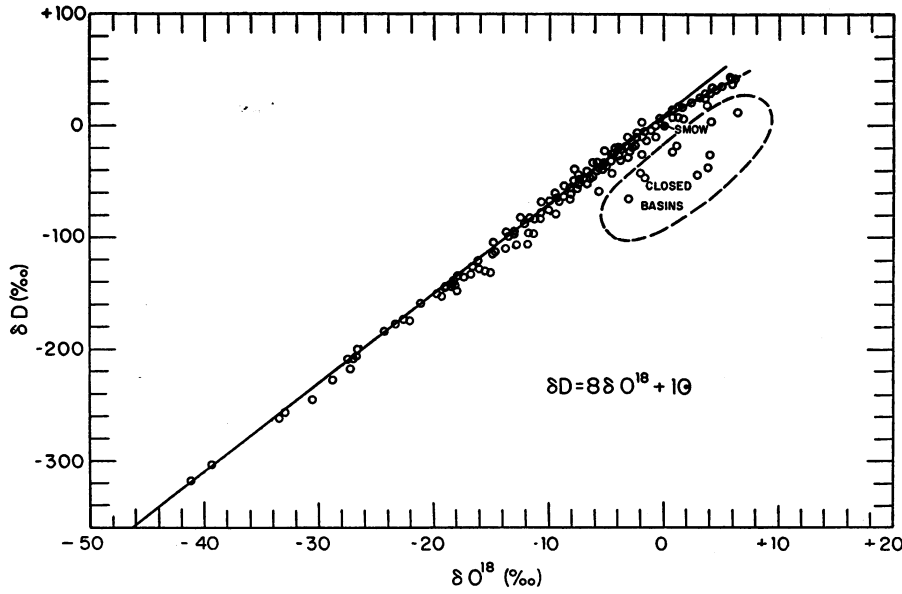
Figure 1.3: Craig (1961), Fig. 1. Original caption: *Deuterium and oxygen-18 variations in rivers, lakes, rain, and snow, expressed as per millage enrichments relative to Standard Mean Ocean Water (SMOW). Points which fit the dashed line at upper end of the curve are rivers and lakes from East Africa.*

Observations of the isotopic composition of meteoric waters at different latitudes have shown a linear relationship between δ^{18}O and δD, at a first order approximation (Craig, 1961, Fig. 1.3 p. 10):

$$\delta D = a\, \delta^{18}O + b \tag{1.11}$$

with a=8. This linear fit with a slope of 8 is known as the *meteoric water line*. It is mainly the result of the ratio of the equilibrium fractionation coefficients for δ^{18}O and δD, with $(\alpha_{eq,\delta D} - 1)/(\alpha_{eq,\delta^{18}O} - 1)$ being very close to 8. In reality, this slope is not constant but varies with temperature. The meteoric water line lead to define the deuterium excess (d-excess) as the signal in δ^{18}O and δD that deviates from this meteoric water line (Dansgaard, 1964):

$$\text{d-excess} = \delta D - 8\, \delta^{18}O \tag{1.12}$$

In average, d-excess is around 10 ‰ in meteoric waters. Simple models with a simplified Rayleigh distillation model shows that d-excess:

- increases with a decreasing source relative humidity,

- increases with the source temperature (T between 10 and 30 °C),

- increases with the source–site temperature gradient (i.e. when W_s/W_{s0} decreases, Fig. 1.2 p. 9).

Even if d-excess from Greenland ice cores preserves a signal linked to source conditions, it is influenced by the air trajectory and the site temperature and its variations cannot always be interpreted as a source signal only.

$\delta^{18}O$-temperature relationships

Comparing measured δ^{18}O in surface snow throughout Greenland with the measured local temperature makes it possible to reconstruct the so called spatial slope of δ^{18}O, known as α, with $\alpha = \delta^{18}O/T$. This spatial slope was estimated to be 0.67 ‰ °C^{-1} at present for Greenland by Johnsen et al. (1989). Using a larger dataset, Sjolte et al. (2011) estimated the present α to be 0.8 ‰ °C^{-1}. Using the GRIP isotopic record and the present-day Greenland spatial slope of 0.8 ‰ °C^{-1} to reconstruct past temperature, the Last Glacial Maximum (LGM, $\sim$25 ka b2k) would be less than 10 °C colder. However, other tools than water isotopes have been used to reconstruct the past temperature in Greenland, suggesting a much colder LGM.

One of these alternative methods is based on the measurement of the present-day borehole temperature profile, obtained after an ice core has been drilled. The heat diffusion in the ice is a slow process, and therefore the ice keeps a memory of the past temperature history at the surface of the ice sheet. An ice flow model is then needed to reconstruct what was the past temperature history and its influence of the present-day measured borehole temperature, compared to the influence of the geothermal heat flux, heating the ice from the bedrock, and the lateral advection of ice/heat towards the periphery of the ice sheet. (e.g., Johnsen et al., 1995; Dahl-Jensen et al., 1998; Cuffey and Clow, 1997). Such methods are well suited for reconstructing the major temperature anomalies (Little Ice Age, Medieval warmth, Holocene climatic optimum) back to the LGM. Paleo surface reconstructions beyond the LGM are difficult due to the warming effect of of the geothermal heat flux that wipes out the surface temperature signal close to bedrock. Using borehole temperature measurements from GRIP, Dahl-Jensen et al. (1998) reconstructed a last glacial maximum 23°C colder than present day (Fig. 3.12 p. 85). When calculating the temporal slope which is the slope between variations in time of δ^{18}O and temperature (taking here the borehole-based temperature reconstruction for GRIP), it appears that the past temporal slope is lower than the present day observed spatial slope of 0.8 ‰ °C^{-1}.

Another method to reconstruct past Greenland temperature relies on nitrogen isotopes measured in the ice bubbles that are effected by local temperature variations where the snow is deposited. This method is described in details in Chap. 3. Temperature reconstructions from this method also suggest that the past sensitivity of water isotopes to temperature change is lower than the present-day spatial slope (e.g., Lang et al., 1999; Landais et al., 2004b; Huber et al., 2006; Capron et al., 2010a).

In the following chapters, we will combine δ^{18}O data with temperature reconstructions based on δ^{15}N data in order to characterise changes in isotopes-temperature relationships through time (over a sequence of Dansgaard-Oeschger events) and space (comparing results from the NEEM, NGRIP, GISP2 and GRIP ice cores).

What drives δ^{18}O and d-excess in Greenland?

We have introduced above simple Rayleigh distillations models. Water isotopes are also implemented in atmospheric general circulation models (AGCM) to improve our understanding of the hydrological cycle. This has been done for example by Werner et al. (2000), whose simulations supported LGM temperature reconstruction from borehole and δ^{15}N thermometry. Moreover, their results suggested that the seasonality of the precipitation at the LGM was shifted towards summer snow precipitation, explaining (at least partly) the low past sensitivity of water isotopes to temperature. Masson-Delmotte et al. (2011) investigated the last interglacial period in Greenland and also reconstructed a temporal slope lower than the present-day spatial slope. A review on the climatic parameters influencing δ^{18}O and δD in snow falling in Greenland and Antarctica was made by Jouzel et al. (2003), and we report the conclusions for Greenland hereafter.

- The main driver of the isotopic signal in Greenland is the source-site temperature gradient, in agreement with a Rayleigh distillation model (Fig. 1.2 p. 9). During glacial-interglacial as well as stadial-interstadial changes, the temperature change in Greenland is much larger than the temperature change in source regions. Therefore, in a first approximation, δ^{18}O is mainly affected by the temperature in Greenland, with a minor effect of the source temperature.

- source effects: using Dye-3 δ^{18}O, d-excess data and simple isotopic modelling, Johnsen et al. (1989) showed that during GS, the source of vapour is shifted southwards, where the temperature is higher. This enhances the distillation process and creates an anomalously low δ^{18}O signal in the snow falling in Greenland. The relative humidity at the source can also influence δ^{18}O of the precipitation falling in Greenland.

- origin of precipitation: AGCMs equipped with water tagging suggest that during cold periods, and especially periods of voluminous Laurentide ice sheet, the relative contribution of moisture coming from the Pacific, across the Canadian Arctic, may increase (Werner et al., 2001; Bromwich et al., 2004). This moisture arrives in Greenland with a low δ^{18}O signal, decreasing the mean δ^{18}O signal in the ice. Logically, this effect may be larger in Northern Greenland and decrease going south.

- seasonality of precipitation: at present, the snow fall in central Greenland is distributed year-round in average. However, inter annual variability of precipitation seasonality influence the δ^{18}O registered in ice cores (Persson et al., 2011). Over long timescales, AGCMs suggest there are pronounced changes in the seasonal cycle of snowfall between cold and warm periods like glacial/interglacial periods (e.g., Werner et al., 2000). During cold periods, the winter storm tracks tend to move southwards, bypassing Greenland. Consequently the snow reaching Greenland is mainly the summer snow, with the summer isotopic signal causing the measured δ^{18}O to be higher relative to the mean annual temperature. δ^{18}O actually records the accumulation-weighted surface temperature.

- dust load in the atmosphere: in a cloud, dust particles act as condensation nuclei. A high dust load facilitates the condensation of vapour. This may affect the supersaturation function. Unfortunately this effect remains quite unknown.

- possible changes in the vertical structure of the atmosphere: δ^{18}O is influenced by the condensation temperature in the cloud. If the vertical temperature gradient in the atmosphere changes, this affects δ^{18}O, even if the temperature at the surface of the ice sheet remains unchanged.

The sensitivity of δ^{18}O and d-excess to site (T$_{site}$) and source temperature (T$_{source}$) has been tentatively reconstructed by Masson-Delmotte et al. (2005a), using the MCIM model constrained by GRIP δ^{18}O and d-excess data:

$$\Delta\delta^{18}\text{O} = 0.88\Delta\text{T}_{\text{site}} - 0.58\Delta\text{T}_{\text{source}} + 0.9\Delta\delta^{18}\text{O}_{\text{sw}} \qquad (1.13)$$

$$\Delta\text{d-excess} = -0.16\Delta\text{T}_{\text{site}} + 0.74\Delta\text{T}_{\text{source}} - 1.9\Delta\delta^{18}\text{O}_{\text{sw}} \qquad (1.14)$$

where Δ refers to anomalies from present-day conditions, and $\Delta\delta^{18}O_{sw}$ is the sea water isotopic composition anomaly compared to present-day. In summary, δ^{18}O is mostly sensitive to a site temperature change, and d-excess to a source temperature change. For d-excess, the site temperature effect increases with increased site temperature variations and is believed to mask the source signal in d-excess for the Dansgaard-Oeschger events in Greenland (site temperature changes up to +16°C, Huber et al., 2006) or glacial-interglacial temperature changes (e.g., Landais et al., 2004a; Masson-Delmotte et al., 2005a; Jouzel et al., 2007b).

1.3 ^{17}O excess: a tracer for source relative humidity

1.3.1 Definition and fractionation coefficients

In meteoric water, a linear relationship between $\ln(\delta^{17}\text{O} + 1)$ and $\ln(\delta^{18}\text{O} + 1)$ is observed, with a slope of 0.528 (Meijer and Li, 1998; Landais et al., 2008a; Luz and Barkan, 2010). By analogy to the d-excess, this has led to the definition of the ^{17}O excess (Barkan and Luz, 2005):

$$^{17}\text{O excess} = \ln(\delta^{17}\text{O} + 1) - 0.528\ln(\delta^{18}\text{O} + 1) \qquad (1.15)$$

Unlike d-excess that is a linear function of δ^{18}O, ^{17}O excess is a logarithmic function of δ^{18}O. This has implications for calculating the isotopic composition d-excess and ^{17}O excess of a water mass resulting from the mixing of two different water masses: in a δ^{18}O vs δD diagram, the mixing line for d-excess is straight while it is curved for ^{17}O excess (Fig. 1.4, black lines).

Measurements between 10 to 40°C in conditions of liquid-vapour equilibrium have shown that the ratio $\ln(^{17}\alpha_{eq})/\ln(^{18}\alpha_{eq})$ is equal to 0.529 and does not vary with temperature (Barkan and Luz, 2007; Luz et al., 2009). This estimation is in agreement with a theoretical determination of the equilibrium fractionation factor (Van Hook, 1968). As a consequence, ^{17}O excess is not expected to vary between the vapour and the liquid phase for equilibrium processes, like rain formation. For kinetic fractionation, the slope is not 0.529 but lower, equal to 0.518, as determined by experimental investigations (Barkan and Luz, 2007; Luz et al., 2009).

Barkan and Luz (2007) and Luz et al. (2009) showed that during evaporation processes, ^{17}O excess is insensitive to temperature and mainly depends on the relative humidity. This

has been later supported by e.g. a modelling study from Risi et al. (2010), using a single column model equipped with a parametrisation for convection processes, to represent evaporation processes over tropical and subtropical oceans. This study also showed that on the way to the poles, the ^{17}O excess signal can be slightly lowered by the evaporative recharge happening at mid to low latitude (Fig. 1.4).
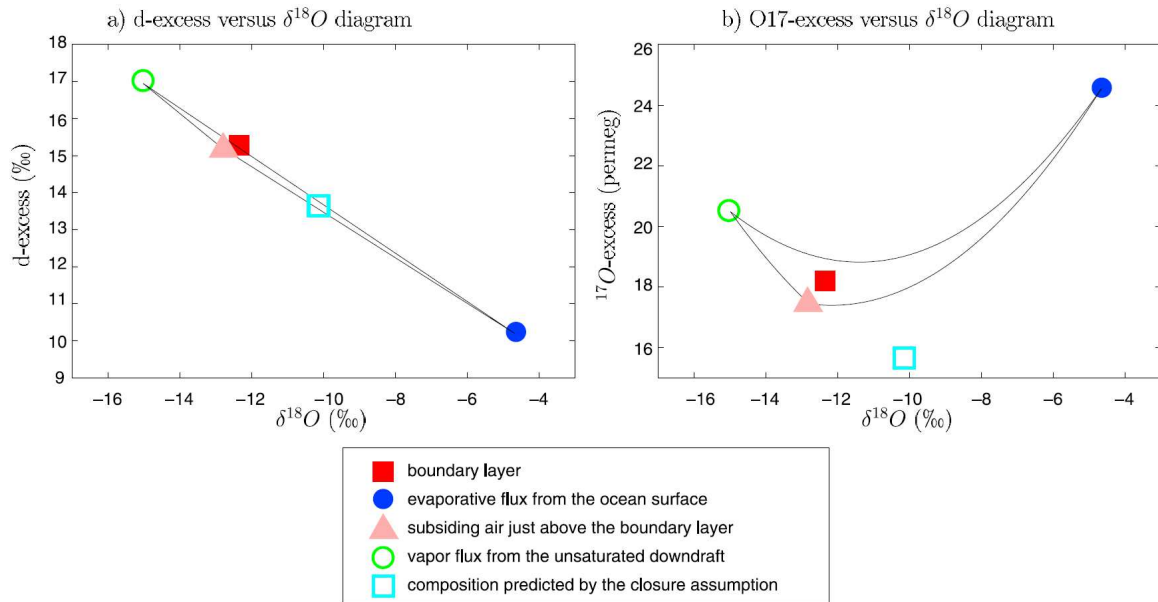
Figure 1.4: Risi et al. (2010), Fig.2. Original caption: *Isotopic composition of the boundary layer simulated by the model (red solid square) in $\delta^{18}O$ versus (a) d-excess and (b) ^{17}O excess diagrams. The composition of the unsaturated downdraft vapour mass flux into the boundary layer, the evaporative flux from the ocean, and the subsiding environment just above the boundary layer are shown with green open circles, blue solid circles, and magenta solid triangles, respectively. Mixing lines (lines representing the ensemble of possible mixtures between two samples) are in black. The isotopic composition of the boundary layer predicted by closure assumption for the simulated surface conditions is shown with cyan open squares.*

1.3.2 ^{17} excess measured in polar environments: pioneer results
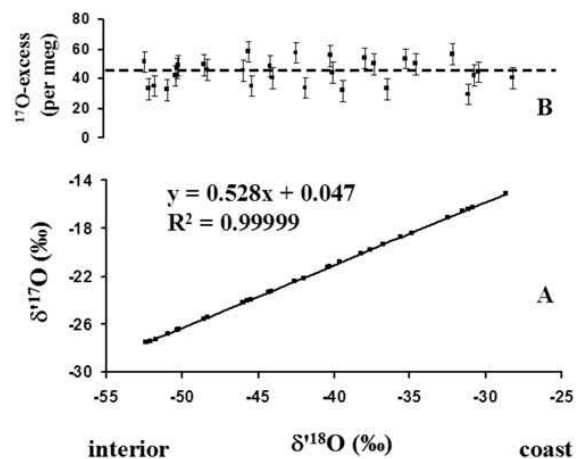
Figure 1.5: Landais et al. (2008a), Fig. 1. Original caption: *(A) The relationship among $\delta'^{17}O$ [ln($\delta^{17}O$ + 1)] and $\delta'^{18}O$ [ln($\delta^{18}O$ + 1)] and (B) ^{17}O excess in the Antarctic transect.*

We have seen that the relative humidity at the source is preserved in the ^{17}O excess of a vapour mass that reaches the poles (Greenland or Antarctica). Now the question is: is
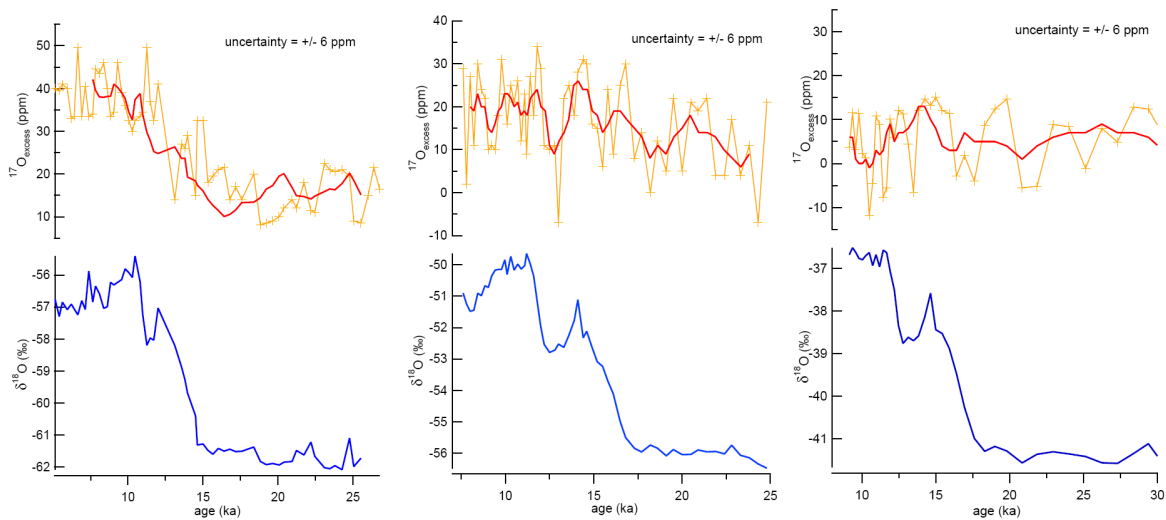
Figure 1.6: Winkler et al. (2012), Fig.2. Original caption: *Upper panel: record of ^{17}O excess during the last deglaciation for the ice core sites of Vostok (a) from Landais et al. (2008a), EDC (b) and TD (c). The thick red lines represent a 5 point moving average. The temporal resolution of the data corresponds to about 2 data points per 1000 yr. Lower panel (blue): Here we present δ^{18}O values which were measured earlier by equilibration method; the Vostok data are from Vimeux et al. (1999), while the EDC data were published by EPICA community members (2006) and more recently the TD data by Stenni et al. (2010). Our δ^{18}O measurements done by the fluorination method are not presented here, but are in agreement within $\pm 0.5\permil$ with previous measurements (most of the difference is explained by a storage effect).*

this ^{17}O excess signal preserved in polar ice cores or is affected by other effects, e.g. kinetic effects during snow formation? This has been investigated by Landais et al. (2008a), by measuring the ^{17}O excess signal in surface snow samples along a transect from Terra Nova Bay (74.7°S 159.7°E) to Dome C (75.1°S 123.4°E), Fig. 1.5. The flat profile of ^{17}O excess along this transect suggests that ^{17}O excess is not affected by the colder temperature when going inland Antarctica, supporting for present-day the preservation of the source relative humidity signal in the ^{17}O excess measured in polar surface snow.

Landais et al. (2008a) and Winkler et al. (2012) measured the ^{17}O excess at Vostok (Central Antarctica), EPICA Dome C (EDC, East Antarctica) and Taldice (TD, coastal East Antarctica), over the last deglaciation (Fig. 1.6). They first observed different mean ^{17}O excess levels for all sites at present, and suggested different oceanic source regions characterised by different relative humidity for each site, as supported by AGCM simulations. Then, a different ^{17}O excess change was observed from the glacial to the interglacial period, for each site (stable at TD, +12 permeg at EDC, +20 permeg at Vostok). Winkler et al. (2012) explained these observations by a different change in relative humidity at the oceanic source region of each site (stable at TD, -10% at EDC). For the remote continental Vostok site, sensitivity tests with the MCIM evidenced that "*the dependence of ^{17}O excess on local temperature is highly sensitive to the choice of the supersaturation function*", meaning that local effects influence ^{17}O excess at Vostok, and possibly at EDC. Their general conclusion is that ^{17}O excess data from Antarctic coastal sites do preserve the signal of relative humidity changes in the oceanic source region over the last deglaciation, while ^{17}O excess at the Vostok site was influenced by local effects.

Further investigations at Vostok on present-day seasonal cycles of δ^{18}O, d-excess and

^{17}O excess have suggested that kinetic fractionation happening at low temperature, as well as a possible input of stratospheric water, where the ^{17}O excess is impacted by mass independent fractionation, are likely to affect the present and past Vostok ^{17}O excess (Landais et al., 2012a; Winkler et al., 2013).

In Sect. 1.4 of this chapter we continue the work of understanding ^{17}O excess in polar regions for present-day, and focus on the NEEM ice core drilling site, NW Greenland. This paves the way for an investigation of past ^{17}O excess variations in the NEEM ice core during a sequence of Dansgaard-Oeschger events, that will be carried out in Chap. 5.

1.3.3 ^{17}O excess measurements

Conversion of H_2O into O_2: fluorination line
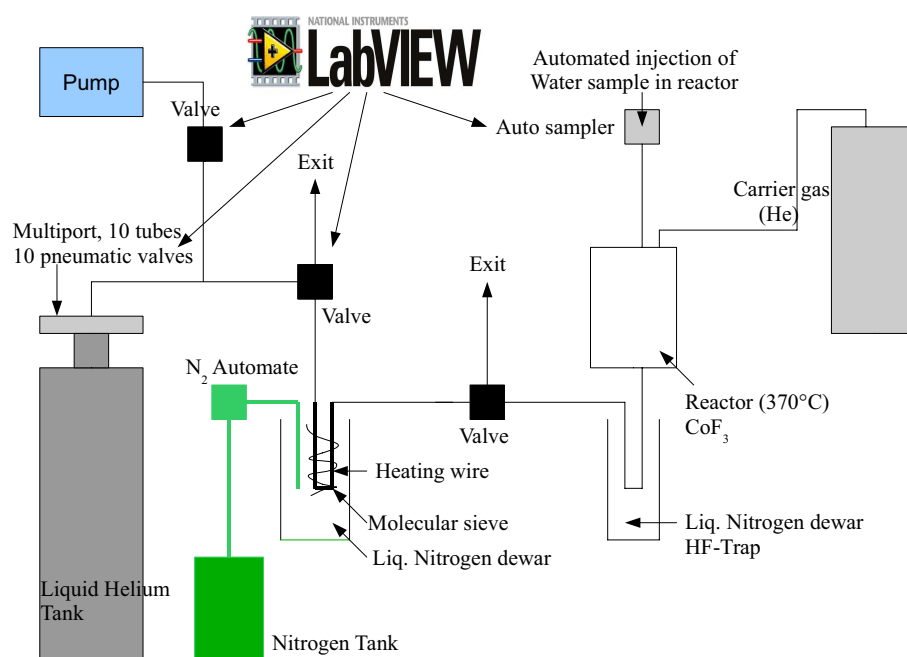
Figure 1.7: Winkler (2012), Fig. 3.1. Schematic diagram of the fluorination setup at LSCE.

High precision isotopic ratio measurements are traditionally performed by mass spectrometry measurement (see next section), meaning that the discrimination in between isotopes is done through mass measurements. To measure δ^{18}O and δ^{17}O, it is therefore necessary to separate the oxygen atoms from the hydrogen atoms, so that the measured oxygen masses are not influenced by the isotopic composition of hydrogen. To measure ^{17}O excess from the water molecule, the water also needs to be injected as a gas into the mass spectrometer. One way to do this is to quantitatively convert the water into oxygen O_2. This can be done by a fluorination reaction, as developed by Barkan and Luz (2005):

$$2H_2O + 4CoF_3 \rightarrow 4CoF_2 + 4HF + O_2 \tag{1.16}$$
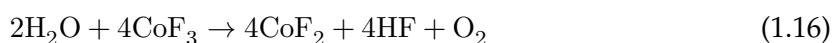
At LSCE, the experimental setup used to measure ^{17}O excess was built by A. Landais following Barkan and Luz (2005), see schematic diagram Fig. 1.7. Under a constant helium flow of $20\,\text{mL}\,\text{min}^{-1}$, A 2μL sample of liquid water is injected in a nickel tube heated up to 370°C, where the reaction with CoF_3 takes place. Then, the obtained O_2 and HF go

through a liquid nitrogen trap where HF gets frozen, while O$_2$ is quantitatively collected on a following molecular sieve trap also cooled with liquid nitrogen. The oxygen trapping on the molecular sieve lasts 20 min. Then, the oxygen trap is isolated from the nickel column and heated up briefly (1 min) in a first step to release the entrapped helium that degas faster than oxygen and gets pumped out. The oxygen trap now contains only water-derived oxygen. This trap is connected to a tube manifold cooled at liquid helium temperature and heated up so that the oxygen is released and trapped (during 8 min) inside one stainless steel tube of the tube manifold.

This procedure is completely automated and controlled by a Labview program. At LSCE, a 10-tubes manifold is available, so that 10 individual water samples can be converted into pure oxygen in one day. After 40 min to allow time for the oxygen to unfreeze, the tube manifold is connected to the mass spectrometer for measurements of δ^{18}O and δ^{17}O over night. We start and end each daily 10-samples measurement routine by one or several measurements of a water standard that undergo exactly the same experimental procedure as the samples. This is necessary to reference our measurements vs international water standards and to daily check the stability of the fluorination system and of the mass spectrometer.

Mass spectrometry measurements
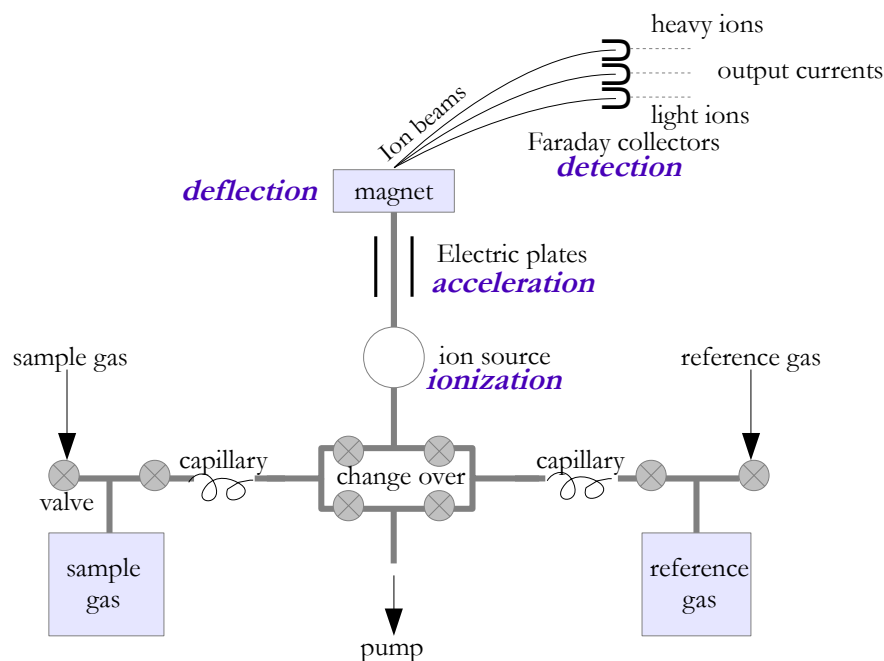
Figure 1.8: Principle of a mass spectrometer. In a dual inlet mode, sample gas (left) and reference gas (right) are alternatively introduced into the ionisation chamber of the mass spectrometer, through the changeover valves.

The water-derived oxygen is measured by mass spectrometry to determine its isotopic composition (Fig. 1.8 p. 17). The gas to be measured is introduced in the ionisation chamber (or source) of the mass spectrometer through a capillary. There, a filament is heated, releasing electrons that ionise the molecules when hitting them: O$_2$ becomes O$_2^+$. Then, the ionised molecules (charge q) go through electric plates, with an electric potential V, and get

accelerated. Their kinetic energy is given by:

$$qV = \frac{mv^2}{2} \tag{1.17}$$

with m their mass and v their velocity.

The ionised and accelerated particles then go through a magnetic field so the curvature of the trajectory is modified (deflection). The curvature radius r can be expressed as:

$$r = \sqrt{\frac{2mV}{qB^2}} \tag{1.18}$$

The parameters V and B (magnetic field) can be tuned in the mass spectrometer, but are kept constant over a set of measurements. Eq. 1.18 thus clearly shows that the ions are separated by their mass/charge ratio. As long as all the oxygen ions are all charged with one positive charge, they are correctly separated by their mass difference.

Then, each ion with its mass/charge ratio hits a Faraday cup, where the neutralisation of the ion beam generates a current (detection). This current goes through an amplifier, in a negative feedback mode: the input current is amplified, but this amplification is attenuated, and this negative amplification is controlled by a resistance. Amplifiers collecting ions derived from abundant isotopes are equipped with a high resistance (high attenuation of the amplification), while low resistances are used for amplifiers corresponding to rare isotopes. The final signal is registered in Volts. It is then used to calculate isotopic ratios.

At LSCE, a Delta-V mass spectrometer (Thermo Finnigan, Germany) is used, in a dual inlet mode: the sample and reference gases (both pure oxygen) are alternatively introduced in the mass spectrometer, 16 times each, so that each sample gas measurement is bracketed by reference gas measurements, and its isotopic composition is calculated vs the 2 adjacent reference gas measurements. This procedure improves the reproducibility of the measurements. We perform two sets of 16 measurements for each sample gas introduced.

The mass spectrometer is equipped with 10 Faraday cups and measures simultaneously 10 different mass/charge ratios (hereafter we assume they all have one positive charge): 28, 29, 30, 32, 33, 34, 36, 38, 40, 44. Mass/charge ratios 32, 33, 34 (noted M_{32}, M_{33}, M_{34}) correspond to the following oxygen molecules:

- M_{32}: $^{16}O_2$;

- M_{33}: $^{16}O^{17}O$, $^{17}O^{16}O$;

- M_{34}: $^{16}O^{18}O$, $^{18}O^{16}O$, $^{17}O_2$.

Assuming that the 3 isotopes are randomly distributed in the different isotopic molecules, the composition of each mass can be written in a probalistic way. We note P_i the probability to have the oxygen isotope ^iO, with i=16, 17 or 18:

$$M_{32} = P_{16}P_{16} \tag{1.19}$$

$$M_{33} = P_{16}P_{17} + P_{17}P_{16} = 2\,P_{16}P_{17} \tag{1.20}$$

$$M_{34} = P_{16}P_{18} + P_{18}P_{16} + P_{17}^2 = 2\,P_{16}P_{18} + P_{17}^2 \tag{1.21}$$

The measured isotopic ratios ^{33}R and ^{34}R can be written as:

$$^{33}R = \frac{M_{33}}{M_{32}} = \frac{2\,P_{17}}{P_{16}} = 2\,^{17}R \tag{1.22}$$

$$^{34}R = \frac{M_{34}}{M_{32}} = \frac{2\,P_{18}}{P_{16}} + \left(\frac{P_{17}}{P_{16}}\right)^2 = 2\,^{18}R + \,^{17}R^2 \tag{1.23}$$

Based on the measurements of masses 32, 33 and 34, it is then possible to calculate the exact ^{17}R and ^{18}R isotopic ratios:

$$^{17}R = \frac{^{17}O}{^{16}O} = \frac{^{17}P}{^{16}P} = \frac{1}{2}\,^{33}R \tag{1.24}$$

$$^{18}R = \frac{^{18}O}{^{16}O} = \frac{^{18}P}{^{16}P} = \frac{1}{2}\left(^{34}R - \,^{17}R^2\right) = \frac{1}{2}\left(^{34}R - \frac{1}{2}\,^{33}R^2\right) \tag{1.25}$$

Calculating ^{17}O excess gives:

$$^{17}O\text{ excess} = ln\left(\frac{^{17}R_{sample}}{^{17}R_{std}}\right) - 0.528 \cdot ln\left(\frac{^{18}R_{sample}}{^{18}R_{std}}\right) \tag{1.26}$$

$$^{17}O\text{ excess} = ln\left(\frac{^{33}R_{sample}}{^{33}R_{std}}\right) - 0.528 \cdot ln\left(\frac{\left(^{34}R_{sample} - \frac{1}{2}\,^{33}R^2_{sample}\right)}{\left(^{34}R_{std} - \frac{1}{2}\,^{33}R^2_{std}\right)}\right) \tag{1.27}$$

The measured ^{17}O excess for this work had all values between 10 and 70 permeg, while δ^{18}O values ranged from ~ -45 to $\sim -26\,‰$. Therefore, to approximate eq. 1.27 by

$$^{17}O\text{ excess} = ln\left(\frac{^{33}R_{sample}}{^{33}R_{std}}\right) - 0.528 \cdot ln\left(\frac{^{34}R_{sample}}{^{34}R_{std}}\right) \tag{1.28}$$

would have an effect less than 0.1 permeg on the calculated ^{17}O excess (see also Kaiser and Röckmann, 2008). We use eq. 1.28 to calculate ^{17}O excess.

Referencing ^{17}O excess vs VSMOW

All our water-derived oxygen samples are measured vs the same laboratory pure oxygen. To reference our ^{17}O excess measurements vs VSMOW (by definition, ^{17}O excess (VSMOW) = 0), we make water samples referenced vs VSMOW to go through exactly the same experimental steps as our water samples: conversion into oxygen by our fluorination line and measurement by mass spectrometry vs our laboratory oxygen standard. Mass spectrometers are usually subject to non-linearity effects. In particular, our mass spectrometer at LSCE measures different ^{17}O excess values in samples that have different δ^{18}O values, even if these two samples in reality have exactly the same ^{17}O excess. To solve this problem we use two water standards of known δ^{18}O and ^{17}O excess, with very different δ^{18}O values, covering the range of δ^{18}O in our samples. Our first laboratory standard is equivalent to VSMOW. Our second laboratory standard is very close to and referenced versus SLAP (Standard Light Antarctic Precipitation), with δ^{18}O (SLAP)=-55.5 ‰ (Gonfiantini, 1978) and ^{17}O excess (SLAP)=0 permeg (Schoenemann et al., 2013). This way, we can quantify what is the error in the measured ^{17}O excess of a sample due to its δ^{18}O value, and correct for this effect. All our ^{17}O excess samples are therefore calibrated on the VSMOW-SLAP scale. More details on our referencing procedures can be found in Winkler (2012).

1.4   Triple isotopic composition of oxygen in surface snow and water vapour at NEEM (Greenland)

Abstract. The isotopic composition of water in polar ice cores is commonly used to reconstruct the climatic conditions both at the site of precipitation and at the site of oceanic source region. Theoretical studies have suggested that the variability of the parameter ^{17}O excess resulting from the triple isotopic composition of oxygen in water should be driven by the relative humidity of the oceanic source region. Our new ^{17}O excess measurements in surface water vapour and snow at the Greenland NEEM camp demonstrate the potential of ^{17}O excess as a marker of source relative humidity. Using concomitant measurements of water vapour and precipitation, we first confirm the theoretical relationship between the fractionation coefficients at vapour-solid equilibrium $\alpha^{17}_{eq\_vap\_sol}$ and $\alpha^{18}_{eq\_vap\_sol}$ associated respectively with $\delta^{17}O$ and δ^{18}O: ln $(\alpha^{17}_{eq\_vap\_sol})/\ln(\alpha^{18}_{eq\_vap\_sol}) = 0.528$. Our data reveal ^{17}O excess seasonal variations in Greenland firn over the years 2003-2005. Their magnitude is of the order of 25 ppm, with a minimum in July leading d-excess maximum level reached ∼3 months later. This is in agreement with our understanding of ^{17}O excess and d-excess variations in polar regions with minima in ^{17}O excess in phase with maxima in source relative humidity and maxima in d-excess largely influenced by source temperature increase. In a large northern Atlantic sector, relative humidity reaches its seasonal maximum in summer, earlier than the sea surface temperature maximum which takes place in fall.

1. Introduction

Water isotopes (δD, δ^{18}O) have largely been used in the last decades to characterize past climate and hydrological cycle variations. In particular, measurements of δD or δ^{18}O in polar ice cores have documented polar temperatures in Antarctica and Greenland over respectively the past 800,000 and 123,000 years before present (EPICA community members, 2004; NGRIP members, 2004; Jouzel et al., 2007a). Combining δD and δ^{18}O measurements gives access to a second order parameter, deuterium excess (d-excess = δD $-8*\delta^{18}$O). From variations in ice core d-excess, past changes in the climate of the evaporative source regions (e.g. sea surface temperature) can be inferred (e.g. Vimeux et al., 1999, 2002; Cuffey and Vimeux, 2001; Stenni et al., 2001, 2010; Masson-Delmotte et al., 2005b; Jouzel et al., 2007a).

Along its way from the evaporation sources to the precipitation site, water masses undergo (1) mass loss by condensation and precipitation leading to isotopic distillation and (2) water vapour recharge through surface evaporation. At each phase change (evaporation, condensation, inverse sublimation), two types of fractionation may occur between the water vapour and condensed water (ice or liquid). Equilibrium fractionation is driven by the different water saturation pressures of the isotopic molecules. Kinetic fractionation is produced by the different diffusion rates in air of the different water isotopic molecules.

Despite a complex evolution of the isotopic composition of the water along the air mass trajectories, it is possible to link the final isotopic composition found in the ice cores to climatic parameters such as temperature or humidity in the regions of evaporation and/or precipitation. Based on theoretical models, methods have been developed to estimate site and source temperature from δD and δ^{18}O. Because of under-constrained equations, they had to assume simple relationships between relative humidity and source temperature (Vimeux et al., 2002) or ignore relative humidity changes (Stenni et al., 2001). These inversions have shown that δ^{18}O and d-excess are not unbiased markers of T$_{site}$ and T$_{source}$, respectively (Vimeux et al., 2002; Masson-Delmotte et al., 2005a; Jouzel et al., 2007a).

Water isotopes modelling has been used for quantifying the different influences on δ^{18}O and d-excess and improve climate reconstruction from ice cores. However, atmospheric general circulation models equipped with water isotopes are still unable to simulate a realistic glacial-interglacial shift in Antarctic or Greenland d-excess (e.g. Risi et al., 2010; Werner et al., 2011). The interpretation of water stable isotopes in ice cores is generally performed using isotopes modelling along a water mass trajectory (e.g. Jouzel and Merlivat, 1984; Johnsen et al., 1989; Ciais and Jouzel, 1994; Vimeux et al., 2002; Stenni et al., 2001, 2010; Masson-Delmotte et al., 2005b), possibly including recycling (e.g. Noone, 2008) or in intermediate com-

plexity model of atmospheric transport and isotopic distillation (e.g. Fisher, 1992; Hendricks et al., 2000; Kavanaugh and Cuffey, 2003). The results of these models are sensitive to poorly constrained parametrisations such as the relationship between water supersaturation in polar clouds and temperature, the fraction of water vapour remaining in the cloud or thresholds driving freezing conditions.

Recent analytical developments have made it possible to accurately measure a new tracer of the hydrological cycle, ^{17}O excess resulting from the combination of $\delta^{17}O$ and $\delta^{18}O$ in water: ^{17}O excess = $\ln(\delta^{17}O + 1) - 0.528 * \ln(\delta^{18}O + 1)$ (Barkan and Luz, 2005; Landais et al., 2008a). It should be noted that this anomaly is not related to mass independent fractionation as for the $^{17}\Delta$ anomaly observed in many molecules containing oxygen (e.g. Thiemens, 1999). ^{17}O excess only refers to fractionation processes in the hydrological cycle and has been introduced recently (Barkan and Luz, 2007; Landais et al., 2008a,b). Its definition is taken by analogy with the d-excess definition [d-excess=$\delta D - 8 * \delta^{18}O$ (Dansgaard, 1964)] since there is a linear relationship of slope 0.528 between $\ln(\delta^{17}O + 1)$ and $\ln(\delta^{18}O + 1)$ for meteoric waters (Meijer and Li, 1998; Landais et al., 2008a; Luz and Barkan, 2010). Laboratory experiments and measurements of ^{17}O excess of water vapour over the Southern Ocean have shown that ^{17}O excess is not affected by temperature at equilibrium fractionation and that ^{17}O excess in water vapour at evaporation mainly depends on relative humidity (Barkan and Luz, 2007; Uemura et al., 2010). This contrasts with d-excess which is sensitive to temperature at equilibrium fractionation. This is one of the reason why d-excess increases along air mass trajectories towards polar regions, reaching maximum values in central Antarctica (e.g. Masson-Delmotte et al., 2008). On the opposite, measurements of ^{17}O excess in surface snow in Antarctica have revealed stable levels along a traverse between Terra Nova Bay (coastal site, 74°50′S 164°30′E) and Dome C (East Antarctic plateau, 75°06′S 123°20′E) (Landais et al., 2008a). These measurements suggested that, unlike d-excess, ^{17}O excess in polar snowfall preserve the signature of the first vapour without subsequent biases along the air mass trajectory.

This simple interpretation should still be carefully considered since increasing kinetic effect during solid precipitation at very low temperatures may cause a decrease of ^{17}O excess with temperature in remote stations of East Antarctica (Miller, 2008; Luz and Barkan, 2010; Winkler et al., 2012). Moreover, an impact of stratospheric water vapour input has been suggested to influence ^{17}O excess in Central Antarctica (Miller, 2008; Winkler et al., 2012). This effect, if true, can only be significant in the remote regions of East Antarctica (such as at the Vostok station) where there is a combination of low accumulation rate and high water input from the stratospheric polar clouds (Gallée and Gorodestkaya, 2010). Calculations based on available data for stratospheric-tropospheric fluxes and ^{17}O excess measurements at the tropopause suggest that, even in Vostok, the maximum contribution should be of 6 ppm (Landais et al., 2008b). At NEEM, with a 10 times larger accumulation rate and no significant input from the stratospheric polar clouds, the contribution is less than 0.6 ppm. Another argument in favour of negligible contributions of stratospheric water vapour input in Greenland is the low level of natural tritium observed there over the last decades compared to the 10 times larger levels observed in remote East Antarctica stations where stratospheric input may be significant (Fourré et al., 2006). The numerous questions concerning the interpretation of ^{17}O excess in polar regions and the few available observations of ^{17}O excess motivate an improved documentation of spatial and temporal ice core ^{17}O excess variations. Combined with $\delta^{18}O$ and d-excess, ^{17}O excess should indeed improve past climate reconstructions.

The added value of ^{17}O excess has been investigated in modelling studies. $\delta^{17}O$ was implemented in the mixed cloud isotopic model (MCIM) (Ciais and Jouzel, 1994) by Landais et al. (2008a). This model was used to produce a quantitative interpretation of climatic changes over the last deglaciation based on the combined measurements of $\delta^{18}O$, d-excess and ^{17}O excess on the Vostok ice core, East Antarctica (Risi et al., 2010). The advantages of this method is that (1) the cloud parameters of the MCIM are tuned using an additional constraint, ^{17}O excess and (2) ^{17}O excess records help to disentangle the effects of source temperature and source relative humidity. Still, no experimental determination of the fractionation coefficient used for $\delta^{17}O$ at the vapour-solid equilibrium is available so far forcing modelling studies to rely only on its theoretical determination (Van Hook, 1968). Here, we aim at providing new information on $\delta^{17}O$ solid-vapour equilibrium fractionation and processes controlling seasonal ^{17}O excess variations from the first $\delta^{17}O$ measurements conducted on Greenland samples.

Within the frame of the International Polar Year, the new deep drilling project - NEEM - was initiated in North-West Greenland in 2007 to obtain a continuous climatic record back to the last interglacial period (http://neem.nbi.ku.dk/). This project has endorsed a program of surface isotope sampling (water vapour and precipitation) and shallow core drillings. (Steen-Larsen et al., 2011) describe the first δD and $\delta^{18}O$ measurements conducted on water vapour and precipitation, as well as seasonal cycles of the last 50

years using shallow cores sampled in 2008. Here, we take advantage of some of these samples to perform the first study of ^{17}O excess in Greenland water, snowfall and firn.

In Section 2, we will summarize the sampling procedures at NEEM as well as the analytical method allowing high precision ^{17}O excess measurements. The results for the water vapour and precipitation samples will be discussed as well as the variations of ^{17}O excess over three recent seasonal cycles from analyses of the top of a shallow core at NEEM (Section 3). Data will be interpreted using simple isotopic modelling. Measurements of water vapour vs. precipitation ^{17}O excess will be used to constrain the fractionation factor associated with δ^{17}O for solid-vapour equilibrium. Seasonal isotopic measurements and MCIM modelling will finally be combined to propose a coherent picture of climatic variations of the site and source climatic conditions (Section 4).
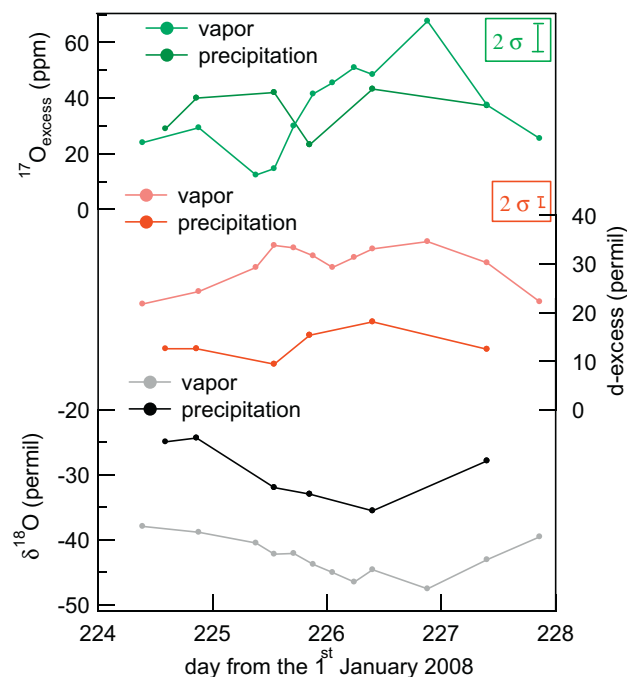
Figure 1.9: Evolution of the isotopic composition of water vapour and concomitant precipitation between August, 11th and August, 14th, 2008. From top to bottom: ^{17}O excess of the low level water vapour (light green) and of the precipitation (dark green); d-excess of the low level water vapour (light red) and of the precipitation (red); δ^{18}O of the low level water vapour (grey) and of the precipitation (black). Error bars are indicated in the top right corner for ^{17}O excess and d-excess. (For interpretation of the references to colour in this figure legend, the reader is referred to the web version of this article.)

2. Measurements and results

2.1. Sampling

Precipitation and water vapour sampling was performed in July-August 2008 at NEEM. The detailed sampling procedures are given in (Steen-Larsen et al., 2011). In short, the precipitation samples were collected on an event and sub-event basis from a white-painted wood table about 1.5 m above the snow surface located in the clean upwind zone of the camp. Surface atmosphere water vapour was collected using a cryogenic vapour trap (Craig and Gordon, 1965). The air was sampled from 3 m above the snow surface during 2 h to collect approximately 2-3 mL of water. The sampling frequency varied between one sampling every 4 h (12-13 August) and two samples a day (morning and evening). δD and δ^{18}O measurements of each sample were reported in (Steen-Larsen et al., 2011). Of particular interest is a passage of a cyclonic weather system between the 11th and the 14th of August, 2008. This event is recorded by isotopic depletion in the water vapour and precipitation samples. We have chosen this specific event, well documented thanks to high sampling frequency, to perform ^{17}O excess measurements on this period.

The shallow core NEEM07S3 (80.05 m depth) was drilled in 2007 and analysed for both δD and δ^{18}O between 1.15 and 19.65 m, depicting seasonal cycles between 1964 and 2005 (Steen-Larsen et al., 2011). Firn diffusion is known to affect the variability of δ^{18}O, δ^{17}O and δD (Johnsen et al., 2000; Johnsen, 1977). In order to minimize the influence of diffusion, we have targeted our ^{17}O excess measurements on the most recent seasonal cycles (years 2003-2005). At NEEM, the diffusion length was indeed estimated to ∼5.5 and ∼3.5 cm of snow respectively for the years 2003 and 2005 (Steen-Larsen et al., 2011). It slightly (∼20%) damps the magnitude of the most recent seasonal cycles (Appendix A). Since the annual layer thickness corresponding to these years is of the order of 60 cm, the phasing of the most recent seasonal cycles of δ^{18}O, d-excess and ^{17}O excess is not affected by diffusion (Appendix A).

2.2. Method for ^{17}O excess measurements

The ^{17}O excess measurements presented here have been obtained following the experimental set-up described by (Barkan and Luz, 2005). Basically, water is converted to oxygen by fluorination with CoF$_3$ reagent and the produced pure oxygen is trapped in a tube manifold immersed in liquid helium. Each oxygen tube is then analysed by dual inlet on a Thermo Delta V for δ^{17}O and δ^{18}O (two runs of 16 dual inlet measurements). Each water sample was converted and measured three times.

Two flasks of our working water standard are analysed daily to check the performance of both the fluorination line and the mass spectrometer. The $\delta^{18}O$ values, with associated uncertainties of 0.06‰, are expressed with respect to V-SMOW after calibration of our working standard vs V-SMOW and SLAP. V-SMOW is by definition associated with $\delta^{18}O$ and ^{17}O excess values of 0. With our method, we found a $\delta^{18}O$ value of -55‰ for SLAP. For coherency with previous measurements of $\delta^{18}O$ on the same samples (Steen-Larsen et al., 2011), we used the reference value of -55.5‰ for $\delta^{18}O$ of SLAP and stretched our $\delta^{18}O$ values on this VSMOW-SLAP scale (see Supplementary material). As for ^{17}O excess, the associated uncertainty is of 5 ppm (in this paper we use ppm instead of permeg as in previous studies following the recommendation of Coplen, 2011). In addition to SLAP which was not available in large quantity for the fluorination method at LSCE, we have chosen to take the ^{17}O excess reference value for the Dome F standard ($\delta^{18}O = -58$‰; ^{17}O excess = 1 ppm) given by Luz and Barkan (2010). This standard has been measured with ^{17}O excess = 21 ppm on average at LSCE during the course of the measurements displayed in this study. Because the first fractionation coefficients measured for the triple isotopic composition of oxygen in water were obtained by the group of Luz and Barkan (Barkan and Luz, 2005, 2007), we decided to correct our results for the 20 ppm difference between the two institutes. An important work of intercalibration has been performed between LSCE and the group of Luz and Barkan at the Institute of Earth Science in Jerusalem. Based on the systematic increase observed in the difference in ^{17}O excess for the same water with decreasing $\delta^{18}O$, we decided to use a linear scaling so that our ^{17}O excess values are corrected by 0.34 ppm ‰$^{-1}$ (^{17}O excess$\delta^{18}O$ $^{-1}$). As a concrete example for this correction, if we measure a sample with $\delta^{18}O = -35$‰ and ^{17}O excess = 50 ppm, we correct the ^{17}O excess value by 12 ppm (50 + 0.34 * 35 = 38 ppm). This correction has a significant influence on mean ^{17}O excess values but not on the relative ^{17}O excess variations on which are based the conclusions of this paper. Indeed, relative variations of $\delta^{18}O$ are <14‰, which results in a correction <5 ppm (14 * 0.34 = 4.7 ppm), hence of the same order as our analytical uncertainty.

The $\delta^{18}O$ measurements performed with our method can be compared to the $\delta^{18}O$ measurements performed by the classical CO_2 equilibration method with a similar analytical precision and published in Steen-Larsen et al. (2011). The same internal water working standards have been used for the two methods. For the shallow core samples, all the values agree within 0.15‰ with a mean of the absolute differences between the two series of measurements of

0.05‰. For the water vapour and precipitation samples, differences of up to 0.7‰ are observed. This may be caused by storage effects on these small samples as $\delta^{18}O$ is systematically higher in our series of measurements performed 1-2 years later than in the first series of measurements. We did not measure any significant (<5 ppm) difference in ^{17}O excess between a bottle of working standard correctly stored and a bottle of working standard affected by evaporation in a way that its $\delta^{18}O$ increased by 1‰.

3. Results
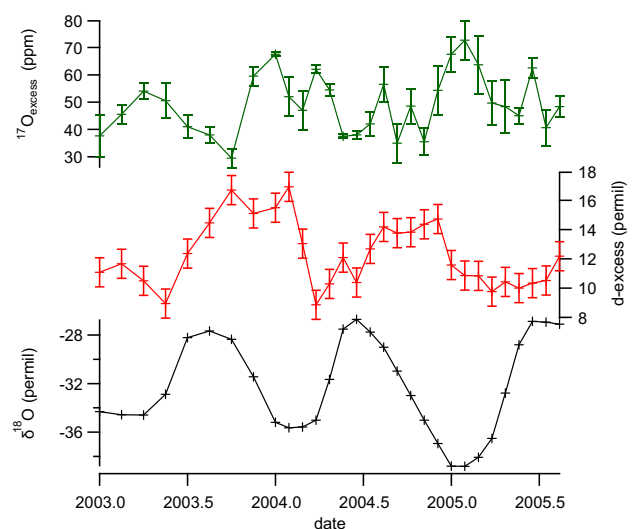
Figure 1.10: Seasonal evolution of the isotopic composition of water on a shallow core drilled at NEEM (NEEM07S3). From top to bottom: ^{17}O excess, d-excess and $\delta^{18}O$. The timescale was constructed so that the maximum of $\delta^{18}O$ occurs the 1st of August and its minimum the 1st of February (Steen-Larsen et al., 2011). Data are given as Supplementary material.

3.1. Water vapour vs. precipitation

Fig. 1.9 displays the evolution of ^{17}O excess, d-excess and $\delta^{18}O$ of precipitation and water vapour between the 11th and the 14th of August 2008. There is a clear shift in both $\delta^{18}O$ and d-excess between the water vapour and the precipitation samples. For the precipitation samples, $\delta^{18}O$ is more than 10‰ higher than the vapour samples, as expected for the condensed phase from fractionation theory. The d-excess of the precipitation is 15‰ lower than the water vapour d-excess. Assuming equilibrium between surface vapour and snow, this large difference in d-excess is explained from the solid-vapour equilibrium fractionation coefficients given by Merlivat and Nief (1967) and Majoube (1971). By contrast,

^{17}O excess has the same mean value (35 ± 13 ppm) in the water vapour and in the solid phase.

3.2. Seasonal cycle

Fig. 1.10 displays the evolution of ^{17}O excess, d-excess and δ^{18}O of the upper part of the shallow core (NEEM07S3) for years 2003-2005. A clear seasonal cycle is visible for δ^{18}O with higher values during summer (maximum the 1st of August by construction of the ice core chronology) and lower values during winter (minimum the 1st of February by construction of the ice core chronology). The d-excess cycle is shifted by ∼3 months and reaches the highest values ∼3 months later, in autumn, as previously observed in other Greenland ice cores (Hoffmann et al., 1998). Our ^{17}O excess data show an anti-phase with δ^{18}O (R2 = 0.3, p = 0.0015) with the highest values at the exact timing of δ^{18}O minima. Because only three seasonal cycles have been measured, we recognize that the phase relationships we claim remain partly subjective.

4. Simple modelling of water isotopes in polar snow

To quantify the different climatic influences on the isotopic composition of Greenland surface snow, we use the Mixed Cloud Isotopic Model (MCIM) (Ciais and Jouzel, 1994) adapted for the calculation of ice ^{17}O excess (Landais et al., 2008a; Risi et al., 2010). The MCIM describes the isotopic processes at each phase transition and thus the isotopic composition of (1) the condensed phase (liquid water or solid ice) and (2) the water vapour at each step from the oceanic source region to the precipitation site on the ice sheet. During liquid precipitation, only equilibrium fractionation occurs. Kinetic fractionation is taken into account for snowflakes formation. For this process, the relative proportion of equilibrium versus kinetic fractionation is controlled by a parametrisation of supersaturation as a linear function of temperature.

The model receives as main inputs (1) the characteristics of the oceanic moisture source: temperature, relative humidity, wind speed and surface atmospheric pressure of the source region as well as the isotopic composition of the surface ocean and (2) the condensation characteristics: condensation temperature and atmospheric pressure at the precipitation site (and possible intermediate steps). The MCIM includes several adjustable parameters (Ciais and Jouzel, 1994) such as the dependence of supersaturation on temperature or the fraction of condensate remaining in the cloud. This model has already extensively been tuned and used to interpret the isotopic composition of ice in Antarctica (e.g. Vimeux

et al., 1999; Stenni et al., 2001, 2010; Kawamura et al., 2007; Landais et al., 2008a) as well as in Greenland (e.g. Landais et al., 2004a; Masson-Delmotte et al., 2005b,a; Sodemann et al., 2008). In all these studies, the linear dependence of the supersaturation function with temperature, S = a − b * T, was tuned with *a* ranging between 1 and 1.02 and *b* between 0.002 and 0.004.

We have also conducted isotopic modelling using the model of Johnsen et al. (1989) (see details in Steen-Larsen et al., 2011). Once the supersaturation function of each model is tuned to fit the isotopic composition of surface snow (S = 1 − 0.008 T in Steen-Larsen et al. (2011)), both models predict the same variations of δ^{18}O, d-excess and ^{17}O excess in response to changes in climatic conditions. Here, we only use and show results from the MCIM.

5. Discussion

5.1. Fractionation coefficient between vapour and solid

In their analysis of vapour-precipitation isotopic composition, Steen-Larsen et al. (2011) have concluded that the surface water vapour is at isotopic equilibrium with the surface snow. The origin of water vapour could not be unambiguously identified: one possibility is that the equilibrium occurs between surface snow and low level water vapour; the other possibility is that low level water vapour equilibrates with snowfall. During the passage of the cyclonic system, surface water vapour δ^{18}O follows variations of δ^{18}O of precipitation with a lag of about 6 h (Fig. 1.9). There is thus evidence for a link between the isotopic composition of the snowfall and the subsequent isotopic composition of the surface vapour.

Table 1.2 presents the isotopic composition of the precipitation and the isotopic composition of the low level water vapour. In the last two columns, we have calculated the slope of the relationships between water vapour and precipitation isotopic compositions in a ln(δ^{17}O + 1) vs. ln (δ^{18}O +1) plot and in a δD/δ^{18}O plot so that:

$$\lambda_{vap-prec}^{17} = \frac{ln(\delta^{17}O+1)_{vap} - ln(\delta^{17}O+1)_{prec}}{ln(\delta^{18}O+1)_{vap} - ln(\delta^{18}O+1)_{prec}} \quad (1.29)$$

$$\lambda_{vap-prec}^{D} = \frac{\delta_{vap}^{D} - \delta_{prec}^{D}}{\delta^{18}O_{vap} - \delta^{18}O_{prec}} \quad (1.30)$$

with *vap* and *prec* indicating that the corresponding isotopic measurements were performed respectively on the water vapour or on the precipitation samples.

As already pointed out by Steen-Larsen et al. (2011), the δD-δ^{18}O values of precipitation and water vapour strongly support equilibrium between

Table 1.2: Isotopic composition of the precipitation (prec) and low level water vapour (vap) sampled between the 11th of August and 14th of August 2008 at NEEM. Day: since January 1st 2008. $\lambda^{17}_{\text{vap-prec}}$ and $\lambda^D_{\text{vap-prec}}$ are the slopes of the lines linking the isotopic compositions of low level water vapour and concomitant precipitation in a $\ln(\delta^{17}O + 1) - \ln(\delta^{18}O + 1)$ and dD – d18O plot, respectively. The uncertainties associated with individual $\lambda^{17}_{\text{vap-prec}}$ and $\lambda^D_{\text{vap-prec}}$ can directly be calculated from the uncertainties associated with the measurements of $\delta^{18}O$ (0.05‰), d-excess (1‰) and ^{17}O excess ($\sim$5 ppm). It leads to an uncertainty of 0.1 for $\lambda^D_{\text{vap-prec}}$ and of 0.001 for $\lambda^{17}_{\text{vap-prec}}$.

Day	$\delta^{18}O$ prec (‰)	d-excess prec (‰)	^{17}O excess prec (ppm)	$\delta^{18}O$ vap (‰)	d-excess vap (‰)	^{17}O excess vap (ppm)	$\lambda^{17}_{\text{vap-prec}}$	$\lambda^D_{\text{vap-prec}}$
224.6	−24.91	12.6	29	−38.33	22.8	26	0.528	7.24
224.9	−24.33	12.6	40	−38.83	24.2	29	0.529	7.20
225.5	−31.98	9.4	42	−42.23	33.8	15	0.530	5.62
225.8	−32.99	15.4	23	−43.50	32.0	39	0.527	6.42
226.4	−35.53	18.1	43	−44.63	33.1	48	0.527	6.35
227.4	−27.86	12.5	37	−43.08	30.2	37	0.528	6.83
$\lambda_{\text{vap-prec}}$, average							0.528	6.6
$\lambda_{\text{vap-prec}}$, standard deviation							0.001	0.6

vapour and surface snow or snowfall. We find that $\lambda^D_{vap-prec}$ is equal to 6.6 ±0.6; a comparable value is obtained when using the isotopic composition of surface snow instead of the isotopic composition of each individual precipitation event. We can calculate theoretically the isotopic composition of the snow in equilibrium with low level water vapour. For this purpose, we use the isotopic composition of the water vapour (Table 1.2) and the fractionation coefficients at −10°C (the 3 m air temperature monitored at NEEM during the sampling) for vapour-solid equilibrium given by Majoube (1971) for $\delta^{18}O$ and Merlivat and Nief (1967) for δD. Then, using the measurements of δD and $\delta^{18}O$ in water vapour and the theoretical values of δD and $\delta^{18}O$ for the snow in equilibrium with this water vapour in Eq. 1.30, we calculate the value for $\lambda^D_{\text{vap-solid, equilibrium}}$ at solid-vapour equilibrium: 6.3 ±0.3. This value is in good agreement with the $\lambda^D_{\text{vap-prec}}$ experimental values given in Table 1.2 hence supporting the equilibrium between precipitation and water vapour. Despite this good agreement, it should be noted that the $\delta^{18}O$ difference between water vapour and solid precipitation cannot always exactly be predicted by the vapour- solid equilibrium given by Majoube (1971) for $\delta^{18}O$ at the measured temperature (underestimation by ∼20%). This may be due to a significant part of liquid-vapour equilibrium fractionation during water vapour-snow equilibrium and/or to a 20% surface snow remobilisation in the surface water vapour. These effects could not be better quantified during the 2008 field season and it should be noted that much more controlled experiments were deployed during the 2011 NEEM field season to better document them.

Measurements of ^{17}O excess in the precipitation

and water vapour allow one to calculate $\lambda^{17}_{\text{vap-prec}}$, with a value of 0.528 ±0.001. The same result is obtained when using mean isotopic composition of surface snow instead of the one of precipitation and we performed simple sensitivity tests to check that 20% of snow remobilization does not affect this result. This value is similar to the theoretical ratio obtained from vapour pressure isotope effect between $\ln(\alpha^{17}_{\text{eq\_vap\_sol}})$ and $\ln(\alpha^{18}_{\text{eq\_vap\_sol}})$ [(0.529 to 0.5285 between 0 and −40°C, Van Hook, 1968), $\alpha^{17}_{\text{eq\_vap\_sol}}$ and $\alpha^{18}_{\text{eq\_vap\_sol}}$ being the fractionation at vapour-solid equilibrium for the ratios $H_2^{17}O/H_2^{16}O$ and $H_2^{18}O/H_2^{16}O$, respectively. The fact that the observed $\delta^{17}O$-$\delta^{18}O$ relationship is identical to the theoretical relationship calculated by Van Hook (1968) for water vapour-ice equilibrium supports that it can be used with confidence for water isotopic modelling in the absence of laboratory fractionation experiments. Note that we find a slightly different value for the water vapour– solid equilibrium (0.528 ±0.001) than has been found for the water vapour-liquid equilibrium [0.529 ± 0.001 (Barkan and Luz, 2005)]. This is not unexpected since theoretical calculations by Van Hook (1968) also predict a slightly higher slope for the water vapour-liquid equilibrium (0.5295) than for the water vapour-solid equilibrium (0.5285-0.529).

5.2. Seasonal cycle and implication for the interpretation of water isotopes in Greenland ice core

The main features of the seasonal cycle are: (1) a 10‰ difference of $\delta^{18}O$ between summer and winter, (2) a 5‰ difference in d-excess between autumn and spring and (3) a strong anticorrelation between

^{17}O excess and δ^{18}O with a difference of ∼25 ppm between winter and summer in ^{17}O excess. Note that the 25 ppm amplitude of the ^{17}O excess seasonal cycle means that the triple isotopic composition of snow in Greenland is not aligned on the meteoric water line at the seasonal scale. This indicates that seasonal changes in the relative influence of kinetic and equilibrium fractionations occurred at the oceanic source region, along the trajectory, or at the precipitation site. We thus use the MCIM with different tunings and climatic forcings and explore the conditions permitting to reproduce these seasonal variations. Such a sensitivity study is important to further use the MCIM for interpreting isotopic records in deeper NEEM ice cores.

5.2.1. Explaining the water isotopes seasonal cycles with a constant source of moisture We have explored the different tuning parameters of the MCIM: proportion of ice remaining in the cloud, evaporative coefficient of the liquid into vapour, freezing coefficient of the liquid into ice, temperature of first appearance of ice, supersaturation dependence with temperature, temperature range of coexistence of liquid and water in the cloud. Most of these parameters affect the mean level of δ^{18}O, d-excess and ^{17}O excess but not the phase of the isotopic composition of the precipitation with respect to the seasonality of climatic parameters (temperature and relative humidity of the source, site temperature). Still, the MCIM seasonal outputs are strongly influenced by the dependence of the supersaturation function with temperature. We have thus first adjusted the other parameters to have the best agreement with the annual mean levels of δ^{18}O, d-excess and ^{17}O excess at NEEM and then studied the effect of the supersaturation function.

Fig. 1.11 illustrates the impacts of different supersaturation functions (ranging between S = 1 − 0.001T and S = 1 − 0.007T) on the simulated seasonal cycles of d-excess and ^{17}O excess vs. δ^{18}O at NEEM. This exercise has been performed for different source climatic conditions, i.e. for relative humidities rh varying between 0.7 and 0.9 and source temperatures (Tsource) varying between 15 and 25°C. The site condensation temperature has been adjusted in order to reproduce the NEEM seasonal δ^{18}O variations. As expected, the amplitude of the seasonal cycle of condensation temperature is smaller than the one of surface temperature (amplitude of about 30°C). This is linked to the seasonality of the precipitation at NEEM (less precipitation events during the coldest part of the year, Steen-Larsen et al., 2011) and to the temperature gradient between the surface and condensation altitude because of the existence of an inversion espe-

cially in winter in Greenland (e.g. Loewe, 1936; Hoch et al., 2007).

This first approach relies on the crude assumption of constant climatic conditions at the moisture source along a seasonal cycle. This leads to the following features. Irrespective of the supersaturation used within the range of tested values, the simulated d-excess is systematically too low compared to the data except for a very warm (≥25°C) and dry (rh ≤ 0.7) source region. Such evaporative conditions are only encountered in regions of strong evaporation and cyclone genesis (Trigo, 2006) which are not consistent with estimates of Greenland moisture sources based on atmospheric modelling, from retrotrajectories analyses or GCMs water tagging (Sodemann et al., 2008; Schmidt et al., 2007; Werner et al., 2011). As for ^{17}O excess, the antiphase between δ^{18}O and ^{17}O excess is better captured when using the following supersaturation dependency with temperature, S = 1 − 0.001T, and a source relative humidity fixed to 0.7 (the temperature of the source has only a very small influence). However, even if the difference is not significant from a statistical point of view because of the scattering of the data points over several seasonal cycles, the distance between the MCIM curve and the data points is smaller for a tuning with S = 1 − 0.004T than for S = 1 − 0.001T (Fig. 1.11). Moreover, earlier studies with the MCIM over Greenland used a value for supersaturation dependency with temperature close to S = 1 − 0.004T from the relationship observed between d-excess and δ^{18}O at the seasonal scale (Masson-Delmotte et al., 2005b,a; Hoffmann et al., 2001; Landais et al., 2004a; Sodemann et al., 2008).

5.2.2. Explaining the water isotopes seasonal cycles with a varying source of moisture In the previous paragraph, we could not definitively choose between a supersaturation of S = 1 − 0.001T and S = 1 − 0.004T. The previous approach is too rough because it did not consider changes in source climatic conditions over the course of the year. In this section, we examine the effect of seasonal variations of source climatic conditions on the seasonal variability of ^{17}O excess and d-excess.

In order to take into account seasonal changes at the moisture sources, we use the monthly surface air temperature and relative humidity from the NCEP/NCAR reanalysis project (Kalnay et al., 1996) over our period of interest (2003-2005). Moisture sources were chosen in the North Atlantic Ocean on two different locations: a northern location (50-55°N, 25-40°W) in better agreement with GCMs water tagging and a subtropical location (32-42°N, 25-40°W) as inferred from water isotopes interpretation (Johnsen
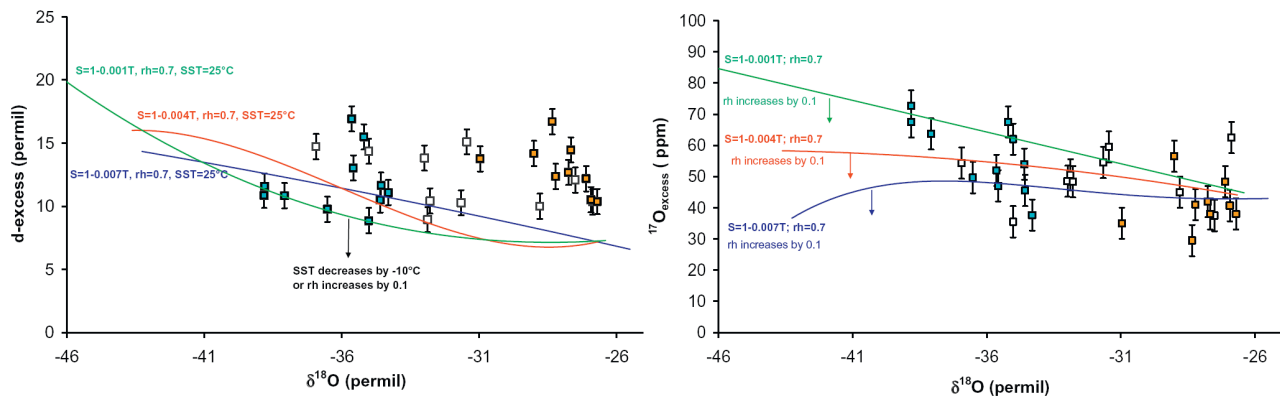
Figure 1.11: (a), left Observed and simulated d-excess as a function of $\delta^{18}O$. Data from the NEEM snow pits are depicted as open squares. Winter data (Dec 21st to March 21st) are highlighted in blue while summer data (21st June to 21st September) are depicted in orange. Model results are represented as solid lines, different colours showing simulations obtained with different supersaturation functions. The model outputs would be shifted as indicated by the black arrow in response to changes in sea surface temperature (SST) or relative humidity (rh) of the evaporative region. **(b), right** Same as (a) but for ^{17}O excess. The vertical arrows only depict the impact of a change in rh (SST has no significant impact). (For interpretation of the references to colour in this figure legend, the reader is referred to the web version of this article.)

et al., 1989). The seasonal variations of NCEP relative humidity and of temperature at these two locations are very comparable to the long term measurements performed within the frame of IAEA at the surface ocean near Iceland (Ship A, 62°N 33°W) and at the surface of the Atlantic subtropical ocean (Ship E, 35°N 48°W) [IAEA/WMO, 1969-79]. In these two regions, surface air relative humidity is maximum in early summer (i.e. when evaporation is maximum due to summer insolation) and surface temperature peaks in early autumn because of the thermal inertia of the ocean. We do not take into account possible mixing from other regions. We are aware that this is a simplification albeit useful to quantify seasonal source conditions on the d-excess and ^{17}O excess seasonality in Greenland.

As displayed on Figs. 1.12 and 1.13, using one or the other Atlantic sources with the classical supersaturation S = 1 − 0.004T allows to correctly reproduce the phasing of the seasonal cycle of ^{17}O excess. With S = 1 − 0.001T, the modelled ^{17}O excess seasonal cycles (not displayed) have an amplitude 20 ppm larger than those presented on Figs. 1.12 and 1.13. This is fine for reproducing the ^{17}O excess seasonal cycles with a source in the Northern Atlantic but a bit too large when considering the subtropical Atlantic source. As for d-excess seasonal cycles, the best way to reproduce correctly their amplitude and phasing is to consider a subtropical Atlantic moisture source. This good agreement for the phasing for both ^{17}O excess and d-excess is mainly due to the differences in seasonal variations of relative humidity and temperature in the North Atlantic that influence, respectively, ^{17}O excess and d-excess

at NEEM. Relative humidity of the source peaks in July explaining the antiphase between ^{17}O excess and $\delta^{18}O$ at NEEM. Source oceanic temperature reaches its maximum in September-October, i.e. delayed ~3 months compared to the maximum in the Greenland temperature, explaining the maximum level of d-excess reached ~3 months later than the $\delta^{18}O$ maximum at NEEM. These results directly confirm that the main influences on polar ^{17}O excess and d-excess are strongly influenced by respectively relative humidity and temperature at evaporation sources at the ocean surface.

The good matching between observed and simulated d-excess and ^{17}O excess when considering a subtropical source is in agreement with the analysis presented by Johnsen et al. (1989) studying the seasonal variability of Greenland ice core $\delta^{18}O$ and d-excess only. It should, however, be noted that back trajectories studies (e.g. Sodemann et al., 2008) and GCMs analyses (e.g. Schmidt et al., 2007) suggest a more northward moisture source than the subtropical Atlantic for Northwest Greenland. While using such northward source region with the MCIM does not strongly modify the modelled ^{17}O excess annual cycle, it leads to (1) a too flat d-excess seasonal cycle and (2) a systematic shift between modelled and measured d-excess of about 12‰. This low bias for d-excess in Greenland snow was also identified by previous studies using the MCIM (i.e. Sodemann et al., 2008). If this bias is not simply caused by a failure to identify the correct source region for the precipitation, it is either due to the MCIM itself which was initially dedicated to the interpretation of snow isotopic content in central East-Antarctic (Vimeux et al.,
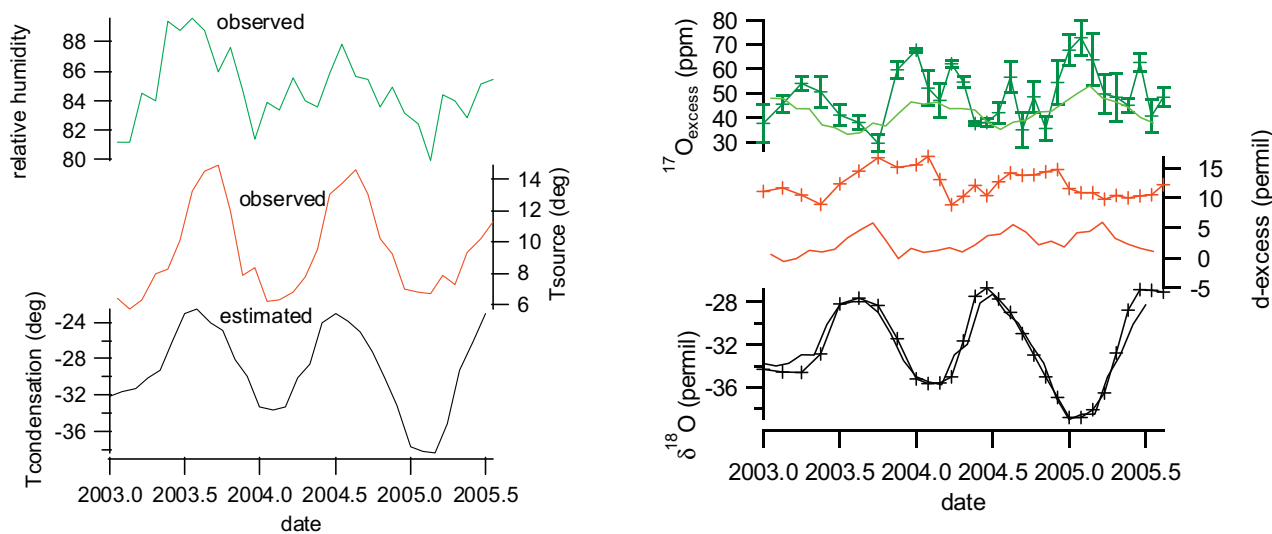
Figure 1.12: MCIM simulation of the isotopic composition of water over three seasonal cycles at NEEM using seasonal climatic conditions from a North Atlantic source region (50-55°N, 25-40°W) and a supersaturation function of: S = 1 − 0.004T. (Left panel) From top to bottom: seasonal variations of the source relative humidity; seasonal variations of the source surface temperature; temperature of condensation (NEEM) adjusted so that the simulated δ^{18}O evolution (right panel) fits the measured δ^{18}O evolution. (Right panel) From top to bottom: seasonal variations of ^{17}O excess (measurements: dark thin line; model: light thick line); seasonal variations of d-excess (measurements: thin line; model: dark line); seasonal variations of δ^{18}O (measurements: thin line; model: dark line).

2002; Stenni et al., 2001) or to the parametrisation of the isotopic fractionation coefficient for δ^{18}O vs. δD. To illustrate this second possibility, the recent study by Luz et al. (2009) suggests that the kinetic fractionation coefficients for δ^{18}O and δD can change significantly with temperature which is not considered in the MCIM or in any other models equipped with isotopes. ^{17}O excess should not be affected by such an effect since Barkan and Luz (2007) found no evidence for change in the relationship between kinetic fractionation coefficients associated with δ^{17}O relatively to δ^{18}O.

In the previous data-model comparison, we have considered a constant geographical source. As indicated by the work of Fisher et al. (1995) or Vimeux et al. (1999) for example, moisture uptake from a single source is simplified and several moisture sources may be present. If the moisture sources were to change with seasons, this would have an effect on the mean level and seasonal variability of ^{17}O excess and d-excess. In particular, we have found that a location of the NEEM moisture sources in the tropical Atlantic ocean correctly explained the high observed ^{17}O excess mean level because of low relative humidity there (down to 70%). It is also the moisture source region enabling to predict the higher d-excess mean level even if it is still too small compared with observations as largely discussed above. However, another possible contribution neglected here is a recycling source of moisture above the Arctic ocean that could

be significant in summer-fall. Indeed, Kurita (2011) has recently evidenced that water vapour above the Arctic ocean is associated with a high d-excess level. ^{17}O excess measurements in water vapour over this region are still lacking to know if it has the same behaviour than d-excess but we can already speculate that if a significant part of moisture arriving over the NEEM site originates from the Arctic ocean, it may contribute to the high levels of ^{17}O excess and d-excess observed there.

6. Conclusions and perspectives

We have presented the first measurements of ^{17}O excess in Greenland on two different types of samples from NEEM. Measurements of ^{17}O excess in the water vapour and concomitant precipitation in August 2008 have shown similar levels in the water vapour and in the precipitation or surface snow. Previous measurements of δD and δ^{18}O on the same samples have shown that low level water vapour and/or surface snow are at equilibrium. Our ^{17}O excess measurements thus confirm the theoretical value of 0.528 for the ratio between $\ln(\alpha^{17}_{eq\_vap\_sol})$ and $\ln(\alpha^{18}_{eq\_vap\_sol})$ (Van Hook, 1968). These results will be fundamental to the implementation of δ^{17}O in atmospheric general circulation models equipped with water isotopes or simple distillation models. In this first experimental determination of the solid-
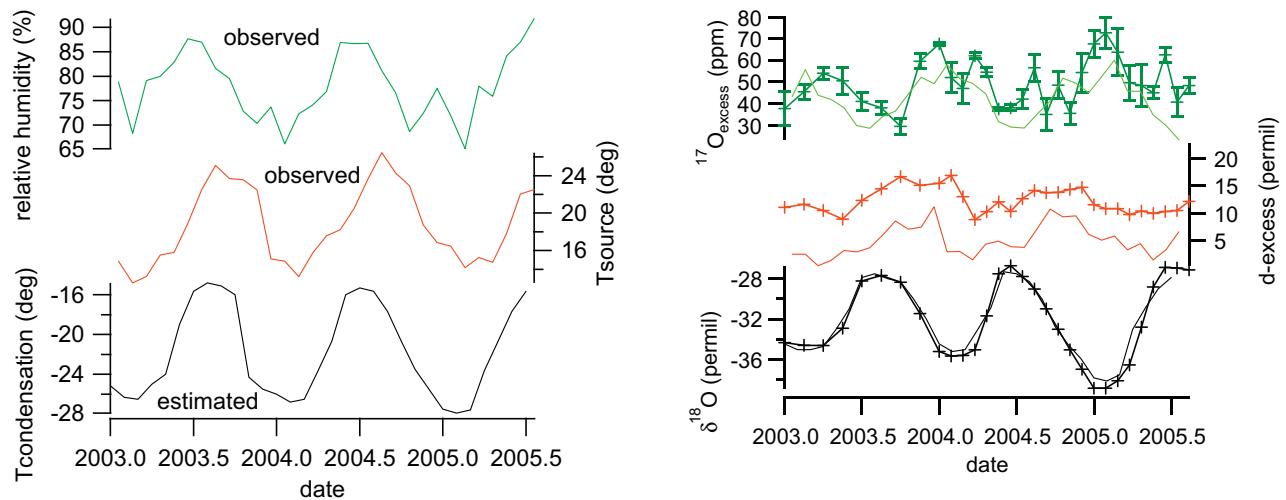
Figure 1.13: Same as Fig. 1.12 but for a tropical source region in the North Atlantic (32-42°N, 25-40°W).

vapour fractionation coefficients for $\delta^{17}O$, the conditions are clearly less defined than in a laboratory experiment; in particular, we could not test the influences of temperature and relative humidity. An important perspective of this first study is thus to design a laboratory experiment enabling to measure the fractionation associated with $\delta^{17}O$ at the water vapour-solid equilibrium.

We have also presented seasonal variations of ^{17}O excess between 2003 and 2005 from analyses of a shallow core drilled at NEEM. The ^{17}O excess seasonal variations are of the order of 25 ppm in antiphase with the $\delta^{18}O$ variations. This contrasts with the d-excess cycle that lags the $\delta^{18}O$ cycle by $\sim$3 months, confirming that ^{17}O excess and d-excess are complementary tracers. The different seasonal variations of ^{17}O excess and d-excess can be explained by simple isotopic modelling and reflect the seasonality of air temperature and relative humidity of the evaporative regions. Indeed, observed seasonal variations of relative humidity and temperature at the surface of a broad part of the northern Atlantic are in phase respectively with ^{17}O excess (maximum in July) and d-excess (maximum reached in September– October). In this study, we have used the MCIM model (Ciais and Jouzel, 1994) including the description of $\delta^{17}O$ (Landais et al., 2008a). We have shown that the seasonal variations of $\delta^{18}O$, d-excess and ^{17}O excess can be simulated when using the classical supersaturation function of S = 1 − 0.004T and a subtropical Atlantic source region.

Our study has paved the way for more measurements and interpretation of ^{17}O excess in Greenland snow and ice, especially along the deep NEEM ice core, and has shown the potential of ^{17}O excess for the general interpretation of water isotopes in polar ice cores. In the future, in order to better decipher the influences of supersaturation tuning and of the

climatic conditions of the evaporative regions on the seasonal cycles of d-excess and ^{17}O excess, it would be useful to study spatial and seasonal variations of water isotopic composition in other Greenland sites and in Arctic surface vapour. Additional understanding should also be provided by the combination of water isotopic measurements on an event basis with back-trajectories and isotopic calculations. Finally, the inclusion of ^{17}O excess in GCMs equipped with water isotopes is certainly an important step for our understanding of the complex interactions between climate and water cycle.

Acknowledgements

Appendix A

The effect of diffusion in the NEEM firn has been quantified for $\delta^{18}O$ and d-excess using a modelling

approach (Steen-Larsen et al., 2011). Fig. 1.14 displays the outputs of this classical diffusion model for the six last seasonal cycles on a depth scale starting from the surface. The impact of diffusion on the δ^{18}O signal is evidenced by a <20% reduction of the seasonal cycle amplitude for this period. As for the d-excess, this calculation produces a limited damping of the seasonal cycle (<10%) together with a shift of the d-excess seasonal cycle that increases with diffusion. Diffusion in the firn is driven by solid-vapour equilibrium. The d-excess phase shift is thus due to the variations in the respective equilibrium fractionation factors for δD ($\alpha^D_{\text{vap-solid, equilibrium}}$) and for δ^{18}O
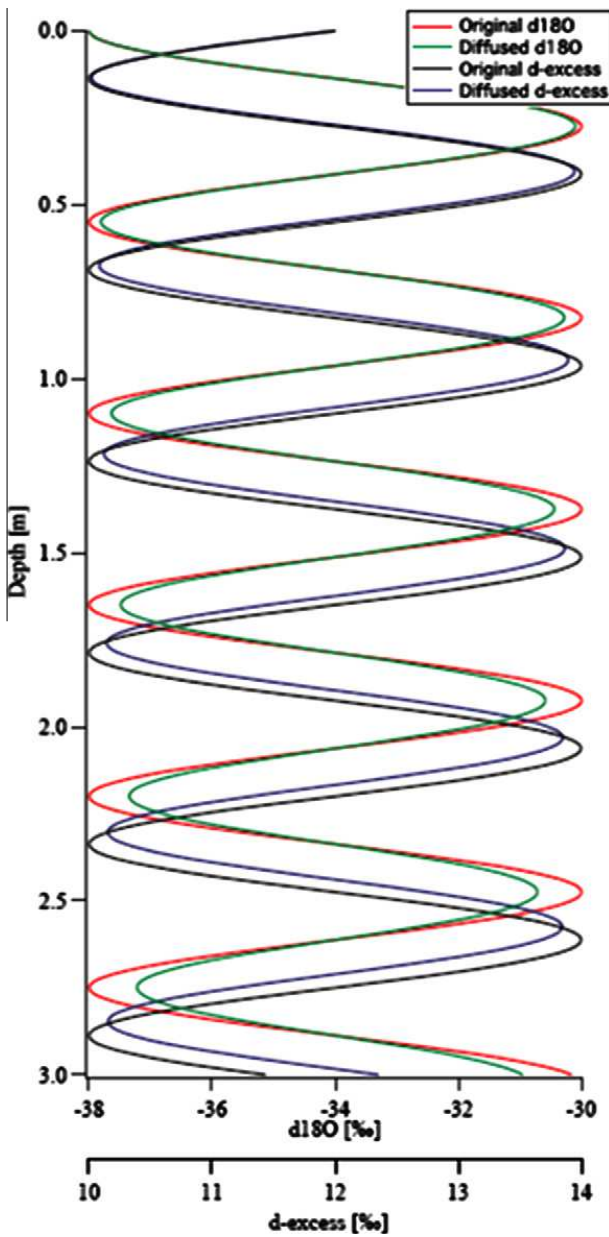
Figure 1.14: Influence of the diffusion on the δ^{18}O and d-excess profiles of the top 3 m (~6 seasonal cycles) for a shallow ice core drilled at the NEEM site (Steen-Larsen et al., 2011).

($\alpha^{18}_{\text{vap-solid, equilibrium}}$) at low temperatures ($-20$°C):

$$\frac{\alpha^D_{\text{vap-solid, equilibrium}} - 1}{\alpha^{18}_{\text{vap-solid, equilibrium}} - 1} = 9.3 \qquad (1.31)$$

This ratio is indeed significantly different from the slope of 8 defining the d-excess (d-excess = δD $- 8 * \delta^{18}$O), which produces a small phase shift of d-excess. This shift remains limited (<1 month) for our time period of interest.

^{17}O excess has not yet been implemented in the calculations of Steen-Larsen et al. (2011) and the impact of diffusion cannot be quantified with the same methodology. In order to estimate the impact of diffusion on ^{17}O excess, we had three complementary approaches:

(a) We observe that the relationship between the equilibrium fractionation factor for δ^{17}O ($\alpha^{17}_{\text{vap-solid, equilibrium}}$) and δ^{18}O ($\alpha^{18}_{\text{vap-solid, equilibrium}}$) at low temperatures is (Van Hook (1968), this study):

$$\frac{ln(\alpha^{17}_{\text{vap-solid, equilibrium}})}{ln(\alpha^{18}_{\text{vap-solid, equilibrium}})} = 0.528 \qquad (1.32)$$

which is the same value than the slope of 0.528 defining the ^{17}O excess (^{17}O excess = ln(δ^{17}O + 1) −
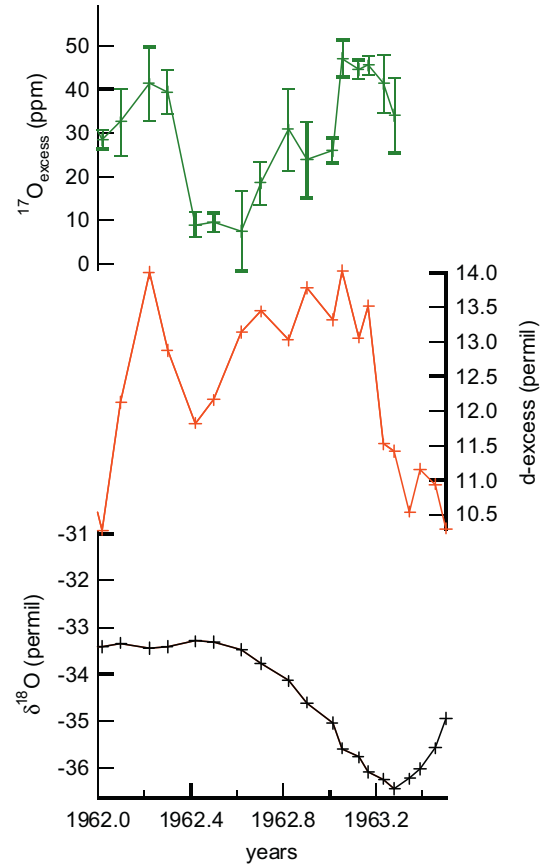
Figure 1.15: ^{17}O excess, d-excess and δ^{18}O profiles at the bottom of the shallow core (18-19 m deep).

0.528 * ln (δ^{18}O + 1)). As a consequence, we do not expect any artificial shift for the ^{17}O excess seasonal cycle to be produced by diffusion as for d-excess.

(b) The δ^{18}O and ^{17}O excess are anti-phased over the seasonal cycle. We thus propose a simple calculation on a two layers system, one characterized by a δ^{18}O of -36‰ and a ^{17}O excess of 60 ppm (winter layer) and one characterized by a δ^{18}O of -28‰ and a ^{17}O excess of 35 ppm (summer layer). We allow diffusion between the two layers so that the δ^{18}O difference between summer and winter is reduced by 20%. If δ^{17}O diffuses in the same way than δ^{18}O through a ratio of 0.528 between the logarithms of the fractionation coefficients (Eq. 1.30), we find that the final seasonal amplitude of the ^{17}O excess is 19 ppm instead of the initial 25 ppm, hence a reduction of 24% of the initial amplitude of the seasonal cycle. The fact that the amplitude of the ^{17}O excess cycle is more affected than the amplitude of the δ^{18}O seasonal cycle is due to the logarithm definition of the ^{17}O excess which makes it more sensitive to mixing effects.

(c) We performed a few measurements of ^{17}O excess at the bottom of the NEEM shallow core corresponding to years 1962-1963 (Fig. 1.15). Despite the fact that the winter 1961-1962 is not very well marked in the δ^{18}O profile, we observe a clear seasonal cycle in ^{17}O excess with a seasonal amplitude of 25 ppm (and therefore very comparable to the amplitude of the most recent seasonal cycles). The seasonal cycle of ^{17}O excess for 1961-1962 has the same phase with respect to δ^{18}O as observed in the upper part of this shallow ice core, with a minimum in summer and maximum in winter. As expected from considerations on the equilibrium fractionation coefficients, we do not detect any phase shift in of ^{17}O excess that could be attributed to diffusion.

Altogether, we conclude that, over the last three seasonal cycles, diffusion has only a second order influence on the δ^{18}O, d-excess and ^{17}O excess variations.

Appendix B. Supplementary data

1.5 Outlook

^{17}O excess and d-excess do not have the same sensitivity to oceanic vapour source conditions: ^{17}O excess is insensitive to temperature changes at the vapour source but sensitive to relative humidity changes, while d-excess is sensitive to both. In particular, sensitivity tests from Risi et al. (2010), modelling the ^{17}O excess from the evaporation of the ocean to Antarctica, have shown that a 1% increase in source relative humidity results in a 1 permeg decrease in ^{17}O excess.

We have shown that for present day seasonal cycles, ^{17}O excess shows minima in July corresponding to relative humidity maxima, while d-excess shows maxima 3 months later, corresponding to temperature maxima in the oceanic source regions. A combination of these two signals, together with δ^{18}O, is promising for future investigations of the past water cycle. In Chapter 5 p.139, ^{17}O excess measurements will be performed in Greenland ice from the last glacial period and used together with δ^{18}O and d-excess to study past rapid climatic events of millennial variability, the Dansgaard-Oeschger events and Heinrich events.

In Chapter 3, δ^{18}O from different Greenland ice cores will be compared to their corresponding δ^{15}N-based temperatures, for each ice core, in order to study the spatial distribution of δ^{18}O sensitivity to temperature, over a sequence of abrupt temperature changes during the last glacial period. This will help to reconstruct what influenced Greenland water isotopes in the past.

Chapter 2

Absolute referencing of methane isotopes

2.1 Introduction

Methane is a greenhouse gas playing a significant role in the energy budget of the planet, and reacting as fast as less than years to climatic changes. Methane mixing ratio and isotopes are currently measured at different research laboratories around the world. To make results from different laboratories comparable, they must be expressed versus the same standards.

For methane concentration, a method is recognised by the WMO (World Meteorological Organisation) as the reference, and used to produce a suite of air standards with known concentration covering present-day and past concentrations measured in ice cores (Dlugokencky et al., 2005). For isotopes in general, the initial standard for ^{13}C, called PDB, was the isotopic composition of the rostrum of a belemnita from the Pee Dee formation in South Carolina. No material is available form this formation anymore. The IAEA (International Atomic Energy Agency) created an new standard anchored to PDB, called Vienna Pee Dee Belemnita (VPDB). For water, the standard is currently VSMOW, Vienna Standard Mean Ocean Water, and is supposed to be representative of the present-day oceanic composition (see Sect. 1.2.2 p. 6). Such international recognised standards are usually called primary standards. However, so far there is no universal procedure to reference methane isotopes vs primary standards. No gas is certified with a known methane isotopic composition from a recognised institution as the IAEA or the WMO.

The work of my first year of PhD was, in collaboration with Peter Sperlich, PhD student at CIC, to develop a protocol for absolute referencing of methane gas isotopes, and making full air standard with known concentration and isotopic composition of methane. Such a standard is needed for intercomparison between different laboratories measuring methane isotopes.

In this chapter, we first give a short overview of methane in the climate system (Sect. 2.2) and then report the article published by Sperlich et al. (2012), presenting the development of the protocol for absolute referencing of methane gas isotopes (Sect. 2.3 p. 36).

2.2 The methane cycle

Methane is the third most potent greenhouse gas (GHG) in the atmosphere, after water vapor and carbon dioxide (CO_2), characterised by a high radiative power (3.7 10^{-4} W m^{-2} ppb^{-1}) and a relatively short residence time in the atmosphere (9 years) compared to CO_2 (Delmas et al., 2005). Changes in atmospheric methane budget results from changes in the contribution of different sources and sinks. The methane global mean concentration in the atmosphere in 2011 was around 1800 ppbv (Advanced Global Atmospheric Gases Experiment (AGAGE) data). The anthropogenic
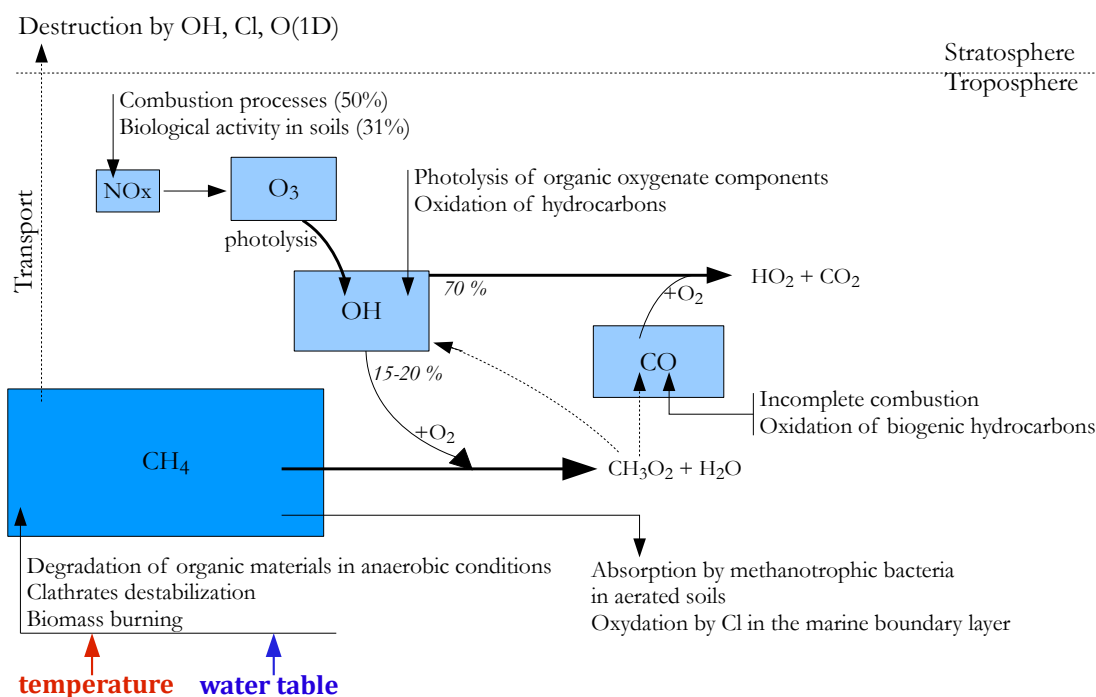
Figure 2.1: Main processes affecting methane mixing ratio in the atmosphere. Based on values from (Delmas et al., 2005).

contribution to the total emissions is around 60–70 % (Denman et al., 2007). Figure 2.1 summaries the main processes affectig the atmospheric methane mixing ratio.

2.2.1   Methane sources

Bacteria decomposing organic materials without oxygen are the principal methane producers, using 2 main pathways: acetate fermentation and CO_2 reduction (Chanton et al., 2006). The precursors of methane are thus meteoric water, dissolved inorganic carbon and organic matter. Anaerobic conditions are found in areas such as wetlands in the tropics and bogs in temperate and boreal regions. Tropical wetlands constitute the main source of atmospheric CH_4 (Quay et al., 1999; Whiticar, 1993; Bousquet et al., 2011). Biomass burning, ruminants, termites, paddy fields, living plants and release of gas hydrates are the other significant contributors of atmospheric methane. Because biological processes are mainly responsible for the production of methane, the main climatic parameters impacting the production of methane are temperature (especially in high latitudes) and soil water level (especially in the tropics) (Walter et al., 2001; Ringeval et al., 2010). The extend of tropical wetlands, and therefore their total emissions, is linked to the strength of the monsoon (Clement et al., 2004).

2.2.2   Methane sinks

Methane is mainly consumed by photochemical oxidation by the OH radical in the troposphere and stratosphere, and by methanotrophic bacteria in ventilated soils (Khalil and Rasmussen, 1983; Quay et al., 1999). OH oxidation follows several chemical reactions ending by the production of carbon dioxide. This path represents roughly 80% of the methane destruction and also 15 to 20% of the OH destruction (Delmas et al., 2005). The concentration of OH radical is the main factor modulating the methane lifetime in the troposphere. Different chemical components influence this process of oxidation (Delmas et al., 2005, Chap. 7):

- CO : the reaction $CO + OH + O_2 \rightarrow HO_2 + CO_2$ is the main sink of OH. Indeed, this reaction has a larger time constant compared to the oxidation of methane [1]. An increase of CO in the atmosphere will reduce the availability of OH to oxidise methane, and in this way increase the lifetime of methane.

- O_3 : photolysis of O_3 is the principal source of OH. Thus, both the solar flux and the concentration of O_3 potentially influence the concentration of OH.

- NO_x : their concentration is a limiting factor for the production of O_3.

2.2.3 Interhemispheric gradient

Mostly produced in the Northern Hemisphere where the land surface is larger than in the Southern Hemisphere, methane has a similar sink in both hemispheres. The mixing between the Northern and Southern hemispheres is not instantaneous but on the order of one year. Thereby, an interhemispheric gradient of methane exists, around 100 ppbv at present (AGAGE data). The past interhemispheric gradient can be reconstructed by comparison of methane concentration measured in Greenland vs Antarctic ice cores (Dällenbach et al., 2000; Baumgartner et al., 2013).

2.2.4 Using methane isotopes for source partitioning

Each of the sources and sinks of methane has a specific isotopic signature in δ^{13}C-CH$_4$ and δD-CH$_4$ (Quay et al., 1999, and Fig. 1 p. 39). Combined with mixing ratio and interhemispheric gradient, the isotopic composition of methane helps to identify the sources and sinks mix and hereby the mechanisms at play within the carbon cycle (e.g., Bousquet et al., 2006). However, given the quite high number of possibilities in sources and sinks and the few constraints (only two isotopes), the source partitioning is an under constrained problem. A comparison of methane isotopes with alternative proxies is needed (e.g., with charcoal databases for biomass burning reconstructions). For paleoclimate reconstructions, the isotopic composition of each source can also vary with time. δ^{13}C-CH$_4$ can vary with the type of organic material that is degraded, e.g. the C3/C4 plant ratio in the wetlands, or if the isotopic composition of a plant type is changing (Möller et al., 2013; Schaefer and Whiticar, 2008). δD-CH$_4$ can vary with the isotopic composition of the meteoric water, by changing the the isotopic signature of the precipitations or the latitudinal location of the methane source (Waldron et al., 1999; Whiticar et al., 1986; Chanton et al., 2006; Bock et al., 2010).

2.2.5 Methane registered in ice cores

Polar ice sheets (Greenland, Antarctica) store snow falling each year at the top of the ice sheet. The surface layers progressively bury and compact the underlying layers of snow. In this process called firnification (Sect. 3.2.1 p. 53), the atmosphere is trapped in-between the snow grains, in air bubbles. Extracting air from polar ice thus gives direct access to the past atmosphere, back to 800 ka b2k (kilo years before 2000 AD) for Antarctic ice and 120 ka b2k for Greenland ice (Loulergue et al., 2008; NGRIP members, 2004; Landais et al., 2005). Measurements of the mixing ratio and isotopic composition of paleoatmospheric methane can be used as paleoclimatic proxies to better understand how the biosphere was affected by previous climate changes. Moreover, methane concentration being a global signal, its measured variations in different ice cores can be used to synchronise ice cores on the same timescale (Blunier and Brook, 2001; Blunier et al., 2007; Brook et al., 2005; Capron et al., 2010b; Veres et al., 2013; Bazin et al., 2013).

---

[1]Oxidation of methane : $6 .10^{-15}$; oxidation of CO : $2.5 .10^{-13}$. Unit : cm^3 molecule^{-1} second^{-1}.

Paleoclimate studies using methane data have already been performed over the Holocene (Chappellaz et al., 1993; Blunier et al., 1995; Sowers, 2010; Sapart et al., 2012b), the last deglaciation (Schaefer and Whiticar, 2008; Fischer et al., 2008; Sowers, 2006), and the last glacial period (Dällenbach et al., 2000; Flückinger et al., 2004; Bock et al., 2010; Baumgartner et al., 2012). Firn sampling campaigns made possible to measure methane from the firn air itself, linking ice cores measurements to present-day atmospheric measurements (Bräunlich et al., 2001; Francey et al., 1999; Sapart et al., 2012a).

2.3   A combustion setup to precisely reference δ^{13}C and δ^2H isotope ratios of pure $\mathrm{CH_4}$ to produce isotope reference gases of δ^{13}C-CH$_4$ in synthetic air

We report here the article published by Sperlich et al. (2012) in *Atmospheric Measurements Techniques*. In addition, figure 2.2 p. 37 shows pictures corresponding to the schematic figure of the setup (see Fig. 3 p. 42). The detailed description of the setup can be found in Sect. 2 p. 39 and following.

The initial oven to combust methane built at CIC by P. Sperlich was inspired by a similar system already existing at the University of Bern (a combustion chamber made of quartz, filled with copper oxide pellets that releases oxygen when heated). P. Sperlich was mainly involved in the improvements of this initial oven (reduction chamber, additional water trap, valve manifold) and design of the system to mix synthetic isotope reference gases and to measure their composition in methane concentration and isotopes, and did as well most of the article writing. I was mainly involved in the tests and measurements concerning this oven (completeness of the combustion, total trapping of the produced carbon dioxide and water, δ^{13}C-CO$_2$ measurements by dual-inlet mass spectrometry, repeatability of these pure methane measurements). The δD-H$_2$O measurements have been performed by the stable water isotope laboratory at CIC.
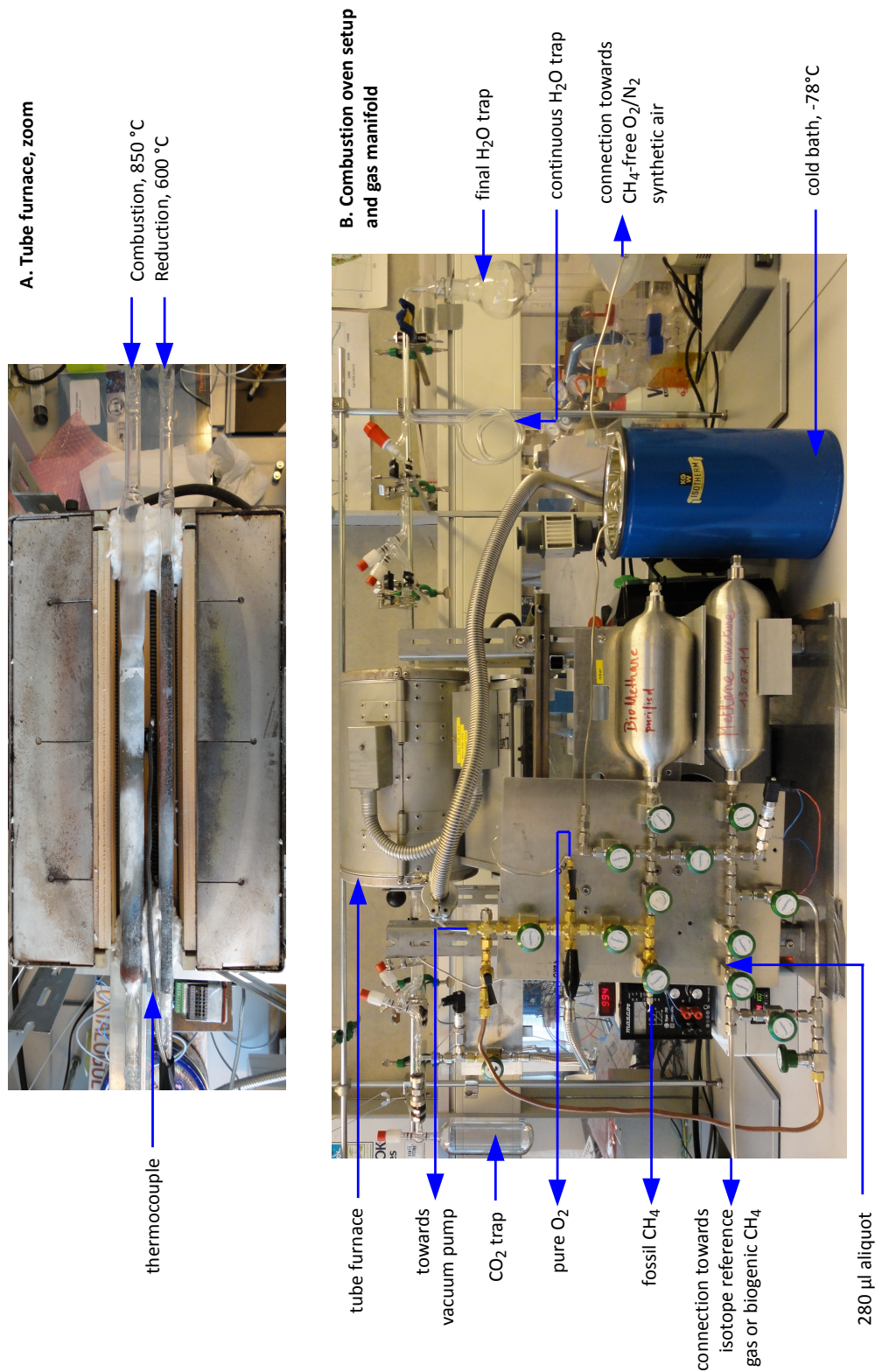
Figure 2.2: Combustion setup: pictures. A, top: the tube furnace open. B, bottom: the gas manifold. See corresponding schematic figure p. 42 and the detailed description p. 39 and following.

**Atmospheric
Measurement
Techniques**
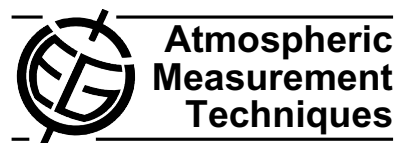
A combustion setup to precisely reference δ^{13}C and δ^2H isotope ratios of pure CH$_4$ to produce isotope reference gases of δ^{13}C-CH$_4$ in synthetic air

P. Sperlich[1,*,**], **M. Guillevic**[1,2,**], **C. Buizert**[1], **T. M. Jenk**[1], **C. J. Sapart**[3], **H. Schaefer**[4], **T. J. Popp**[1], **and T. Blunier**[1]

[1]Centre for Ice and Climate, University of Copenhagen (CIC), Copenhagen, Denmark
[2]Laboratoire des Sciences du Climat et de l'Environment (LSCE), Gif sur Yvette, France
[3]Institute for Marine and Atmospheric Research Utrecht (IMAU), Utrecht University, Utrecht, The Netherlands
[4]National Institute for Water and Atmospheric Research (NIWA), Wellington, New Zealand
[*]now at: Max-Planck-Institute for Biogeochemistry (MPI-BGC), Jena, Germany
[**]These authors contributed equally to this work.

Correspondence to: P. Sperlich (psperl@bgc-jena.mpg.de)

Abstract. Isotope records of atmospheric CH$_4$ can be used to infer changes in the biogeochemistry of CH$_4$. One factor currently limiting the quantitative interpretation of such changes are uncertainties in the isotope measurements stemming from the lack of a unique isotope reference gas, certified for δ^{13}C-CH$_4$ or δ^2H-CH$_4$. We present a method to produce isotope reference gases for CH$_4$ in synthetic air that are precisely anchored to the VPDB and VSMOW scales and have δ^{13}C-CH$_4$ values typical for the modern and glacial atmosphere. We quantitatively combusted two pure CH$_4$ gases from fossil and biogenic sources and determined the δ^{13}C and δ^2H values of the produced CO$_2$ and H$_2$O relative to the VPDB and VSMOW scales within a very small analytical uncertainty of 0.04 ‰ and 0.7 ‰, respectively. We found isotope ratios of −39.56 ‰ and −56.37 ‰ for δ^{13}C and −170.1 ‰ and −317.4 ‰ for δ^2H in the fossil and biogenic CH$_4$, respectively. We used both CH$_4$ types as parental gases from which we mixed two filial CH$_4$ gases. Their δ^{13}C was determined to be −42.21 ‰ and −47.25 ‰ representing glacial and present atmospheric δ^{13}C-CH$_4$. The δ^2H isotope ratios of the filial CH$_4$ gases were found to be −193.1 ‰ and −237.1 ‰, respectively. Next, we mixed aliquots of the filial CH$_4$ gases with ultrapure N$_2$/O$_2$ (CH$_4$ ≤ 2 ppb) producing two isotope reference gases of synthetic air with CH$_4$ mixing ratios near atmospheric values. We show that our method is reproducible and does not introduce isotopic fractionation for δ^{13}C within

the uncertainties of our detection limit (we cannot conclude this for δ^2H because our system is currently not prepared for δ^2H-CH$_4$ measurements in air samples). The general principle of our method can be applied to produce synthetic isotope reference gases targeting δ^2H-CH$_4$ or other gas species.

1   Introduction

Methane is a powerful greenhouse gas and therefore of major interest when studying the climate system. Records of CH$_4$ in the recent atmosphere exhibit small changes in seasonal and spatial patterns (e.g. Dlugokencky et al., 2009; Tyler et al., 2007). In contrast, ice core records of CH$_4$ mixing and isotope ratios show much stronger variability on decadal to glacial time scales (e.g., Bock et al., 2010; Ferretti et al., 2005; Fischer et al., 2008; Loulergue et al., 2008; Sowers, 2006). The isotopic composition of atmospheric CH$_4$ is a function of the relative strengths of its sinks and sources, which are themselves characterized by distinct signatures of the carbon and hydrogen isotope ratios (e.g. Quay et al., 1999), see Fig. 1. Therefore, changes in the biogeochemistry of CH$_4$ can be inferred by analyzing the CH$_4$ mixing ratio and isotope records. Isotope ratios are reported using the delta notation according to Eq. (1):
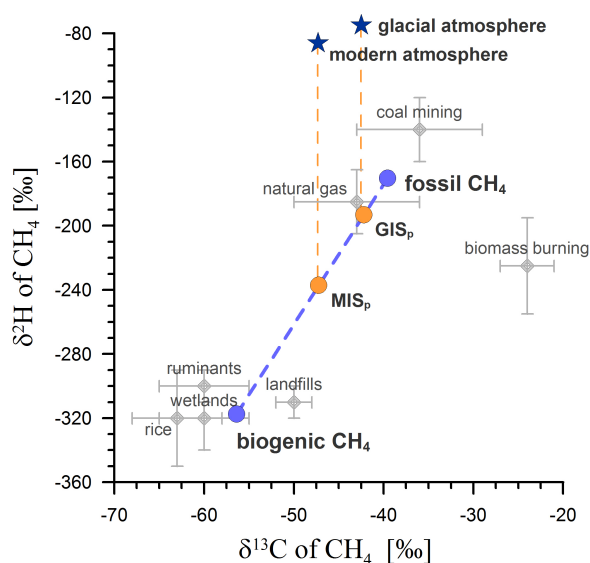
Fig. 1. Dual isotope signatures of CH$_4$ for δ^{13}C and δ^2H. Grey diamonds mark the field of δ^{13}C and δ^2H isotopes of CH$_4$ according to its source (Quay et al., 1999). Blue circles indicate δ^{13}C and δ^2H pairs of the parental CH$_4$ gases (fossil and biogenic CH$_4$). Based on our fossil and biogenic CH$_4$, we can produce filial CH$_4$ mixtures with δ^{13}C and δ^2H isotope values that fall on the dashed blue mixing line. The two filial CH$_4$ gas mixtures are indicated by orange circles where GIS$_p$ and MIS$_p$ represent the δ^{13}C of glacial and modern atmospheric samples, respectively. Isotope signatures of glacial and modern atmospheric CH$_4$ are indicated by the dark blue stars.

$$\delta = \left(\frac{R_{\text{sample}}}{R_{\text{standard}}} \right) - 1, \tag{1}$$

where R denotes the ratio of the heavy over the light isotope in the sample and the standard, respectively. Dual inlet-isotope ratio mass spectrometry (DI-IRMS) and gas-chromatography coupled isotope ratio mass spectrometry (GC-IRMS) are commonly applied to measure the isotope ratios of atmospheric CH$_4$ (Merritt et al., 1995b; Rice et al., 2001), following the principle of identical treatment (Werner and Brand, 2001). Isotope reference gases are used to anchor the sample to the international isotope scales, which is VPDB for δ^{13}C-CH$_4$ and VSMOW for δ^2H-CH$_4$. Ideally, the isotope reference gas is similar in mixing ratio and isotopic composition to the measurand (Werner and Brand, 2001; Brand et al., 2009) to allow for the highest analytical precision and accuracy. Accurate referencing is vital. This becomes particularly obvious when datasets from different laboratories are merged for the interpretation of spatial atmospheric processes (Levin et al., 2012). It is essential to unambiguously determine whether different observations are due to natural variability or analytical offsets. Even very small

offsets in isotope values can have a large impact on the quantification of sink and source budgets (Mikaloff Fletcher et al., 2004). One limitation to the accuracy of CH$_4$ isotope measurements is the accuracy to which the true isotope value of the isotope reference gas is known. Laboratories can increase their compatibility by circulating a suite of isotope reference gases in so called round-robins. Round-robins have been conducted for more than 14 yr and included several measurands, e.g. CH$_4$ mixing ratios and CO$_2$ isotopes in air to highlight accuracy offsets and to identify scale contraction effects (Brand, 2011). However, the comparison is limited as the flasks are not permanently available to each laboratory. To our knowledge, round-robin results for CH$_4$ isotopes in air have not been published yet. The compatibility of measurements on CH$_4$ isotopes in air could be achieved by establishing a suite of unique isotope reference gases that are available to all laboratories, as it is done for CH$_4$ mixing ratios (Dlugokencky et al., 2005) and CO$_2$ isotopes (Ghosh et al., 2005), respectively. An ideal suite of isotope reference gases would cover the isotope and mixing ratio variability of modern and glacial atmospheres. Despite the obvious demand, such a suite of unique isotope reference gases is currently not available for isotopes of CH$_4$. Even pure CH$_4$ gases with certified isotope ratios are currently not available from recognized authorities (such as the International Atomic Energy Agency, IAEA, or the National Institute of Standards and Technology, NIST). Here, we present a method that can potentially be used to produce large amounts of isotope reference gases for atmospheric CH$_4$ with targeted and precisely referenced isotope ratios.

2 Methods

2.1 Method overview

This method is designed to produce atmospheric isotope reference gases for CH$_4$, based on a suite of initial gases that are needed for the process. All standards and gases employed are listed in Table 1, using the terminology of Coplen (2011). Figure 2 illustrates the relationship of the measured gases to the VPDB and VSMOW isotope scales. We prepared two pure CH$_4$ gases that are referred to as fossil and biogenic CH$_4$, respectively, with regards to their origin. Next, we determined the isotopic composition of the fossil and biogenic CH$_4$ versus VPDB and VSMOW for δ^{13}C and δ^2H, respectively. This was achieved with a pure, referenced CO$_2$ gas (referred to as CO$_2$-40339) and three isotope reference waters (named DC'02, NM'09 and -15). The mentioned isotope reference materials are calibrated versus international measurement standards, specified by Verkouteren (1999) for CO$_2$ and IAEA (2009) for H$_2$O. From the parental fossil and biogenic CH$_4$, we mixed two filial CH$_4$ gases. We matched the δ^{13}C value of the filial mixtures to atmospheric values reported for the present day and the last glacial maximum

P. Sperlich et al.: Isotope reference gas for atmospheric CH$_4$ **2229**

Table 1. Overview of gases and waters. All gases used for measuring, mixing and referencing are mentioned in the top panel, the bottom panel displays all waters that were used to reference the δ^2H-CH$_4$. The application and reference path of each measure are described in the second column while the third column informs on material type and purity level if applicable. The fourth column shows the relevant isotope ratios of applied reference material, the fifth column identifies the distributor of materials or specifies the origin of the measure if not commercially purchased.

Gas name	Application	Gas type, purity	δ^{13}C [‰]	Origin
RM 8563	international measurement standard	CO$_2$	−41.56	IAEA
CO$_2$-40339	isotope reference gas	CO$_2$, 99.998 Vol. %	−35.41	Air Liquide, Denmark
fossil CH$_4$	parental gas, CH$_4$ mixing	CH$_4$, 99.995 Vol. %		Air Liquide, Denmark
biogenic CH$_4$	parental gas, CH$_4$ mixing	CH$_4$		biogas plant, northern Germany
GIS$_p$	pure CH$_4$, glacial δ^{13}C	mixed CH$_4$		fossil and biogenic CH$_4$
MIS$_p$	pure CH$_4$, modern δ^{13}C	mixed CH$_4$		fossil and biogenic CH$_4$
GIS	synthetic isotope reference gas, glacial δ^{13}C	CH$_4$ in air		GIS$_p$ with CH$_4$-free air
MIS	synthetic isotope reference gas, modern δ^{13}C	CH$_4$ in air		MIS$_p$ with CH$_4$-free air
NEEM	sample, referenced with GIS and MIS	atmospheric air		NEEM camp, Greenland
CH$_4$-free air	matrix air for gas mixing	N$_2$/O$_2$, labline 5.0		Strandmøllen, Denmark
O$_2$	oxidation combustion ractor	O$_2$, 99.995 mol %		Air Liquide, Denmark

Water name	Application	Type	δ^2H [‰]	Origin
VSMOW-2	international measurement standard	H$_2$O	0.0	IAEA
SLAP-2	international measurement standard	H$_2$O	-427.5	IAEA
DC′02	isotope reference material	H$_2$O	−427.6	Dome C, Antarctica
NM′09	isotope reference material	H$_2$O	−257.3	NEEM camp, Greenland
−15	isotope reference material	H$_2$O	−111.1	internally produced

(Quay et al., 1999; Fischer et al., 2008). The filial CH$_4$ mixtures will hereafter be referred to as the glacial isotope standard (GIS$_p$) and the modern isotope standard (MIS$_p$), respectively, where the index "p" specifies a pure CH$_4$ gas. Both δ^{13}C-CH$_4$ and δ^2H-CH$_4$ isotope ratios of GIS$_p$ and MIS$_p$ were precisely referenced versus CO$_2$-40339 and the isotope reference waters, see Fig. 1 and section 2.2. Next, aliquots of GIS$_p$ and MIS$_p$ were blended with CH$_4$-free air, until atmospheric mixing ratios of CH$_4$ were reached. This resulted in two synthetic isotope reference gases containing CH$_4$ with δ^{13}C values akin to the glacial and modern atmosphere which will be referred to as GIS and MIS, respectively. We then used GIS and MIS as isotope reference gas to reference a tank of atmospheric air (taken at a clean air site in Northwest Greenland (77.45° N, 51.06° W) in July 2008, hereafter referred to as NEEM) according to the principle of identical treatment (Werner and Brand, 2001). Finally, our results for δ^{13}C-CH$_4$ of NEEM were compared to the results that two external laboratories found for NEEM (not for δ^2H-CH$_4$ because our setup is currently not equipped for such measurement).

2.2 Calibration of pure CH$_4$

Figure 3a shows a schematic of the setup used to quantitatively combust pure CH$_4$ to CO$_2$ and H$_2$O, which were subsequently trapped for consecutive isotope analysis. This procedure will hereafter be referred to as the offline combustion method. The combustion unit is a vacuum system consisting of two quartz glass tubes of 10 and 12 mm inner diameter (ID) and 350 mm in length. Both are routed through a tube furnace (300 mm heated length, 60 mm ID) and are filled with copper oxide (61205-100G, Sigma-Aldrich, Denmark) throughout the heated zone. The copper oxide is held in place by quartz glass frits to one side and with quartz wool to the other side. Tubes outside the furnace are made of borosilicate glass. Figure 3a shows the H$_2$O section to the right side and the CO$_2$ section with the gas inlet to the left side of the furnace. The H$_2$O section is made of a glass tube with 10 mm outer diameter (OD). It consists of a double loop used as a continuous H$_2$O trap which leads into a 250 ml bottle trap. The tear-shaped bottle bottom enables focusing the H$_2$O in a narrow, well defined spot for easy pipetting of the sample into a septum-sealed sample vial for subsequent δ^2H analysis. The tubes in the CO$_2$ section are of 12 mm OD, only the branch to the gas inlet is of 6 mm OD so it can be connected to a 1/4″ stainless steel T-piece. A 250 ml cylindrical trap with a stopcock is connected with a 1/2″ Ultra-Torr connector. It can be removed to transfer the CH$_4$-derived CO$_2$ for subsequent analysis. Figure 3b displays the gas manifold, which represents the interface between the combustion unit and all peripheral units such as the pump, gas tanks and sample cylinders. Manifold and combustion unit are connected via a flexible stainless steel tube that prevents the propagation of vibrations from the pump to the glass system. A pressure gauge (2 bar max) between combustion unit and flexible tube is used to quantify the amount of introduced sample gas
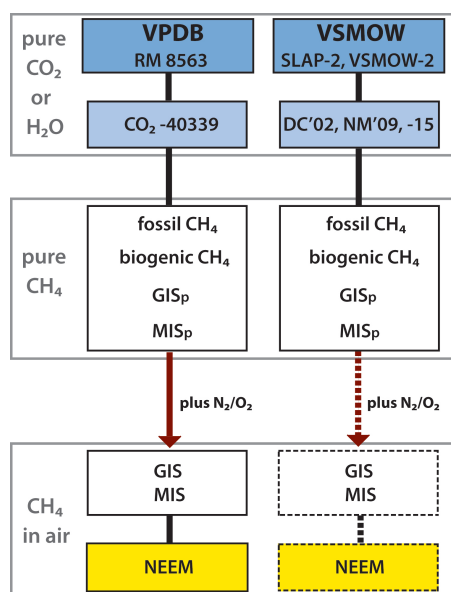
Fig. 2. Shown are the relations of measurements to the VPDB and VSMOW isotope scales in a top-down hierarchy. The dark blue boxes represent the isotope scales and name the international measurement standard used to reference our isotope reference materials, shown in light blue boxes. These isotope reference materials were used to reference the pure CH_4 gases to the respective isotope scale. The red arrows indicate the step where GIS and MIS are produced by diluting the referenced GIS_p and MIS_p with CH_4 free air, respectively. The yellow boxes in the bottom line represent the sample level. NEEM was referenced according to this reference scheme and is thus anchored to the isotope scales via the respective hierarchy of isotope reference materials. GIS, MIS and NEEM could not be referenced to the VSMOW scale because the GC-IRMS setup is not prepared for isotope measurements of δ^2H on CH_4 in air (therefore indicated by arrows and boxes in dashed lines). Grey boxes group the type of measurement standards, isotope reference materials and gas mixtures.

and to indicate pressure changes inside the combustion unit. The pressure in the mixing part of the manifold is measured by a second pressure gauge (60 bar max). Two 1 l sample cylinders in the high pressure part of the manifold are used as reservoirs to mix and store pure CH_4 gases. The copper inside the combustion unit is oxidized with O_2 (Table 1) at temperatures of 600 °C according to Reaction (R1):

$$2Cu + O_2 \rightleftharpoons 2CuO, \tag{R1}$$

O_2 is released during the combustion by the reverse reaction of (R1) when the furnace is heated to 850 °C. The copper either serves as a reducing or oxidizing agent (O_2 acceptor or donor) depending on the furnace temperature setting (Merritt et al., 1995a). In the beginning of a combustion process, the continuous H_2O trap was cooled to −78 °C. Aliquots of 120–160 ml CH_4 were injected into the evacuated combustion

reactor at ambient temperatures, resulting in pressures of about 200 mbar. Subsequently, the oven was heated to 850 °C so that the copper oxide in the combustion unit released the oxygen for the CH_4 oxidation (Merritt et al., 1995a).

The combustion process is accelerated by submerging either the CO_2 or the H_2O trap in liquid nitrogen (−196 °C), while the respective other trap is heated to room temperature. Alternately, cooling the CO_2 or the H_2O trap to liquid nitrogen temperatures forces the CO_2 and H_2O back and forth through the system and thereby transports the CH_4 through the combustion reactor. This process is hereafter referred to as cryo-transfer, where each cryo-transfer lasted approximately 10 min. Each cryo-transfer cycle generates more CO_2 and H_2O until the CH_4 is quantitatively combusted. While the CO_2 is driven back and forth through the combustion reactor, the H_2O accumulates in the continuous H_2O trap. Whenever the CO_2 trap is cooled for a cryo-transfer, the newly produced H_2O first freezes in the CO_2 trap along with the CO_2 and is then transferred to the continuous H_2O trap during the following cooling of the final H_2O trap with liquid nitrogen. The transfer of H_2O into the continuous H_2O trap was accelerated by heating the CO_2 trap and the glass lines with a heat gun.

The number of cryo-transfer cycles is critical as isotope fractionation occurs during the combustion process. Incomplete oxidation leads to an offset between the $\delta^{13}C$ of the initial CH_4 and the $\delta^{13}C$ of the CO_2 derived from it (described in detail by Merritt et al., 1995a, and Zeng et al., 1994). Tests showed reproduced $\delta^{13}C$ values when the samples were quantitatively combusted. This was the case after 25 cryo-transfer cycles for test with sample sizes between 115 and 160 ml and combustion temperatures between 840 and 860 °C (Fig. 4). Higher temperatures in the combustion unit increase the equillibium pressure of oxygen over the copper and thereby the oxidation rate, thus, requiring less cryo-transfers for a complete combustion. However, we chose to limit the oxidation temperature to 850 °C in order to increase the life-time of the combustion reactor, following Merritt et al. (1995a) and Zeng et al. (1994).

N_2O might form from traces of N_2 and O_2 in the oxidation reactor (Vaughn et al., 2004) and must be eliminated to avoid mass interferences with CO_2 in the DI-IRMS (Ghosh and Brand, 2004). Therefore, we reduced N_2O to N_2 and O_2 in the reduction reactor (Fig. 3a) according to the following Reaction (R2):

$$N_2O + Cu \rightarrow N_2 + CuO \tag{R2}$$

First, we freeze all sample gas by cooling the traps to liquid nitrogen temperatures and thereby cryo-focus the samples in the traps before we close the trap valves. Next, the reduction unit is evacuated while held at a constant temperature of 850 °C. This step liberates any O_2 in the reduction unit according to Reaction (R1), thereby increasing the reduction capacity of the copper in preparation for the following reduction process (Kapteijn et al., 1996). Afterwards, the oven
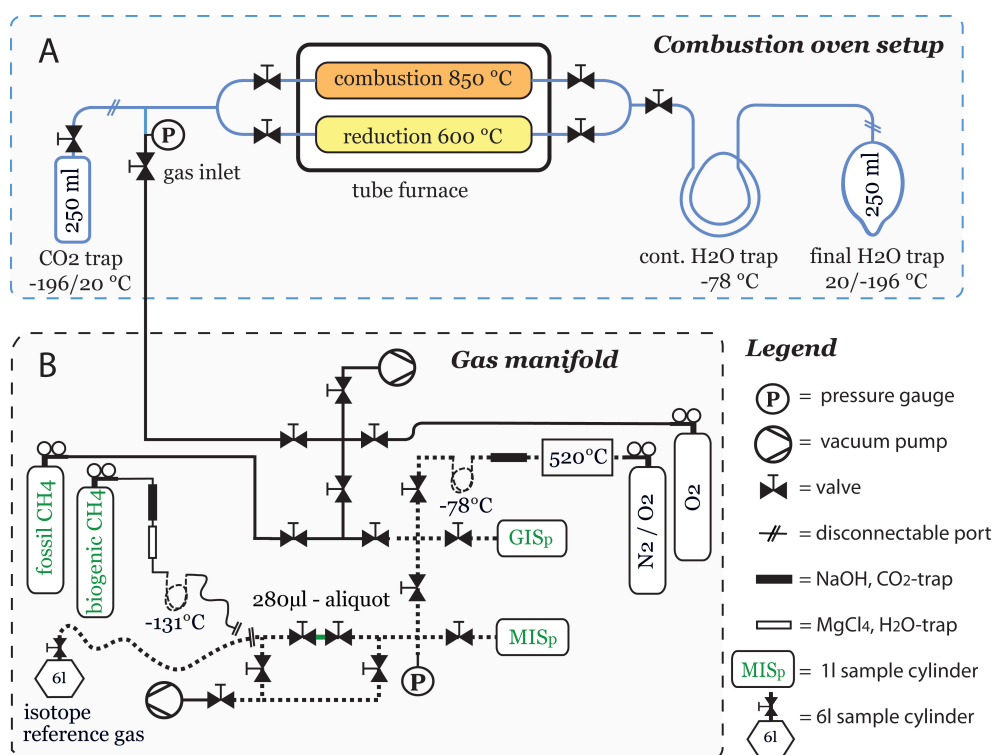
Fig. 3. Schematic figure of the setup. The top panel **(A)** illustrates the combustion and reduction reactors as well as the CO$_2$ and the two H$_2$O traps. The blue lines indicate the glass parts of this vacuum component. The diagonal parallel lines indicate the disconnection ports, where the CO$_2$ trap and the H$_2$O trap can be removed to transfer the sample. The bottom panel **(B)** shows the gas manifold that facilitates mixing and aliquoting the samples. Solid black lines represent the brass components used for gas introduction and evacuation. Dotted black lines indicate stainless steel components that take pressures of up to 60 bars. Diagonal parallel lines show the disconnection port that either connects the tank of biogenic CH$_4$ or the reservoir for the isotope reference gas. The aliquot volume of 280 µl is indicated by the green line between the valves

temperature is decreased to 600 °C and we cryo-transfer the sample gas 10 times through the reduction unit, where N$_2$O is reduced according to Reaction (R2). While O$_2$ is absorbed by the copper, N$_2$ remains in the sample gas (Kapteijn et al., 1996). The CO$_2$ does not react with the copper at 600 °C. This way, N$_2$O is quantitatively eliminated from the sample gas. Subsequently, the CO$_2$ trap is submerged in liquid nitrogen for four minutes until all CO$_2$ is trapped. Extending the CO$_2$ trapping time to 20 min showed no effect on the δ^{13}C values. The CO$_2$ trap is closed and disconnected for subsequent analysis. The continuous H$_2$O trap is heated and all H$_2$O focussed in the bottom of the tear-drop-shaped H$_2$O trap by submerging the latter in liquid nitrogen. Afterwards, the H$_2$O is melted within the small tear and the H$_2$O trap is disconnected to transfer the H$_2$O with a pipette into a 0.7 ml glass vial (548-0036, VWR International, Denmark) for subsequent δ^2H analysis. The glass vial is crimp-sealed with a septum to prevent loss through evaporation.

The combustion unit gets re-oxidized with pure O$_2$ at 600 °C in preparation for the consecutive sample. The O$_2$

absorption time depends on the oxidation level of the copper. We re-oxidized the combustion reactor after each sample by maintaining a constant O$_2$ pressure of 900 mbar for 10 min. It takes one day to prepare and combust one sample including the time to prepare the setup for the consecutive experiment.

We measured the δ^{13}C of CO$_2$ produced from the CH$_4$ combustion by DI-IRMS (Delta V Plus, Thermo Finnigan, Germany). For δ^2H in H$_2$O, we used commercial instruments, either a high Temperature Conversion/Elemental Analyser coupled to an IRMS (TC/EA-IRMS, Thermo Finnigan, Delta V Advantage) or laser spectroscopy (Picarro Inc. USA) as described by Gkinis et al. (2010).

We performed a sensitivity test for the effect of laboratory air leakage on the measured δ^{13}C-CH$_4$ and monitored the variability of laboratory air in all combusted samples. We conclude that leakage or system blanks have no significant effect on our results (detailed information in the Supplement).
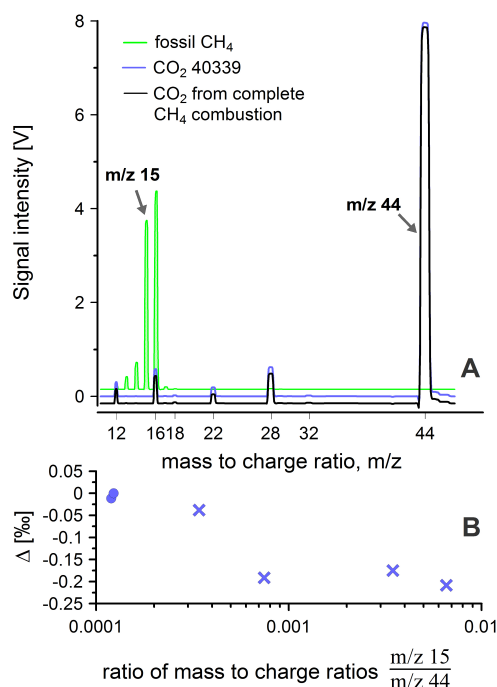
Fig. 4. Assessment of the completeness of the combustion of pure CH$_4$ gases. **(A)** Shown are three scans of mass abundances, each resulting from the injection of one gas into the ion source of the dual inlet IRMS. The lines result from pure CH$_4$ (green line), the pure CO$_2$-40339 (blue line) and CO$_2$ derived from a completely combusted CH$_4$ sample (black line). Because all measurements have the same background signal and would overlap, the green and the black line are artificially offset by 0.15 V and −0.15 V, respectively, to highlight the details. Both CH_4^+ and CO_2^+ decompose in the source, but a signal on mass to charge ratio m/z 15 can only result from injection of CH$_4$, while only injected CO$_2$ produces a signal on m/z 44. The ratio of m/z 15 over m/z 44 can therefore be used to quantify the remaining fraction of CH$_4$ within the CO$_2$ of a combusted sample. A high ratio of m/z 15 over m/z 44 indicates a large fraction of CH$_4$ in the CO$_2$ gas, hence an incomplete combustion. **(B)** The difference between measured and expected $\delta^{13}C$-CH_4 (Δ) in dependence on the completeness of combustion. CO$_2$ from completely combusted CH$_4$ gas shows ratios of m/z 15 over m/z 44 of ≤ 0.0002 (blue circles), indicating absence of CH$_4$. Incomplete CH$_4$ combustion produces offsets in normalised $\delta^{13}C$-CH_4 (blue crosses). Complete combustion is reached after 25 cryo-transfers when m/z 15 over m/z 44 in the CH$_4$ derived CO$_2$ is ≤ 0.0002 and the $\delta^{13}C$-CH_4 offset becomes negligible.

2.3 Preparation of pure CH$_4$ gases and mixing of GIS$_p$ and MIS$_p$

We mixed fossil and biogenic CH$_4$ to obtain GIS$_p$ and MIS$_p$ (Fig. 1). The fossil CH$_4$ was commercially purchased and has a high purity level of 99.995 %. The biogenic CH$_4$ was taken from a biogas reactor in northern Germany (Table 1) and needed purification prior to its use. Biogenic CH$_4$ is

produced when methanogenic bacteria ferment organic material in anaerobic conditions. This process is commercially used to generate biogenic CH$_4$ as a green fuel from agricultural products with CH$_4$ contents of up to ∼ 95 %. The remaining 5 % mostly constist of atmospheric air but also of traces of CO$_2$, H$_2$O and H$_2$S that are also generated during the biogas production. We received a 50 l tank of biogenic CH$_4$ and removed CO$_2$, H$_2$O and H$_2$S while a CH$_4$ aliquot was transferred from the source tank to a 1 l sample cylinder at the manifold (Fig. 3b). A 1.5 m long, 1/4″ OD tube was filled with sodium hydroxide and magnesium perchlorate hydrate to absorb CO$_2$ and H$_2$O, respectively. Subsequently, a coiled 1/8″ tube (2 m long) submerged in a liquid nitrogen/n-Pentane slush froze out H$_2$S and residual H$_2$O at −131 °C. Aliquots of purified biogenic CH$_4$ could then be introduced into the combustion unit from the 1 l sample cylinder for analysis as described in Sect. 2.2. We introduced biogenic CH$_4$ into both 1 l sample cylinders shown in Fig. 3b. Afterwards, we added fossil CH$_4$ and controlled the mixing ratio between biogenic and fossil CH$_4$ in each mixture by terminating the flow of fossil CH$_4$ when the pressure indicated that the desired mixing ratio was reached. We produced GIS$_p$ and MIS$_p$ with biogenic CH$_4$ contents of 15 % and 52 % , respectively, and analysed their isotopic composition using the offline combustion method (Sect. 2.2). Detailed information on the determination of the purity level of the purified biogenic CH$_4$ is available in the Supplement.

2.4 Producing and measuring synthetic isotope reference gases GIS and MIS

The N$_2$/O$_2$ mixture that we used for mixing the synthetic isotope reference gases consisted of N$_2$ and O$_2$ in atmospheric mixing ratios but additionally contained 2 ppmv of CH$_4$. This CH$_4$ fraction needed to be removed prior to blending. Therefore, the N$_2$/O$_2$ mixture was routed through a combustion furnace built from a 60 cm long piece of 1/2″ OD seamless stainless steel tube. The central 20 cm of this tube is filled with a catalyst (SF-PH-102S-1008201, PureSphere, South Korea) and heated to 520 ± 1 °C. Downstream of the oven, two traps in series removed H$_2$O from the air flow. The first trap is a 1 m long, 1/4″ OD line filled with magnesium perchlorate, which is followed by a 2 m coil of 1/8″ OD tube submerged in ethanol-dry ice (−78 °C). The furnace is efficiently removing CH$_4$ from the N$_2$/O$_2$ mixture to ≤ 2 ppbv, i.e. the detection limit of the laser spectrometer used to monitor the CH$_4$ fraction (Picarro Inc, USA). The process steps applied for the purification are shown in Fig. 3b. The purified N$_2$/O$_2$ mixture is hereafter referred to as CH$_4$-free air (Table 1).

The produced isotope reference gases based on GIS$_p$ and MIS$_p$ will be referred to as GIS and MIS, respectively. We started preparing the mixing of the synthetic isotope reference gas by transferring an aliquot of GIS$_p$ or MIS$_p$ to the designated aliquot volume of 280 ± 1 µl (Fig. 3b) while

Table 2. Mean δ^{13}C and δ^2H isotope values of pure CH$_4$ gases (top panel) and of NEEM, measured with the produced isotope reference gases (bottom panel). The calculations of the uncertainties are explained in Sect. 3 and are based on n repetitive measurements. "oc" denotes the offline combustion method, DI-IRMS refers to Dual Inlet IRMS and laser spec. indicates δ^2H measurements by laser spectroscopy. The * indicates the δ^2H measurements that needed correction for a 4.4 ‰ system offset (Sect. 3). The indices GIS and MIS indicate the applied isotope reference gas for the measurement of NEEM. The laboratory agreement shows the difference between the referencing of NEEM with our GC-IRMS setup and our produced isotope reference gases compared to the mean value of the two external laboratories. Our GC-IRMS system can currently not measure δ^2H-CH$_4$.

Measurand	δ^{13}C [‰]	δ^{13}C method	δ^2H [‰]	δ^2H method	n
fossil CH$_4$	-39.56 ± 0.04	oc, DI-IRMS	-170.1 ± 0.7	oc, TC/EA-IRMS	4
biogenic CH$_4$	-56.37 ± 0.04	oc, DI-IRMS	-317.4 ± 0.7	oc, TC/EA-IRMS	4
GIS$_p$	-42.21 ± 0.04	oc, DI-IRMS	-193.1 ± 0.7	oc, TC/EA-IRMS	3
MIS$_p$	-47.25 ± 0.04	oc, DI-IRMS	-237.1 ± 0.7	oc, laser spec.*	2
Measurand	δ^{13}C [‰]	δ^{13}C method	Daily system error [‰]	Laboratory agreement [‰]	n
NEEM$_{GIS}$	-47.29 ± 0.06	GC-IRMS	-0.29 ± 0.04	0.02	3
NEEM$_{MIS}$	-47.32 ± 0.06	GC-IRMS	-0.34 ± 0.06	-0.01	6

measuring the pressure within this section. We used two 6 l air sample flasks (SilcoCan, Restek, USA) to mix and store the synthetic isotope reference gases. Each flask was flushed with CH$_4$-free air and evacuated 3 times prior to the mixing to remove residual air. We first filled the evacuated target flask with CH$_4$-free air through a line bypassing the aliquot (Fig. 3b). This was to introduce CH$_4$-free air into the target flask so potential adsorption effects between gas and flask-wall could take place with CH$_4$-free air rather than with CH$_4$ to minimise potential isotope fractionation of CH$_4$. At a pressure of 1 bar, the CH$_4$-free air flow was re-routed through the aliquot volume to inject the CH$_4$ into the flask. We continued filling the flask with CH$_4$-free air until we reached the calculated pressure to obtain the desired CH$_4$ mixing ratio. We produced one mixture of MIS and one of GIS. The determined CH$_4$ mixing ratio for MIS was 1800 ± 20 ppb and for GIS 1420 ± 20 ppb (the large error bars result from the GC-IRMS system that is not optimised for high precision measurements of CH$_4$ mixing ratios). GIS exceeded the CH$_4$ mixing ratio reported for the glacial atmosphere by a factor of ~ 4, which is due to our limitation to further dilute GIS$_p$, given the maximum pressure of the sample flask of 2.8 bar. A larger mixing reservoir would avoid this limitation.

We used a GC-IRMS setup designed for measurements of atmospheric samples to test the produced isotope reference gases. Our GC-IRMS system and data analysis is similar to the method described by Sapart et al. (2011) where CH$_4$ is pre-concentrated, cryo-focussed and chromatographically separated from other sample components before it is combusted to CO$_2$ and H$_2$O within a He carrier gas flow. In a first step, the isotope ratios of the CH$_4$ derived CO$_2$ of standards and samples are referenced via the flat-topped peaks of our pure, referenced CO$_2$-40339, which is injected into the IRMS through the reference open split. In the consecutive data processing, the measurements of the samples are referenced to the VPDB scale by applying a simple correction

algorithm that accounts for the systematic errors as determined by blocks of 3 standard measurements that bracket blocks of 3 sample measurements according to Werner and Brand (2001).

For the following tests, we assumed that the δ^{13}C values of GIS and MIS are identical to those of GIS$_p$ and MIS$_p$ and that our gas-mixing method does not cause isotopic fractionation. The deviation between GC-IRMS measurements of GIS or MIS and the respective DI-IRMS measurements of GIS$_p$ or MIS$_p$ then represents the quantity of the daily system offset of the GC-IRMS setup and could then be used in the data correction algorithm. Thereby, GIS and MIS serve as standards to anchor the δ^{13}C-CH$_4$ in NEEM to the VPDB isotope scale. In order to validate our method to produce isotope reference gases, we compare our final results for NEEM to the δ^{13}C-CH$_4$ values that two external laboratories have reported for NEEM. These are the Institute for Marine and Atmospheric Research in Utrecht (IMAU), University of Utrecht, the Netherlands, using the system described by Sapart et al. (2011) and the Institute for Climate and Environmental Physics (Bern), University of Bern, Switzerland. IMAU measured NEEM with -47.31 ± 0.05 ‰ (Sapart et al., 2012) and Bern with -47.30 ± 0.11 ‰ (J. Schmitt, personal communication, 2011), respectively.

3 Results and discussion

All results of CH$_4$ isotope ratios measured by DI-IRMS, TC/EA-IRMS, laser spectroscopy and GC-IRMS, respectively, are summarized in Table 2. Based on the pooled standard deviation of 13 samples (fossil and biogenic CH$_4$, GIS$_p$ and MIS$_p$) the precision of the offline combustion method for pure CH$_4$ gases is 0.04 ‰ for δ^{13}C and 0.7 ‰ for δ^2H. Two of those samples were measured for δ^2H using laser spectroscopy as part of a larger batch of measurements which

needed correction for a 4.4‰ offset of unknown origin. We speculate this offset resulted from isotope fractionation due to evaporation/condensation processes within the sample vials when an autosampler failure caused a significantly longer storage time at room temperature.

We found δ^{13}C and δ^2H values of -39.56 ± 0.04‰ and -170.1 ± 0.7‰ in our fossil CH$_4$ and -56.37 ± 0.04‰ and -317.4 ± 0.7‰ in our biogenic CH$_4$ in line with values reported by Quay et al. (1999) for those sources. We mixed these CH$_4$ gases and matched the δ^{13}C values in the filial mixtures to glacial and present atmospheric values. GIS$_p$ and MIS$_p$ show δ^{13}C values of -42.21 ± 0.04‰ and -47.25 ± 0.04‰, respectively. Resulting δ^2H values for GIS$_p$ and MIS$_p$ are -193.1 ± 0.7‰ and -237.1 ± 0.7‰, respectively. The δ^2H values do not correspond to atmospheric values. Atmospheric δ^2H-CH$_4$ is so strongly enriched in ^{2}H due to sink fractionation (Quay et al., 1999) that it cannot be realised by mixing of CH$_4$ from commonly available sources (Fig. 1). Repeated referencing of the produced isotope reference gases GIS and MIS versus CO$_2$-40339 in our GC-IRMS system revealed (i) an offset of the measured versus the true value and (ii) a day to day variability of the offset. The observed systematic offset in our GC-IRMS system shows a typical variability between 0 and 0.05‰ throughout one day and a maximum variability of 0.4‰ between different days. The propagated uncertainties of the day to day variability ranges between 0.04‰ and 0.06‰. The variation of the uncertainty demonstrates the importance of measuring isotope reference gases and samples following the principle of identical treatment. We repeatedly measured NEEM against GIS and MIS, applied the offset corrections and obtained -47.29 ± 0.06‰ and -47.32 ± 0.06‰, respectively. All uncertainties of the GC-IRMS measurements on atmospheric samples shown in Table 2 are independently calculated by propagating the standard errors of the mean (because we produced one mixture of each GIS and MIS, uncertainties based on the gas mixing are not included). The NEEM air was also measured at IMAU and Bern, both partners in the NEEM project. We found a difference of 0.02‰ and -0.01‰ between our NEEM results being referenced versus GIS and MIS, respectively, and the mean of IMAU and Bern. The results agree well within the uncertainty of the measurements. Our results show that our method to produce isotope reference gases is reproducible and does not introduce significant isotopic fractionation.

4   Conclusions

We developed a high precision method to reference the δ^{13}C and δ^2H isotopic composition of pure CH$_4$ samples on the VPDB or VSMOW scale, respectively. Based on the pooled standard deviation, we estimate the reproducibility of our offline combustion method to 0.04‰ and 0.7‰ for δ^{13}C and δ^2H, respectively. Referenced parental CH$_4$ gases were

mixed to obtain pure CH$_4$ gases with precisely referenced isotopic composition of δ^{13}C near atmospheric values. Based on these CH$_4$ mixtures, we created synthetic isotope reference gases with atmospheric CH$_4$ concentrations and δ^{13}C-CH$_4$ isotope values. The synthetic reference gases allow us to detect and correct for system drifts and offsets in our GC-IRMS setup for atmospheric samples demonstrating the importance of our effort to produce atmospheric reference gases. We measured an air sample from a Greenland clean air site and found our results as determined with our produced isotope reference gases to be in excellent agreement with the results from partner laboratories. Isotope measurements are becoming increasingly precise. Therefore, it is important to establish a suite of isotope reference gases for δ^{13}C in CH$_4$ covering the whole range of investigated δ^{13}C and CH$_4$ mixing ratios, as was done for CH$_4$ mixing ratios (Dlugokencky et al., 2005) and for CO$_2$ isotope ratios (Ghosh et al., 2005). Our method can be used to produce synthetic isotope reference gases for δ^{13}C-CH$_4$ in air at various mixing ratios. The system can be adapted for mixing isotope reference gases in large tanks with pressures of up to 60 bar, requiring additional tests on the stability of large volume mixtures. With a source gas that is more enriched in δ^2H, the suite could be extended to atmospheric values of δ^2H-CH$_4$. Further, additional components (e.g. N$_2$O, CO$_2$, CO) can potentially be added, which would be beneficial for new analytical systems, which are measuring multiple components in one sample. However, we feel that it is important to complement multi-component isotope reference gas mixtures with single-component isotope reference gases because the combination of the two enables to identify analytical interferences with other trace gases present. Most important for the future would be to initialise a program to produce and maintain such isotope reference gases in order to provide them to the community in a long term perspective, thereby fulfilling the requirements of the WMO-GAW.

CH$_4$ as well as Michael Bock, Barbara Seth and Jochen Schmitt for measuring δ^{13}C-CH$_4$ in "NEEM" air. Many thanks also to Mads Dam Ellehøj, Henriette Lerche and Bo Vinther for the δ^2H measurements, to Colleen Templeton and furthermore to Pantmann Labglass for Danish Design glass-blowing. Furthermore, we would like to thank the three anonymous reviewers for their constructive comments that helped improve the manuscript.

Edited by: A. C. Manning

References

Bock, M., Schmitt, J., Möller, L., Spahni, R., Blunier, T., and Fischer, H.: Hydrogen Isotopes Preclude Marine Hydrate CH$_4$ Emissions at the Onset of Dansgaard-Oeschger Events, Science, 328, 1686–1689, 2010.

Brand, W. A.: GAW Report No. 194, 15th WMO/IAEA Meeting of Experts on Carbon Dioxide, Other Greenhouse Gases and Related Tracers Measurements Techniques, Jena, Germany, 7–10 September 2009, 2011.

Brand, W. A., Coplen, T. B., Aerts-Bijma, A. T., Bohlke, J. K., Gehre, M., Geilmann, H., Groning, M., Jansen, H. G., Meijer, H. A. J., Mroczkowski, S. J., Qi, H. P., Soergel, K., Stuart-Williams, H., Weise, S. M., and Werner, R. A.: Comprehensive inter-laboratory calibration of reference materials for δ^{18}O versus VSMOW using various on-line high-temperature conversion techniques, Rapid Commun. Mass Sp., 23, 999–1019, 2009.

Coplen, T. B.: Guidelines and recommended terms for expression of stable-isotope-ratio and gas-ratio measurement results, Rapid Commun. Mass Sp., 25, 2538–2560, 2011.

Dlugokencky, E. J., Myers, R. C., Lang, P. M., Masarie, K. A., Crotwell, A. M., Thoning, K. W., Hall, B. D., Elkins, J. W., and Steele, L. P.: Conversion of NOAA atmospheric dry air CH$_4$ mole fractions to a gravimetrically prepared standard scale, J. Geophys. Res.-Atmos., 110, D18306, doi:10.1029/2005JD006035, 2005.

Dlugokencky, E. J., Bruhwiler, L., White, J. W. C., Emmons, L. K., Novelli, P. C., Montzka, S. A., Masarie, K. A., Lang, P. M., Crotwell, A. M., Miller, J. B., and Gatti, L. V.: Observational constraints on recent increases in the atmospheric CH$_4$ burden, Geophys. Res. Lett., 36, L18803, doi:10.1029/2009GL039780, 2009.

Ferretti, D. F., Miller, J. B., White, J. W. C., Etheridge, D. M., Lassey, K. R., Lowe, D. C., Meure, C. M. M., Dreier, M. F., Trudinger, C. M., van Ommen, T. D., and Langenfelds, R. L.: Unexpected changes to the global methane budget over the past 2000 years, Science, 309, 1714–1717, 2005.

Fischer, H., Behrens, M., Bock, M., Richter, U., Schmitt, J., Loulergue, L., Chappellaz, J., Spahni, R., Blunier, T., Leuenberger, M., and Stocker, T. F.: Changing boreal methane sources and constant biomass burning during the last termination, Nature, 452, 864–867, 2008.

Ghosh, P. and Brand, W. A.: The effect of N$_2$O on the isotopic composition of air−CO$_2$ samples, Rapid Commun. Mass Sp., 18, 1830–1838, 2004.

Ghosh, P., Patecki, M., Rothe, M., and Brand, W. A.: Calcite-CO$_2$ mixed into CO$_2$-free air: a new CO$_2$-in-air stable isotope reference material for the VPDB scale, Rapid Commun. Mass Sp., 19, 1097–1119, 2005.

Gkinis, V., Popp, T. J., Johnsen, S. J., and Blunier, T.: A continuous stream flash evaporator for the calibration of an IR cavity ring-down spectrometer for the isotopic analysis of water, Isotopes in Environmental and Health Studies, 46, 463–475, doi:10.1080/10256016.2010.538052, 2010.

IAEA: Reference Sheet for International Measurement Standards, The International Atomic Energy Agency in cooperation with the National Institute for Science and Technology (NIST), 5 May 2009, 2009.

Kapteijn, F., RodriguezMirasol, J., and Moulijn, J. A.: Heterogeneous catalytic decomposition of nitrous oxide, Appl. Catal. B-Environ., 9, 25–64, 1996.

Levin, I., Veidt, C., Vaughn, B., Brailsford, G., Bromley, T., Heinz, R., Lowe, D., Miller, J. B., Poß, C., and White, J.: No inter-hemispheric δ^{13}CH$_4$ trend observed, Nature, 486, E3–E4, 2012.

Loulergue, L., Schilt, A., Spahni, R., Masson-Delmotte, V., Blunier, T., Lemieux, B., Barnola, J. M., Raynaud, D., Stocker, T. F., and Chappellaz, J.: Orbital and millennial-scale features of atmospheric CH$_4$ over the past 800,000 years, Nature, 453, 383–386, 2008.

Merritt, D. A., Freeman, K. H., Ricci, M. P., Studley, S. A., and Hayes, J. M.: Performance and Otpimization of a Combustion Interface for Isotope Ratio Monitoring Gas-Chromatography Mass-Spectrometry, Anal. Chem., 67, 2461–2473, 1995a.

Merritt, D. A., Hayes, J. M., and Marias, D. J. D.: Carbon Isotopic Analysis of Atmospheric Methane by Isotope-Ratio-Monitoring Gas-Chromatography Mass-Spectrometry, J. Geophys. Res.-Atmos., 100, 1317–1326, 1995b.

Mikaloff Fletcher, S. E., Tans, P. P., Bruhwiler, L. M., Miller, J. B., and Heimann, M.: CH$_4$ sources estimated from atmospheric observations of CH$_4$ and its ^{13}C/^{12}C isotopic ratios: 2. Inverse modeling of CH$_4$ fluxes from geographical regions, Global Biogeochem. Cy., 18, 15, GB4005, doi:10.1029/2004GB002224, 2004.

Quay, P., Stutsman, J., Wilbur, D., Snover, A., Dlugokencky, E., and Brown, T.: The isotopic composition of atmospheric methane, Global Biogeochem. Cy., 13, 445–461, 1999.

Rice, A. L., Gotoh, A. A., Ajie, H. O., and Tyler, S. C.: High-precision continuous-flow measurement of δC^{13} and δD of atmospheric CH$_4$, Anal. Chem., 73, 4104–4110, 2001.

Sapart, C. J., van der Veen, C., Vigano, I., Brass,, M., van de Wal, R. S. W., Bock, M., Fischer, H., Sowers, T., Buizert, C., Sperlich, P., Blunier, T., Behrens, M., Schmitt, J., Seth, B., and Röckmann, T.: Simultaneous stable isotope analysis of methane and nitrous oxide on ice core samples, Atmos. Meas. Tech., 4, 2607–2618, doi:10.5194/amt-4-2607-2011, 2011.

Sapart, C. J., Martinerie, P., Chappellaz, J., van de Wal, R. S. W., Sperlich, P., van der Veen, C., Bernard, S., Sturges, W. T., Blunier, T., Witrant, E., Schwander, J., Etheridge, D., and Röckmann, T.: Reconstruction of the carbon isotopic composition of methane over the last 50 yr based on firn air measurements at 11 polar sites, Atmos. Chem. Phys. Discuss., 12, 9587–9619, doi:10.5194/acpd-12-9587-2012, 2012.

Sowers, T.: Late quaternary atmospheric CH$_4$ isotope record suggests marine clathrates are stable, Science, 311, 838–840, 2006.

Tyler, S. C., Rice, A. L., and Ajie, H. O.: Stable isotope ratios in atmospheric CH$_4$: Implications for seasonal sources and sinks, J. Geophys. Res.-Atmos., 112, D03303, doi:10.1029/2006JD007231, 2007.

Vaughn, B., Miller, J., Ferretti, D. F., and White, J. W. C.: Stable isotope measurements of atmospheric CO$_2$ and CH$_4$, in: Handbook of Stable Isotope Analytical Techniques, edited by: Groot, P. A., Vol. 1, 272–304, Elsevier B.V., 2004.

Verkouteren, R. M.: Preparation, characterization, and value assignment of carbon dioxide isotopic reference materials: RMs 8562, 8563, and 8564, Anal. Chem., 71, 4740–4746, 1999.

Werner, R. A. and Brand, W. A.: Referencing strategies and techniques in stable isotope ratio analysis, Rapid Commun. Mass Sp., 15, 501–519, 2001.

Zeng, Y. Q., Mukai, H., Bandow, H., and Nojiri, Y.: Application of gas-chromatography combustion-isotope ratio mass-spectrometry to carbon isotopic analysis of methane and carbon-monoxide in environmental-samples, Anal Chim. Acta, 289, 195–204, doi:10.1016/0003-2670(94)80103-7, 1994.

2.4   Supplementary informations

This section has been published as a supplementary to Sperlich et al. (2012).

2.4.1   Purity of biogenic CH_4

Impurity quantification in biogenic CH_4

The biogenic CH_4 was sampled at a biogas power plant in northern Germany that uses agricultural crops to produce CH_4 which is pumped into the local gas grid. This requires a high purity level of the CH_4 which is achieved by coupling the biogas plant to an industrial purification reactor that increases the CH_4 content to about 95% by removing H_2S, H_2O and CO_2. The remaining 5% comprise mostly N_2, O_2, CO_2 and traces of H_2S. For our purposes, the biogenic CH_4 needed further purification. Non-CH_4 carbon containing molecules that could impact on the isotope measurements were removed. H_2S, which possibly degrades the analytical systems was furthermore reduced.

To assess the composition and purity of the gases, mass abundance scans were performed by dual-inlet IRMS analysis for high purity fossil CH_4, biogenic CH_4 as well as purified biogenic CH_4. The mass abundance scans were then compared to analyse their content of non-CH_4 components. In general, mass abundance scans of a pure CH_4 show diverse spectra of masses because certain fractions of CH_4 molecules decompose and/or re-combine to secondary molecules within the ion source, as a result of the electron bombardment (Brunnée and Voshage, 1964). Ions producing these spectra can therefore be an artefact, suggesting the abundance of non existing gas species in the sample gas. Converting mass abundances to gas compositions therefore introduces an error. The mass abundance scans are thus not the most accurate method to quantify impurities within a CH_4 gas. However, we will show that comparing mass abundance scans of CH_4 with different purity level allows for a sufficient estimate.

Carbon containing impurities

The performed mass abundance scans were evaluated by ISODAT 3.0, the software used to control the mass spectrometer. The results for the purified biogenic CH_4 are shown in Table 2.1 and Figure 2.3, indicating very small signals on m/z 26, 29, 30 and 44 which are caused by non-CH_4 hydrocarbon ions. We allocated molecules with their chemical formulas to the peaks: $C_2H_2^+$, $C_2H_5^+$, $C_2H_6^+$, $C_3H_8^+$ and CO_2^+, thus containing one to three carbon atoms per molecule.

We assume that mass abundance signals on m/z 12, 13, 14, 15, 16 and 17 are caused by CH_4-derived ions containing one carbon and variable numbers of hydrogen atoms. The sum of peak areas from mass abundances that derive from CH_4 molecules was compared to the sum of peak areas from mass abundances that possibly results of non-CH_4 hydrocarbons (m/z 26, 29, 30, 44) which were weighted for the maximum number of carbon atoms. This is based on the assumption that the entire signal on m/z 26, 29, 30 and 44 is derived from hydrocarbons and that all ions causing the peak on m/z 44 comprised of $C_3H_8^+$ with three carbon atoms instead of CO_2^+. This is important because one molecule of C_3H_8 produces 3 molecules of CO_2 in the combusted sample. Therefore, one molecule of $C_3H_8^+$ contributes three times stronger to the signal on m/z 44 than one molecule of CO_2. We also assume that non-CH_4 hydrocarbons are stable in the ionisation chamber and do not contribute to signals m/z 12 to m/z 17.

In this most conservative scenario, a maximum of about 0.55% of the carbon that was detected in the ion source resulted from an ion containing more than one carbon atom. A similar analysis of our high purity fossil CH_4 reveals that about 0.67% of the detected ions were derived from ions containing at least two carbon atoms. The company providing the high purity fossil CH_4 specifies the purity level of its CH_4 N45 with 99.995% with a mixing ratio of non-CH_4 hydrocarbons ≤ 20 ppmv. Therefore, we conclude that the scan procedure over-estimates the content of non-CH_4 hydrocarbons by two orders of magnitude due to processes inside the ion source. Based on the comparison of the mass abundance scans from purified biogenic CH_4 and fossil CH_4, we can assume a similar purity level.

A simple mass balance calculation based on the assumption of a 99.995 % purity level shows, that the average $\delta^{13}C$ isotope ratio of the impurities would have to be higher than 744 ‰ or lower than -856 ‰ to affect the determined carbon isotope ratios of the biogenic CH_4 by more than the given uncertainty. Because these extreme carbon isotope ratios are highly unlikely in naturally occurring gases, we conclude that our biogenic CH_4 is sufficiently purified from non-CH_4 hydrocarbons.

H_2S

The low H_2S content of both purified and unpurified biogenic CH_4 samples could only be detected by the most sensitive Faraday cup detector of the IRMS. Because this detector was saturated for the very abundant CH_4 ions, we related the H_2S signal on m/z 34 to the O_2 signal on m/z 32 which is constant in both the purified and un-purified biogenic CH_4. The purification step decreased the H_2S by 75%. However, this is at a very low concentration levels where the evaluation of the H_2S peaks is unreliable. Given that H_2S was reduced to prevent degradation of the analytical system and is not expected to alter the measurements on CH_4 isotope ratios we consider the observed reduction as sufficient.

2.4.2   Effect of system leakage

Monitoring Argon in the sample

Mass abundance scans using dual-inlet IRMS were performed on each combusted CH_4 sample. Any leakage of laboratory air into the offline combustion setup would increase the relative abundance of Argon (Ar) compared to the mass abundance of CO_2. We interpreted the ratio of the peak heights of Ar (m/z 40) to CO_2 (m/z 44) as indicator for laboratory

Table 2.1: Mass abundances in the purified biogenic CH_4 as evaluated by ISODAT 3.0. The evaluation parameters were extremely tuned to be able to capture very small abundances and therefore compromising the accuracy of the quantification. Hence, peak numbers 8 and 9 show opposing sizes in peak area and height. The CH_4-derived ions were identified following Brunnée and Voshage (1964).

number of identified peak	magnetic field [steps]	m/z	ion	peak height [mV]	peak area [mV * steps]
1	5385	12	C^+	648	1964
2	5665	13	CH^+	1842	5837
3	5935	14	CH_2^+	3855	12182
4	6190	15	CH_3^+	22075	74717
5	6450	16	CH_4^+	25370	78391
6	6690	17	CH_5^+ or $^{13}CH_4^+$	485	1673
7	6920	18	H_2O^+	823	2760
8	7365	20	$H_2^{18}O^+$	4	22
9	8630	26	$C_2H_2^+$	2	25
10	9020	28	N_2^+	795	3249
11	9210	29	$C_2H_5^+$	15	86
12	9400	30	$C_2H_6^+$	10	65
13	9765	32	O_2^+	221	995
14	10120	34	H_2S^+	not evaluated	not evaluated
15	11140	40	Ar^+	19	128
16	11795	44	$C_3H_8^+$ or CO_2^+	33	202

air leakage into the offline combustion setup during a combustion process. To increase the sensitivity of this comparison, we used the Ar signal of a Faraday cup with a 100 times stronger. The resulting ratio is 0.006 +/- 0.0003 for the pure CO_2-40339. We found the same ratio in the combusted samples stemming from fossil CH_4. We found a ratio of 0.03 in the biogenic CH_4 which is higher due to the containing 5% of atmospheric air. We found these ratios to be stable for the respective CH_4 type. These measurements give us confidence that the measurements were not affected by leakage into the system during the aliquotation, the combustion or the sample transfer into the dual-inlet IRMS.

Sensitivity test for laboratory-air leakage

The effect of an undetected CO_2 blank can be estimated with the following sensitivity test. The offline combustion system was evacuated, closed off and tested for leaks in over-night test prior to each measurement. A sample would only be introduced if the pressure increase overnight stayed below the detection limit of our piezoelectric pressure gauge (1 mbar precision). We give a conservative estimate of the maximum effect an undetected leak would have as blank contribution. We assume a pressure increase of 1 mbar in the system of ~ 600 ml volume, which corresponds to a leakage of 0.6 ml. If we conservatively assume 1 part per thousand of the leakage is CO_2 with a $\delta^{13}C$ isotope ratio of -7 ‰ a small biogenic CH_4 sample with a $\delta^{13}C$ of -56 ‰ would be most affected. A mass balance calculation shows that the maximum possible blank contribution would affect a 120 ml sample of biogenic CH_4 with -56 ‰ by 0.0002 ‰ which is by two orders of magnitude lower than the precision of our method. We conclude that any undetected potential blank has no significant effect on our results. The blank contribution is most likely even lower because most of the combusted samples were about 50% larger than anticipated in the calculation. Also, the lab air contains more depleted CO_2 from human breath which is more depleted in ^{13}C. Any
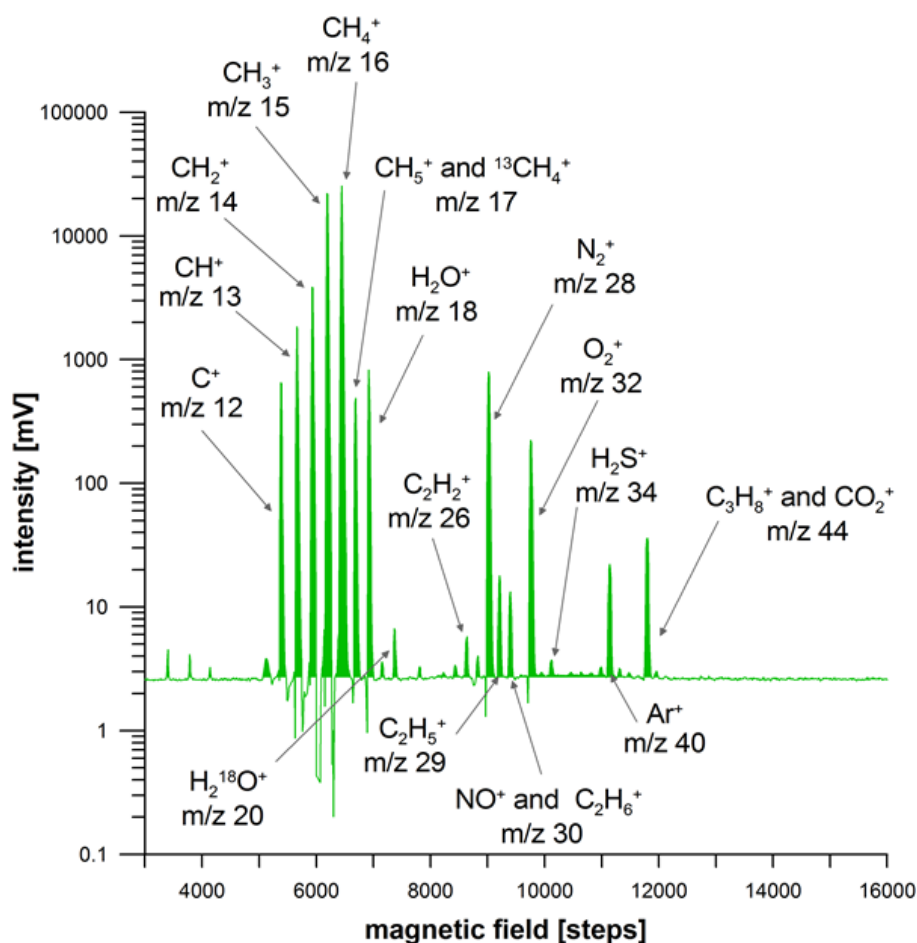
Figure 2.3: Shown is a scan of mass abundances between m/z 5 and m/z 60 when purified bio-methane is introduced into the ion source of the dual inlet IRMS. The y-axis is set to logarithmic scale to better visualise the low abundances. Chemical formulas and m/z ratios identify the respective peaks, indicated by the arrows.

additional CH_4 leakage would furthermore reduce this blank effect due to its lower isotopic leverage.

2.5   Outlook

Published methane mixing ratio and isotopes from ice cores, measured in different laboratories, will be used to better understand how the biosphere reacted to abrupt climate changes of the last glacial period. We will focus on a sequence of Dansgaard-Oeschger events encompassing a Heinrich event (Chap. 5 p. 139).

Chapter 3

δ^{15}N from entrapped air in Greenland ice cores: gas age scale, temperature and accumulation rate reconstruction

3.1 Introduction

3.1.1 Motivations

As we have seen is Sect. 1.2.4 p. 12, water isotopes are an integrated tracer of the hydrological cycle. The signal in δ^{18}O is currently interpreted in accumulation-weighted temperature in Greenland. However, other mechanisms are at play and quantifying their effect on water isotopes remains an under constrained problem. An alternative technique consists in using the isotopic composition of nitrogen trapped in the ice bubbles, δ^{15}N, combined with firn modelling (e.g., Lang et al., 1999; Severinghaus and Brook, 1999; Landais et al., 2004a; Grachev and Severinghaus, 2005; Kobashi et al., 2011). The comparison of water isotope records together with a δ^{15}N-based temperature reconstruction gives insights into the hydrological processes that affected in the past the water isotopes recorded in the snow deposited at the surface of the Greenland ice sheet (e.g., Huber et al., 2006). Moreover, a precise quantification of the amplitude of the Greenland temperature increase at the onset of a DO event is clearly a useful information to validate climate models.

The aim of this chapter is to present the method based on δ^{15}N and firn model and use it to reconstruct the temperature at different drilling sites in Greenland, paving the way for a spatial comparison of past temperatures in Greenland. Such spatial reconstructions will be finalised in the next chapter. This method also gives access to an estimation of the past accumulation rate. Combined to scenarios based on ice flow models, such reconstructions are useful to build an envelope of likely past accumulation rates for the Greenland ice sheet. This point is critical to help ice sheet models to reproduce the past dynamics of the Greenland ice sheet, in order to better predict its future evolution and possible contribution to sea-level rise.

3.1.2 Brief presentation of the method used in this chapter

The δ^{15}N registered in the ice bubbles is affected by physical processes occurring in the firn only. First, the thickness of the firn, depending on local temperature and accumulation rate,

determine the gravitational enrichment affecting δ^{15}N. Second, during an abrupt temperature increase (for example, at the onset of a DO event), the firn surface warms rapidly but its base remains cold because of the slow diffusion of heat in snow and ice. The resulting temperature gradient in the firn leads to thermal fractionation of gases: the heavy nitrogen isotopes migrate towards the cold bottom of the firn, where air is progressively trapped into air bubbles. As a result, a sharp peak in δ^{15}N is seen in the gas phase as a counterpart to the rapid increase in water stable isotopes in the ice phase. This δ^{15}N signal is then preserved in the entrapped air. Using δ^{15}N data and firn modelling, past surface temperature and accumulation rate variations can be reconstructed (Schwander et al., 1997; Goujon et al., 2003): the input temperature and accumulation rate histories for a given firn model can be tuned in order for the modelled δ^{15}N to match the measured ones. This method has already been applied to specific DO events on the NGRIP, GRIP and GISP2 ice cores (Lang et al., 1999; Huber et al., 2006; Landais et al., 2004a, 2005; Goujon et al., 2003; Severinghaus and Brook, 1999; Capron et al., 2010b) and will be applied for the first time to the NEEM ice core in Chapter 4.

3.1.3 Organisation of this chapter

In this chapter, the compaction of snow to ice is first explained briefly, together with the processes affecting gas isotopes in the firn (Sect. 3.2.1). The measurement technique used at LSCE for nitrogen isotopes is presented in Sect. 3.3.

In Sect. 3.4, we report the comparison of the Goujon and Schwander firn models, done in collaboration with Ph. Kindler from the University of Bern. These models are first compared to present-day measured firn density profiles and measured δ^{15}N data. They are then used to reconstruct the gas age scale, LID (lock-in-depth), temperature and accumulation rate for the NGRIP ice core. We propose a methodology to quantify the uncertainties associated with these climatic reconstructions. Uncertainty estimates are necessary for comparison to different methods, like past temperature history reconstructions based on borehole temperature measurements, or accumulation history based on ice flow models.

In Sect. 3.5, we present new δ^{15}N data measured at LSCE for the GRIP ice core, by A. Landais and F. Prié. Additional published δ^{15}N data for GRIP and GISP2 are used with the Goujon firn model to reconstruct the past temperature and accumulation rate histories at GRIP and GISP2. We compare these reconstructions to temperature estimates based on borehole temperature measurements and accumulation rate estimates based on ice flow models.

In Sect. 3.6, new NEEM δ^{15}N data measured in the framework of this PhD are used to determine the deepest level of the NEEM unfolded ice. In Sect. 3.7, the available NEEM δ^{15}N data and the Goujon model are used to reconstruct the NEEM gas age scale.

Finally, in the next chapter Sect. 4.2, we present new δ^{15}N data measured on the NEEM ice core, for the period 37-42 ka b2k, and apply for the first time the Goujon firn model to reconstruct the past temperature variations at NEEM. This quantitative temperature reconstruction for NEEM is compared to temperature reconstructions from NGRIP, GRIP and GISP2 using exactly the same method. This makes possible to reconstruct past spatial gradients of temperature and accumulation rate in Greenland. This reconstruction will be compared to published model simulations as well as the measured water isotope spatial gradients. In Sect. 4.4 of the next chapter, NGRIP δ^{15}N data and the Schwander firn model

will be used to reconstruct temperature and accumulation rate at NGRIP from the Holocene to the Eemian. The sensitivity of the NGRIP water isotopes to this δ^{15}N-based NGRIP temperature will be studied in detail.

3.2   Estimation of past temperature changes: δ^{15}N from air bubbles trapped in ice

3.2.1   Firn or the transformation of snow to ice
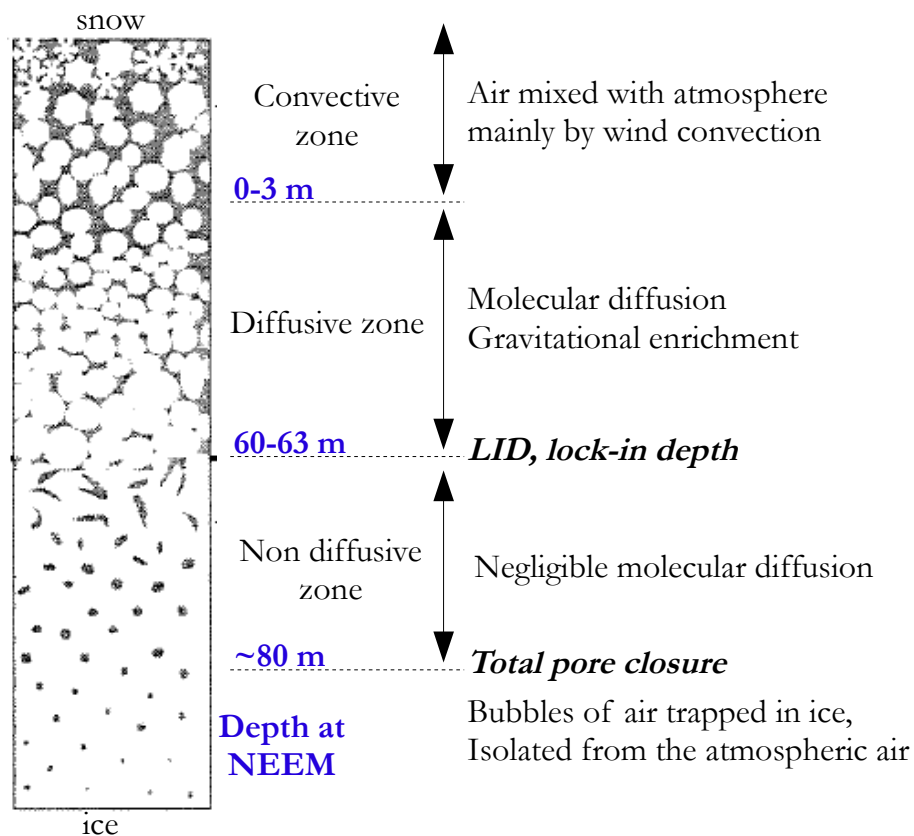
Figure 3.1: Schematic of the firn or snow/ice transition, adapted from Blunier and Schwander (2000). In blue: depths estimations for the present-day NEEM site (Buizert et al., 2012; Guillevic et al., 2013).

At the surface of the Greenland ice sheet, a given snow layer is progressively buried under new snow layers and finally compacted to ice. The different physical processes are described in Sect. 3.4.2 p. 59. At the surface, the initial snow density is $\sim$0.35 g.cm^{-3} while pure ice density is $\sim$0.92 g.cm^{-3}, depending on the ice temperature.

Firn is a porous medium where the snow density has not reached yet the ice density, and where gases are not completely trapped into bubbles. The snow compaction progressively closes the pores, and air gets trapped in-between the snow grains. The ability of air to diffuse in-between the open pores thus decreases with depth (e.g., Schwander et al., 1988; Buizert et al., 2012; Witrant et al., 2012). From a certain depth in the firn, the open porosity is so low than the diffusion of air is negligible. Once all the pores are closed, the entrapped air can only move with the progressive burial of the firn matrix. Based on gas diffusion, the firn can be described by three different zones (e.g., Sowers et al., 1992; Blunier and Schwander,

2000). The three zones can also be well identified for example in the δ^{15}N profile measured in the firn at NEEM (Fig. 3.2 p. 55):

- the **convective zone**: at the very top of the firn, the air in the snow is well mixed with atmospheric air. No gravitational enrichment of δ^{15}N occurs, δ^{15}N in the firn equals the atmospheric δ^{15}N;

- in the **diffusive zone** above the lock-in-depth (LID), the balance of gravity and molecular diffusion increasingly enriches δ^{15}N with depth, a process called gravitational fractionation (Schwander et al., 1988; Craig et al., 1988). The thickness of this zone is called diffusive column height (DCH). A thermal fractionation is also possible if there is a temperature gradient. In Fig. 3.2 p. 55, a seasonal thermal gradient affects δ^{15}N in the top 30 to 40 m (warmer surface in summer, colder in winter, compared to the average firn temperature);

- at the LID, molecular diffusion becomes negligible because of firn compaction. Gravitational enrichment of δ^{15}N stops. The δ^{15}N signal at the LID is then preserved in the pores;

- in the **non-diffusive zone**, the process of air trapping into closed pores continues until a certain density is reached, where all pores are closed. At NEEM, this depth is estimated to be around 80 m, where it was not possible anymore to pump air from the firn (Buizert et al., 2012).

Atmospheric air can diffuse in the firn and the air of the gas at the LID is a mixture of air of different ages, younger than the surrounding ice (e.g., Schwander and Stauffer, 1984). This mean age difference is called Δage:

$$\Delta\text{age} = \text{ice age} - \text{gas age} \qquad (3.1)$$

Below the LID, air moves only with the firn motion, and therefore the Δage remains constant. Because the thermal signal contained by δ^{15}N is the gas counterpart to the thermal signal registered in the water isotopes, δ^{15}N variations can be used to create a common age scale between the ice and the entrapped gases. However, the δ^{15}N information alone is not enough; firn models are necessary to reconstruct how deep was the LID and what was the age of the ice at the LID. So far, studies of present-day firns (mainly from Greenland and Antarctica) have shown that the measured density profiles (and therefore LID and Δage) mainly depend on the accumulation rate and temperature (e.g., Herron and Langway, 1980; Barnola et al., 1991; Schwander et al., 1997; Arnaud et al., 2000). It has been recently questioned if dust content or soluble impurities content in the snow may also affect the densification processes (Hörhold et al., 2012; Freitag et al., 2013). However Capron et al. (2013) noticed the absence of obvious link between δ^{15}N data and dust content at the same depth for different Antarctic sites. To include a parametrisation of this potential dust effect in firn models would be needed to test whether it significantly modifies density profiles over time or not.

δ^{15}N data measured in ice core are mainly the result of gravitational and thermal diffusion in the firn. However, gas diffusion and gradual bubble enclosure in the firn may smooth the δ^{15}N signal. This has been discussed more in details in Kindler et al. (2014), see Sect. 3.2 p. 125 of this thesis.
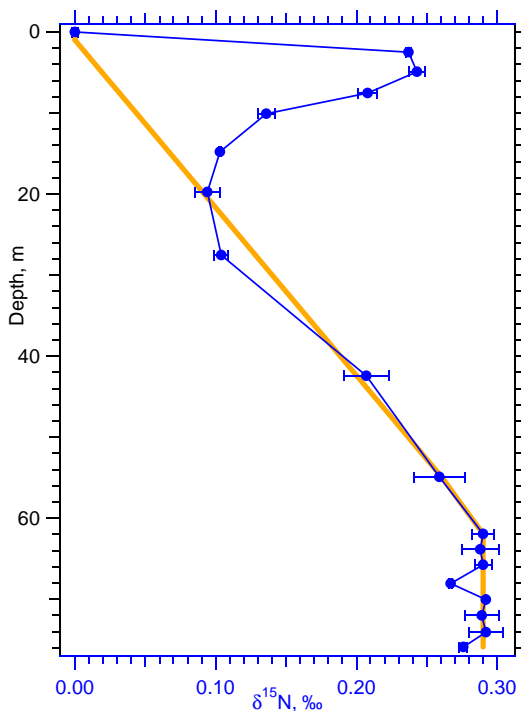
Figure 3.2: Present-day δ^{15}N profile in the firn at NEEM. Blue dots: isotopic composition of nitrogen in the firn at NEEM, measured at LSCE, (Guillevic et al., 2013). The error bars represent a 2 σ uncertainty. Orange line: modelled gravitational enrichment of δ^{15}N assuming a convective zone of 1 m and the LID at 61 m (diffusive column height of 60 m). From the surface down to ~40 m, the deviation of δ^{15}N from the gravitational signal is due to thermal diffusion caused by the seasonal temperature anomalies in the firn.

3.2.2 LID estimation based on δ^{15}N data

At a given firn site, the LID can be estimated based on δ^{15}N data (or other gases, e.g., Schwander et al., 1993; Buizert et al., 2012). We give the example of the NEEM firn, where δ^{15}N data were measured in firn air samples from different depths (Fig. 3.2 and Guillevic et al., 2013). In this firn profile, it appears clearly that the δ^{15}N data start to have a constant value from 62 m. This depth can therefore be considered as a maximum LID. Then, the six δ^{15}N data points on the vertical yellow line (Fig. 3.2) have a mean value of 0.290±0.003‰. This corresponds to a diffusive column height of 60±0.7 m, to which the convective zone thickness should be added to obtain the LID. Assuming no convective zone, the minimal LID for this firn site at NEEM would be 60±0.7 m while the maximum LID would be 62 m. Buizert et al. (2012) studied two nearby firn sites at NEEM, based on δ^{15}N data and other gases, and concluded that a 3 m convective zone was present, with a LID at 63 m depth. In this chapter, we consider that the LID at NEEM is located between 60 and 63 m depth.

3.3 δ^{15}N from the entrapped air: experimental techniques

3.3.1 Extraction of air from the ice: melt-refreeze technique

To measure the isotopic composition of nitrogen and oxygen gases by isotope-ratio mass spectrometry, the extraction of these gases without the water phase is necessary. To do so, we use at LSCE a manual melt-refreeze technique, described in great details by Landais et al. (2003a) and Capron (2010). We summarise here the important steps of the process and refer the reader to these references for more details.

First, the ice sample to be measured is cleaned by removing ~3-4 mm of ice on each side, maximum 24 hours before the gas extraction. Then, the ice sample is placed in a glass cylinder immersed in an ethanol bath at -20°C. The cylinder is then connected to an extraction

line: the exit of the cylinder is equipped with a glass-metal transition, and the top metal part of the cylinder can then be screwed to the extraction line. A gold-coated ring insures that the connexion is leak-tight. The air in the cylinder is pumped away during 40 min with a turbo-molecular pump (vacuum pressure generally around 0.3 bar). The cylinder is then isolated and the ethanol bath removed to allow a complete melting of the ice. The entrapped gas is now in the volume of the cylinder, and the water at the bottom. The bottom of the cylinder is hold in contact with a copper plate itself immersed in liquid nitrogen, to slowly refreeze the water from the bottom. This procedure avoids as much as possible the trapping of air bubbles in the refrozen ice. The sides of the cylinder as well as the connexion to the line are moderately heated with a hair-drier, so that the water vapour is (as much as possible) frozen only at the bottom of the cylinder. This also insures that any residual water in the upper part of the cylinder is transferred to the ice below. Then, a connection is established between the cylinder and a stainless-steel tube immersed in liquid helium. The cylinder is opened and the air (without water vapour) is cryo-trapped in the tube. After near complete trapping of the gas (97% after 8 min, without causing isotopic fractionation Landais et al., 2003b), the tube can be closed by a valve, removed from the liquid helium tank and connected to the mass spectrometer.

3.3.2 Gas isotopes measured by mass spectrometry

The tube entrapping the air to be analysed is connected to the sample side of our dual inlet mass spectrometer (Delta V plus, Thermo Scientific). Our internal reference gas (dried atmospheric air sampled at LSCE) is connected to the reference side (Fig. 1.8 p. 17). The mass spectrometer is equipped with 10 Faraday cups and measures simultaneously 10 different mass/charge ratios: 28, 29, 30, 32, 33, 34, 36, 38, 40, 44. This configuration makes possible to measure simultaneously the isotopic composition of nitrogen (N_2, masses 28, 29, 30), oxygen (O_2, masses 32, 33, 34) and argon (Ar, masses 36, 38, 40). The elemental ratios O_2/N_2, O_2/Ar, Ar/N_2 and CO_2/N_2 are also measured.

The sample and reference gases are introduced in their respective bellows. The measurement sequence is automated and comprises 16 times a measurement of the reference gas followed by a measurement of the sample gas and finishing by a reference gas measurement. This measurement procedure is registered as a "method" by the software used to monitor the mass spectrometer (ISODAT 3.0). Each sample measurement is thus bracketed by a reference measurement, that are both used to calculate the sample isotopic composition. This method is repeated twice and constitutes a "measurement sequence" applied to each gas sample. A pressure adjustment between the sample and gas bellow pressures is done before each sequence.

3.3.3 Data corrections

Corrections to the obtained measurements of nitrogen and oxygen isotopes can be applied to improve the reproducibility (0.02‰ for the raw data, 0.006‰ for the corrected data). These corrections have been first described by Sowers et al. (1989) and later improved by Severinghaus and Brook (1999); Caillon (2001); Severinghaus et al. (2003); Landais et al. (2003a): pressure imbalance correction (when the sample and reference gas bellows do not have the same pressure), CO_2 mass interference correction (the CO_2-derived CO^+ fragment

interfering with nitrogen isotopes), chemical slope correction (δ^{15}N varies with the O$_2$/N2 ratio). We refer to Landais et al. (2003a) for the details.

3.3.4 Referencing versus atmospheric air

The results corrected for pressure imbalance and mass interferences are then calculated versus the international standard gas for δ^{15}N. Until now, this standard is atmospheric air, which is assumed to be globally well mixed and constant over time (Mariotti, 1983; Hattori, 1983). To achieve this international referencing of our results, we evacuate a glass aliquot, close it and open it in the park of LSCE, to fill it with atmospheric air. This aliquot is connected to the very same gas extraction line as the cylinder. A water trap immersed in ethanol at -90°C is placed between the aliquot and the stainless-steel cryo-trap in liquid helium. The air from the aliquot is then transferred to the cryo-trap during 10 min. It is then measured by dual inlet mass spectrometry, versus the same internal standard as for the ice samples. This way, the internal standard can be calibrated versus atmospheric air. We perform atmospheric air calibration of our internal standard at least 3 times before and after a measurement campaign, lasting usually one to two months. Our δ^{15}N data expressed versus atmospheric air can now be compared to δ^{15}N measurements performed at different laboratories around the world.

3.4   Firn models inter-comparison: application to past NGRIP climate reconstruction

This section is planned to be submitted as an article from M. Guillevic, Ph. Kindler et al. All model runs from the Goujon model have been performed by myself and all model runs performed with the Schwander model by Ph. Kindler. We compared the results together and I did most of the writing.

3.4.1   Introduction

Ice cores are unique archives giving direct access to the past atmosphere. Once the air is extracted from the ice, its composition can be analysed to reconstruct the past concentration in greenhouse gases. Because of the porous nature of the firn of an ice sheet, the air is trapped at a certain depth in the firn, in ice that is older than the air (Schwander and Stauffer, 1984). This age difference between ice and air is called Δage. A gas age scale specific to each ice core site is necessary to compare time leads and lags between local temperature evolution and greenhouse gases concentration.

To reconstruct such a gas age scale, the isotopic composition of nitrogen (δ^{15}N) in the air can be used. Indeed, δ^{15}N is constant around the globe at orbital time scales (Mariotti, 1983; Hattori, 1983) and therefore the δ^{15}N signal registered in the ice bubbles is due to firn processes only. First, the balance of diffusion and gravitational enrichment makes δ^{15}N to increase in the firn with depth, until a certain depth or lock-in depth (LID), where the porosity of the firn is low enough so that diffusion is negligible. Below the LID, the air moves only by advection of the firn matrix downwards. Second, because the diffusion of nitrogen is about 10 times faster than the diffusion of heat in the ice, any temperature gradient in the firn creates a thermal signal in δ^{15}N, the heavy isotopes migrating towards the cold part of the firn. At the onset of a Dansgaard-Oeschger event for example, the heavy isotopes accumulate at the bottom of the firn which is colder than the surface. The gravitational and thermal fractionation effects lead to the observed δ^{15}N in the ice bubbles. Firn models are classically used to reconstruct the firn thickness history together with its temperature profile, in order to reconstruct the past δ^{15}N and Δage. The input temperature and accumulation scenarios for the firn models are tuned such that the modelled δ^{15}N history matches measured data, in terms of mean level as well as position of the δ^{15}N peaks with depth. Therefore, running a firn model for a given ice sheet site not only produces a LID and a gas age scale, but also a reconstruction of most likely past temperature and accumulation rate histories.

δ^{15}N from the NGRIP ice core in Greenland well records the 25 Dansgaard-Oeschger events occurring during the last glacial period (Huber et al., 2006; Capron et al., 2010a; Kindler et al., 2014), because the temperature variations at play are abrupt and large enough (up to +16°C in a few decades, e.g. Huber et al., 2006), and do not get smoothed out by heat diffusion in the firn. In Antarctica, the past temperature variations are quite gradual (EPICA community members, 2006) and so far firn models do not reproduce the measured δ^{15}N variations during the last glacial period or the deglaciation at semi-coastal or inland sites in Antarctica (Landais et al., 2006; Capron et al., 2013). It is not certain whether present-day Antarctic firns are valid analogues for the glacial Antarctic firns. The δ^{15}N thermometer can therefore be applied to Greenland ice cores with confidence, but the current

understanding of firn processes may not be valid for the past glacial period in Antarctica.

For the last glacial period in Greenland, large discrepancies between firn model based and ice flow model based accumulation rate histories have been recently reported (Huber et al., 2006; Guillevic et al., 2013; Kindler et al., 2014; Rasmussen et al., 2013). The reconstruction of past accumulation rate and temperature is critical for estimating the sensitivity of the Greenland ice sheet to climate change, and this discrepancy needs to be investigated. In particular, accumulation reconstructions made with a Dansgaard-Johnsen type ice flow model (Dansgaard and Johnsen, 1969) for the GRIP, NGRIP and NEEM sites do not have uncertainties estimations (Rasmussen et al., 2013). Firn model based reconstructions of accumulation rate also lack an estimation of their uncertainties (Guillevic et al., 2013; Kindler et al., 2014). Therefore, up to now it is not possible to conclude if the differences in firn model and ice flow model based accumulation reconstructions are due to large errors or significant discrepancies in between these two methods.

Hereafter, we aim to quantify the uncertainties of the firn model method when reconstructing the LID, Δage, temperature and accumulation rate. We do this study on the NGRIP ice core in Greenland, for which a complete δ^{15}N dataset from the Holocene to the Eemian is now available (Kindler et al., 2014, and references therein). We test the effect of using different densification equations, a different modelisation of the heat diffusion, and different timescales, on the reconstructed LID, Δage, temperature and accumulation rate. A diversity of firn models have been reported in the literature, either empirical or based on physical processes (e.g., Herron and Langway, 1980; Barnola et al., 1991; Schwander et al., 1997; Arnaud et al., 2000; Spencer et al., 2001; Goujon et al., 2003). We focus on the models from Goujon et al. (2003), Schwander et al. (1997) and Herron and Langway (1980), hereafter named Goujon model, Schwander model and HL model, because they use quite different methods to model the densification and heat diffusion processes. The HL model uses empirical equations to model the densification, while the densification equations used in the Goujon and Schwander models are partly physically based. The Schwander model calculates the heat diffusion from the surface down to 1300 m depth, while the Goujon model is equipped with heat diffusion from surface to bedrock. Based on these tests, we calculate the uncertainties associated with the reconstructed climate parameters. We can then conclude whether the Goujon and Schwander firn models agree with the Dansgaard-Johnsen ice flow model when reconstructing past accumulation rate histories at NGRIP.

3.4.2   Firn models

The Goujon firnification model

The Goujon model (Goujon et al., 2003) is a dynamical version of the 1-D densification model by Arnaud et al. (2000). It has been tuned using two firn density profiles from Antarctica: Vostok and Byrd. It uses a time step of one year for both densification and heat diffusion calculation. The spatial resolution in the top 150 m is 0.25 m; it increases with depth to 25 m at bedrock. The main improvement compared to the Arnaud model is the calculation of heat diffusion in the ice, across the entire ice sheet from surface to bedrock, using a simplified version of the heat diffusion model in the ice from Ritz (1989). These simplifications are done according to Paterson (1994), where horizontal heat diffusion and

internal heat production are neglected:

$$\rho c \frac{\partial T}{\partial t} = k \frac{\partial^2 T}{\partial z^2} + \frac{\partial k}{\partial z} \frac{\partial T}{\partial z} \tag{3.2}$$

Here k denotes the thermal conductivity and c the specific heat capacity. We use a constant NGRIP bedrock temperature of -2.4°C (Dahl-Jensen et al., 2003). The vertical ice flow is calculated using the analytical solution from Lliboutry (1979) for the horizontal ice flow and assuming incompressibility of the ice. The Goujon model is therefore able to model a rough estimate of the present-day borehole temperature profile. This output can be compared to present-day measurements of borehole temperature and constitutes an additional constraint to the model. This has been already done for the GISP2 and Vostok sites (Goujon et al., 2003).

The densification rate equations (per year) are the same as in Arnaud et al. (2000). In the first stage of densification, snow is compacted by grain boundary sliding (Alley, 1987). In the second stage, firn is compacted by elastic and plastic deformation of grains, following a power-low creep mechanism (Arzt, 1982; Arzt et al., 1983). The third stage is the densification of bubbly ice (Arnaud et al., 2000): cylindrical and spherical pores are deformed and progressively compacted, until the ice density is reached. No further densification occurs.

The depth of the transition between first and second stage of densification is parametrised by a density threshold. By comparison of the Byrd and Vostok density profiles, Arnaud et al. (2000) proposed an empirical function making this threshold (D_0, relative density = firn density/ice density) to be a function of temperature (T, in K):

$$D_0 = 0.00226\, T + 0.03 \tag{3.3}$$

The lock-in depth (LID), below which the air is no longer exchanging with overlaying layers, is defined as the depth where the ratio of closed (P_{closed}) to total (P_{total}) porosity reaches 0.13. This ratio at a given depth is itself a function of the density (Goujon et al., 2003):

$$\frac{P_{closed}}{P_{total}} = 0.37 \cdot \left(\frac{1-D}{1-Dc} \right)^{-7.6} \tag{3.4}$$

with D the relative density at a given depth and Dc the relative density at the close-off depth or COD, the depth where on average the air gets trapped into the bubbles. The COD density is itself defined by (Martinerie et al., 1994, ρ in $kg\,m^{-3}$ and T in K):

$$\frac{1}{\rho_{COD}} = \frac{1}{\rho_{ice}} + 6.95 \cdot 10^{-7} \cdot T - 4.3 \cdot 10^{-5} \tag{3.5}$$

The ice density ρ_{LID} is an empirical function of temperature, calculated by a fit through the data from Bader (1964), with t the ice temperature in Celsius:

$$\rho_{ice} = 0.9165 - 1.4438 10^{-4} t - 1.5175 10^{-7} t^2 \tag{3.6}$$

This LID definition based on the porosity of the ice is in agreement with the LID density threshold proposed by Schwander et al. (1997), Equ. 3.7. The Goujon model also includes a convective zone that can be adapted to the site, with a constant value over time. This convective zone affects the diffusive column height and therefore $\delta^{15}N_{grav}$ but not the heat diffusion in the ice, that still occurs. This model is validated for present-day conditions

in Greenland and Antarctica (Landais et al., 2006; Arnaud et al., 2000). It therefore covers interglacial and glacial conditions for Greenland. To our knowledge, density profiles modelled by the Goujon model have been compared to measured profiles for Byrd and Vostok only (Arnaud et al., 2000). We extend here this study to other present-day firn sites.

The Schwander firnification model

The Schwander firn densification and heat diffusion model (Schwander et al., 1997) consists out of three parts: densification of the firn, heat diffusion and gas diffusion in the firn. The densification of the first part of the firn ($345 \, \text{kg} \, \text{m}^{-3} < \rho < 550 \, \text{kg} \, \text{m}^{-3}$) is calculated with the Herron-Langway model (Herron and Langway, 1980). The second part ($550 \, \text{kg} \, \text{m}^{-3} < \rho < 800 \, \text{kg} \, \text{m}^{-3}$) is calculated according to Barnola et al. (1991) and the third part ($\rho > 800$ $\text{kg} \, \text{m}^{-3}$) after Wilkinson and Ashby (1975). The density where the bubbles are closed is defined after the empirical formula from Martinerie et al. (1994) for the COD (Equ. 3.5), with a slight correction of -14 $\text{kg} \, \text{m}^{-3}$ to subtract the non-diffusive zone (ρ in $\text{kg} \, \text{m}^{-3}$ and T in K):

$$\frac{1}{\rho_{\text{LID}}} = \frac{1}{\rho_{\text{ice}}} + 6.95 \cdot 10^{-7} \cdot \text{T} - 4.3 \cdot 10^{-5} - \frac{1}{14} \tag{3.7}$$

Heat diffusion in the ice is calculated using the same simplification as in the Goujon model (equ. 3.2), with an annual layer resolution to a depth of 300 m, from there with a 100 m resolution down to 1300 m, where the heat flux is defined to be zero.

The diffusion of the air in the firn is calculated with a one dimensional box model (Schwander et al., 1993). The age of the gas at the LID has typical values of 10 to 20 yr.

The Herron-Langway model

In 1980, M.M. Herron and C.C. Langway proposed an empirical firn densification model, where the densification rate depends on the surface temperature and accumulation rate. Densification of snow occurs until a density of 550 $\text{kg} \, \text{m}^{-3}$ is reached. Densification of firn occurs down to a density of 820 to 84 $\text{kg} \, \text{m}^{-3}$. This model does not cover the densification of bubbly ice. The two sets of equations defining the first and second stages of densification have been tuned using measured density profiles from 17 sites in Greenland and Antarctica, covering temperatures from -57 to -15°C and accumulation rates from 0.022 to 0.5 m.w.e.a^{-1}. Because the HL model is tuned over so many different sites, it performs in general very well to reconstruct density profiles and is still widely used in the ice core community. Hereafter, we use the HL densification model together with the same LID definition as in the Schwander model.

Modeling δ^{15}N with firn models

The Goujon and Schwander models use the following equations to model δ^{15}N. In the firn, δ^{15}N is the sum of two effects:

- gravitational effect (Craig et al., 1988; Schwander, 1989): the heavy isotopes preferentially migrate towards the bottom of the firn according to the barometric equation:

$$\delta^{15}\text{N}_{\text{grav}} = \exp\left(\frac{\Delta \text{mgz}}{\text{RT}_{\text{mean}}}\right) - 1 \cong \frac{\Delta \text{mgz}}{\text{RT}_{\text{mean}}} \tag{3.8}$$

with Δm being the mass difference between the light and heavy isotope, g the acceleration constant, z the firn depth, R the ideal gas constant, and T_{mean} the mean firn temperature. An increase in accumulation rate increases the firn column depth and therefore increases δ^{15}N$_{\mathrm{grav}}$; on the other hand, a high temperature accelerates the densification processes and leads to shallower LID.

- thermal effect (Severinghaus et al., 1998; Leuenberger et al., 1999): a temperature increase after a cold period will create a transient peak in δ^{15}N$_{\mathrm{therm}}$ at the cold bottom part of the firn, that gets enriched in heavy isotopes according to (Chapman and Cowling, 1970):

$$\delta^{15}\mathrm{N}_{\mathrm{therm}} = \left(\frac{\mathrm{T_t}}{\mathrm{T_b}}\right)^{\alpha_{\mathrm{T}}} - 1 \tag{3.9}$$

with T_t and T_b (in K) being the temperatures of the top and bottom parcel, respectively, and α_T the thermal diffusion constant (Leuenberger et al., 1999):

$$\alpha_{\mathrm{T}} = 4.61198 \cdot 10^{-3} \cdot \ln\frac{\mathrm{T_f}}{113.65} \tag{3.10}$$

with T_f the mean firn temperature (in K) calculated from the cold (T_c) and hot (T_h) parcels temperature (also in K):

$$\mathrm{T_f} = \frac{\mathrm{T_c} \cdot \mathrm{T_h}}{\mathrm{T_h} - \mathrm{T_c}} \cdot \ln\left(\frac{\mathrm{T_h}}{\mathrm{T_c}}\right) \tag{3.11}$$

This can be simplified into (Severinghaus and Brook, 1999):

$$\delta^{15}\mathrm{N}_{\mathrm{therm}} \cong \Omega_{\delta^{15}\mathrm{N}} \cdot \Delta\mathrm{T} \tag{3.12}$$

with ΔT the temperature difference between top and bottom of the firn. The thermal diffusion sensitivity $\Omega_{\delta^{15}N}$ (‰· K^{-1}) has been estimated by laboratory experiments between -60 to 0°C (Grachev and Severinghaus, 2003b):

$$\Omega_{\delta^{15}\mathrm{N}} = \frac{8.656}{\mathrm{T_f}} - \frac{1232}{\mathrm{T_f^2}} \ (\pm 3\%) \tag{3.13}$$

To model the δ^{15}N$_{\mathrm{therm}}$, the Schwander model uses Equ. 3.9 while the Goujon model uses Equ. 3.12. Using these two different formulas to calculate δ^{15}N$_{\mathrm{therm}}$ does not lead to different results (Sect. 3.4.5).

Taking together the gravitational and thermal effects, the measured δ^{15}N is the sum:

$$\delta^{15}\mathrm{N} \ = \ \delta^{15}\mathrm{N}_{\mathrm{grav}} \ + \ \delta^{15}\mathrm{N}_{\mathrm{therm}} \tag{3.14}$$

3.4.3 Validation of the models for present-day

To check whether the firn models used here are robustly applicable over the climatic conditions covered by Greenland ice cores (from present day back to 120 ka ago), the models should perform well for present conditions in Greenland (similar to Greenland Interstadials (GI) conditions) and central Antarctica (similar to Greenland Stadials (GS) conditions). We run the firn models in a stable mode, assuming isothermal firns. For the Goujon model, in

order to get an isothermal firn, we set the bedrock temperature equal to the mean surface temperature. Note that in sites with very low accumulation rates like Dome C and South Pole, the firns may actually not be isothermal but influenced by the warmer bedrock temperature, as it has been measured for the Vostok firn site (Salamatin et al., 1994; Barkov and Uvarov, 1973; Goujon et al., 2003). We run the models with constant temperature and accumulation rates (Table 3.1 p. 64), for five different sites: NEEM, GRIP, NGRIP (Greenland), EPICA Dome C and South Pole (Antarctica). We focus on two parameters critical to model a correct $\delta^{15}N$: the density profile because modelled LID are a function of the density, and the depth of the LID, where gravitational enrichment of gases stops.
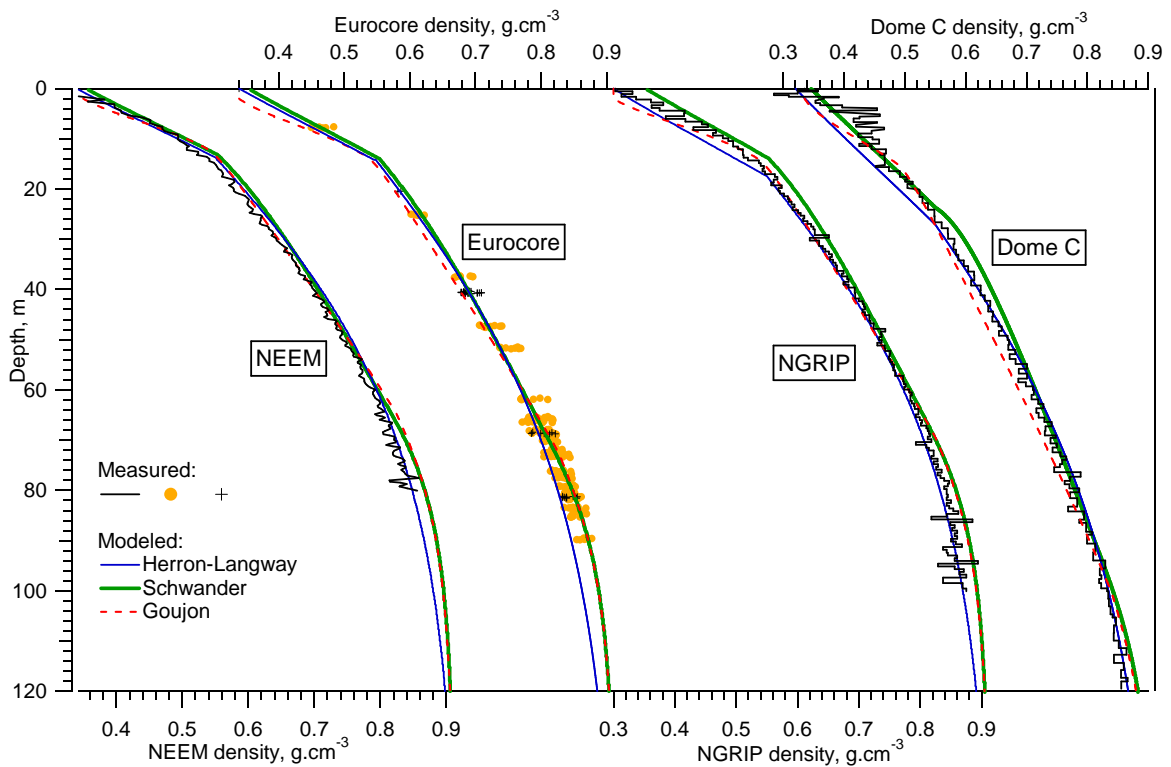
Figure 3.3: Measured and modelled firn density profiles for NEEM, GRIP (Eurocore), NGRIP and Dome C. Black line, black crosses, orange dots: measured. NEEM: NEEM07S3 core, Steen-Larsen et al. (2011). GRIP: Eurocore drilling project 1989, Schwander et al. (1993); black crosses: measured at the University of Bern (KUP); orange circles: measured at Laboratoire de Glaciologie et de Géophysique de l'Environnement, Grenoble (LGGE). NGRIP: S4 core, NGRIP members. Dome C: Landais et al. (2006). Blue line: Herron-Langway model (Herron and Langway, 1980). Green line: Schwander model (Schwander et al., 1997), all runs have been made using a constant surface density of 0.35 g.cm^{-3}. Red dotted line: Goujon model (Goujon et al., 2003).

The modelled density profiles are shown in Fig. 3.3. On average, the HL model performs best, which is not surprising since this model has been tuned using the largest number of measured firn density profiles. However, in the lowest part of the firn, the HL model underestimates the density at GRIP, while both the Goujon and Schwander model overestimate the density at all sites except for GRIP.

The modelled LID are reported in Table 3.1. Following Landais et al. (2006), we expect a difference up to ~3% between modelled and measured LID, due to the uncertainty in the estimation of surface temperature and accumulation rate at the site. Note that when

Table 3.1: Characteristics of present-day firns: GRIP, NGRIP, NEEM, Dome C and South Pole. modelled LID and densities at LID by different firn models, assuming an isothermal firn. The LID difference in % is calculated as: $100(\text{LID}_{modelled} - \text{LID}_{measured})/\text{LID}_{measured}$. References: (a) Steen-Larsen et al. (2011). (b) Buizert et al. (2012). (c) Guillevic et al. (2013). (d) Schwander et al. (1993). (e) Landais et al. (2006). (f) Battle et al. (1996). (g) Gow (1965).

	NEEM	GRIP	NGRIP	Dome C	South Pole
	(a),(b),(c)	*(d)*	*(e)*	*(e)*	*(f) (g)*
Measured present-day characteristics					
Surface temperature, °C	-29.0	-31.7	-31.7	-54.5	-49.4
Accumulation rate, m.i.e.a^{-1}	0.216	0.23	0.19	0.027	0.076
Surface density, g.cm^{-3}	0.34	0.34	0.30	0.32	0.35
Density at LID, g.cm^{-3}	0.792 to 0.800	0.815	0.81	0.824	
LID, m	60 to 63	71	67	98	115
modelled with the Goujon model					
Density at LID, g.cm^{-3}	0.810	0.811	0.812	0.827	0.824
LID, m	61.8	69.1	66.7	97.1	101.8
LID difference, %	-1.9 to +3.0	-2.7	-0.4	-0.9	-11.5
modelled with the Schwander model					
Density at LID, g.cm^{-3}	0.810	0.812	0.812	0.826	0.823
LID, m	63.6	70.4	66.8	94.6	105.6
LID difference, %	+1.0 to +6.0	-0.8	-0.3	-3.5	-8.2
modelled with the Herron-Langway model					
Density at LID, g.cm^{-3}	0.810	0.812	0.812	0.826	0.822
LID, m	64.8	74.3	71.8	93.9	105.0
LID difference, %	+2.9 to +8.0	+4.6	+7.2	-4.2	-8.7

focusing on reconstructing the past δ^{15}N, it is critical that the models perform well at the LID. Anomalies at the surface (because of varying surface densities) or below the LID will not have any impact on the modelled LID, and therefore on the δ^{15}N. For the Greenland sites (high temperature and accumulation rates), the Goujon model reproduces the data derived LID with a difference of $\pm 3\%$, the Schwander model with -1% to +6%, and the HL model with +3% to +8%. For the Antarctic sites, the difference is -12% to -1% with the Goujon model, -8% to -3.5% for the Schwander model, and -9% to -4% for the HL model. For the Goujon and Schwander models, we note that for all sites except South Pole, the LID difference between modelled and measured values falls within the $\sim 3\%$ difference due to possible uncertainties in surface temperature and accumulation rate estimates, as calculated by Landais et al. (2006). However, this difference increases to respectively 12.5% and 8% for the Goujon and Schwander models for the South Pole site. It is quite surprising that the Goujon and Schwander firn models do not perform well at South Pole, while they correctly reproduce the LID at other sites with warmer and colder temperature, as well as higher and lower accumulation rates. We note that for South Pole, we use a surface temperature value and an LID estimation from Battle et al. (1996), while the accumulation rate was determined from pit studies by Gow (1965). It is possible that the accumulation rate at South Pole varied in between these two studies. Alternatively, it may be possible that firn models do not capture the effect of the particular South Pole conditions (anomalously high accumulation rate combined to low temperature). We consider hereafter that the Goujon and Schwander

firn models reproduce the LID with an accuracy of 3% in average.

3.4.4 Past climatic reconstruction at NGRIP

Match point	Depth, m, for: δ^{18}O	δ^{15}N	Δdepth, m	Δage, a ss09sea06bm	GICC05/AICC2012	$\sigma_{\Delta age}$, a
Holocene	1490.23	1515.3	25.07	817	845	52
YD	1520.48	1542.32	21.84	654	620	43
Bølling	1602.98	1629.4	26.42	990	1087	68
DO2	1792.73	1817.8	25.07	1578	1538	112
DO3	1868.08	1890.7	22.62	1163	1117	91
DO4	1888.43	1910.3	21.87	1380	1397	114
DO5	1950.58	1971.9	21.32	1259	1180	98
DO6	1972.58	1993.0	20.42	1159	1180	112
DO7	2007.78	2027.0	19.22	1273	1178	105
DO8	2068.83	2086.6	17.77	1195	1139	93
DO9	2099.08	2116.2	17.12	1097	1014	71
DO10	2123.78	2139.4	15.62	1093	1044	89
DO11	2156.83	2172.7	15.87	1225	1135	78
DO12	2221.18	2233.8	12.62	945	921	74
DO13	2256.38	2268.6	12.22	819	786	66
DO14	2344.93	2355.8	10.87	848	844	77
DO15	2364.73	2376.8	12.07	944	969	79
DO16	2401.58	2413.1	11.52	755	753	67
DO17	2419.73	2430.8	11.07	944	974	152
DO18	2465.38	2474.0	8.62	1111	1098	193
DO19	2534.13	2542.2	8.07	1081	987	178
DO20	2578.13	2585.51	7.38	811	799	154
DO21	2685.93	2692.3	6.37	488	506	116
DO22	2745.88	2750.55	4.67	478	431	106
	2818.88	2823.87	4.99	481	420	105
DO23	2895.48	2900.2	4.72	483	464	110
DO24	2937.28	2944.3	7.02	932	809	155
DO25	3002.18	3007.4	5.22	536	579	125

Table 3.2: NGRIP ice core: correspondence between δ^{15}N and δ^{18}O peaks. δ^{18}O data are averaged over 55 cm (bag data) and we use here the depth at the middle of the 55 cm interval. The Δage is calculated according to two timescales: ss09sea06bm and GICC05/AICC2012. The Δdepth (Δage) is obtained by calculating the difference between ice and gas depth (age).

Classically, firn models are used to produce a modelled δ^{15}N profile that is compared to the measured δ^{15}N data. A Δage history is as well produced, that is also compared to available Δage match-points. Modelled δ^{15}N and Δage are the result of the temperature and accumulation rate scenarios, controlling the position of the LID and the ice age at the LID. After choosing a given timescale, the input temperature and accumulation rate scenarios are tuned, so that the reconstructed δ^{15}N and Δage match best the measured data. This tuning procedure is done using an iterative approach, as depicted in Fig. 3.4. At the

end of this tuning procedure, a best estimate of the past history for the temperature, the accumulation rate, the LID, the δ^{15}N and the Δage are reconstructed.

While the modelled δ^{15}N and Δage can be directly compared to measurements from the ice core, this is not the case for the modelled LID, temperature and accumulation rate. We list here different aspects that modify firn model-based reconstructions that will be studied in detail. (i) Using a different timescale modifies the value of the Δage match points as well as the evolution with time of temperature and accumulation scenarios. We test the effect of using different timescales in Sect. 3.4.4, where we focus on DO-23, the period where the available ss09sea06bm and AICC2012 timescales differ the most. (ii) To investigate the effect of using different firn models, we perform the following preliminary test. We first use the temperature and accumulation scenarios reconstructed for the all NGRIP ice core by Kindler et al. (2014), using the ss09sea06bm timescale and the Schwander

Figure 3.4: The best estimates of temperature and accumulation rate scenarios are found using an iterative approach.

model. We then use exactly the same inputs (time scale, temperature, accumulation) but the Goujon model, and obtain "Goujon-based" reconstructions of the δ^{15}N, Δage, LID. Comparing these results, the difference in the modelled δ^{15}N, Δage and LID when using the Goujon or the Schwander model is negligible, except during DO-2 to the Bølling-Allerød. This period is studied in detail in Sect. 3.4.4. (iii) Finally, we test the effect of applying different strategies to tune the temperature and accumulation rate scenarios, in order to match the measured δ^{15}N. We do this test for DO-23, a period of gradual temperature decrease where Δage match points are scarce.

NGRIP ice core data

At present, the NGRIP ice core site is located on the ice divide, at 2917 m above sea level, where the ice sheet thickness is 3085 m (NGRIP members, 2004). The NGRIP δ^{15}N record is made of two distinct data sets: from 1391.1 to 2464 m, δ^{15}N data were measured at the University of Bern with a pooled standard deviation of 0.02 ‰ and a spatial resolution of 1.1 m (every two bags) corresponding to 55 a (Kindler et al., 2014). From 2464 to 3083.33 m, the measurements were performed every two bags (1.1 m) corresponding to every 110 a, at Laboratoire des Sciences du Climat et de l'Environnement, Gif sur Yvette, France, with a pooled standard deviation of 0.006 ‰(Landais et al., 2004a, 2005; Capron et al., 2010a,b, 2012; Kindler et al., 2014).

Comparing peaks of δ^{15}N from the entrapped air and water isotopes from the ice, we identify Δdepth tie points and calculate their corresponding Δage according to the ss09sea-06bm and GICC05/AICC2012 timescales (Table 3.2). When the GICC05 annual layer counting is available (Holocene to DO-16), we calculate the Δage uncertainty as the Maximum Counting Error (MCE, Rasmussen et al., 2006) difference between the ice and gas depths. For DO-17 to DO-25, we calculate $\sigma_{\Delta_{age}}$ as 13% of its value, since the durations of ss09sea06-bm and AICC2012 disagree by up to 13% in this part of the ice core. To account for the data

resolution, we add a time uncertainty of $\pm 25\,\text{a}$ down to 2464 m and $\pm 55\,\text{a}$ from there to the bottom of the core.

As a first guess for the input temperature (Fig. 3.4), we use the NGRIP water isotope record (NGRIP members, 2004). At present in Greenland, a linear relationship can be assumed between water isotopes ($\delta^{18}\text{O}$) and temperature (T):

$$\text{T} = \frac{1}{\alpha}(\delta^{18}\text{O} + \beta) \tag{3.15}$$

with α=0.69 and β=-13.6‰ according to Dansgaard (1964), using different Greenland sites with -30<T<0°C, or α=0.8 according to Sjolte et al. (2011). For the accumulation rate, we use as a first guess the ss09sea06bm accumulation rate. The input temperature is tuned by varying α and β and the accumulation rate is tuned as well, in order for the output $\delta^{15}\text{N}$ to match the measured data and the output Δage to match the defined Δage tie points, within uncertainties.

Timescale uncertainty

The ice timescale used when running the firn model may influence the reconstructed temperature and accumulation scenarios. Indeed, the ice timescale provides the number of years between a peak seen in the water isotopes in the ice and the corresponding peak seen in $\delta^{15}\text{N}$ in the gas phase, constraining Δage estimations. The timescale is therefore a strong constraint for firn models when reconstructing the ice age at LID. For the NGRIP ice core, we have calculated the Δage using two timescales: ss09sea06bm and GICC05/AICC2012 (Table 3.2 and Sect. 3.4.4).

From the depth-age relationship in the ice, one can calculate the annual layer thickness. Changing the timescale implies a modification of the annual layer thickness along the ice core (Fig. 3.6.c and 3.5.c). To reconstruct the past accumulation rate history, an ice flow model calculating the thinning along the ice core is needed. Dividing the annual layer thickness by the thinning produces a past accumulation rate history. An accumulation rate history therefore depends on the timescale and ice flow model used to estimate annual layer thickness and thinning. For the NGRIP ice core, a Dansgaard-Johnsen type model was used, producing the ss09sea06bm timescale and thinning.

In this section, we use the Goujon and Schwander firn models together with the ss09sea06bm and AICC2012 timescales (see below) for the NGRIP ice core. We compare how the modelled $\delta^{15}\text{N}$ are influenced by each timescale, for each firn model. We focus on the period of DO-23 where the ss09sea06bm and AICC2012 timescales disagree.

Timescales used   The ss09sea06bm time scale (NGRIP members, 2004) covers the entire NGRIP ice core and has been created using one-dimensional ice flow model developed by Dansgaard (1964), called Dansgaard–Johnsen (DJ) model. The ice flow parameters of the model are tuned to obtain the best match between modelled and observed depth-age horizons in the ice cores. In the Appendix from Andersen et al. (2006), it is explained that "*The bottom of the NGRIP 2003 core at 3085.0 m was given the age of 123 ka BP (before 1950) based on correlation with the Iberian margin MD95-2042 sediment core (Shackleton et al., 2000)*". The thinning function calculated from the DJ model is then used to correct the observed annual layer thickness in the core for the effect of ice flow induced thinning, thereby producing an accumulation rate history. No uncertainty estimate is provided with this timescale.
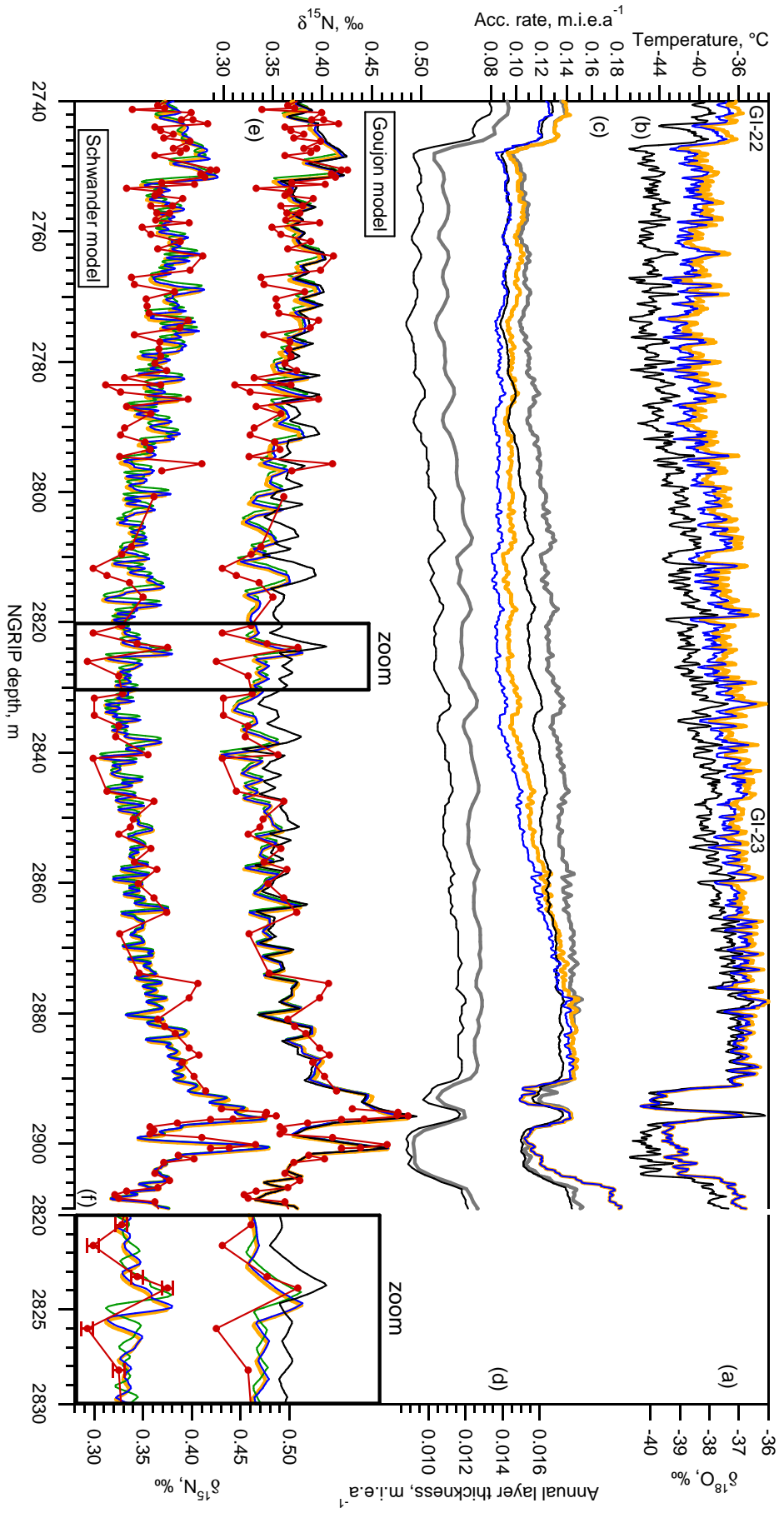
Figure 3.5: DO 23 in the NGRIP ice core: effect of using the AICC2012 vs ss09sea06bm timescales when running firn models. **(a)** Black: NGRIP δ18O, ‰ (NGRIP members, 2004). **(b)** Temperature scenarios. Yellow line: AICC2012 tuning, scenarios (i) and (ii). Blue line: ss09sea06bm tuning, scenario (iii). **(c)** Accumulation rates, m.i.e.a⁻¹. Calculated using the thinning function from the DJ model and annual layer thickness from the AICC2012 timescale (grey line) or from the ss09sea06bm timescale (black line). Yellow line: AICC2012 tuning, scenarios (i) and (ii). Blue line: ss09sea06bm tuning, scenario (iii). **(d)** Annual layer thickness, m.a⁻¹. Black: ss09sea06bm, NGRIP members (2004). Gray: AICC2012, (Veres et al., 2013; Bazin et al., 2013). Red dots: measured data (Landais et al., 2005), and all others modelled with the Goujon model. Yellow line: scenario (i). Green line: scenario (ii). Blue line: scenario (iii). Black line: modelled using the ss09sea06bm timescale, temperature from scenario (iii) (b, blue) and the original ss09sea06bm accumulation rate, black line in (c). **(f)** Colour code same as (e), modelled with the Schwander model. To the right, a zoom on 2820–2830 m is shown.

The GICC05 (Greenland Ice Core Chronology 2005) has been produced based on annual layer counting of several parameters measured continuously on the NGRIP, GRIP and Dye3 ice cores and featuring a clear annual cycle, back to 60 ka b2k (Vinther et al., 2006; Svensson et al., 2006; Rasmussen et al., 2006; Svensson et al., 2008). The GICC05 timescale covers the NGRIP ice core from the surface down to 2427 m. This timescale has the great advantage to provide an estimation of its dating uncertainty, with an estimator called Maximum Counting Error (MCE). The MCE is the sum from the surface to a given depth of all the annual layers considered as uncertain, and therefore counted as 0.5 a $\pm$0.5 a. All the certain layers are counted as 1 a $\pm$0 a. The MCE can be regarded as a 2 σ error estimate (Rasmussen et al., 2006).

The Antarctic Ice Core Chronology 2012 or AICC2012 timescale (Bazin et al., 2013; Veres et al., 2013) synchronises Antarctic (Vostok, EDC, EDML, TALDICE) and Greenland (NGRIP) ice cores on the same age scale. This synchronisations uses absolute age markers (volcanic eruptions dated and registered in ice cores, anomalies in the Earth magnetic field imprinted in the beryllium content in the ice) as well as age match points in between ice cores (e.g., based on methane concentration variations). From present back to 60 ka b2k, the AICC2012 time scale is tied to GICC05 and is therefore exactly equivalent. At the bottom of the NGRIP ice core, the dating is constrained by orbital tie-points, based on O_2/N_2 data from the Vostok ice core. The NGRIP ice age at 3084 m is estimated to be $\sim$120.0 $\pm$1.9 ka b2k, which is $\sim$3 ka younger than estimated by the ss09sea06bm timescale.

Table 3.3: Effect of different timescales and firn models: Last Glacial Maximum and DO-23 in the NGRIP ice core. The average δ^{15}N levels have been calculated using values from Kindler et al. (2014) and Landais et al. (2005). Results are shown for the Goujon (G.) and Schwander (Sch.) models and correspond to the average over the gas depth interval. Firn ΔT is $T_{surface}$ - T_{LID}.

	LGM	**DO-23**			
Ice depth, m	1604.2–1793.7	2746.6–2891.6			
Gas depth, m	1634.7–1802.7	2753.8–2891.9			
Average δ^{15}N, ‰	0.4136	0.355			
Timescale	ss09sea06bm	ss09sea06bm		AICC2012	
Duration, a	8110	14000		12335	
Firn model	G.	Sch.	G.	Sch.	G.	Sch.
Average δ^{15}N, ‰	0.395	0.407	0.354	0.354	0.354	0.353
LID ice age, a	1029	1076	456	474	456	472
LID, m	78.04	78.43	71.22	71.06	71.19	71.01
δ^{15}N$_{grav}$, ‰	0.403	0.406	0.357	0.356	0.357	0.356
Firn ΔT, °C	-0.58	0.04	-0.17	-0.18	-0.19	-0.18
δ^{15}N$_{therm}$, ‰	-0.008	0.001	-0.002	-0.002	-0.003	-0.003

Effect of two different durations for DO-23   Dansgaard-Oeschger event 23 is a particularly long event, characterised by a 10 °C warming at its onset (Landais et al., 2005; Kindler et al., 2014) followed by a quite slow cooling towards GS conditions. The precise position of the GI-23 to GS-23 transition is actually quite difficult to define. Two different timescales are available for this period: the ss09sea06bm timescale and the AICC2012 timescale.

From 2427 m down to the bottom of the core, ss09sea06bm and AICC2012 differ by their

absolute age as well as by the duration of events. In particular, the duration of GI-23 to GS-23 differs. For GI-23 + GS-23 (2746.55–2891.60 m, Table 3.3), the AICC2012 timescale proposes a duration of 12335 a, while the ss09sea06bm timescale suggests a duration of 14000 a which is 13% more. Speleothem records from the Alps (the NALPS record, Boch et al., 2011) provide another duration estimation for this period, assuming that climatic changes in Europe and Greenland are synchronous over this time period. Unfortunately, there is a gap at the end of GS-23 in the NALPS speleothem data, so we take instead the duration GI-23 + GS-23 + GI-22, which lasts 14860 a according to NALPS. On the NGRIP core (2717.63–2891.60 m), these events last 14625 a according to AICC2012 (-1.6% compared to NALPS) and 16410 a according to ss09sea06bm (+10.4% compared to NALPS, +12.2% compared to AICC2012).

To test the effect of using different durations for DO-23 on the reconstruction of temperature and accumulation rate, we do the following tests. First, we use the AICC2012 timescale for the NGRIP ice core from bedrock up to 2900 m (onset of GI-23) and tune input temperature and accumulation rates in order to match the measured δ^{15}N data and estimated AICC2012-Δage tie points (Fig. 3.5, yellow lines). From 2900 m to 2740 m (GI-23 + GS-23): (i) we use the AICC2012 duration and Δage and tune temperature and accumulation rate accordingly (Fig. 3.5, yellow lines); (ii) we use the ss09sea06bm duration but the AICC2012-tuned temperature and accumulation rate from scenario (i) (Fig. 3.5, green lines); in scenario (iii), we use the ss09sea06bm duration and Δage and tune accordingly the temperature and accumulation rate histories (Fig. 3.5, blue lines).

The climatic history before DO-23 for all scenarios is exactly the same. Differences seen during DO-23 are only due to a different duration between GI-23 and GI-22. In scenario (ii), the longer ss09sea06bm duration induces modelled δ^{15}N shifted towards shallower depths compared to scenario (i) (Fig. 3.5, green lines). While this feature is notable, the resulting δ^{15}N profile with the ss09sea06bm (ii) and AICC2012 (i) timescales are almost identical, independent of which firn model was used (Table 3.3). In scenario (iii), the ss09sea06bm-Δage tie points are of increased values compared to the one calculated using the AICC2012 time scale (Table 3.2). When using the ss09sea06bm duration instead of the AICC0212 one, in order to increase the Δage, we need to reduce the accumulation rate by 10% (to get an older age at LID, but this also leads to a shallower LID) and to reduce the temperature by 1°C (to still keep the same LID) (Fig. 3.5, blue lines). This effect is the same with both the Goujon and Schwander models. On the contrary, the modelled LID is not influenced by using a different timescale, either because the input temperature and accumulation rate scenarios are unchanged (scenarios (i) and (ii), Fig. 3.5e and f, yellow and green lines) or because they are tuned in order to still match the δ^{15}N mean level, even with the new timescale (scenarios (i) and (iii), Fig. 3.5e and f, yellow and blue lines).

Based on these tests, we estimate the effect of the timescale uncertainty on the reconstruction of temperature and accumulation rate as follows:

- we assume that no timescale uncertainty leads to no "timescale-induced" accumulation rate and temperature uncertainties;

- as shown for DO-23, a 13% uncertainty in the duration of the event leads to a $\pm10\%$ change in the firn models tuned accumulation rate and a $\pm1°$C change in the temperature level. We take this as another estimate of the timescale uncertainty effect;

- we make a linear interpolation in between the above two estimations to calculate the timescale uncertainty effect for the whole NGRIP ice core. We use the 2σ uncertainty (in % of absolute age value) provided by the GICC05 annual layer counted timescale from present back to 60 ka b2k (3% on average), and 13% for older ice.

This gives an uncertainty (due to time scale uncertainty) of 2.2% in accumulation rate and 0.2°C in temperature between surface and 2429 m (GICC05 timescale), and 10% in accumulation rate and 1°C from 2429 m down to bedrock (AICC2012 timescale).

The Last Glacial Maximum: bedrock temperature effect
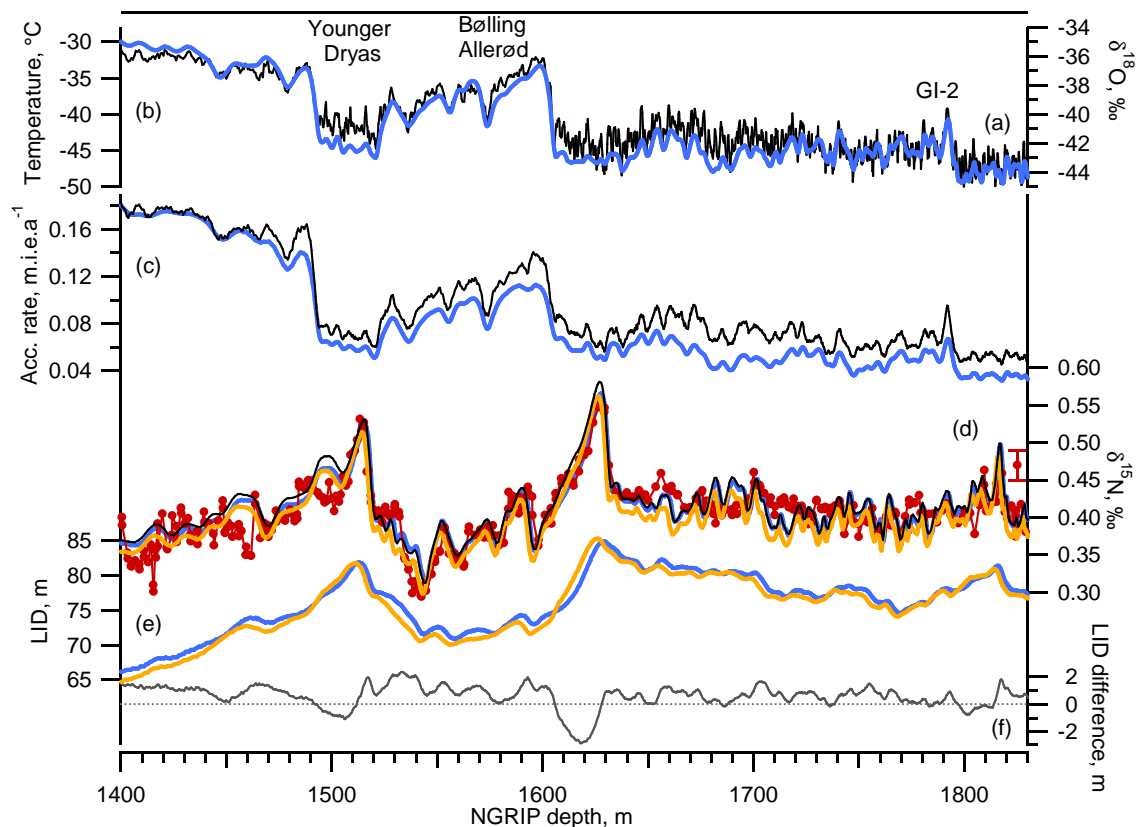
Figure 3.6: The Last Glacial Maximum: bedrock temperature effect on the modelled δ^{15}N. **(a)** Black: δ^{18}O, ‰. **(b)** Blue: firn-model-tuned temperature, °C, used in all runs (Kindler et al., 2014). **(c)** Accumulation rate, m.i.e.a^{-1}. Black: ss09sea06bm. Blue: ss09sea06bm-firn-model-tuned accumulation rate, used in all runs (Kindler et al., 2014). **(d)** δ^{15}N, ‰ and **(e)** modelled LID. Red dots: measured δ^{15}N, (Kindler et al., 2014). Blue line: using the Schwander model and the ss09sea06bm timescale. Yellow line: using the Goujon model, the same input temperature and accumulation rates as for the Schwander model, and the ss09sea timescale. Black line: same as yellow line but the input temperature is lowered by 1°C everywhere. **(f)** LID difference, m: LID$_{Schwander}$ - LID$_{Goujon}$.

DO-2 to Bølling-Allerød is the only period where significant discrepancies can be found between the Goujon- and Schwander-modelled δ^{15}N, Δage and LID, while using the same time scale, input temperature and accumulation rate (blue line, Fig. 3.6b and c). This long period is characterised by a low and stable accumulation rate (0.04 to 0.06 m.i.e.a^{-1}, Fig. 3.6c). The modelled δ^{15}N and LID are shown in Fig. 3.6d and e (Schwander model in blue, Goujon model in yellow) and Table 3.3.

Considering the average between 1634.7-1802.7 m, the Goujon-LID is 0.4 m shallower than the Schwander-LID; this may explain the position of the Goujon-modelled-δ^{15}N, slightly moved towards shallower depth. This would also partly (by 0.003 ‰) explain the observed slightly lighter (by 0.012 ‰) Goujon-δ^{15}N mean level. The rest of the mean Goujon-Schwander δ^{15}N difference is due to different firn temperature gradients. During this period, the bottom of the firn in the Goujon model is indeed warmer than the surface by 0.6 °C, being influenced by the warmer bedrock temperature. This firn temperature gradient induces a thermal fractionation lowering the δ^{15}N at the LID by 0.008 ‰, therefore explaining the rest of the Schwander-Goujon difference for the mean δ^{15}N level. To correctly model the mean level and position of δ^{15}N data with the Goujon model (Fig. 3.6d, black line), the input temperature (blue line, Fig. 3.6b) has to be lowered constantly by 1°C over this period.

Goujon et al. (2003) have shown the influence of the warm bedrock temperature on the base of the present-day Vostok firn, and modelled a significant influence of the bedrock temperature on the past Vostok glacial firn. This can be simply explained by the low present-day accumulation rate at Vostok (0.023 m.i.e.a^{-1}, Bender et al., 1994a), likely lower during the glacial period, leading to a slow advection of the surface temperature down to the base of the firn. At sites with a high accumulation rate (present-day at GRIP, GISP2, NGRIP and NEEM), the firn temperature is dominated by the surface temperature, while the bedrock temperature is of minor importance.

We conclude that the NGRIP firn was noticeably influenced by the bedrock temperature from DO-2 to the Bølling-Allerød. This test suggests that during periods of low accumulation rate like the LGM, calculating the temperature in the ice down to the bedrock is necessary to accurately estimate the mean firn temperature and firn temperature gradient.

Effect of different tuning strategies

In periods with abrupt temperature variations, the scenarios of temperature and accumulation can be well constrained by the measured Δage and δ^{15}N data. On the contrary, tuning of temperature and accumulation during periods of several millennia with relatively small climatic variability can be difficult, because we then lack Δage tie points, and different combinations of temperature and accumulation can produce the same firn thickness, and therefore the same δ^{15}N. We test here two different tuning strategies, hereafter named strategy (i) and (ii). For both strategies, the first guess temperature scenario is calculated using the NGRIP water isotope record, and the first guess accumulation rate is the one calculated using the ss09sea06bm timescale and thinning.

Strategy (i) (Fig. 3.7, blue lines) uses the Schwander model and is exactly the one applied and described in Kindler et al. (2014). The tuning of the temperature reconstruction is divided into three steps. In step (a), different α scenarios are calculated (see equ. 3.15) to produce several temperature scenarios as first inputs for the firn model. The modelled δ^{15}N scenarios are then compared in a 2 ka time window to the measured data, in order to find the best α value. The time window is then moved forward in time by 250 a to find the next best alpha. This procedure is repeated until the whole time period is covered. Like this, for each 250 a time step, a "best" α is found. This α time series is splined by 2 ka and used in step (b), where now the temperature level (β, equ. 3.15) and the accumulation rate are varied. The best scenario for temperature and accumulation is chosen in the same way as in step (a). The obtained β time series is splined by 2 ka, as for α, as well as the used reduction
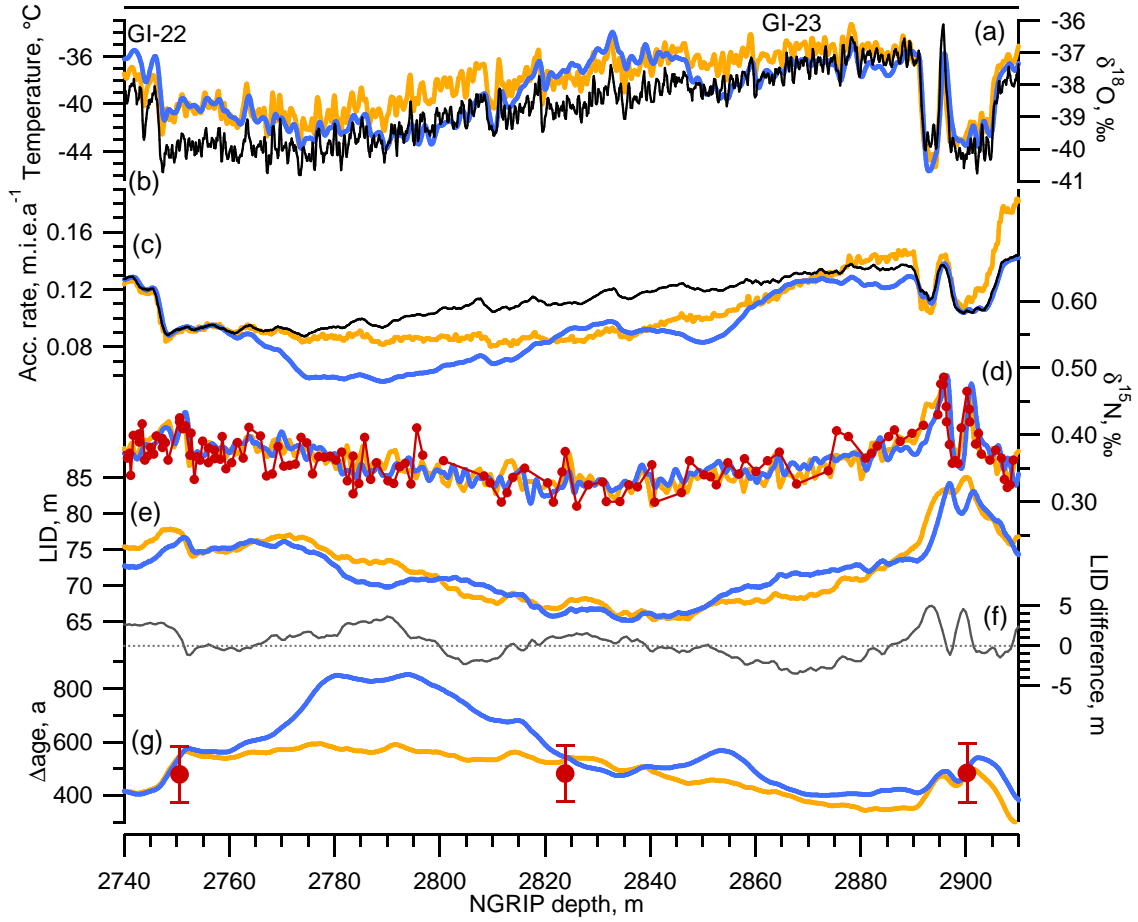
Figure 3.7: Two different firn model tunings well reproducing the measured δ^{15}N and Δage data. Blue: tuning strategy (i) using the Schwander model, Kindler et al. (2014). Yellow: tuning strategy (ii) using the Goujon model. **(a)** Black, NGRIP δ^{18}O, ‰(NGRIP members, 2004). **(b)** Temperature scenarios, °C. **(c)** Accumulation rate scenarios, m.i.e.a^{-1}. Black: original ss09sea06bm scenario. **(d)** δ^{15}N, ‰. Red dots: measured, Landais et al. (2005). **(e)** LID, m. **(f)** LID difference (LID$_{yellow}$−LID$_{blue}$), m. **(g)** Δage, a. Red dots: tie points, ice age difference between peaks of δ^{18}O in the ice and δ^{15}N in the gas. The error bars reflect the δ^{15}N data resolution (see text).

(in %) of the original ss09sea06bm accumulation rate. In step (c), the input temperature and accumulation rate are tuned manually where modelled and measured δ^{15}N and Δage data still disagree.

Strategy (ii) (Fig. 3.7, yellow lines) uses the Goujon model and first corrects the NGRIP water isotope record from the sea-water isotopic composition effect (Jouzel et al., 2003):

$$\delta^{18}O_{\text{corr}} = \delta^{18}O - \Delta\delta^{18}O_{\text{ocean}} \frac{1 + \delta^{18}O}{1 + \Delta\delta^{18}O_{\text{ocean}}} \quad (3.16)$$

with $\Delta\delta^{18}O_{ocean}$ the difference between the oceanic isotopic composition in the past and at present (Bintanja et al., 2005). Strategy (ii) uses a time-window corresponding to a unique DO event, from the sharp onset to the next stadial. The time window considered for the tuning is therefore variable from one DO to the next. For each time window, the "best" α is found first, then β and the percentage of accumulation rate reduction. This is done in an iterative way as depicted in Fig. 3.4. If unique solutions for α, β and the accumulation rate

reduction are not possible to match the measured data, the DO event is split into smaller time windows. The time window is then moved to the next DO event. This strategy favors the temperature reconstruction where (as much as possible) constant α and β can be used for a given DO event. As a result, the tuned temperature variations should scale as much as possible with the δ^{18}O variations, at the time scale of a DO event. Finally, we check that using the Schwander or Goujon model with the same tuned input from strategy (i) or (ii) has no effect: we run the tuned inputs from each strategy with both firn models and obtain no difference in the modelled δ^{15}N, Δage and LID. We are thus confident that the possible differences in the tuned temperature and accumulation rate are due to the different tuning strategies.

An example is given in Fig. 3.7 which depicts DO-23 with its long and gradual temperature decrease. Strategies (i) and (ii) both lead to the same modelled δ^{15}N (within the measurement uncertainty of 0.006 ‰), match the Δage match points and produce very similar temperature and accumulation rate scenarios near Δage match points. However the tuned scenarios are quite different in periods of stable climate missing Δage match points (2770 m - 2820 m). In such periods, firn models are under constrained and temperature-accumulation solutions are not unique. One way to choose between the two tuning strategies would be to favour the temperature scenario that parallels best the water isotope profile (strategy (ii), yellow lines in Fig. 3.7). This relies on the assumption that water isotopes and temperature keep a constant factor in between them, even over millennia, but this has however been challenged. Since the late 90' it was clear that the present-day Greenland spatial slope between water isotopes and temperature could not be applied to the glacial climate, as already suggested by Dansgaard et al. (1969) (e.g., Cuffey and Clow, 1997; Dahl-Jensen et al., 1998; Severinghaus et al., 1998; Lang et al., 1999). Moreover, Landais et al. (2004a) evidenced the need within a DO event to use a variable water isotope-temperature relationship, in order for a firn model to reproduce the measured gas isotopes. Their study was performed on the NGRIP ice core covering DO-18 to DO-20, using measured δ^{15}N and δ^{40}Ar with the Goujon model to reconstruct the surface temperature history.

δ^{18}O is the result of a Rayleigh distillation process and therefore the mean annual δ^{18}O signal as measured in ice cores depends on the Greenland local temperature, the vapour source temperature and relative humidity, the vapour source mix, the seasonality of precipitations, and the eventual temperature difference between the cloud condensation temperature and the ice sheet surface temperature (e.g., Jouzel et al., 2003). Therefore, even if Greenland temperature is stable, a change in other parameters influencing water isotopes can lead to a change in the δ^{18}O-temperature relationship. To model δ^{15}N data, it is therefore unknown how far it can be assumed that the water isotope-firn surface temperature relationship is constant.

Not only the two temperature but also the corresponding accumulation scenarios are different. None of the firn model tuned accumulation scenarios match the original ss09sea-06bm accumulation rate, in terms of absolute value as well as general shape over all DO-23. Scenario (i) features a considerably reduced accumulation rate at the end of DO-23, which could be unrealistic, producing the bump seen in the modelled Δage. On the other hand, scenario (ii) features nearly constant accumulation rates during the temperature decrease from DO 23 which may be unrealistic too. It has been recently proposed that the dust or calcium content in the ice affects the firnification process (Hörhold et al., 2012; Freitag et al., 2013). A quantification of this effect is necessary and it would be interesting to include it in

firn models and see what best accumulation rate reconstruction is obtained. The available studies of dust effect on the densification suggest an increased densification rate with the dust content. Qualitatively, we thus expect lower tuned accumulation rates in periods of high dust content (like depth 2760-2820 m in NGRIP, at the end of DO-23) compared to period of low dust content in the ice (like depth 2840-2880 m in NGRIP, at the beginning of DO-23).

While the temperature reconstruction can be better constrained during periods of rapid variability (onset of DO events) due to more Δage match points, a less accurate tuning is probably achieved during low variability periods (missing Δage match points). Therefore the uncertainty of temperature and accumulation reconstructions is probably increased in these periods. On the contrary, the LID is mostly constrained by the δ^{15}N mean level. Both LID scenarios agree with a difference of ± 2 m (2σ) on average over DO-23. The LID difference is not particularly reduced where Δage and Δdepth match points are present (Fig. 3.7f). To accurately reconstruct past temperature and accumulation rate in periods of no temperature variability, it would be useful to combine δ^{15}N with δ^{40}Ar data, in order to directly estimate the past firn thickness (e.g., Severinghaus et al., 1998; Kobashi et al., 2008).

3.4.5 Uncertainty estimation for gas age scale, LID, temperature and accumulation rate reconstructions

Thermal sensitivity of nitrogen isotopes   In the literature, the thermal sensitivity of nitrogen isotopes is calculated in two different ways. Leuenberger et al. (1999) proposed a formulation for α_T in pure nitrogen with a uncertainty of 0.09% at 241K (Equ. 3.10). However, the difference between the thermal sensitivity of nitrogen isotopes in pure nitrogen or in air is not quantified in this study. Later, experimental measurements of the δ^{15}N thermal sensitivity in air have been reported in Grachev and Severinghaus (2003a), Equ. 3.13, with a precision of 3%. We have run the Goujon model for all NGRIP ice core with exactly the same input parameters and changed only the formulation of the δ^{15}N thermal sensitivity. On average, the difference in between the two modelled δ^{15}N$_{\text{therm}}$ is less than 10^{-5} ‰. Using these two different formulas to calculate δ^{15}N$_{\text{therm}}$ does not lead to different results.

Δage

As shown in Sect. 3.4.4, the Δage match points are well reproduced by firn models. We consider that at the match points, the modelled Δage uncertainty is equal to the Δage match point uncertainty. In between the match points, different tuning strategies lead to different reconstructions of Δage (Fig. 3.7). The absolute difference in the modelled Δage between 2900.2 and 2750.55 m increases when going further away from a Δage match point, and this can be approximated by $0.05\Delta t$, with Δt the time difference in years between the ice age at a given depth and the nearest Δage match point. Following Rasmussen et al. (2013), we therefore estimate the uncertainty in the modelled Δage by a linear interpolation of the $\sigma_{\Delta age}$ of two adjacent Δage match points, plus $0.05\Delta t$.

Lock-in depth

Using Equ. 3.8, we can write the LID as a function of the measured δ^{15}N and the modelled δ^{15}N$_{\text{therm}}$:

$$\text{LID} = z_{\text{c}} + \frac{\delta^{15}\text{N}_{\text{grav}} \, \text{R} \, \text{T}_{\text{mean}}}{\Delta\text{m} \, \text{g}} \tag{3.17}$$

$$\text{with } \delta^{15}\text{N}_{\text{grav}} = \delta^{15}\text{N} - \delta^{15}\text{N}_{\text{therm}} = \delta^{15}\text{N} - \Delta\text{T} \, \Omega_{\delta^{15}\text{N}} \tag{3.18}$$

$$\text{which gives: LID} = z_{\text{c}} + (\delta^{15}\text{N} - \Omega_{\delta^{15}\text{N}}\Delta\text{T})\frac{\text{R} \, \text{T}_{\text{mean}}}{\Delta\text{m} \, \text{g}} \tag{3.19}$$

What contributes to the LID uncertainty is the thickness of the convective zone z_c, the measurement uncertainty of δ^{15}N data, the uncertainty of $\Omega_{\delta 15N}$, how well firn models reproduce the firn temperature gradient $\Delta T = T_{surf} - T_{LID}$ and the mean firn temperature T_{mean}. We can then write the LID uncertainty as:

$$\sigma_{LID} = \sqrt{\sigma_{z_c}^2 + \sigma_{\delta^{15}N}^2 \left(\frac{R \, T_{mean}}{\Delta m \, g}\right)^2 + \sigma_{\Omega_{\delta 15N}}^2 \left(\frac{\Delta T \, R \, T_{mean}}{\Delta m \, g}\right)^2 + \sigma_{\Delta T}^2 \left(\frac{\Omega_{\delta 15N} \, R \, T_{mean}}{\Delta m \, g}\right)^2}$$
$$\overline{+ \sigma_{T_{mean}}^2 \left(\frac{R(\delta^{15}N - \Delta T \Omega_{\delta 15N})}{\Delta m \, g}\right)^2} + unknown \tag{3.20}$$

"Unknown" reflects the parameters that may influence the LID but for which no quantification of the effect is available so far, e.g. the dust effect (Hörhold et al., 2012; Freitag et al., 2013) and the wind effect (Martinerie et al., 1994).

It has been recently proposed that measuring additional stable gas isotopes (krypton, xenon) may help to reconstruct the past convective zone thickness (Kawamura et al., 2013). Such data are not available for the NGRIP ice core. Estimating past convective zone thickness for Greenland (Summit, NGRIP, NEEM) have been discussed by Guillevic et al. (2013), see Sect. A4 p. 109 of this thesis, who concluded that deep convective zones were unlikely, and that a convective zone of 0 to 3 m was the most probable. We thus calculate σ_{LID} with σ_{zc}=0 m and σ_{zc}=3 m. $\sigma_{\delta^{15}N}$ is 0.02‰ for Bern data and 0.006‰ for LSCE data. $\sigma_{\Omega_{\delta 15N}}$ is estimated to be 3% (Grachev and Severinghaus, 2003a). The thermal conductivity in the ice is well known but tests in Sect 3.4.4 showed that taking into account the effect of bedrock temperature may create a firn temperature gradient of up to 0.6°C during the LGM. We therefore use $\sigma_{\Delta T}$=0.6°C.

What remains hard to estimate is $\sigma_{T_{mean}}$. Indeed, this depends on how well firn models are able to reconstruct the mean firn temperature, assuming that the LID and the ice age at LID are perfectly known, which is the case where both δ^{15}N and Δage data are available. We have performed simple calculations with the firn models, showing that over a wide range of temperature (-55 to -20°C) and accumulation rate (0.03 to 0.2 m.i.e.a^{-1}), a 5% change in the LID corresponds to a 1°C change in surface temperature or a 12.5% change in accumulation rate. Considering that the Goujon and Schwander models reproduce present-day LID with an error of 3% (Table 3.1), and assuming that the error in modelled LID arises from inaccuracy in firn models temperature sensitivity only (and not accumulation rate sensitivity), this corresponds to $\sigma_{T_{mean}}$=0.6°C on average for both models. This should be taken as a maximum error estimate. This estimate is valid when the Δage is perfectly known. However, there is also an uncertainties linked to the Δage estimation, calculated previously. Sensitivity tests in the previous section showed that a 13% change in the duration of DO-23 (which

is equivalent to the same change in the Δage) leads to a 1°C change in the reconstructed surface temperature. We use this estimation here to calculate the Δage uncertainty effect on $\sigma_{T_{mean}}$. $\sigma_{T_{mean}}$ is then the sum of the uncertainty due to the "firn sensitivity" uncertainty and the one due to the Δage uncertainty.

We can now calculate σ_{LID} for the all NGRIP ice core, depending on the conditions at each depth. Between 1391 and 2464 m (where δ^{15}N data were measured with a pooled standard deviation 0.02‰), we calculate a 4.3 m uncertainty on the reconstructed LID (2σ). Most of the uncertainty is here due to the δ^{15}N measurement uncertainty. Between 2464 m and bedrock (δ^{15}N data measured with a pooled standard deviation of 0.006‰), we obtain a LID uncertainty of 2.7 m (2σ). Adding a +3 m convective zone uncertainty, we estimate the LID uncertainty to be -4.3\+5.3 m between 1391 and 2464 m and -2.7\+4.1 m between 2464 m and bedrock.

Temperature and accumulation rate reconstruction

The estimation of temperature and accumulation rate uncertainty (hereafter σ_T and σ_{acc}, respectively) is not straightforward, because in Equations 3.8 and 3.12 defining δ^{15}N$_{grav}$ and δ^{15}N$_{therm}$, only the temperature is present, not the accumulation rate. We identify the following uncertainties to be taken into account in the calculation of σ_T and σ_{acc}: $\sigma_{\delta^{15}N}$, σ_{zc}, $\sigma_{\Omega_{\delta^{15}N}}$, $\sigma_{\Delta T}$, $\sigma_{\Delta_{age}}$, and finally how accurate is the sensitivity of firn models. We note that all these uncertainties also contribute to σ_{LID}, calculated previously.

We use here the following approach. First, we calculate a new $\sigma_{LID,new}$ that takes into account $\sigma_{\delta^{15}N}$, σ_{zc}, $\sigma_{\Omega_{\delta^{15}N}}$ and $\sigma_{\Delta T}$. Then, using this $\sigma_{LID,new}$ and the firn modelled-LID sensitivity to temperature and accumulation rate changes estimated previously, we can calculate to which change in temperature only or accumulation rate only the LID uncertainty $\sigma_{LID,new}$ corresponds to. The LID uncertainty probably leads to errors in both temperature and accumulation simultaneously (not only one parameter), so these estimates should be considered as an upper uncertainty estimation. We then add the effect of the Δage uncertainty to the temperature and accumulation rate uncertainties, considering that a 13% change in Δage induces a 1°C change or a 10% accumulation rate change. And finally, we add the effect of the accuracy of firn models (reproducing the LID with an accuracy of 3%, corresponding to a 0.6°C difference or a 7.5% difference in accumulation rate). We obtain the following results:

- between 1391 and 2464 m (Bern δ^{15}N data), the temperature is known -1.9\+1.8°C and the accumulation rate -20\+22%.

- between 2464 m and bedrock (LSCE δ^{15}N data), the temperature is known -3.0\+2.9°C and the accumulation rate -29\+31%.

These estimates vary with depth. In particular, since $\sigma_{\Delta_{age}}$ is included in the calculation of σ_T and σ_{acc}, the uncertainty in the temperature and accumulation rate reconstruction increases when going further away in time from the nearest Δage match point. We believe that this is realistic, since the comparison of two different tuning strategies showed that the reconstructed scenarios differ more from each other when Δage data are lacking (Fig. 3.7). The uncertainty estimates that we propose here can of course be improved if further sensitivity tests are performed with firn models.

3.4.6 Conclusion

Past LID and Δage for the NGRIP ice core from the Holocene back to the Eemian have been previously reconstructed using δ^{15}N data and the Schwander firn model (Kindler et al., 2014). We have compared this reconstruction with scenarios obtained with the Goujon firn model. The Goujon and Schwander models, while using different equations to model the densification of the snow, produce very similar Δage and LID when the same input temperature and accumulation rate scenarios are used. This gives confidence in the ability of firn models to correctly model densification processes. We suggest that the firn temperature is influenced by the warmer bedrock temperature during periods of low temperature and accumulation rate like the Last Glacial Maximum. Modelling the ice temperature from surface to bedrock in firn models should therefore be included during such periods.

We have proposed a methodology to estimate the uncertainty assigned to LID, Δage, accumulation and temperature reconstructions linked to this method. On average for the NGRIP ice core, the temperature has been reconstructed with a -1.9\+1.8°C uncertainty between 1391 and 2464 m (Bern δ^{15}N data) and a -3.0\+2.9°C uncertainty between 2464 m and bedrock (LSCE δ^{15}N data). The accumulation rate has been reconstructed with a -20\+22% uncertainty between 1391 and 2464 m and -29\+31% between 2464 m and bedrock. Therefore, within uncertainties, the firn-model-based accumulation reconstruction for NGRIP is in agreement with the 20% higher accumulation rate reconstructed with the Dansgaard-Johnsen ice flow model.

An automated tuning of the input temperature and accumulation scenarios needed for firn models to match measured δ^{15}N data would make such reconstructions less time consuming and the tuning more reproducible, but the output climatic conditions would not necessarily be closer to the real past histories. Indeed, since several input variations can lead to the same modelled δ^{15}N and since Δage data are not available in periods of stable climate, climatic assumptions are needed to choose one unique scenario. While over short depth intervals, it can be assumed that accumulation rate variations should scale with annual layer thickness variations, this is not necessarily the case for firn surface temperature and δ^{18}O (Landais et al., 2004a). Indeed, δ^{18}O is not only influenced by the Greenland local temperature but also by the history of the water mass (e.g., Jouzel et al., 2003). To use δ^{40}Ar data combined with δ^{15}N and Δage, in order to directly reconstruct the gravitational fractionation affecting nitrogen and argon isotopes and therefore the firn thickness, is another method that has already been used for different time periods in Greenland ice cores (e.g., Severinghaus et al., 1998; Landais et al., 2004b; Kobashi et al., 2008). Another way to better constrain reconstruction of past Greenland temperature and accumulation reconstruction may be to combine a firn model and an ice flow model equipped with heat diffusion from surface to bedrock (e.g., Lundin et al., 2012). This way, the ice cores' timescales may help to constrain past climatic reconstructions.

3.5   Temperature and accumulation rate reconstruction for Summit, Greenland

In this section, we apply the same method as in Sect. 3.4 to reconstruct the past temperature, accumulation rate and gas age scale for the GRIP and GISP2 ice cores, both located close to the Summit of Greenland (map Fig. 3 p. 3). The available δ^{15}N data for these ice cores do not cover the all records, but a selection of Dansgaard-Oeschger events as well as the last deglaciation, covering time slices from the Holocene to DO-19. Up to now, for the time periods when δ^{15}N data are available in the GRIP ice core, such data are not measured in the GISP2 ice core, and vice versa. We therefore adopt the following approach: we assume that the sensitivity of water isotopes to temperature at both sites is the same (see Sect. 3.5.1 for the precise method), and thus reconstruct a Summit best estimate for the temperature and accumulation rate histories, that is constrained by δ^{15}N data from both ice cores. Based on the data we use, we test whether it is possible or not to detect significant differences between GRIP and GISP2 past climatic conditions. We then compare these Summit climatic reconstructions to other temperature and accumulation reconstructions from different methods, for the same location.

3.5.1   Method

We follow the same approach as in Sect. 3.4 for the NGRIP ice core: the input temperature and accumulation scenarios of the Goujon firn model (Goujon et al., 2003, model described in Sect. 3.4.2 p. 59) are tuned in order for the modelled δ^{15}N and Δage to match the measured δ^{15}N data and the identified Δage match points. We use a constant 2 m convective zone for both sites.

For GRIP and GISP2, existing δ^{15}N data are quite scarce, compared to the NGRIP ice core where a continuous record exist (Kindler et al., 2014). For GRIP (Fig. 3.9 p. 82), high resolution δ^{15}N data are available for DO 3 and DO 4 (measured by F. Prié and A. Landais at LSCE, unpublished), DO 9 (Guillevic et al., 2013), DO 12 (Landais et al., 2004b) and DO 19 (Lang et al., 1999). To fit present-day conditions, we also make the Goujon model to reproduce the firn density profile from GRIP (see Sect. 3.4 and Schwander et al., 1993). For GISP2 (Fig. 3.10 p. 83), high resolution δ^{15}N data are available for the 8.2 ka event (Kobashi et al., 2007), the Younger Dryas (Severinghaus et al., 1998), the Bølling Allerød (Severinghaus and Brook, 1999), DO 8 (Orsi et al., 2013, submitted) and DO 21 (Grachev et al., 2007). Additionally, δ^{15}N-excess data (δ^{15}N-excess $= \delta^{15}$N-δ^{40}Ar/4) are available for the the 8.2 ka event (Kobashi et al., 2007) and the Bølling Allerød (Severinghaus and Brook, 1999). Low resolution δ^{15}N from present back to DO-8 were published by Sowers et al. (1997) and Bender et al. (1994b). For DO 21 on the GISP2 core, we have so far 2 m resolution δ^{18}O data only and we therefore disregard the results produced by the firn model over this time period. Since we focus on the glacial period rather than the Holocene, we also do not try to fit the Goujon model to the the high resolution δ^{15}N data covering the Holocene from Kobashi et al. (2008). δ^{15}N data have a pooled standard deviation of 0.006‰ except for for DO-19 in GRIP (0.02‰) and data from Sowers et al. (1997) and Bender et al. (1994b) (0.03‰).

To reconstruct the temperature scenario, we use the water isotope records (Johnsen et al. (1992) for GRIP, Grootes and Stuiver (1997) for GISP2) corrected for the isotopic composition of the ocean (Jouzel et al., 2003). To add an additional constrain on the temperature scena-

Table 3.4: Δage match points between abrupt climatic variations identified in the ice (nomenclature from Rasmussen et al., submitted) and in the gas, for the GRIP and GISP2 ice core. Age and Δage according to the AICC2012 timescale.

Match point	Gas	Depth (m) for: δ^{18}O	gas	Δdepth, m	age (a b2k) for: δ^{18}O	gas	Δage, a	2σ, a
		GRIP						
	CH$_4$	1605.18	1625.80	20.63	11397	11746	349	95
Holocene	CH$_4$	1622.94	1645.30	22.36	11676	12359	683	32
GS-1	CH$_4$	1661.00	1680.85	19.85	12859	13318	459	60
GI-1b	CH$_4$	1674.20	1695.20	21.00	13162	13598	436	120
GI-1d	CH$_4$	1716.28	1738.60	22.33	14017	14438	421	98
GI-1e	CH$_4$	1751.48	1775.70	24.23	14652	15554	902	61
GI-2.2	CH$_4$	1955.80	1978.65	22.85	23609	25021	1412	240
GI-3	CH$_4$	2025.10	2044.35	19.25	27771	28837	1066	129
GI-4	CH$_4$	2046.00	2062.80	16.80	28897	30226	1329	113
GI-5	CH$_4$	2098.80	2112.60	13.80	32499	33494	1095	116
GI-6	CH$_4$	2118.33	2133.20	14.88	33724	34805	1082	107
GI-7	CH$_4$	2148.58	2162.35	13.78	35476	36565	1089	81
GI-8	CH$_4$	2199.73	2212.40	12.68	38194	39231	1036	80
GI-9	δ^{15}N	2223.65	2235.20	11.55	40163	41048	885	67
GI-10	CH$_4$	2244.00	2252.85	8.85	41516	42306	890	224
GI-11	CH$_4$	2271.23	2280.60	9.38	43381	44292	1011	216
GI-12a	δ^{15}N	2283.33	2291.90	8.58	44482	45108	626	132
GI-12c	δ^{15}N	2324.03	2333.93	9.90	46847	47844	996	74
GI-19	δ^{15}N	2558.05	2562.07	4.02	72385	73403	1018	123
		GISP2						
8.2	CH$_4$	1397.77	1416.95	19.19	8289	8471	182	49
	CH$_4$	1661.05	1680.12	19.07	11420	11764	344	81
	δ^{15}N	1661.05	1682.56	21.51	11420	11845	425	82
Holocene	δ^{15}N	1676.47	1699.27	22.80	11670	12420	750	62
	δ^{15}N	1679.98	1702.00	22.02	11760	12515	755	86
GI-1a	CH$_4$	1715.48	1735.10	19.62	12955	13426	471	96
GI-1a	δ^{15}N	1715.48	1736.17	20.69	12955	13449	494	43
GI-1b	CH$_4$	1723.13	1741.90	18.77	13140	13564	424	122
GI-1e	δ^{15}N	1797.63	1820.50	22.88	14687	15633	945	93
GI-4	CH$_4$	2076.31	2095.00	18.69	28896	30386	1490	568
GI-5	CH$_4$	2127.64	2141.60	13.96	32519	33442	1023	419
GI-6	CH$_4$	2146.71	2158.55	11.84	33748	34608	861	254
GI-7	CH$_4$	2178.15	2191.60	13.45	35499	36517	1018	254
GI-8	δ^{15}N	2231.85	2244.40	12.55	38209	39234	1026	103
GI-9	CH$_4$	2255.55	2267.49	11.94	40138	41025	987	67
GI-10	CH$_4$	2276.36	2286.98	10.62	41472	42367	995	96
GI-11	CH$_4$	2304.21	2314.30	10.09	43364	44300	1036	83
GI-12a	CH$_4$	2316.14	2325.90	9.76	44440	45135	695	105
	CH$_4$	2339.62	2348.90	9.28	45920	46388	468	63
GI-12c	CH$_4$	2358.89	2368.08	9.18	46854	47751	897	95
GS-15.1	CH$_4$	2457.99	2465.90	7.92	54608	55526	1018	578
GI-17.1a	CH$_4$	2488.84	2497.90	9.06	57790	58647	857	318
GI-17.1b	CH$_4$	2494.96	2501.90	6.94	58350	58981	631	253
GI-17.2	CH$_4$	2508.04	2513.55	5.51	59593	60395	802	239
GI-18	CH$_4$	2536.04	2540.88	4.84	64360	65207	847	189
GI-19	CH$_4$	2583.97	2587.90	3.93	72219	73034	815	428
GI-20	CH$_4$	2611.99	2616.95	4.96	75903	76769	966	572
GI-21.1e	CH$_4$	2675.98	2678.94	2.95	84185	84568	383	137
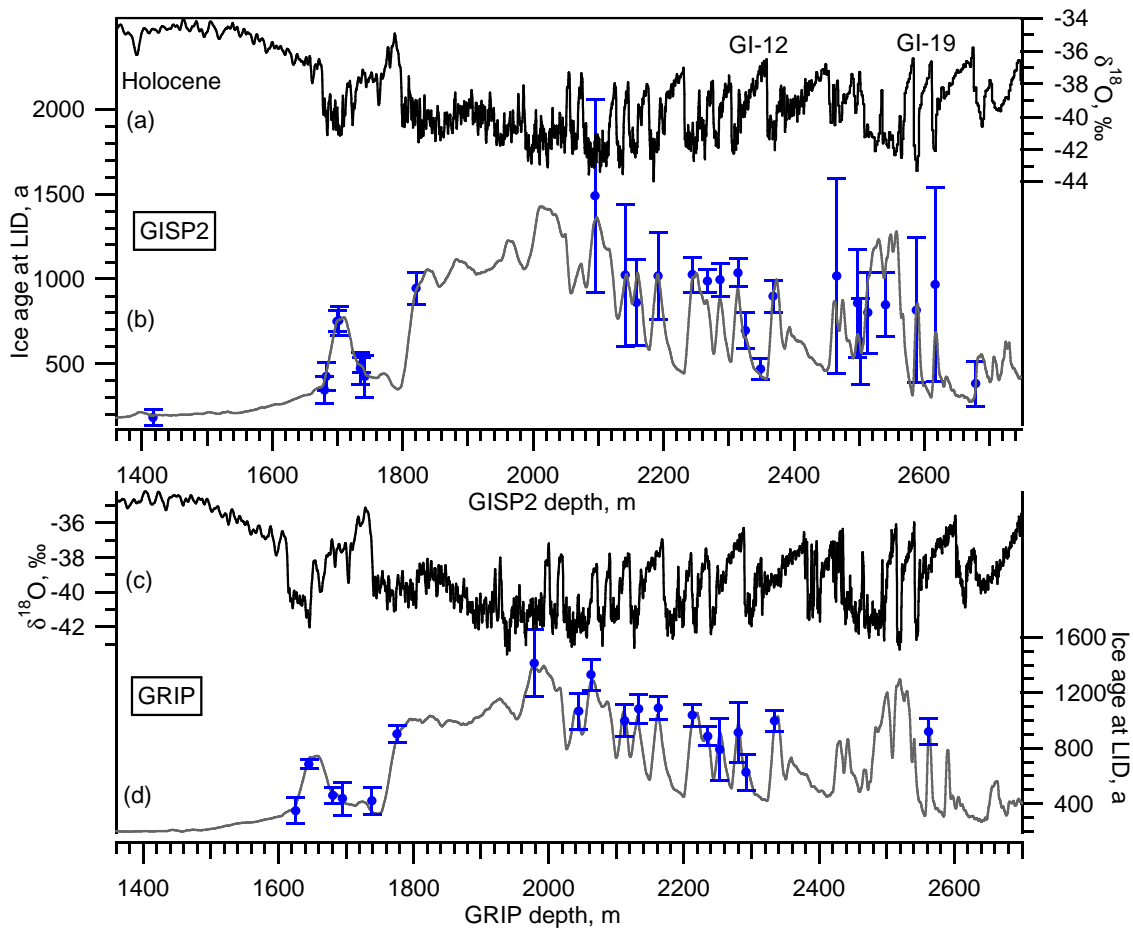
Figure 3.8: Δage match points and reconstruction of the gas age scale. **(a)**: GISP2 δ^{18}O (‰), Grootes and Stuiver (1997). **(b)** Blue dots: GISP2 Δage match points. Grey: GISP2 ice age at LID, a (equivalent to the gas age scale when neglecting the gas age at the LID). **(c)** GRIP δ^{18}O (‰), Johnsen et al. (1992). **(d)** sa me as (b) for the GRIP ice core.

rios reconstructed by the firn model, we assume that between GRIP and GISP2 the δ^{18}O-temperature relationship (α factor) is the same. Therefore, any α values that are tuned over a certain time for an ice core where δ^{15}N data are available (for example, DO 9 in GRIP) will be applied to the other ice core temperature scenario, where there are no δ^{15}N data.

For both ice cores, we use the GICC05 chronology back to 59 ka b2k. Beyond, we use the AICC2012 chronology (Bazin et al., 2013; Veres et al., 2013) that has been constructed for the NGRIP ice core. We transfer GRIP and GISP2 to the AICC2012 chronology using match points between NGRIP, GRIP and GISP2 (I. Seierstad, in prep.). To calculate a first guess accumulation rate, we use the thinning function from Johnsen et al. (2001) for GRIP, reconstructed using a Dansgaard-Johnsen (DJ) ice flow model, and from Cuffey and Clow (1997) for GISP2, using the Cuffey and Clow (CC) ice flow model. We calculate the corresponding accumulation rates for GRIP and GISP2 using the GICC05/AICC2012 annual layer thickness.

The Goujon model also reconstructs the past gas age scale and Δage between ice and gas. Δage data are therefore an additional constrain to this model. Methane concentration variations in the entrapped gas closely follow the δ^{18}O variations seen in the ice (e.g., Blunier and Brook, 2001; Chappellaz et al., 2013), with a time lag of 56±19 a on average for all
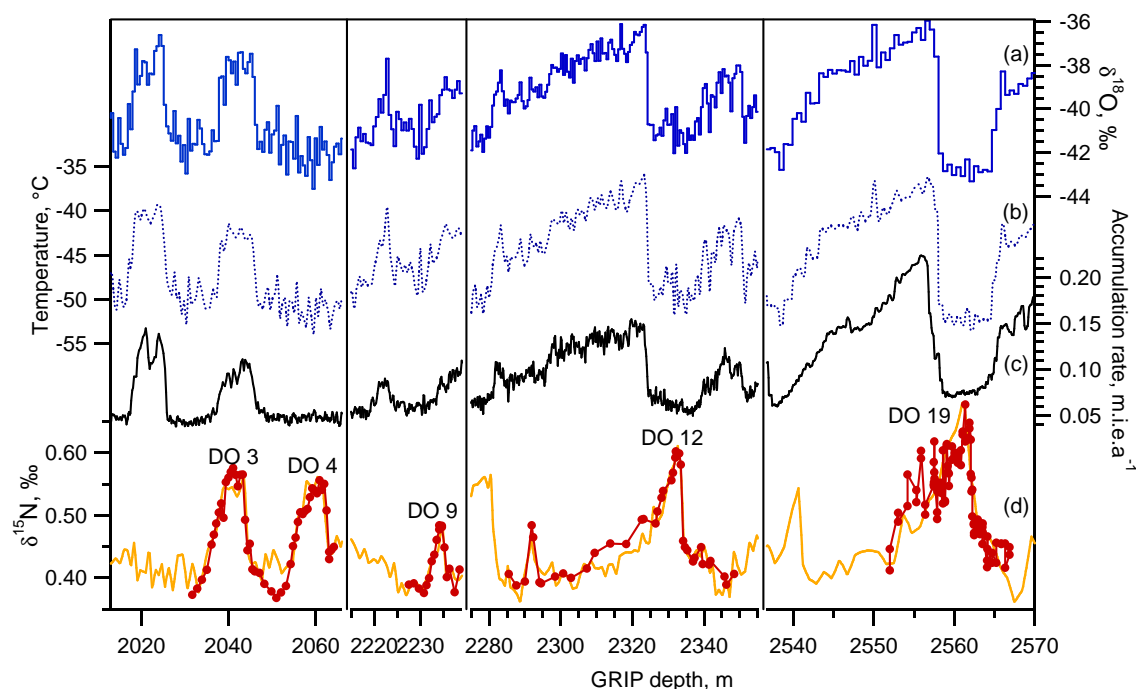
Figure 3.9: δ^{15}N data reconstruction for GRIP. **(a)** δ^{18}O profile used to reconstruct the surface temperature profile. **(b)** Surface temperature scenario. **(c)** Accumulation rate scenario. **(d)** Red dots: δ^{15}N data. DO 3, 4, 9 and 12: measured at LSCE, 2σ=0.007 ‰. DO 3 and 4: measured by F. Prié and A. Landais, pers. com. DO 9: Guillevic et al. (2013). DO 12: Landais et al. (2004b). DO 19: Lang et al. (1999), measured at KUP, 2σ=0.02 ‰. Orange line: modelled δ^{15}N by the Goujon model, using temperature and accumulation scenario shown in (b) and (c).

DO of the last glacial period (Baumgartner et al., 2013). Comparison of CH_4 and δ^{18}O in the same ice core can therefore help to constrain the past Δage. We use the CH_4 data measured by Blunier and Brook (2001) as well as the available δ^{15}N data to define Δage match points between abrupt climatic shifts seen in the ice and in the gas phase (Table 3.4). We apply the same method to define Δage match points for the GISP2 ice core, where methane data from Severinghaus et al. (1998); Severinghaus and Brook (1999); Brook et al. (2000); Ahn et al. (2012) are available (Table 3.4). Comparison of δ^{15}N and CH_4 variations measured on the same ice core suggests that at the onset of abrupt transitions as DO events, methane increase is synchronous to δ^{15}N increase or lagging by in average ~50 a (Huber et al., 2006; Baumgartner et al., 2013, based on NGRIP 0.55 cm resolution data,). Comparison of higher resolution (~1 cm) methane record (Chappellaz et al., 2013) in the NEEM ice core with available δ^{15}N data (Chapter 4) suggests synchronous methane and δ^{18}O changes for the available time periods (DO 8 to 10, 21 and 22). To calculate Δage tie-points in between methane and δ^{18}O abrupt changes, we therefore adopt a mean methane lag of 25±25 a.

The Δage uncertainty is calculated as in Sect. 3.4.5: when the GICC05 annual layer counting is available (Holocene to DO-16), we calculate the Δage uncertainty as the Maximum Counting Error (MCE, Rasmussen et al., 2006) difference between the ice and gas depths. For DO-17 to DO-19, we calculate $\sigma_{\Delta age}$ as 10% of its value, since the durations of the GICC05modelext and AICC2012 disagree by up to 10% in this part of the ice core.

We consider our temperature and accumulation reconstructions valid from present-day back to DO 19, in the periods where both δ^{15}N and Δage data were available (Fig. 3.12,
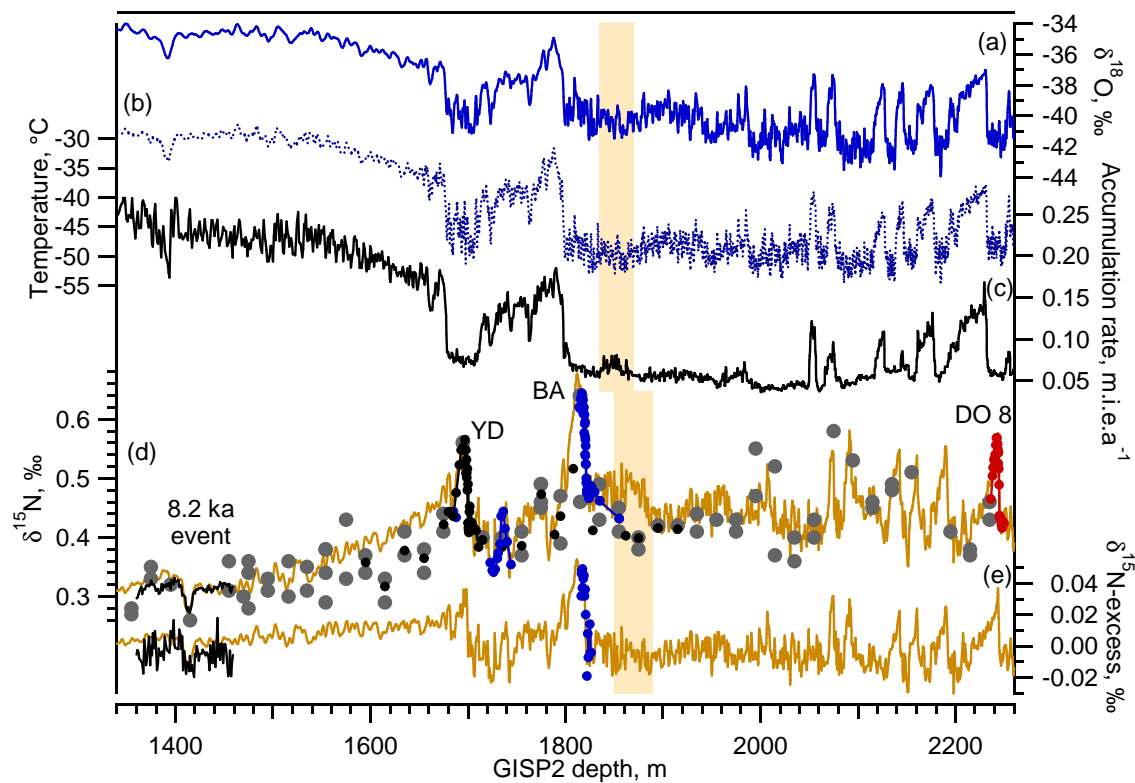
Figure 3.10: $\delta^{15}N$ data reconstruction for GISP2. Yellow shaded area: anomalously high accumulation rate at GISP2 (Rasmussen et al., 2008), creating a bump in the modelled $\delta^{15}N$. **(a)** $\delta^{18}O$ profile used to reconstruct the surface temperature profile, Meese et al. (1997). **(b)** Surface temperature scenario. **(c)** Accumulation rate scenario. **(d)** $\delta^{15}N$ and **(e)** $\delta^{15}N$-excess. Orange line: modelled by the Goujon model, using temperature and accumulation scenario shown in (b) and (c). Black dots: Bender et al. (1994b). Grey dots: Sowers et al. (1997). 8.2 ka event: black line, Kobashi et al. (2007). Younger Dryas (YD): green dots, Severinghaus et al. (1998). Bølling-Allerød (BA): blue dots, Severinghaus and Brook (1999). DO 8: red dots, (Orsi et al., 2013, submitted).

yellow shaded areas). In such periods, the uncertainty (2σ) is ~2°C for the temperature reconstruction and ~20% for the accumulation rate reconstruction (see method in Sect. 3.4.5). The uncertainty is bigger (and difficult to estimate) where we have only Δage from CH_4; an estimation of such an uncertainty has been done in Rasmussen et al. (2013), by comparison of different reconstructions from different firn models.

3.5.2 Results and discussion

GRIP-GISP2 comparison

The $\delta^{15}N$ and $\delta^{15}N$-excess modelled by the Goujon model are shown in Fig. 3.9 for GRIP and 3.10 for GISP2. The reconstructed gas age scales can be found in Fig. 3.8 for GRIP and GISP2. Using the available data (Δage, $\delta^{15}N$, $\delta^{15}N$-excess) from GRIP and GISP2 to constrain the firn model, and assuming the same temperature sensitivity of the water isotopes (α) for GRIP and GISP2, we are able to produce a temperature scenario for each site that makes the firn model to well reproduce Δage and $\delta^{15}N$ data, for each site. The choice of keeping the same α value for GRIP and GISP2, and the high similarities between the two isotopic records (89% common variance for the period 9-104 ka b2k, Grootes et al., 1993)
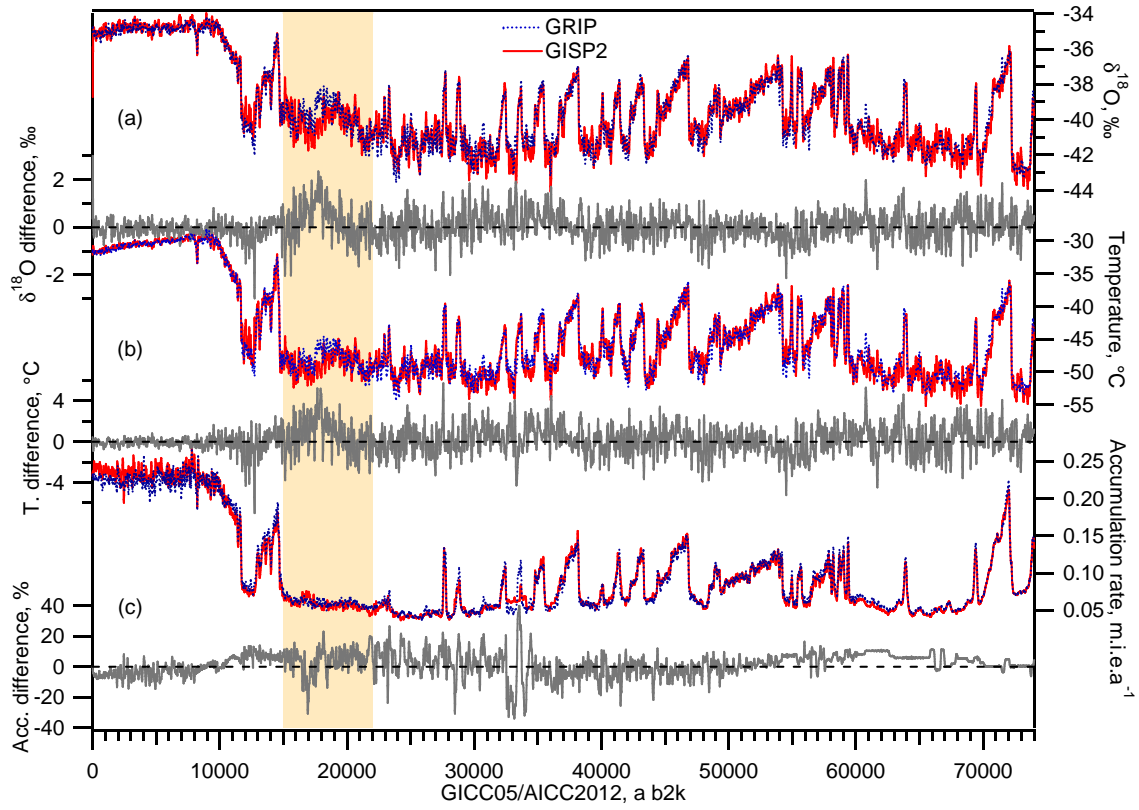
Figure 3.11: Temperature and accumulation reconstruction: GRIP-GISP2 comparison. Blue dotted line: GRIP. Red: GISP2. Gray: GRIP-GISP2 difference. **(a)** δ^{18}O, ‰. **(b)** Temperature reconstruction, °C. **(c)** Accumulation rate, m.i.e.a^{-1}. Yellow shaded area: major discrepancy between GRIP and GISP2 in therm of δ^{18}O, temperature and accumulation rate.

make the temperature difference between GRIP and GISP2 very similar to the isotopic difference between GRIP and GISP2 (Fig. 3.11). On average for the period 10-74 ka b2k, the temperature difference GRIP-GISP2 is 0.1°C. The largest isotopic (and temperature) difference can be found in the so called mystery interval, ∼15-20 ka b2k, yellow shaded area in Fig. 3.11, where GRIP isotopes are higher than at GISP2 by ∼2‰. No δ^{15}N data are available for the GRIP site in this period.

The accumulation rate reconstructions are very similar (Fig. 3.11), 5% higher at GRIP on average. For the investigated period (10-74 ka b2k), we obtain the following δ^{18}O-accumulation rate relationships:

$$A = \exp(0.202\,\delta^{18}O + 5.508)\ \ R^2 = 0.86\ \ \text{for GRIP} \tag{3.21}$$

$$A = \exp(0.199\,\delta^{18}O + 5.366)\ \ R^2 = 0.81\ \ \text{for GISP2} \tag{3.22}$$

A small part of the mystery interval constitutes an exception to the GRIP-GISP2 accumulation rate similarity, where a bump has been identified in the GISP2 annual layer counting (Meese et al., 1997; Rasmussen et al., 2008), creating a bump in the reconstructed accumulation rate. No corresponding bump can be identified in the available GISP2 δ^{15}N data (Fig. 3.10). It may be possible that the ice experienced a lower thinning at GISP2 during this time period, caused by a non-symmetric east-west destabilisation of the Greenland ice sheet margins (M. Koutnik, pers. com.). A different precipitation pattern in Greenland may

also cause migration of the ice divide (Rasmussen et al., 2008). Interestingly, the onset of this GISP2 accumulation bump occurred at ∼18 ka b2k, corresponding to the onset of Heinrich event 1 (Chap. 5). An ice flow model incorporating ice divide migration, as developed by M. Koutnik, would be necessary to conclude whether different ice flows between GRIP and GISP2 are responsible for this observed pattern.

Comparison with other methods
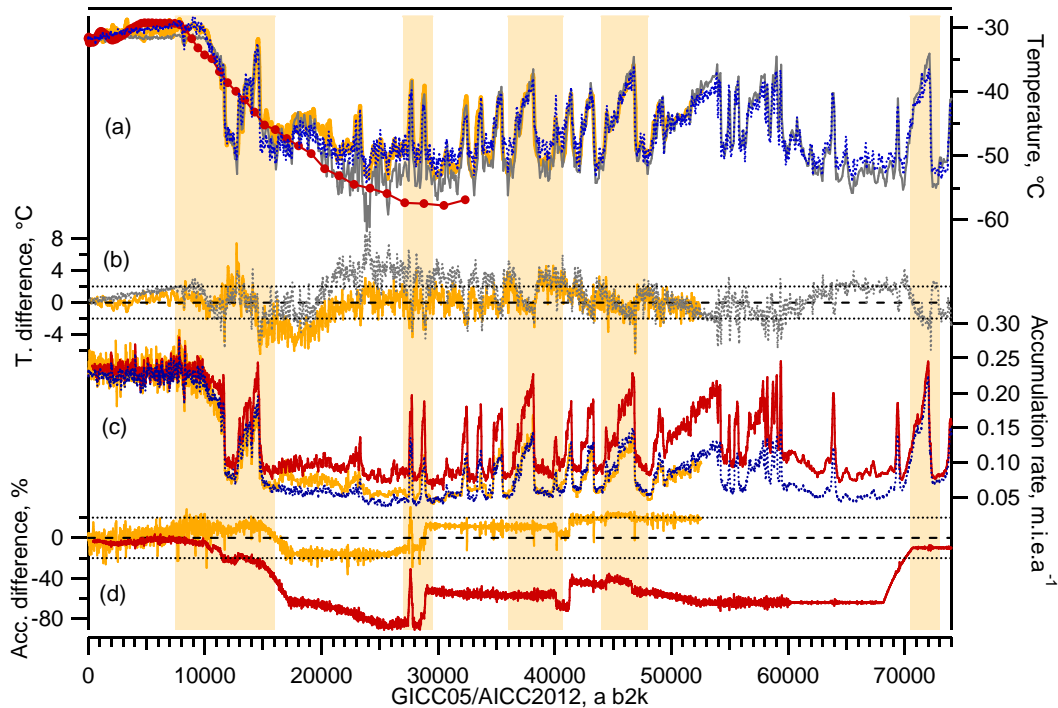
Figure 3.12: Temperature and accumulation rate reconstructions for Summit: comparison of different methods. **(a)** Temperature reconstructions, °C. $\delta^{15}N$ method: GRIP, blue dotted line, this study. Method based on water isotope measurements and isotope modelling: GRIP (gray, Masson-Delmotte et al., 2005a). Borehole temperature inversion: GISP2 (yellow, Cuffey and Clow, 1997) and GRIP (red, Dahl-Jensen et al., 1998). **(b)** Temperature differences, °C. Grey dotted line: GRIP (firn method)-GRIP (isotopic method). Yellow: GISP2 (firn method)-GISP2 (borehole method). The two horizontal fine dotted lines represent the 2σ uncertainty for the firn model based temperature reconstructions. **(c)** Accumulation rate reconstructions, all adapted to the GICC05/AICC2012 timescale. $\delta^{15}N$ method: GRIP, blue dotted line, this study. Ice flow models: GISP2 (yellow, Cuffey and Clow, 1997) and GRIP (red, Hammer et al., 1997; Johnsen et al., 1995; Dahl-Jensen et al., 1993). **(d)** Accumulation rate differences, %. Red: GRIP (firn method)-GRIP (DJ ice flow method). Yellow: GISP2 (firn method)-GISP2 (Cuffey and Clow, 1997, borehole/ice flow method). The two horizontal fine dotted lines represent the 2σ uncertainty for the firn model based accumulation reconstructions. Time scale: GICC05 back to 59 ka b2k, AICC2012 beyond. The yellow shaded areas indicate periods where the temperature and accumulation rate reconstructions from firn modelling are well constrained, because $\delta^{15}N$ and Δage data were available.

In Fig. 3.12 are compiled reconstructions of temperature and accumulation rates for GRIP and GISP2 from different methods. The uncertainties shown by the fine dotted lines in the temperature and accumulation rate differences take only into account the uncertainty of the firn model method. Around the end of the 90', alternative methods to the water iso-

tope thermometer were developed to reconstruct the temperature at a given ice core site in Greenland: one method consists in using δ^{15}N data and a firn model (e.g., Schwander et al., 1997), another method is based on ice flow and heat diffusion model, constrained by the time scale of a given ice core and the measured borehole temperature profile (e.g., Cuffey and Clow (1997) for the GISP2 ice core, Johnsen et al. (1995) and Dahl-Jensen et al. (1998) for the GRIP ice core).

We compare our firn model-based GRIP temperature reconstruction with the water isotope-based reconstruction from Masson-Delmotte et al. (2005a), Fig. 3.12 a and b. The water isotope-based temperature is reconstructed using the mixed cloud isotopic model (MCIM, Ciais and Jouzel, 1994, and p. 9 of this thesis), a Rayleigh distillation model, constrained by GRIP δ^{18}O and d-excess data. The sensitivity of water isotopes to temperature is tuned by adding a parameter accounting for seasonality effect and another one linked to ice sheet size. The firn model-based and the water isotope-based reconstructions agree within uncertainties, except from 20 to 35 ka b2k where the firn model-based temperature is significantly warmer. At the onset of GI-3 and GI-4, we note that the firn model-based temperature increases are significantly smaller. Our firn model-based reconstruction may help to constrain the seasonality and ice sheet size factors used in future MCIM simulations.

The GISP2 firn model-based temperature reconstruction is in agreement with the borehole/ice flow reconstruction from Cuffey and Clow (1997) within uncertainties, except in the mystery interval (15-20 ka b2k), where the firn model-based reconstruction is lower. To reconstruct the GISP2 temperature, the borehole/ice flow method uses the GISP2 water isotopes and one α value for the all glacial period. However, Kindler et al. (2014) showed that for the NGRIP site, α is not constant but varies from 0.3 to 0.7 during the last glacial period (see Fig. 7 p. 130). Allowing a varying α in the borehole/ice flow method may be interesting to test but this could also create an under constrained problem.

For the accumulation rate, the GISP2 firn model-based reconstruction is in agreement with the borehole/ice flow model reconstruction from Cuffey and Clow (1997) within uncertainties, for the all period. On the contrary, the GRIP firn model-based accumulation scenario and the reconstruction from the Dansgaard-Johnsen ice flow model (Dansgaard and Johnsen, 1969; Johnsen et al., 1992) agree only in periods of warm climate (Holocene and DO 19), while from 15 to 70 ka b2k the Dansgaard-Johnsen accumulation is much higher. The same discrepancy has been observed for the NGRIP ice core, but with a smaller magnitude (Kindler et al. (2014), see p. 132 of this thesis). These observations will be discussed further in Sect. 4.2 p. 95.

3.5.3 Conclusion and outlook

We have reconstructed the Δage, temperature and accumulation rate a GRIP and GISP2 from present-day back to DO-19, using new and published δ^{15}N and Δage data and the Goujon firn model. To do so, we have assumed that the water isotope sensitivity to temperature is identical at GRIP and GISP2. Given the available δ^{15}N and Δage data for GRIP and GISP2, these reconstructions of temperature and accumulation rate with the Goujon firn model for both sites suggests that the water isotope sensitivity to temperature is the same for GRIP and GISP2, and that accumulation rates are also very similar. The uncertainty of our firn model based method and the scarcity of δ^{15}N data do not allow us to detect any significant climatic differences between GRIP and GISP2. However, if higher resolution δ^{15}N

data become available in the future, they may lead to a different conclusion.

Within the uncertainty of our firn model method, our GISP2 temperature and accumulation rate reconstructions are in agreement with those from Cuffey and Clow (1997), in most of the periods. This is also the case for our GRIP temperature scenario and the one reconstructed by Masson-Delmotte et al. (2005a), using an simple isotopic model constrained by GRIP $\delta^{18}O$ and d-excess data, except for DO-3 and DO4, where our temperature is significantly higher, while the amplitude of our temperature increases at the onset of these two DO is significantly smaller. Finally, our GRIP accumulation rate best estimate is in agreement with the reconstruction from the Dansgaard-Johnsen model during the Holocene and DO-19, while our scenario is up to 80% lower from the Bølling-Allerød to DO-19. This will be discussed in detail in Sect. 4.2 p. 95.

We have shown in the previous section that when $\delta^{15}N$ and Δage data are available, past temperature and accumulation rates can be reconstructed with a good precision using firn models (see Sect. 3.4). Such reconstructions for Summit can then be compared to the NEEM (Guillevic et al., 2013) and NGRIP (Kindler et al., 2014) reconstructions, to estimate the spatial variations of temperature and accumulation rate in Greenland during the Last Glacial Period. This will be done in the following chapter.

3.6 Gas data from the NEEM ice core: when does the folding start?
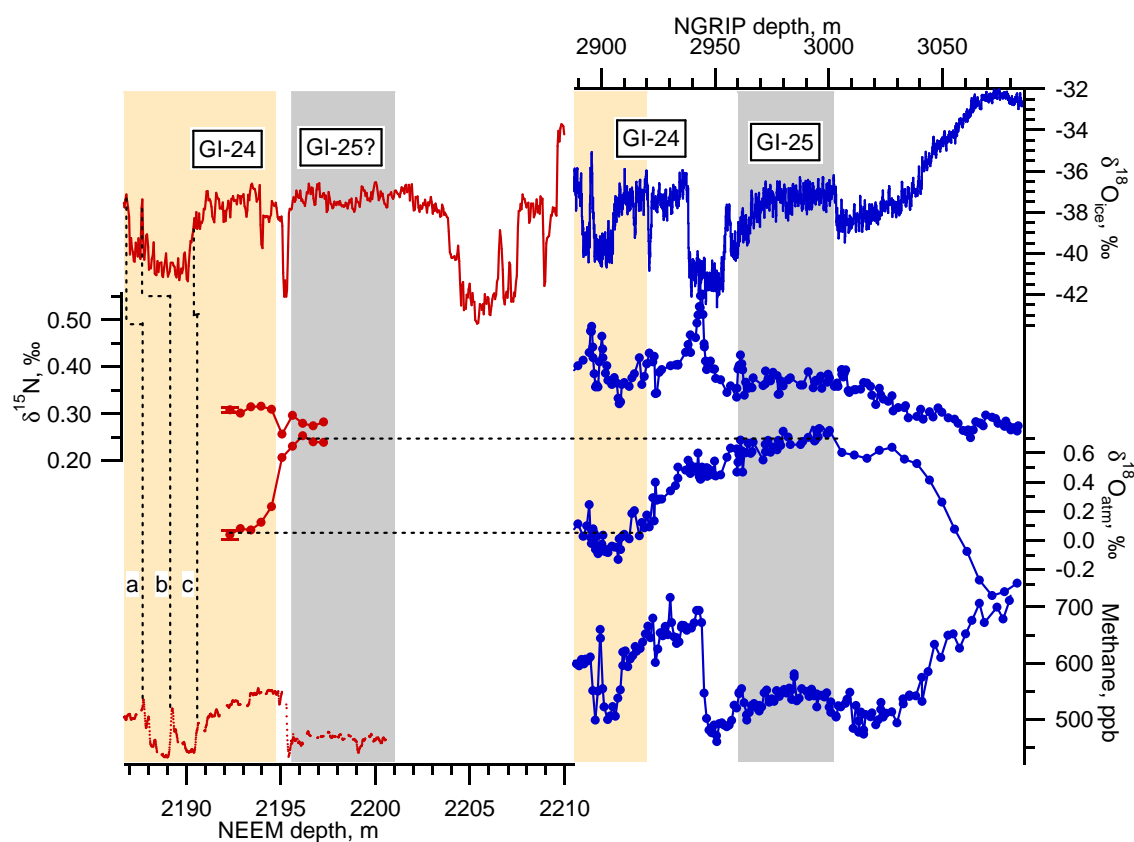
Figure 3.13: Evidence of ice flow disturbance at the bottom of the NEEM ice core based on gas isotopes data, by comparison to the NGRIP ice core. NEEM δ^{18}O: 5 cm resolution data, measured at CIC, unpublished. NEEM δ^{15}N and $\delta^{18}O_{atm}$ data: measured at LSCE, unpublished. NEEM methane data: CIC data measured by laser spectroscopy, uncalibrated data, C. Stowasser pers. com., see Chappellaz et al. (2013) for the calibrated data. NGRIP δ^{18}O: NGRIP members (2004). NGRIP methane, δ^{15}N and $\delta^{18}O_{atm}$: Landais et al. (2005); Capron et al. (2010b, 2012).

By comparison to Antarctic ice cores, it has been shown that the NGRIP ice core from Greenland records the last glacial inception, from the Eemian towards the Last Glacial Period, in an undisturbed chronological order (NGRIP members, 2004; Landais et al., 2005). When drilling the NEEM ice core in north West Greenland, the aim was to recover an ice record of the penultimate deglaciation. While ice from the penultimate glacial period is indeed present in the NEEM ice core, a detailed study of the NEEM ice, gas and radar profiles evidenced folding at the bottom of the ice core (Dahl-Jensen and NEEM community members, 2013).

In this section are reported new δ^{15}N and $\delta^{18}O_{atm}$ data measured at the bottom of the NEEM ice core. These new data are used to better characterise at which depth starts the folding in the NEEM ice core.

3.6.1 NEEM gas isotopes data

Together with A. Landais and F. Prié at LSCE, we have measured 10 new δ^{15}N and $\delta^{18}O_{atm}$ data points in the NEEM ice core between 2192.3 and 2197.3 m, complementing the dataset

already published in Dahl-Jensen and NEEM community members (2013). These data are measured using the melt-refreeze technique described in Sect. 3.3. The δ^{15}N pooled standard deviation is 0.006‰. To reconstruct the past δ^{18}O$_{\text{atm}}$ atmospheric signal, δ^{18}O$_{\text{atm}}$ measurements have been first corrected for eventual gas loss during ice storage using the δO$_2$/N$_2$ ratio measured in the same samples (Landais et al., 2010):

$$\delta^{18}\text{O}_{\text{gas loss corrected}} = \delta^{18}\text{O}_{\text{measured}} + 0.01\,(\delta\text{O}_2/\text{N}_2 + 10) \tag{3.23}$$

The obtained data are then corrected for thermal and gravitational fractionation occurring in the firn, using the δ^{15}N$_{\text{therm}}$ and δ^{15}N$_{\text{grav}}$ scenarios reconstructed using the Goujon firn model (Sect. 4.3):

$$\delta^{18}\text{O}_{\text{atm}} = \delta^{18}\text{O}_{\text{gas loss corrected}} - 1.6\,\delta^{15}\text{N}_{\text{therm}} - 2\,\delta^{15}\text{N}_{\text{grav}} \tag{3.24}$$

The resulting δ^{18}O$_{\text{atm}}$ pooled standard deviation is 0.03‰ (Landais et al., 2010). The results are presented in Fig. 3.13.

3.6.2   NEEM-NGRIP comparison

We compare the obtained NEEM gas isotopes records and the NEEM high resolution methane concentration (Chappellaz et al., 2013) with the NGRIP ice core records (Fig. 3.13). Note that the plotted NEEM methane record is uncalibrated, meaning that the measured variations are real features in the ice but the mean level may be inaccurate. The δ^{15}N data measured in NEEM are stable, and would thus correspond to the end of the warm stable part of GI-24. Since the temperature and accumulation rate at NEEM and NGRIP may not have been identical, we don't expected to find identical δ^{15}N levels in both cores, only to identify the same variations. We propose 3 match points between the NEEM ice and gas records (Fig. 3.13, vertical dotted lines, match points a to c). DO-23 and its precursor events are well identified in the NEEM water isotopes and their counterparts can easily be identified in the methane record (match points a, b, c). Moreover, in the yellow shaded area, the NEEM δ^{18}O$_{\text{atm}}$ mean level is very similar to the NGRIP one. These new NEEM gas data therefore confirm that GS-24 and the end of GI-24 are recorded in chronological order.

However, in the grey shaded area, while the NEEM water isotopes are stable and may correspond to GI-24 or GI-25 in the NGRIP ice core, the high δ^{18}O$_{\text{atm}}$ and low methane mean level (compared to the yellow shaded area) suggest that the NEEM ice between 2195 and 2201 m may correspond to GI-25 in the NGRIP ice core. In the NEEM ice, the end of the unfolded ice may start somewhere in between the yellow and grey areas, i.e. at ~2195 m depth. It may be that a piece of ice corresponding to GS-25 and the beginning of GI-24 is missing in between the yellow and grey areas in the NEEM ice core.

3.7   Reconstruction of the NEEM gas age scale

In the framework of the NEEM deep ice drilling project, we have contributed to the reconstruction of the NEEM gas age scale. Using available NEEM δ^{15}N and Δage data and the GICC05modelext timescale (Wolff et al., 2010), we have reconstructed the NEEM Δage along the all ice core using the Goujon firnification model (except in the folded part). This work is included in an article lead by S.O. Rasmussen reporting the construction of the ice and gas NEEM timescales (Rasmussen et al., 2013).

3.8   Conclusions and perspectives of this chapter

In this chapter, we have used new and published δ^{15}N and Δage data from different Greenland ice cores to reconstruct a best estimate of the past gas age scale, lock-in depth, temperature and accumulation rate. We have used the classical method of tuning the input temperature and accumulation rate scenarios of a firn model in order for the modelled δ^{15}N and Δage to match the measured data. We have used two different firn models: the Goujon model (Goujon et al., 2003) and the Schwander model (Schwander et al., 1997).

We have shown that the Goujon and Schwander models, while using different densification equations, produce very similar δ^{15}N and Δage scenarios for climatic conditions covering present and glacial NGRIP conditions. The only exception to this is the NGRIP last glacial maximum, where the warm bedrock temperature may warm up noticeably the bottom of the firn. This effect is taken into account in the Goujon model and it would be a useful development to include it in the Schwander model.

For the GRIP and GISP2 sites near the Summit of Greenland, we were not able to detect any significant difference in the sensitivity of water isotope to temperature in between these two sites, from the present back to DO-19. This conclusion may change if more δ^{15}N become available. Within uncertainties, our reconstruction of GISP2 accumulation rate is in agreement with the one from Cuffey and Clow (1997), that was based on a borehole temperature/ice flow model. On the contrary, our GRIP accumulation scenario is clearly lower (by up to 80%) during the glacial period than the GRIP reconstruction from Johnsen et al. (1992), using a Dansgaard-Johnsen ice flow model. This will be discussed in detail in the next chapter, Sect. 4.2.

We have proposed a methodology to estimate the uncertainty assigned to LID, accumulation and temperature reconstruction linked to the firn modelling method, for periods where δ^{15}N data are available and where the Δage uncertainty is calculated. To better constrain firn model based reconstructions, it would be needed to measure δ^{40}Ar data in addition to δ^{15}N data. This strategy has already been applied (e.g., Severinghaus et al., 1998; Landais et al., 2004b; Kobashi et al., 2008). Unfortunately these measurements are time consuming. Another method would consist in combining a firn model, a borehole temperature model and an ice flow model, constrained by δ^{15}N data, present-day borehole temperature measurements and timescale, in order to reconstruct past scenarios of temperature and accumulation rate. This approach is currently developed by Lundin et al. (2012).

In the next chapter, reconstructions of temperature and accumulation rate for GRIP, GISP2, NGRIP and NEEM, based on measured δ^{15}N data and firn modelling, will be combined to study the spatial gradients of temperature and accumulation rate in Greenland over DO-8 to DO-10. These gradients will be compared to the water isotope gradients.

Chapter 4

Advances in understanding Dansgaard-Oeschger events

4.1 Introduction
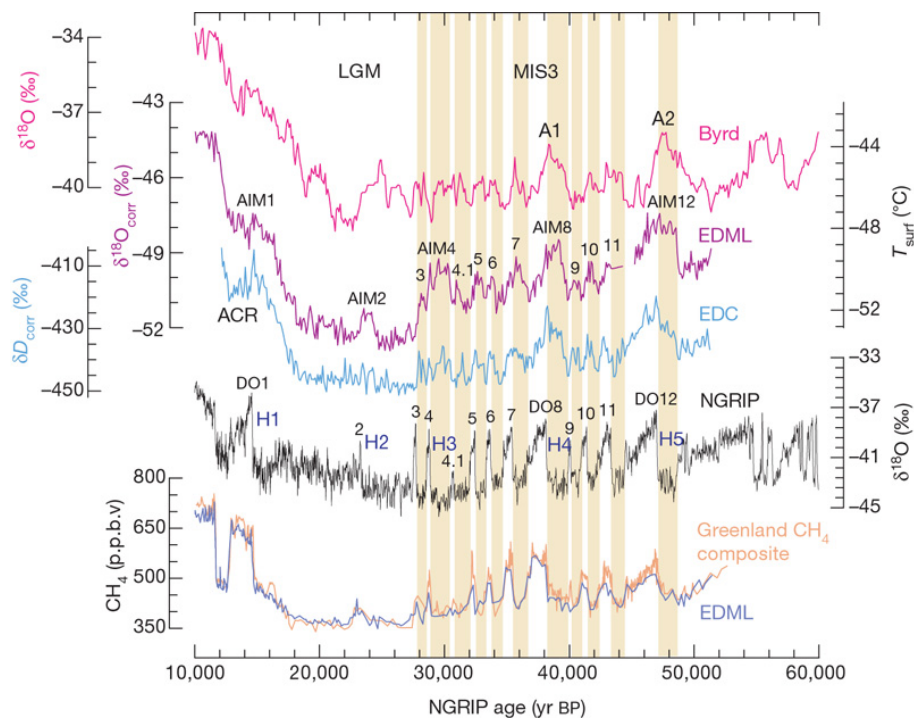
Figure 4.1: EPICA community members (2006), Figure 2. Original caption: *Methane synchronisation of the EDML and the NGRIP records reveals a one-to-one assignment of each Antarctic warming with a corresponding stadial in Greenland. Displayed are 100-yr averages during MIS3 in the EDML, EDC and Byrd ice core for the time interval 10–60 kyr BP in comparison with the NGRIP δ^{18}O record from Northern Greenland. All records are CH_4 synchronised and given on the new GICC05 age scale for the NGRIP ice core, which has been derived by counting annual layers down to 41 kyr and by a flow model for older ages. Yellow bars indicate the Greenland stadial periods that we relate to respective Antarctic temperature increases. The approximate timing of Heinrich layers in North Atlantic sediments is indicated as well. The y axis on the right side indicates approximate temperature changes at EDML based on the modern spatial gradient between δ^{18}O and temperature.*

4.1.1   A brief history

In Greenland ice cores, abrupt climatic variations occurring at the millennial time scale during the last glacial period were first identified in the water isotope record from the Camp Century ice core, north west Greenland (Dansgaard et al., 1969). However, these events could not be found in the water isotopes from the available Devon Island ice core (Canadian Arctic) nor in Antarctic ice cores, and whether these events were of climatic origin was an open question. The Dye 3 ice core was then drilled from 1971 to 1981 in South Greenland, close to the ice divide. The Dye 3 water isotope profile published by Dansgaard et al. (1982) showed close similarities with the Camp Century record and gave confidence to use the water isotope measurement as qualitative indicators of real Greenland temperature variations. This was finally confirmed in 1992 by comparison to the GRIP ice core record, drilled at the summit of Greenland (Johnsen et al., 1992). These events were named *Dansgaard-Oeschger events* by W. Broecker (Jouzel, 2013) and this name perhaps first appeared in Broecker and Denton (1989).

Dansgaard-Oeschger (DO) events are known at present as abrupt and pronounced climatic shifts occurring during the last glacial period, and recorded with great details in the water isotopes from Greenland ice cores. A DO event is classically made of an abrupt temperature increase from 3 to 16°C happening in a few years to a few decades (e.g., Huber et al., 2006; Capron et al., 2010a; Steffensen et al., 2008), followed by a warm period called Greenland Interstadial (GI). The temperature then progressively cools down, with sometimes an abrupt drop at the end. The following cold phase is called Greenland Stadial (GS). In the NGRIP ice core, a complete sequence of 25 DO events is recorded during the last glacial period (NGRIP members, 2004). The warm phase of each DO event is accompanied with low dust and impurities content, high annual layer thickness, high δ^{18}O, low d-excess and high methane concentration by comparison to the cold phase (Johnsen et al., 1989; Masson-Delmotte et al., 2005a; Steffensen et al., 2008; Baumgartner et al., 2013). High resolution records from marine and continental archives also record evidence of DO events throughout the northern hemisphere (Voelker, 2002; Bond et al., 1993). The DO-type millennial variability is also recorded in remote places from Greenland like the Cariaco Basin. Peterson et al. (2000) suggested latitudinal swings of the inter tropical convergence zone (ITCZ) location to explain this observation. The ITCZ would shift southwards during GS, compared to a more northerly position during GI. Such shift in the ITCZ position, leading to intensified summer monsoon strength in East-Asia during GI and modifying the isotopic composition of precipitation in the tropics (Lewis et al., 2010; Pausata et al., 2011a), may also explain the calcite δ^{18}O records from Chinese speleothems, that clearly record the DO variability (Wang et al., 2001; Cai et al., 2006).

4.1.2   Proposed mechanisms for DO variability

During the last glacial period, the DO climatic pattern registered in Greenland is completely different from the pattern registered in Antarctic ice cores: the shape of the water isotope variations are quite smooth in Antarctica compared to Greenland (Fig. 4.1). Precise common chronologies synchronising Antarctic and Greenland ice cores have been developed (Sowers and Bender, 1995; Blunier et al., 1998; Brook et al., 2005; Capron et al., 2010b; Bazin et al., 2013; Veres et al., 2013). Antarctic and Greenland gas records can be synchronised

using methane concentration that is a global signal, as well as other global absolute age markers as volcanic layers or beryllium variations. These common chronologies all show that temperature variations are not in phase in Greenland and Antarctica. This observation made Broecker (1998) and Stocker (1998) to propose the mechanism of the bipolar seesaw: the southern Atlantic Ocean acts as a heat reservoir. This heat is transported towards Greenland via the oceanic circulation (AMOC, Atlantic meridional overturning circulation). When the AMOC is strong, Antarctica is cold and Greenland warm. When the AMOC stops, Greenland cools abruptly while Antarctica warms gradually. The coherency between the observed bipolar behaviour (magnitude of southern warming related to the duration of the northern cooling) and theoretical considerations (on/off Atlantic interhemispheric transport plus inertia of the southern ocean) remains at present one of the best pieces of evidence that oceanic circulation changes are involved in DO events (EPICA community members, 2006). However, the bipolar seesaw mechanism cannot determine whether oceanic circulation changes are the trigger or a consequence of DO events.

Coupled atmosphere-ocean climate models forced by a fresh water flux into the North Atlantic are now able to simulate the DO-type millennial variability observed in Greenland (e.g., Kageyama et al., 2010). The sensitivity of the ocean circulation to changes in freshwater inputs suggests that interactions between ice sheets and ocean circulation are at play. However, these fresh-water forced simulations cannot reproduce the full Greenland temperature changes of 8-16°C between GS and GI, but classically a temperature change of 5-7°C (Kageyama et al., 2010). The ultimate cause and sequence of events remains unknown. Theoretical studies suggest that some modes of ocean circulation may be intrinsically unstable (e.g., Arzel and England, 2010).

Other mechanisms to explain the DO variability invoke sea-ice cover anomalies in the Arctic and especially the Nordic Seas, that could vary abruptly and produce the DO events pattern (Kaspi et al., 2004; Rasmussen and Thomsen, 2004; Jonkers et al., 2010; Dokken et al., 2013): during the cold GS, the Nordic Seas are covered with sea-ice, insulating the persistent mild North Atlantic drift in the subsurface from the cold atmosphere. The subsurface water is warmer than the upper surface water, and at some point this system becomes so unstable that the warm water reaches the surface, melting the sea-ice and releasing heat to the atmosphere, producing a GI in Greenland. Greenland then cools down progressively accompanied with sea-ice cover expansion, towards the next stadial. Li et al. (2005) and Li et al. (2010) modelled a +5 to +7°C Greenland temperature increase in response to Arctic sea ice cover retreat, which is again lower than the measured response in ice cores. Sea-ice variations alone cannot explain the DO temperature changes measured in Greenland ice.

4.1.3   What we do not know about DO events

So far, the trigger of DO-type millennial scale climate variability remains unknown. Different studies proposed solar activity variations (Bond et al., 1992; Braun et al., 2008), calving of ice sheets releasing fresh water into the North Atlantic (van Kreveld et al., 2000), tropical variability (reviewed by Clement and Peterson, 2008) or wind pattern changes (Wunsch, 2006). Broecker and Denton (1990) developed the idea of a salt oscillator, where interactions between ocean, ice sheets and atmosphere create its intrinsic instability: the Atlantic salty surface water mass flows northwards and is being cooled on the way, releasing heat that melts the ice sheets surrounding the North Atlantic (AMOC "on" state). The cold and salty

waters sink down and produce the North Atlantic Deep Water (NADW) that flows back south. The fresh water released by the ice sheet progressively lowers the surface salinity and thus the density of the North Atlantic surface waters, until the deep water formation is not possible anymore (AMOC "off" state), and the climate around the North Atlantic cools down, while Antarctica gradually warms up. In the North Atlantic, the AMOC can restart when the melt water input is low enough, and the evaporation has been at play long enough, so that the surface oceanic water is dense enough to start again the deep water formation.

The existence of a sub-millennial scale climate variability is as well a puzzling feature of DO events. Capron et al. (2010a) described three types of sub-millennial scale events, very well registered in the NGRIP ice core and confirmed in the GRIP, GISP2 and NEEM ice cores: precursor-type peak events, rebound-type events and abrupt cooling (the latter during GI-24 only). The cause of this variability is still unclear. Capron et al. (2010a) suggested a possible influence of a strong 65°N summertime insolation, causing short-lived perturbations of the northern hemisphere ice sheets balance, temperature and/or hydrological cycle. Counterparts of these events are found in Antarctica, suggesting that AMOC changes are at play and that the seesaw mechanism is also working at such short timescales. Deplazes et al. (2013) suggested that the precursor-type peaks before GI-21 and GI-23 are recorded as well in sediments from the Cariaco Basin. Interestingly, available methane and δ^{15}N data (a proxy for local temperature variations registered in the gas phase) from Greenland ice cores suggest synchronous local temperature and methane variations during these abrupt events (Baumgartner et al., 2013).

4.1.4   Organisation of this chapter

In Sect. 4.2, focusing on a sequence of Dansgaard-Oeschger events during MIS3, past temperature and accumulation rate at the NEEM site are reconstructed, using new δ^{15}N data measured during this PhD and firn modelling. The NEEM data are combined with data from other Greenland sites (GRIP, GISP2, NGRIP) to study the regional signature of Dansgaard-Oeschger events in Greenland, in terms of temperature, accumulation rate and water isotope-temperature sensitivity. We pave the way for the extension of this study to MIS5 in Sect. 4.3. If sea-ice cover variations indeed play a role in the DO variability or contribute to the Greenland temperature variations, then the different Greenland ice cores should record spatial variations in agreement with the model study from Li et al. (2010): larger temperature and accumulation increases in south and east Greenland compared to north and west Greenland. This possibility is investigated in the light of our new Greenland ice core data.

It has been shown that the amplitude of the temperature increase in Antarctica is linearly related to the duration of the preceding stadial (EPICA community members, 2006; Capron et al., 2010b; Vallelonga et al., 2012). If the restart of the AMOC is the main contributor of the Greenland warming at the onset of a DO event, it may be expected that the Greenland temperature warming is linked in the same way to the preceding stadial duration. If this is not the case, it would point to other mechanism causing/contributing to the Greenland warming, also explaining why climate models only using AMOC restart to create a DO event cannot well reproduce the Greenland temperature. This is investigated in Sect. 4.4, where the reconstruction of the complete NGRIP temperature from the Holocene to the Eemian is presented.

In each part of this chapter, the temperature reconstructions based on δ^{15}N data and firn modelling are compared to the water isotope records. The aim is to better constrain which parameters influence the water isotope variations and to better understand the hydrological cycle of the Northern Hemisphere during the succession of the DO events.

4.2   Spatial gradients of temperature, accumulation and δ^{18}O-ice in Greenland over a series of Dansgaard - Oeschger events

This section has been published as Guillevic et al. (2013) in the journal *Climate of the Past*. A. Orsi provided new δ^{15}N data from GISP2 (submitted work) and made the temperature reconstruction corresponding to these data. Ph. Kindler measured the new NGRIP δ^{15}N data presented in this work. At LSCE together with A. Landais, L. Bazin and F. Prié, we measured the NEEM δ^{15}N data. I did the firn modelling using the Goujon model and was the main contributor to the article writing, in collaboration with all co-authors.

Climate of the Past

Open Access

Spatial gradients of temperature, accumulation and δ^{18}O-ice in Greenland over a series of Dansgaard–Oeschger events

M. Guillevic[1,2]**, L. Bazin**[1]**, A. Landais**[1]**, P. Kindler**[3]**, A. Orsi**[4]**, V. Masson-Delmotte**[1]**, T. Blunier**[2]**, S. L. Buchardt**[2]**,
E. Capron[5]**, M. Leuenberger**[3]**, P. Martinerie**[6]**, F. Prié**[1]**, and B. M. Vinther**[2]

[1]Laboratoire des Sciences du Climat et de l'Environnement, UMR8212, CEA/CNRS/UVSQ, Gif sur Yvette, France
[2]Centre for Ice and Climate, Niels Bohr Institute, University of Copenhagen, Copenhagen, Denmark
[3]Climate and Environmental Physics, Physics Institute and Oeschger Centre for Climate Change Research,
University of Bern, Bern, Switzerland
[4]Scripps Institution of Oceanography, University of California, San Diego, La Jolla, CA, USA
[5]British Antarctic Survey, Cambridge, UK
[6]UJF Grenoble 1/CNRS, Laboratoire de Glaciologie et Géophysique de l'Environnement (LGGE), UMR5183,
Grenoble, 38041, France

Correspondence to: M. Guillevic (mgllvc@nbi.ku.dk)

Abstract. Air and water stable isotope measurements from four Greenland deep ice cores (GRIP, GISP2, NGRIP and NEEM) are investigated over a series of Dansgaard–Oeschger events (DO 8, 9 and 10), which are representative of glacial millennial scale variability. Combined with firn modeling, air isotope data allow us to quantify abrupt temperature increases for each drill site ($1\sigma = 0.6$ °C for NEEM, GRIP and GISP2, 1.5 °C for NGRIP). Our data show that the magnitude of stadial–interstadial temperature increase is up to 2 °C larger in central and North Greenland than in northwest Greenland: i.e., for DO 8, a magnitude of +8.8 °C is inferred, which is significantly smaller than the +11.1 °C inferred at GISP2. The same spatial pattern is seen for accumulation increases. This pattern is coherent with climate simulations in response to reduced sea-ice extent in the Nordic seas. The temporal water isotope (δ^{18}O)–temperature relationship varies between 0.3 and 0.6 (± 0.08) ‰ °C^{-1} and is systematically larger at NEEM, possibly due to limited changes in precipitation seasonality compared to GISP2, GRIP or NGRIP. The gas age−ice age difference of warming events represented in water and air isotopes can only be modeled when assuming a 26 % (NGRIP) to 40 % (GRIP) lower accumulation than that derived from a Dansgaard–Johnsen ice flow model.

1 Introduction

The last glacial period is characterized by rapid climatic instabilities at the millennial timescale occurring in the Northern Hemisphere and recorded both in marine and terrestrial archives (Voelker, 2002; Bond et al., 1993). The NGRIP (North Greenland Ice Core Project) ice core, northern Greenland, offers a high resolution water isotopes record where 25 rapid events were identified and described with a precise timing (NGRIP members, 2004). These events consist of a cold phase or stadial (Greenland stadial, GS), followed by a sharp temperature increase of 9 to 16 °C at the NGRIP site as constrained by gas isotope measurements (Landais et al., 2004a, 2005; Huber et al., 2006). The warm phase is referred as Greenland interstadial (GI). Temperature then gradually cools down, sometimes with a small but abrupt cooling in the end, to the next stadial state. These temperature variations are associated with significant changes in accumulation rate, with annual layer thicknesses varying by a factor of two between GS and GI at NGRIP (Andersen et al., 2006; Svensson et al., 2008).

The identification of ice rafted debris horizons during GS in North Atlantic sediments (Heinrich, 1988; Bond et al., 1993; Elliot et al., 2001), together with proxy records pointing to changes in salinity (Elliot et al., 2001, 2002),

reduced North Atlantic Deep Water formation (Rasmussen and Thomsen, 2004; Kissel et al., 2008) and Atlantic Meridional Overturning Circulation (AMOC) (McManus et al., 1994), had led to the theory that DO (Dansgaard–Oeschger) events are associated with large scale reorganizations in AMOC and interhemispheric heat transport (Blunier and Brook, 2001). The identification of a systematic Antarctic counterpart to each Greenland DO event (EPICA community members, 2006; Capron et al., 2010) supports this theory. This observation can be reproduced with a conceptual see-saw model using the Antarctic ocean as a heat reservoir and the AMOC as the way to exchange heat between Antarctica and Greenland (Stocker and Johnsen, 2003), as well as with climate models (e.g., Roche et al., 2010). Atmospheric teleconnections can also be at play (Chiang et al., 2008) and influence the timing of Antarctic warming with respect to Greenland cooling (Buiron et al., 2012).

Coupled atmosphere–ocean climate models are now able to reproduce the temperature pattern of DO events in Greenland in response to AMOC changes induced by freshwater forcing in the high latitudes of the Atlantic Ocean (Kageyama et al., 2010). However, modeled amplitudes of temperature changes are typically between 5 and 7 °C (Ganopolski and Rahmstorf, 2001; Li et al., 2005, 2010; Otto-Bliesner and Brady, 2010), significantly smaller than the temperature increase of 8–16 °C reconstructed based on ice core data (Landais et al., 2004a; Huber et al., 2006). The correct amplitude of temperature change over the Bølling-Allerød is only reproduced in a fully coupled and high resolution atmosphere–ocean global circulation model (Liu et al., 2009). However, a large part of the simulated warming is due to the simultaneous large changes in insolation (not at play for most DO events) and atmospheric CO_2 concentration. During DO events, limited CO_2 changes (20 ppm) are depicted by existing data (Indermühle et al., 2000; Bereiter et al., 2012; Ahn et al., 2012). This model–data mismatch motivates us to strengthen the description of the magnitude and spatial patterns of DO temperature changes, using different ice core sites. An improved regional description of past changes in Greenland climate will also be needed for the comparison with regional climate models recently equipped with water stable isotopes (Sjolte et al., 2011). So far, no systematic comparison of the signature of DO events in water stable isotopes and temperature (from gas isotopes) has been conducted over an array of drilling sites. This is the main target of this study.

In 2010, bedrock was reached at the North Eemian Ice Core Drilling (NEEM) site, northwest (NW) Greenland. A new deep ice core, 2.5 km long, is now available (Dahl-Jensen et al., 2013). In this paper, we present new data from the NEEM ice core, together with existing and new measurements conducted on the GISP2 (Greenland Ice Sheet Project 2) and NGRIP ice cores on DO events 8 to 10. The location of these drilling sites is depicted in

Fig. 1 and their present-day characteristics are summarized in Table 1 (see also Johnsen et al., 2001). At present, the main source of NEEM precipitation is located in the North Atlantic, between 30° N and 50° N (Steen-Larsen et al., 2011). The recent interannual variability of water stable isotopes (δ^{18}O, δD) shows similarities with the variability of the Baffin Bay sea-ice extent. Unlike central Greenland where snow falls year round, NW Greenland precipitation occur predominantly in summer according to snow pit studies (Shuman et al., 1995, 2001) and model simulations (Steen-Larsen et al., 2011; Sjolte et al., 2011; Persson et al., 2011). This specificity of the precipitation seasonality explains the particularly weak fingerprint of the North Atlantic Oscillation in NEEM shallow ice cores (Steen-Larsen et al., 2011) compared to GISP2 (Barlow et al., 1993). These regional peculiarities are of particular interest because past changes in precipitation seasonality are likely to affect water stable isotopes values.

Water isotopes are to a first order markers of local condensation temperature changes at the precipitation site (Dansgaard, 1964). However, they are also affected by evaporation conditions (temperature, relative humidity and wind regime, e.g., Merlivat and Jouzel, 1979; Johnsen et al., 1989), atmospheric transport and distillation, condensation conditions, as well as seasonality of precipitation (Werner et al., 2000; Werner et al., 2001; Masson-Delmotte et al., 2005): they are integrated tracers of the hydrological cycle and quantitative indicators of past site-temperature change, albeit with a time-varying relationship with local surface temperature. This temporal variability of the isotope–temperature relationship has been verified in Greenland thanks to independent constraints on past temperatures, either based on the inversion of borehole temperature data or derived from gas isotopes (e.g., Cuffey and Clow, 1997; Dahl-Jensen et al., 1998; Severinghaus and Brook, 1999; Lang et al., 1999; Johnsen et al., 2001; Landais et al., 2004a; Huber et al., 2006; Vinther et al., 2009).

Using the isotopic composition of nitrogen (δ^{15}N) from N_2 trapped in the ice bubbles allows us to quantify the amplitude of past rapid-temperature changes (e.g., Severinghaus and Brook, 1999; Landais et al., 2004a; Huber et al., 2006; Grachev and Severinghaus, 2005; Kobashi et al., 2011). At the onset of a DO event, the firn surface warms rapidly but its base remains cold because of the slow diffusion of heat in snow and ice. The resulting temperature gradient in the firn leads to thermal fractionation of gases: the heavy nitrogen isotopes migrate towards the cold bottom of the firn, where air is progressively trapped into air bubbles. As a result, a sharp peak in δ^{15}N is seen in the gas phase as a counterpart to the rapid increase in water stable isotopes in the ice phase. Using δ^{15}N data and firn modeling, past surface temperature variations can be reconstructed (Schwander et al., 1997; Goujon et al., 2003). This method has already been applied to specific DO events on the NGRIP, GRIP and GISP2 ice
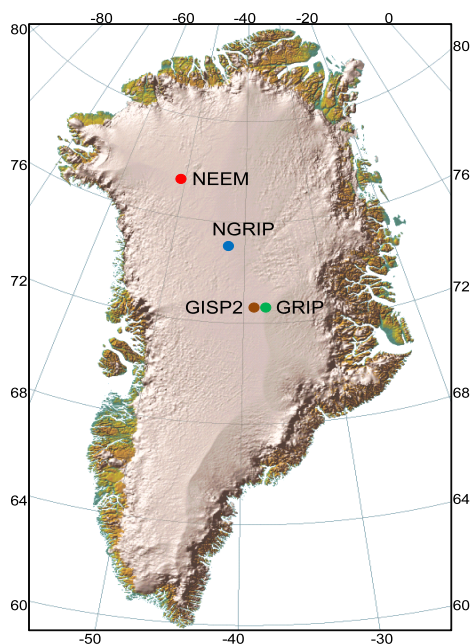
Fig. 1. Greenland map (Simon Ekholm, Danish cadastre) with the ice core sites: NEEM (red), NGRIP (blue), GISP2 (brown) and GRIP (green). Top and bottom numbers indicate longitude (° W), left and right numbers indicate latitude (° N).

cores (Lang et al., 1999; Huber et al., 2006; Landais et al., 2004a, 2005; Goujon et al., 2003; Severinghaus and Brook, 1999; Capron et al., 2010) and will be applied here for the first time to the NEEM ice core.

For this first study of regional variability of temperature changes over DO events, we focus on the series of DO events 8, 9 and 10 during Marine Isotope Stage 3 (MIS3, 28–60 ka b2k, thousand years before 2000 AD). This period is indeed the most widely documented for the millennial scale variability in a variety of natural archives. It is characterized by a large terrestrial ice volume (Bintanja et al., 2005), low atmospheric greenhouse gas concentration (Schilt et al., 2010), decreasing obliquity, low eccentricity and therefore small fluctuations in Northern Hemisphere summer insolation (Laskar et al., 2004). During MIS3, iconic DO events are particularly frequent with short lived interstadials (Capron et al., 2010) and constitute a clear target for model–data comparisons.

In this study, we first present a new δ^{15}N profile covering DO events 8 to 10 on the NEEM ice core. We then produce past temperature and accumulation reconstructions for NEEM and compare them with scenarios obtained with the same method for NGRIP, GISP2 and GRIP, investigating the water isotope–temperature relationships for these four different locations. We finally discuss the implications of our results in terms of regional climate variations.

Table 1. Present-day characteristics of NEEM, NGRIP, GISP2 and GRIP drilling sites (m.i.e., meters ice equivalent).

	NEEM[a]	NGRIP[b]	GISP2	GRIP
Latitude (° N)	77.45	75.10	72.58	72.58
Longitude (° W)	51.06	42.32	38.48	37.64
Elevation (m a.s.l.)	2484	2917	3214	3238
Surface temperature (°C)	~ -29.0	-31.5	-31.4[c]	-31.7[f]
Accumulation rate (m.i.e.a^{-1})	0.22	0.19	0.25[d]	0.23[g]
δ^{18}O (‰)	~ -33.0	-35.5	-35.0[e]	-34.9[g]

Sources: [a] Steen-Larsen et al. (2011); accumulation: 1964–2005 average, NEEM07S3 core. [b] NGRIP members (2004). [c] Cuffey et al. (1995). [d] Meese et al. (1994); accumulation: last 200 a average. [e] Average of the top 200 a of B core (1987–1787), Grootes and Stuiver (1997). [f] Gundestrup et al. (1994). [g] Johnsen et al. (1992), 20–220 a b2k average of the GRIP ice core.

2 Method

2.1 Data

2.1.1 Nitrogen isotope data

The isotopic composition of nitrogen (δ^{15}N) was measured on the NEEM core from 1746.8 to 1811.6 m depth at Laboratoire des Sciences du Climat et de l'Environnement (LSCE), France. We have a total of 84 data points with replicates, with an average depth resolution of 77 cm corresponding to an average temporal resolution of ~ 70 a. On the GRIP ice core, 18 data points covering DO 9 have been measured with an average resolution of 61 cm (equivalent to about 43 a). For these two data sets, we have used a melt–refreeze technique to extract the air from the ice (Sowers et al., 1989; Landais et al., 2004b). The collected air is then measured by dual inlet mass spectrometry (Delta V plus, Thermo Scientific). Data are corrected for mass interferences occurring in the mass spectrometer (Sowers et al., 1989; Bender et al., 1994b). Dry atmospheric air is used as a standard to express the results. The final pooled standard deviation over all duplicate samples is 0.007 ‰.

For the NGRIP core, δ^{15}N was measured at the University of Bern (73 data points from Huber et al. (2006) and 36 new data points on DO 8). A continuous flow method was used for air extraction and mass spectrometry measurement (Huber and Leuenberger, 2004). The associated uncertainty is 0.02 ‰.

For the GISP2 ice core, nitrogen isotopes were measured at Scripps Institution of Oceanography, University of California, using the melt–refreeze technique from Sowers et al. (1989) with a pooled standard deviation of 0.0065 ‰ for the 70 δ^{15}N data points (Orsi et al., 2013). In addition to these data, argon isotopes were also measured using the method from Severinghaus et al. (2003) (46 samples, pooled standard deviation of 0.013 ‰).

2.1.2 δ^{18}O water isotope data

We use the δ^{18}O bag data (one data point corresponds to an average over 55 cm) from the NEEM ice core measured at the Centre for Ice and Climate (CIC), University of Copenhagen, with an analytical accuracy of 0.07 ‰. For the NGRIP and GRIP ice cores, we use the bag data previously measured at CIC, with the same precision (NGRIP members, 2004; Johnsen et al., 1992). The GISP2 δ^{18}O data (Grootes and Stuiver, 1997, 20 cm resolution) are associated with a precision of 0.05 to 0.1 ‰.

2.1.3   Timescale

NEEM, NGRIP, GISP2 and GRIP ice cores are all dated according to the Greenland Ice Core Chronology 2005, GICC05 (Vinther et al., 2006; Rasmussen et al., 2006; Andersen et al., 2006; Svensson et al., 2008). This timescale has been produced based on annual layer counting of several parameters measured continuously on the NGRIP, GRIP and Dye3 ice cores and featuring a clear annual cycle, back to 60 ka b2k. The Maximum Counting Error (MCE), which can be regarded as a 2σ error estimate (Rasmussen et al., 2006) is 1439 a at 38 ka b2k. To transfer this timescale to the NEEM ice core, match points between peaks of electrical conductivity measurements and dielectrical properties, measured continuously on the ice cores, have been used. The obtained timescale for NEEM is called GICC05-NEEM-1 (S. O. Rasmussen, personal communication, 2010). The GISP2 core is matched to NGRIP using the same method as Rasmussen et al. (2008), with match points from I. Seierstad (personal communication, 2012). Using these match points, we scale the Meese et al. (1997) GISP2 timescale, based on annual layer counting, to the GICC05 timescale, in order to keep the information from the annual layer count while producing an age scale consistent with GICC05. The GICC05 age scale gives the age of the ice at each depth, and thus the annual layer thickness at each depth, but not the accumulation rate. This age scale is independent from estimation of thinning and past accumulation rate.

2.1.4   Accumulation rate

Accumulation rate histories for NEEM, NGRIP and GRIP are obtained using a Dansgaard–Johnsen (DJ) ice flow model (Dansgaard and Johnsen, 1969). The ice flow parameters of the model are tuned to obtain the best match between modeled and observed depth-age horizons in the ice cores. The thinning function calculated from the DJ model is then used to correct the observed annual layer thicknesses in the core for the effect of ice flow induced thinning, thereby producing an accumulation rate history. The NEEM version of the DJ model (Buchardt, 2009) is tuned in order to match the GICC05 timescale. For NGRIP, the accumulation rate was first calculated using the ss09sea06bm age

scale (Johnsen et al., 2001; Grinsted and Dahl-Jensen, 2002; NGRIP members, 2004). We recalculated that accumulation according to the more accurate GICC05 timescale. We did the same for the GRIP ss09sea-accumulation rate from Johnsen et al. (2001). Note that the ss09sea, ss09sea06bm and the GICC05 timescales agree within the GICC05 uncertainty between 28 and 60 ka b2k. For GISP2, the accumulation rate was first estimated with a 1 m resolution based on the coupled heat and ice flow model from Cuffey and Clow (1997), with the layer counted timescale from Alley et al. (1993), Meese et al. (1994) and Bender et al. (1994b). This timescale has known issues in the vicinity of DO 8 (Orsi et al., 2013; Svensson et al., 2006), which causes the accumulation history derived from it to be also wrong. Orsi et al. (2013) used the layer thickness from the GICC05 timescale to recalculate the accumulation history. Cuffey and Clow (1997) suggested 3 accumulation scenarios and Orsi et al. (2013) use the "200 km margin retreat" scenario adapted to the GICC05 timescale, compatible with the firn thickness and Δage derived from δ^{15}N data. This accumulation scenario has also been proved to best reproduce ice sheet thickness variations (Vinther et al., 2009).

2.1.5   Ice-gas Δdepth data

Figure 2 presents the NEEM δ^{15}N profile over the sequence DO 8–10. The peaks of δ^{15}N at 1769.4, 1787.5, and 1801.0 m are the result of the maximum temperature gradient in the firn corresponding to the abrupt temperature increases of DO 8, 9 and 10. We assume that δ^{15}N peaks and δ^{18}O-ice peaks are synchronous (see Sect. A2) and thus relate the maximum firn temperature gradient to the peaks in δ^{18}O-ice at 1758.1, 1776.8, and 1790.5 m. The depth differences between the temperature increases recorded in the gas and ice phases, named Δdepth, can thus directly be inferred as 11.3, 10.7, and 10.5 m over DO 8, 9, and 10, respectively (Fig. 2, Table 2, points 1, 5, and 7, respectively). We propose another match point between weaker peaks of δ^{15}N and δ^{18}O, see match point 3 in Table 2 and Fig. A3.

δ^{15}N also increases with accumulation increase, which deepens the firn (see Sect. 2.2), and we believe that this effect explains the beginning of δ^{15}N increase at the onset of each DO event. Several abrupt transitions (Bølling-Allerød and DO 8) have been investigated at high resolution (Steffensen et al., 2008; Thomas et al., 2008), also showing that the accumulation increases before the δ^{18}O shifts with a time lead up to decades and ends after the completion of the δ^{18}O increase. We observe the same feature for DO 8, 9, and 10 on the NEEM core. We thus match the onset of the δ^{15}N increase at the beginning of DO events to the onset of accumulation increase, which occurs before the δ^{18}O increase (Table 2 and Fig. A3, match points 2, 6, 8). Finally, match point 4 is a step in accumulation that we relate to the same step seen in δ^{15}N variations.
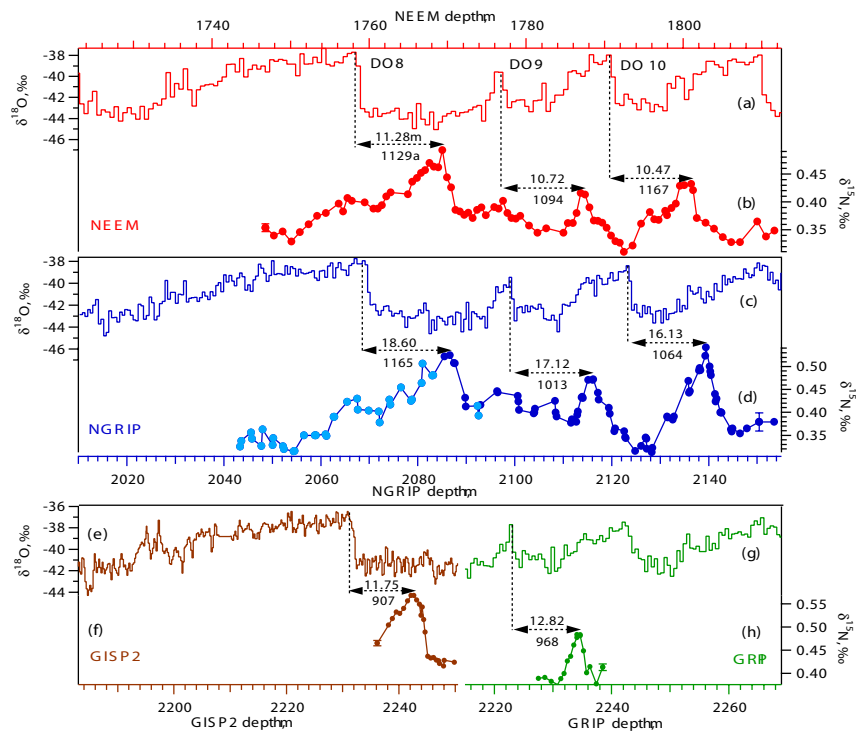
Fig. 2. Water and nitrogen stable isotope data (‰) for NEEM, NGRIP, GISP2 and GRIP. For each δ^{15}N data series the associated uncertainty ($\pm 1\sigma$) is shown. NEEM: **(a)** δ^{18}O bag data (measured along 55 cm samples) measured at CIC, this study; **(b)** δ^{15}N data measured at LSCE, this study. NGRIP: **(c)** δ^{18}O bag data, NGRIP members (2004); **(d)** δ^{15}N data measured at the University of Bern. Dark blue: data points from Huber et al. (2006). Light blue: this study. GISP2: **(e)** δ^{18}O bag data, Grootes and Stuiver (1997); **(f)** δ^{15}N data, Orsi et al. (2013). GRIP: **(g)** δ^{18}O 55 cm bag data, Johnsen et al. (1992); **(h)** δ^{15}N data measured at LSCE, this study.

Table 2. Correspondence between δ^{15}N and δ^{18}O or accumulation for the NEEM and NGRIP cores (see also ig. A3 and D1). δ^{18}O data are averaged over 55 cm (bag data) and we use here the depth at the middle of the 55 cm interval. The age is given according to the GICC05 timescale. The Δdepth (Δage) is obtained by calculating the difference between ice and gas depth (age). The Δage uncertainty is given by the difference between the MCE at the ice depth and the MCE at the gas depth.

Match point	depth (m) for:		Δdepth	age (a b2k) for:		Δage	MCE
	ice	gas		ice	gas		
NEEM							
1, DO 8 δ^{18}O peak	1758.08	1769.35	11.28	38 161	39 290	1129	67
2, DO 8 onset of acc. increase	1759.73	1771.00	11.28	38 274	39 472	1198	79
3, δ^{18}O minor peak	1766.33	1777.05	10.72	38 961	40 119	1158	90
4, acc. step	1775.13	1785.93	10.80	39 953	41 055	1102	51
5, DO 9 δ^{18}O peak	1776.76	1787.50	10.72	40 096	41 190	1094	48
6, DO 9 onset of acc. increase	1778.43	1788.60	10.17	40 254	41 273	1019	43
7, DO 10 δ^{18}O peak	1790.53	1801.00	10.47	41 411	42 559	1167	68
8, DO 10 onset of acc. increase	1791.63	1801.72	10.90	41 499	42 648	1149	69
NGRIP							
1, δ^{18}O minor peak	2028.13	2045.57	17.44	36 657	37 401	744	24
2, DO 8 δ^{18}O peak	2068.00	2086.60	18.60	38 152	39 317	1165	69
3, DO 9 δ^{18}O peak	2099.08	2116.19	17.11	40 131	41 145	1013	46
4, DO 10 δ^{18}O peak	2123.28	2139.41	16.13	41 429	42 493	1064	64

4.2. Spatial gradients of temperature, accumulation and δ^{18}O-ice in Greenland over a series
of Dansgaard - Oeschger events
101

At NGRIP, DO 8, 9 and 10 are seen at 2086.6, 2116.2, and 2139.4 m in the gas phase and at 2068.0, 2099.1, and 2123.3 m in the δ^{18}O from the ice phase (Fig. 2, Table 2 and Fig. D1, match points 2, 3, 4, respectively). For DO 8, δ^{18}O shows a double peak and we use the middle depth for this match point. We propose another match point at the end of DO 8 between weaker peaks of δ^{15}N and δ^{18}O (match point 1). All these Δdepth match points will be used in Sect. 3.1, combined with firn modeling, to reconstruct past surface temperature and accumulation.

2.2 Model description

To reconstruct a surface temperature scenario from the δ^{15}N profiles, we use a classical approach consisting of fitting the output of a firnification and heat diffusion model with the δ^{15}N records (Schwander et al., 1997; Lang et al., 1999; Huber et al., 2006; Goujon et al., 2003; Landais et al., 2004a; Kobashi et al., 2011; Orsi et al., 2013). We use here the semi-empirical firnification model with heat diffusion by Goujon et al. (2003). Adapted to each ice core (see method in Appendix A), this model calculates for each ice age and hence for each corresponding depth level the initial firn depth (defined here as the depth where diffusion of gases stops i.e., lock-in-depth, LID), the age difference between ice and gas at the LID (Δage), and the temperature gradient between the bottom and the top of the firn. It is then possible to calculate the δ^{15}N as the sum of two effects:

– gravitational effect (Craig et al., 1988; Schwander, 1989): the heavy isotopes preferentially migrate towards the bottom of the firn according to the barometric equation:

$$\delta^{15}N_{grav} = \exp\left(\frac{\Delta m g z}{R T_{mean}}\right) - 1 \qquad (1)$$

with Δm being the mass difference between the light and heavy isotope, g the acceleration constant, z the firn depth, R the ideal gas constant, and T_{mean} the mean firn temperature. An increase in accumulation rate increases the firn column depth and therefore increases $\delta^{15}N_{grav}$; on the other hand, a high temperature accelerates the densification processes and shallows the LID.

– thermal effect (Severinghaus et al., 1998): the cold part of the firn is enriched in heavy isotopes according to

$$\Delta\delta^{15}N_{therm} = \left(\frac{T_t}{T_b}\right)^{\alpha_T} - 1 \cong \Omega \cdot \Delta T \qquad (2)$$

with T_t and T_b being the temperatures of the top and bottom parcel, respectively, α_T the thermal diffusion constant, Ω the thermal diffusion sensitivity (Grachev and Severinghaus, 2003), and ΔT the temperature difference between top and bottom of the firn. A transient temperature increase after a stable cold period will create a transient peak in $\delta^{15}N_{therm}$.

The model needs input temperature, accumulation and dating scenarios with a depth-age correspondence. In the standard version of the Goujon model, the temperature scenario is based on a tuned variable relationship between water isotopes and surface firn temperature, with

$$T = \frac{1}{\alpha}(\delta^{18}O + \beta) \qquad (3)$$

where α and β can be variable over time. The reconstructed temperature has thus the shape of the water isotope profile but the temperature change amplitudes are constrained by tuning α and β in order for the modeled δ^{15}N to match the measured δ^{15}N. Several earlier studies have shown that the temporal values of α are lower than the present-day spatial slope for Greenland of 0.80 ‰ °C^{-1} (Sjolte et al., 2011; Masson-Delmotte et al., 2011), which can be used as a maximum value.

3 Results and discussion

3.1 Temperature and accumulation reconstruction

To reconstruct continuous temperature and accumulation scenarios for DO 8 to 10, we run the firnification model from 60 to 30 ka b2k with a time step of one year and try to reproduce the δ^{15}N data as well as the Δdepth match points. Figure 3 shows the comparison between the measured and modeled (scenarios d1 to d3) δ^{15}N over DO 8–10 at NEEM. First we try to reproduce the δ^{15}N data by varying the temperature alone: the measured δ^{15}N amplitudes of DO 8, 9, and 10 can be reproduced with temperature increases at the GS–GI transitions of 8.8, 6.0, and 7.7 °C, respectively (Fig. 3, reconstruction d1). This scenario nicely reproduces both the mean δ^{15}N level and the amplitude of the δ^{15}N peaks. However, the modeled δ^{15}N peaks are systematically at a too shallow depth. To model a larger Δdepth, we systematically lower the temperature scenario used in reconstruction d1 (Fig. 3) by 3.5 °C. This systematically deepens the LID, increasing both Δdepth and δ^{15}N (Fig. 3, reconstruction d2). The modeled Δdepth is therefore closer to the measured one and the amplitude of the δ^{15}N peaks is still correct but the mean δ^{15}N level is systematically too high. From this experiment, we conclude that it is not possible to match both δ^{15}N data and Δdepth by tuning only the temperature scenario.

Several explanations can be proposed to explain the underestimation of the Δdepth by the model:

– the tuning of the Goujon model (LID density, vertical velocity field) is not appropriate for the NEEM site and predicts a too shallow LID. However, we show in Appendix A3 that different tuning strategies have no impact on the modeled LID;

– the Goujon model is not appropriate for the NEEM site. However, this model is valid for present-day at
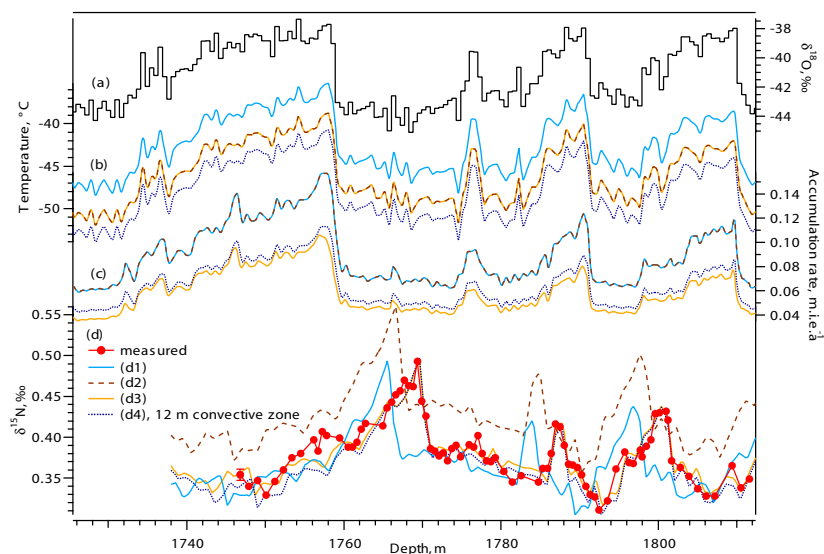
M. Guillevic et al.: Past spatial gradients of temperature, accumulation and δ^{18}O in Greenland   1035

Fig. 3. Measured and modeled δ^{15}N for NEEM on DO 8 to 10, plotted on a depth scale. **(a)** δ^{18}O ice ‰, this study. **(b)** Temperature scenarios and **(c)** accumulation scenarios used to produce the δ^{15}N reconstructions in **(d)** plotted on the same color. Red dots: measured δ^{15}N data. **(d1)** to **(d4)** Modeled δ^{15}N. **(d1)** to **(d3)** using a 2 m convective zone. **(d4)** using a 12 m convective zone.

NEEM (see Appendix A1) and has also been validated for a large range of temperature and accumulation rates covering the expected glacial climatic conditions at NEEM (Arnaud et al., 2000; Goujon et al., 2003; Landais et al., 2006). Moreover, using other firnification models (the Schwander model on NGRIP Huber et al. (2006) and a Herron Langway model on NEEM, see Appendix C) with similar forcings in temperature and accumulation rate does not reproduce the measured ∆depth either;

– fundamental parameters are missing in the description of current firnification models. A recent study has shown that the firn density profile could be strongly influenced by impurities, the density increasing with calcium and dust content in the ice (Hörhold et al., 2012). Calcium and dust in Greenland ice cores are both originating from low-latitude Asian deserts and their content is influenced by source strength and transport conditions (Svensson et al., 2000; Ruth et al., 2007). They covary in Greenland ice cores from seasonal to millennial timescales (Hörhold et al., 2012; Thomas et al., 2008; Steffensen et al., 2008). During cold periods (glacials, stadials), calcium and dust content in Greenland ice cores are strongly enhanced compared to warm periods (interglacials, interstadials) (Mayewski et al., 1997; Ruth et al., 2007; Wolff et al., 2009). Taking this effect into account, the modeled LID during the glacial period should be shallower than the one calculated with the current version of the firnification model calibrated on present-day observations. This would further en-

hance the disagreement between modeled and observed ∆depth;

– the glacial firn layer at NEEM could be subject to variations in the extent of the convective zone due to katabatic winds and/or low accumulation rate. Considering present-day Antarctic sites as an analogue for the past NEEM firn, a convective zone of 0–3 m (like Dome C, Landais et al., 2005) to 12 m (like Vostok, Bender et al., 1994a) can be considered (Sect. A4 and Fig. A2), event though we suggest that the range 0–3 m is most likely (see discussion in Sect. A4). A convective zone has no direct impact on the ∆depth but it lowers the δ^{15}N level. Accounting for such convective zone in the firn model requires lower temperatures, which increases the ∆depth.

– the forcing in accumulation of the firnification model is not correct. To match the observed ∆depth with a correctly modeled δ^{15}N, we need to significantly decrease the accumulation rate compared to the original DJ estimation.

With a 2 m convective zone, by adjusting changes in accumulation rate and the δ^{18}O–temperature relationship (Fig. 3c, b), we manage to reproduce the δ^{15}N profile as presented in Fig. 3, scenario d3. This best δ^{15}N fit corresponds to a mean accumulation reduction of 34 % (30 to 40 %, depending on the DO event). Because the depth-age correspondence is imposed by the layer counting, this accumulation rate reduction by 34 % directly implies the same 34 % decrease in the ice thinning. If we use this accumulation

scenario as input for the DJ model, with keeping the original DJ accumulation scenario in the remaining ice core sections, the output timescale is just at the limit of the age uncertainty estimated by annual layer counting. With a 12 m convective zone (Fig. 3, d4), the δ^{15}N profile can be reproduced using the temperature scenario d3 systematically lowered by 2 °C and the DJ accumulation rate reduced by 28 %.

For NGRIP, the Goujon model can reproduce the measured δ^{15}N profile with the correct Δdepth when using a convective zone of 2 m and the DJ accumulation rate reduced by 26 % over the whole section (Fig. D1). Alternatively, we can use a 12 m convective zone with a 19 % reduction in accumulation; this impacts the mean temperature level, which has to be lowered by 2 °C (not shown). For GRIP, using a 2 m convective zone, we have to decrease the DJ accumulation rate by 40 %. Note that this reduced GRIP DJ accumulation rate is then very close to the GISP2 accumulation rate for the same period (Fig. 4). We further discuss past changes in accumulation rate in Sect. 3.4.

Based on these calculations, we conclude that reducing the DJ accumulation scenario is necessary to match both δ^{15}N data and Δdepth with a firnification model over the sequence of DO 8–10, even when accounting for uncertainties linked with the presence of a convective zone. This reduction has no impact on the reconstructed rapid temperature variations but requires a lower mean temperature level (Fig. 3, d3, d4). Our 19 to 26 % accumulation reduction for NGRIP supports the findings by Huber et al. (2006) where the original accumulation scenario was reduced by 20 %, without convective zone.

3.2 Uncertainties quantification

Following the same method for the four cores, we estimate the uncertainty (1σ) associated with the temperature increases ΔT at the onset of the DO events to be ~ 0.6 °C for NEEM, GRIP, and GISP2, and ~ 1.5 °C for NGRIP. For the δ^{18}O increases, $\Delta\delta^{18}$O, the uncertainty is estimated to be ~ 0.05 ‰ for NEEM, 0.04 ‰ for NGRIP, 0.06 ‰ for GRIP and 0.02 ‰ for GISP2. The thermal sensitivity of δ^{18}O, defined as $\alpha = \Delta\delta^{18}O/\Delta$T, is associated with an uncertainty of 0.05, 0.08, 0.04 and 0.02 ‰ °C^{-1} for NEEM, NGRIP, GRIP and GISP2, respectively. The detailed calculations are given in Appendix B. Note that for DO 8, 9 and 10, the GRIP and GISP2 ice cores depict δ^{18}O increases significantly different from each other even though they are geographically very close to each other. Grootes et al. (1993) calculated an 89 % common variance between these two cores for the interval 9–104 ka b2k and suggested local variability to explain the remaining differences.

3.3 Regional δ^{18}O and temperature patterns

Our best guess temperature and accumulation reconstructions for the four Greenland sites are displayed in Fig. 4 as a function of the GICC05 timescale. Our temperature re-

construction for NGRIP is in good agreement with the one from Huber et al. (2006) where a different firnification model was used (see Fig. D1 in Appendix D). For the GISP2 core, the temperature reconstruction for DO 8 follows the same approach (Orsi et al., 2013): temperature and accumulation scenarios are used as inputs to the Goujon firnification model and constrained using δ^{15}N and δ^{40}Ar measurements. Four different accumulation scenarios were used, with a GS to GI increase of 2, 2.5, 3, and 3.5 times. The difference in temperature increase between these four scenarios is very small ($1\sigma = 0.07$ °C). We report in Table 3 the mean temperature increase for these four scenarios.

For a systematic comparison between the different ice core records, we have used a ramp-fitting approach (Mudelsee, 2000) to quantify the start, end and amplitude of DO increases in δ^{18}O, temperature and accumulation: each parameter is assumed to change linearly between GS and GI states. The magnitude of DO increases are then estimated as the difference between the mean GS and GI values (Table 3). The time periods used on each DO event for this statistical analysis are shown in Figs. A3 and D1.

3.3.1 Temperature sensitivity of δ^{18}O for present-day and glacial climate

For all four sites, the temporal sensitivity of water isotopes to temperature varies from 0.34 to 0.63 ‰ °C^{-1}, being therefore systematically smaller than the present-day spatial gradient of 0.80 ‰ °C^{-1} (Table 3 and Sjolte et al., 2011). This reduction can be explained by precipitation intermittency/seasonality effects (Steig et al., 1994; Jouzel et al., 1997): under glacial boundary conditions, atmospheric models depict a shift of Greenland precipitation towards summer; this has been linked to a southward shift of the winter storm tracks due to the position of the Laurentide ice sheet (Werner et al., 2000, 2001; Krinner et al., 1997; Fawcett et al., 1997; Kageyama and Valdes, 2000). During cold periods, summer snow may represent most of the annual accumulation, inducing a bias of the isotopic thermometer towards summer temperature and lowering α compared to the spatial gradient (associated with a classical Rayleigh distillation). So far, seasonality changes have not been systematically investigated in climate model simulations aiming to represent DO events such as driven by freshwater hosing. In reduced sea-ice experiments by Li et al. (2005) using an atmospheric general circulation model, a 7 °C temperature increase and a doubling of the accumulation rate are simulated in GI compared to GS, accompanied with a relatively higher winter snow contribution that could partly explain the low α that we observe here.

Another argument in favor of such seasonality change comes from observations in the NGRIP ice core: records of different ion and dust show synchronous annual peaks during stadials for these species, whereas peaks occur at different periods of the year during interstadials, as for present-day
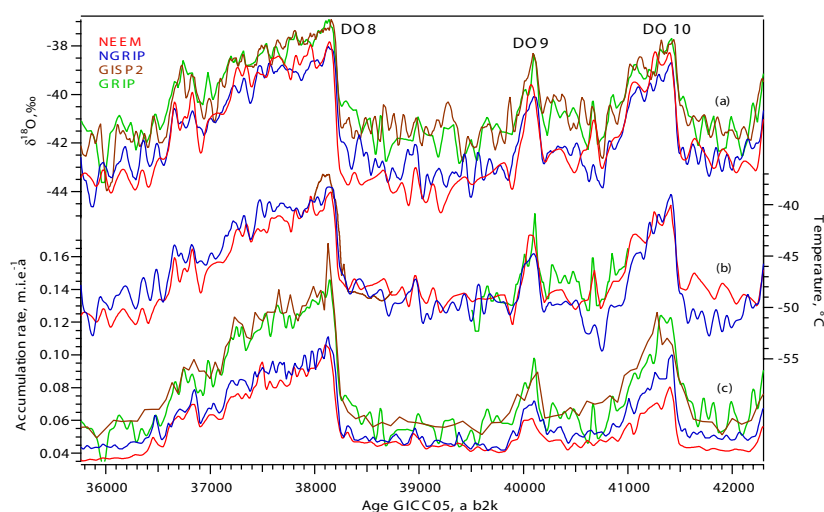
Fig. 4. NEEM (red), NGRIP (blue), GISP2 (brown) and GRIP (green) comparison. **(a)** Water isotopes, 50 yr running average, ‰ vs. VS-MOW. NEEM: this study. NGRIP: NGRIP members (2004). GISP2: Grootes et al. (1993). GRIP: Johnsen et al. (1992). **(b)** Temperature reconstruction, °C. **(c)** Accumulation rate reconstruction, m.i.e.a^{-1}.

(Andersen et al., 2006). A first explanation is that during GS the accumulation rate is so low that ion/dust income are dominated by dry deposition all around the year, producing an ion/dust rich layer at the snow surface. This layer is then separated from the one from the following year by the incoming summer snow, resulting in apparent annual synchronous peaks of all species. This supports the hypothesis of a dramatic decrease of winter precipitation during GS at NGRIP. Andersen et al. (2006) also suggested that changes in transport paths may account for the observed pattern. Indeed, the presence of the Laurentide ice sheet (LIS) has been suggested to allow a split jet stream (Andersen et al., 2006). A shift of the path from south to north of the LIS during GI–GS may explain their data. The GS–GI impurities patterns are therefore again in favor of different atmospheric circulation patterns between GS and GI. No such high resolution measurements are yet available for GRIP, GISP2 and NEEM.

In the mean time, studies of the second order parameter deuterium excess suggest that the main source of water vapor is shifted southwards during GS (Johnsen et al., 1989; Masson-Delmotte et al., 2005; Jouzel et al., 2007; Ruth et al., 2003). The enhancement of the source–site temperature gradient enhances isotopic distillation and produces precipitation with lower δ^{18}O levels during cold periods, increasing α. Contradicting earlier assumptions (Boyle, 1997), conceptual distillation models constrained by GRIP deuterium excess data suggest that this effect is most probably secondary (Masson-Delmotte et al., 2005).

3.3.2   Regional differences between the ice cores sites

The magnitude of GS–GI temperature rise is significantly increasing from NW Greenland to Summit for DO 8 and

10: $+8.8 \pm 0.6$ °C at NEEM, $+10.4 \pm 1.5$ °C at NGRIP, and $+11.1 \pm 0.6$ °C at GISP2 for DO 8; for DO 10, ΔT is largest at NGRIP and smallest at NEEM. In the mean time, the amplitude of $\Delta\delta^{18}$O is decreasing from NW to central Greenland: for DO 8, $\Delta\delta^{18}$O is 5.6 ‰ for NEEM, 4.7 ‰ for NGRIP, 4.2 ‰ for GISP2, and 4.6 ‰ for GRIP (Table 3 and Appendix B for uncertainties estimation). As a result, the α coefficient decreases from NEEM to GISP2 for DO 8 and 10. For DO 9, no significant regional difference can be detected in reconstructed temperatures nor in $\Delta\delta^{18}$O. For this small event, the signal is small compared to the data uncertainties, therefore any spatial gradient becomes difficult to verify. For DO 8 and 10, the larger temporal values of α encountered at NEEM are probably explained by smaller precipitation seasonality effects for this site, which is already biased towards summer at present-day by a factor of 2 to 3.5 (Steen-Larsen et al., 2011; Sjolte et al., 2011; Persson et al., 2011). In other words, because warm periods already undersample the winter snow at NEEM, a winter snow reduction during cold periods at NEEM cannot have an effect as strong as for the NGRIP and the GISP2/GRIP sites, where precipitation are indeed distributed year-round for present-day. We note that α decreases with site elevation (Tables 1 and 3). Interestingly, for DO 8 and 10 the spatial pattern of DO α distribution appears consistent with the spatial patterns of present-day interannual slopes (for summer or winter months), which are also higher in the NW sector (Sjolte et al., 2011). We also note that our spatial patterns of temperature and accumulation increases for DO 8 and 10 are consistent with the pattern obtained by Li et al. (2010). In this study, a 5 °C temperature warming is simulated at

4.2. Spatial gradients of temperature, accumulation and δ^{18}O-ice in Greenland over a series of Dansgaard - Oeschger events

105

Table 3. DO increase (GI-GS) in δ^{18}O, temperature and accumulation (mm.i.e.a^{-1}) for NEEM, NGRIP, GRIP and GISP2. For $\Delta\delta^{18}$O, ΔT and α, for each given DO event, two numbers written with different colors are significantly different from each other. A number in italic is not significantly different from all other numbers. See text for details and Sect. B for uncertainties quantification.

	DO 8				DO 9				DO 10			
	NEEM	NGRIP	GISP2	GRIP	NEEM	NGRIP	GISP2	GRIP	NEEM	NGRIP	GISP2	GRIP
Stadial δ^{18}O	−43.52	−42.74	−41.32	−41.49	−42.66	−42.62	−40.68	−41.03	−42.65	−42.74	−41.33	−41.43
$\Delta\delta^{18}$O	5.57	4.68	4.21	4.57	3.09	2.59	2.37	3.05	4.32	3.97	3.45	3.66
ΔT	8.85	10.42	11.09		6.02	5.50		6.21	7.72	11.56		
α	0.63	0.45	0.38		0.51	0.47		0.49	0.56	0.34		
Stadial acc.	47	49	60	59	46	52	64	61	43	51	58	56
Δacc	58	58	82	81	14	18	23	37	36	45	56	55

Summit with an amplitude decreasing from south to north in response to sea-ice reduction in the Nordic seas.

In addition to differences in seasonality/precipitation intermittency, differences in moisture transportation paths may also modulate the spatial gradients of α over DO events. Although this effect cannot fully explain the fact that the slopes are systematically lower than at present, it could contribute to the difference between the slopes at NEEM, NGRIP and GISP2 (see Sect. 3.3.1). Several studies conducted with isotopic atmospheric general circulation models equipped with water tagging have indeed revealed different isotopic depletions related to the fraction of moisture transported from nearby or more distant moisture sources under glacial conditions (Werner et al., 2001; Charles et al., 2001). In particular, changes in storm tracks were simulated in response to the topographic effect of the Laurentide ice sheet, resulting in the advection of very depleted Pacific moisture towards North Greenland. Indeed, systematic offsets between water stable isotope records of GRIP and NGRIP have been documented during the last glacial period (NGRIP members, 2004). So far, we cannot rule out that changes in moisture origin may cause differences in δ^{18}O variations between NEEM, NGRIP, and GISP2. Assessing the importance of source effects will require the combination of deuterium excess and ^{17}O excess data with regional isotopic modeling and remains beyond the scope of this study.

3.4 Past surface accumulation rate reconstruction and glaciological implications

For NEEM, NGRIP and GRIP (reduced DJ-accumulation) as well as GISP2 (original accumulation from Cuffey and Clow, 1997), accumulation variations follow annual layer thickness variations: for each ice core, the smallest accumulation increase is seen for DO 9 and the largest one where the temperature increase is largest (DO 8 for NEEM, DO 8 and 10 for NGRIP). Accumulation shifts therefore scale with temperature variations (Table 3). This is in agreement with the thermodynamic approximation considering the atmospheric vapor content, and thus the amount of precipitation, as an exponential function of the atmospheric temperature. Comparing the four sites, NEEM and NGRIP show similar accumulation rates, whereas the accumulation is clearly higher at GISP2 and GRIP over the whole time period.

One important finding of our study is the requirement for a lower accumulation rate at NEEM, NGRIP and GRIP over DO 8–10, compared to the initial accumulation rate given by the DJ ice flow model. Taking into account the presence of a possible convective zone at NEEM, our reconstruction based on firn modeling needs to reduce the original DJ accumulation rate by 28 % (12 m convective zone) to 35 % (2 m convective zone).

Several lines of evidence point to an overestimation of the glacial accumulation rates given by the DJ model. First, in their temperature reconstruction for DO 9 to 17, Huber et al. (2006), using the firnification model of Schwander et al. (1997), also had to decrease the accumulation rate calculated by the DJ model by 20 % everywhere to fit the observed Δdepth. We found similar results applying the Goujon model to the NGRIP ice core over DO 8–10. For DO 9 on GRIP, we need to reduce the DJ-accumulation rate by 40 %; the resulting accumulation rate is then very similar to that at GISP2 (Fig. 4). For GISP2 on DO 8, Orsi et al. (2013) used the Goujon model and an accumulation rate of 0.059 m.i.e.a^{-1} for the GS preceding DO 8, as calculated by the ice flow model from Cuffey and Clow (1997) adapted to the GICC05 timescale.

It is very unlikely that GISP2 and GRIP have significantly different accumulation histories. Indeed, at present GRIP is located 28 km east of GISP2 and the ice divide is not between them, therefore no foehn effect is expected (Buchardt et al., 2012). A small (8 %) accumulation difference is reported for the last 200 a (Meese et al., 1994; Johnsen et al., 1992). During the glacial period, the expansion of the ice sheet margins is expected to produce a flatter topography in central Greenland, further reducing a possible foehn effect. Therefore, large differences in past accumulation rates between GISP2 and GRIP are not climatically plausible; the observed discrepancy must be an artifact of the different methodologies deployed to estimate accumulation rates. Note that during the glacial inception, Landais et al. (2004a, 2005) were able to reproduce the measured δ^{15}N at NGRIP with the

original timescale (ss09sea06bm, NGRIP members, 2004) and accumulation values from the DJ model. In the climatic context of the glacial inception, marked by higher temperatures compared to DO 8–10, firnification model and DJ ice flow models seem to agree.

Altogether, these results suggest that the DJ model is consistent with firn constraints during interglacials and inceptions, but a mismatch is obvious during DO 8–10, likely representative of glacial conditions. We now summarize three potential causes that could produce an overestimation of glacial accumulation in the DJ model (for a detailed presentation of this model we refer to Dansgaard and Johnsen, 1969).

a. Wrong age scale produced by the DJ model: the DJ model could underestimate the duration between two given depths in the ice core and thus overestimate the accumulation rate. However, for the NEEM ice core from present until 60 ka b2k, the DJ model is tuned in order to produce an age scale in agreement with the GICC05 timescale (Buchardt, 2009). For the NGRIP core, the ss09sea06bm timescale produced by the DJ model together with the accumulation rate has been validated back to 60 ka b2k by comparison to the GICC05 time sale (Svensson et al., 2008). The cumulated uncertainty associated with the GICC05 timescale at 60 ka b2k is 2600 a (Svensson et al., 2008), which could explain 5 % maximum of accumulation reduction, assuming a systematic undercounting of the annual layers. For the glacial inception at NGRIP, Svensson et al. (2011) have counted annual layers on particular sections during DO 25 and the glacial inception and confirm the durations proposed by the ss09sea06bm timescale. We therefore rule out a possible wrong timescale as the main cause for the disagreement on these particular periods.

b. The changing shape of the Greenland ice sheet over time (thickness and margin location) may affect the reconstructed accumulation rate, as suggested by model studies from Cutler et al. (1995) and Cuffey and Clow (1997). The DJ model assumes a constant ice sheet thickness over time for NGRIP (Grinsted and Dahl-Jensen, 2002) and a variable one for NEEM (Buchardt, 2009; Vinther et al., 2009). Concerning the DJ model applied to the NGRIP site, runs with constant ice sheet thickness histories or the one from Vinther et al. (2009) were compared (Buchardt, 2009, Chap. 5, Fig. 5.22) and agree well for MIS3. Using a constant or variable ice sheet thickness in the DJ model should thus not affect much the reconstructed accumulation rate. The DJ model has one spatial dimension and no effect of margin location changes can be assessed. It would be interesting to incorporate a parametrization that could account for this later effect and perform sensitivity tests.

c. The DJ model assumes that the vertical velocity field (v_z) changes only with surface accumulation rate varia-

tions, all the other parameters being kept constant (basal sliding, basal melt rate, kink height). The best guess input accumulation rate is a tuned exponential function of δ^{18}O (e.g., Johnsen et al., 1995). Tests with a simple DJ model adapted to the GRIP site show that reducing the input surface accumulation rate also reduces the annual layer thicknesses and the total vertical velocity v_z, integrated from top to bedrock. In the output timescale the modeled ice age at a certain depth is older. To still get a correct timescale in agreement with GICC05, we would need to deepen the kink height. The same effect would apply to all other Greenland sites. The shape of v_z and therefore the kink height is also expected to vary with the ice sheet temperature profile and dust content through changes in ice viscosity (for more details we refer to Cuffey and Paterson, 2010, Chap. 9). During the glacial period, the connection between the Greenland ice sheet and the Ellesmere Island ice could also modify the Greenland ice flow. This effect is expected to affect more the ice flow at NEEM, which is the closest site to Ellesmere Island, than at NGRIP, GRIP and GISP2. In 1969, when creating the DJ model to date the Camp Century ice core, the authors assumed a constant kink height over time due to a lack of information (Dansgaard and Johnsen, 1969). Using a variable kink height will also modify th best guess relationship calculated between input accumulation rate and δ^{18}O.

To conclude, there are huge uncertainties on past accumulation rate reconstructions. Comparing three different reconstructions for Summit (Cutler et al., 1995; Cuffey and Clow, 1997; Johnsen et al., 2001), we suggest that the glacial accumulation rate reconstructed by the DJ model has to be taken as a high boundary, the low boundary being at least 50 % lower. This may apply to NGRIP and NEEM. Our firn-model-based accumulation rates lie in this envelope. We suggest that both thickness and margin location changes should be taken into account in the DJ model. A better agreement between the Cutler et al. (1995) model, the Cuffey and Clow (1997) model and the DJ model may also be found by using a variable kink height in the DJ model.

4   Conclusions and perspectives

Air and water stable isotopes measurements from four Greenland deep ice cores (GISP2, GRIP, NGRIP and NEEM) have been investigated over a series of Dansgaard–Oeschger events (DO 8, 9 and 10), which are representative of glacial millennial scale variability. We have presented the first δ^{15}N data from the NEEM core and combined them with new and previously published δ^{15}N data from NGRIP, GRIP and GISP2. Combined with firn modeling, air isotope data allow us to quantify abrupt temperature increases for each ice core site. For DO 8, the reconstructed temperature increase is 8.8 °C for NEEM, 10.4 °C for NGRIP, and 11.1 °C for

GISP2. Our data show that for DO 8 and 10, the magnitude of GS–GI increase is up to 2 °C larger in central (GISP2) and North Greenland (NGRIP) than in NW Greenland (NEEM). The reconstructed accumulation increases follow the same spatial pattern. These observations are in agreement with a study of spatial Greenland response to reduced sea-ice extent in the Nordic seas (Li et al., 2010). no spatial gradient is detected for the small DO 9 event. The temporal δ^{18}O–temperature relationship varies between 0.3 and 0.6 ‰ °C^{-1} and is systematically larger at NEEM, possibly due to limited changes in precipitation seasonality compared to GISP2 or NGRIP. The relatively high isotope–temperature relationship for NEEM will have implications for climate reconstructions based on NEEM water isotopes data. Further paleotemperature investigations are needed to assess the stability of this relationship over glacial–interglacial variations. In particular, it would be interesting to compare the presented reconstruction with the temperature–water isotopes relationship over the different climatic context of MIS 5. A better understanding of the causes of the regional isotope and temperature gradients in Greenland requires further investigations of possible source effects (using deuterium excess and ^{17}O excess), and an improved characterization of atmospheric circulation patterns. We hope that our results will motivate high resolution simulations of DO type changes with climate models equipped with water stable isotopes, in order to test how models capture regional gradients in temperature, accumulation and isotopes, and to understand the causes of these gradients from sensitivity tests (e.g., associated with changes in ice sheet topography, SST patterns, sea ice extent).

The gas age−ice age difference between abrupt warming in water and air isotopes can only be matched with observations when assuming a 26 % (NGRIP) to 40 % (GRIP) lower accumulation rate than derived from the Dansgaard–Johnsen ice flow model. We question the validity of the DJ model to reconstruct past glacial accumulation rate and recommend on the time interval 42 to 36 ka b2k to use our reduced accumulation scenarios. We also suggest that the DJ ice flow model is too simple to reconstruct a correct accumulation rate all along the ice cores and propose to test the incorporation of variable ice sheet margins location and kink height in this model. Our results call for a systematic evaluation of Greenland temperature and accumulation variations during the last glacial–interglacial cycle, combining continuous δ^{15}N measurements with firnification modeling. Using a correct accumulation rate is of high importance to reconstruct accurate ice- and gas-age scales and to calculate fluxes based on concentrations of different species in the ice. Moreover, a better estimation of past surface accumulation rates at precise locations in Greenland would help to constrain past changes in ice flow with implications for ice sheet mass balance and dynamics.

Appendix A

The Goujon firnification model: method

The firnification model has only one space dimension and calculates the vertical velocity field along the vertical coordinate and the temperature profile across the entire ice sheet for each time step of one year. In the firn, it calculates the density profile from the surface to the close-off depth. The density profile and the accumulation history allow us to obtain the ice age at LID and, assuming gas age equal to zero at LID, the Δage. The temperature field from surface to bedrock is then used to reconstruct the density profile in the firn, the firn temperature gradient, and from there the δ^{15}N at LID. We follow Goujon et al. (2003) where the LID is defined as the depth where the ratio closed to total porosity reaches 0.13. The model is adapted to each ice core site in terms of vertical velocity field, basal melt rate, ice sheet thickness, elevation, surface temperature and accumulation scenarios (Table 1). We assume a convective zone of 2 m at the top of the firn.

A1 Validation of the Goujon firnification model for present day at NEEM

We use the present-day characteristics of the firn at NEEM to validate the Goujon firnification model. During the 2008 summer field season, a shallow core was drilled at the S2 site at NEEM. Firn air was sampled at different depths from the surface to 80 m depth in this borehole (for more details see Buizert et al., 2012). From these air samples, δ^{15}N was measured at LSCE (Fig. A1). The increasing δ^{15}N with depth reflects the gravitational fractionation. Given the vertical resolution in the data, we do not see a clear convective zone. Below 62 m depth, δ^{15}N is constant: the nondiffusive zone is reached. We thus have a LID of 62 m at NEEM for present-day according to these δ^{15}N data only. In Buizert et al. (2012), using measurements of different gases in the firn and several diffusion models, the S2 borehole is described as follows: a convective zone of 3 m, a diffusive zone of 59 m down to 63 m depth (LID), and a nondiffusive zone down to 78.8 m depth (total pore closure depth). Following this description and assuming no thermal effect, we calculated the corresponding gravitational fractionation affecting δ^{15}N (Fig. A1, blue line). Annual layer counting of the corresponding shallow core and matching with the GICC05 timescale gives an ice age at LID of 190.6 a b2k $\pm$1 a, and 252.5 a at the total pore closure depth. The age of CO_2 is calculated to be 9.6 a at LID and 69.6 a at the total pore closure depth, producing a Δage of 181 a and 183 a, respectively. The best estimate for the true Δage is estimated to be 182 +3/−9 a (Buizert et al., 2012). We observe that from the LID, the Δage becomes constant within uncertainties. Considering the diffusion coefficient to be 1 for CO_2 and using 1.275 for N_2 as in Buizert et al. (2012), the age of N_2 is 7.5 a at the LID, giving a Δage of 183 a.

M. Guillevic et al.: Past spatial gradients of temperature, accumulation and $\delta^{18}O$ in Greenland   **1041**

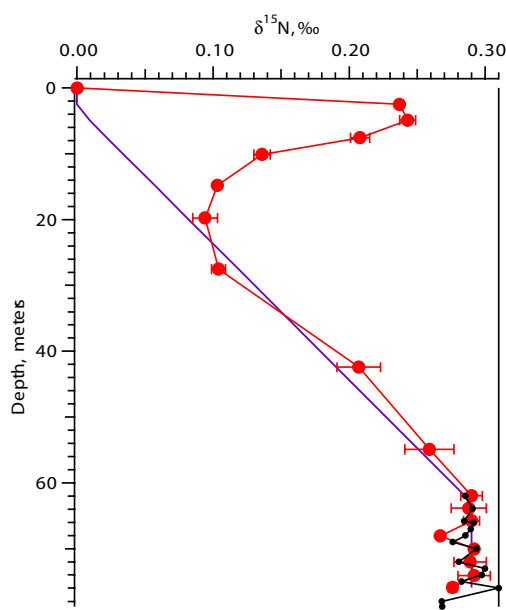**Fig. A1.** Present-day firn at NEEM. Red dots: $\delta^{15}N$ data measured at LSCE. Blue line: gravitational fractionation for $\delta^{15}N$, assuming a convective zone of 3 m and the LID at 63 m depth (Buizert et al., 2012). Black dots: modeled $\delta^{15}N$ with the Goujon firnification model.

We run the Goujon model using the NEEM07S3 shallow core age scale and $\delta^{18}O$ for the top 60 m (Steen-Larsen et al., 2011) and the NEEM main core below. The $\delta^{18}O$ record is used to reconstruct the past temperature variations using $\alpha = 0.8$ (Sjolte et al., 2011); we use $\beta = 9.8$ in order to obtain the measured average present-day temperature of $-29\,°C$ (Steen-Larsen et al., 2011). Using the density profile measured along the NEEM07S3 core and the corresponding age scale, the past accumulation history was reconstructed (Steen-Larsen et al., 2011) and used here as input for the firnification model. The firnification model estimates the LID at 61.4 m depth. Modeled $\delta^{15}N$ values agree well with the measured ones in this region (Fig. A1). At 63 m depth, the estimated ice age is 189 a (according to the NEEM07S3 core dating, which agrees very well with the S2 core dating). Ignoring the gas age at LID thus results in an overestimation of the $\triangle$age by less than 10 yr for present-day.

A2 Reconstruction of the past gas age scale

Simulations with the Goujon model show that at the onset of DO events 8, 9 and 10, the heat diffusion in the firn is slow enough so that the peaks of maximum temperature gradient in the firn are synchronous with the $\delta^{18}O$ peaks. We thus consider that the peaks of $\delta^{15}N$ occur at the same time as the $\delta^{18}O$ peaks. However, the Goujon model has no gas diffusion component and this has two consequences: (a) the

gas age at LID, due to the time for air to diffuse in the firn, is assumed to be zero; (b) any broadening of the initial $\delta^{15}N$ peak by gas diffusion in the firn is not taken into account. For present-day, the gas age at LID is 9.6 a for CO_2 (Buizert et al., 2012) and we calculate it to be 7.5 a for N_2. The Schwander model calculates a N_2 age up to 20 a at the LID over DO 8 to 10 for NGRIP (Huber et al., 2006). The Goujon model thus systematically overestimates the $\triangle$age by 10 to 20 yr in the glacial period, which is within the mean $\triangle$age uncertainty of 60 yr (Table 2). For the NGRIP core, our temperature reconstruction with the Goujon model (without gas diffusion) is in agreement with the temperature reconstruction from Huber et al. (2006) where the Schwander model (with gas diffusion) is used (Fig. D1). We thus consider that the lack of gas diffusion in the Goujon model has an impact that stays within the error estimate (Appendix Sect. B).

For DO 8 to 10 at NEEM, we present the measured and modeled $\delta^{15}N$ data plotted on an age scale in Fig. A3. The $\triangle$age calculated by the model (Fig. A3, subplot d) is used to synchronize the gas record to the ice record. We have also reported here the $\triangle$age tie-points from Table 2 and we can see that the modeled $\triangle$age reproduces these points, within the error bar.

A3 Sensitivity tests

A3.1 Vertical velocity field

In the firnification model, we used two different parameterizations for the vertical velocity field: the analytical solution from Lliboutry (1979), as in the original model from Goujon et al. (2003), and a Dansgaard–Johnsen type vertical velocity field (Dansgaard and Johnsen, 1969). In the later case, we used the same parametrization as used in the DJ model to calculate past accumulation rates (ice sheet thickness, kink height, fraction of basal sliding, basal melt rate) and then tried different kink heights between 1000 m and 1500 m above bedrock. All these tests produce the same modeled LID and, hence, the same modeled $\delta^{15}N$. The different parameterizations actually produce very similar vertical velocity fields in the firn. Because $\delta^{15}N$ is only sensitive to processes occurring in the firn, huge modification of the vertical velocity field deep in the ice (for example by modifying the kink height) has no impact here.

A3.2 Basal temperature

We also varied the basal temperature between $-2.99\,°C$ as measured at present in the borehole (Simon Sheldon, personal communication, 2012) and $-1.68\,°C$, which is the melting temperature as calculated in Ritz (1992) and can be considered as a maximum basal temperature. There is no difference in the modeled LID. Indeed, the relatively high accumulation rate even in the glacial period makes the burial of the snow layers quite fast. As a result, the firn temperature is

4.2. Spatial gradients of temperature, accumulation and δ^{18}O-ice in Greenland over a series of Dansgaard - Oeschger events

109

mostly influenced by the surface temperature but not by the bedrock temperature.

A4   Effect of a convective zone

The Goujon model is written in a way that there is neither heat diffusion nor densification of the firn in the convective zone. No densification of the top firn may be acceptable on the first 2 m but becomes unrealistic when increasing the convective zone. Alternatively, instead of a "true" convective zone, we can prescribe a nongravitational zone, where heat transfer in ice still occurs. This reduces the diffusive column height (DCH) used to calculate the gravitational enrichment of δ^{15}N but does not modify its thermal fractionation.

A convective zone deeper than 2 m during the glacial period at NEEM is possible, created by strong katabatic winds due to a steep ice sheet flank, like the 14 m convective zone at YM85 site in Antarctica (Fig. A2 and Kawamura et al., 2006). However, during the glacial period, the Greenland ice sheet may have been connected to Ellesmere Island and the lateral margins were extended compared to present. This would create a flatter surface at the NEEM site, possibly also NGRIP, and would not favor the existence of strong katabatic winds. Marshall and Koutnik (2006) modeled the icebergs delivery from the Northern Hemisphere ice sheets over DO events and showed that the ice sheet margins from Greenland and the Canadian Arctic do not particularly respond to DO events, because these regions remain too cold even during GI. This is not in favor of abrupt change in the convective zone due to ice sheet shape changes at the GS–GI transition.

A convective zone may also be created by a low accumulation rate (as observed at Vostok or Dome F, Fig. A2). The deepest known convective zone (23 m) is reported at the zero-accumulation site Megadunes in Antarctica (Severinghaus et al., 2010). However, note that there is no convective zone at Dome C (Landais et al., 2006) where the present-day annual mean accumulation rate is 2.5 cm w.e.a^{-1}, slightly higher than at Vostok and Dome F. Our best guess accumulation rate for NEEM, NGRIP and GRIP during MIS3, using a 2 m convective zone, is always higher than at Dome C today (Fig. A2). This is also true for the GISP2 site (Orsi et al., 2013). All these observations are in favor of no deep convective zone at NEEM, NGRIP, GRIP and GISP2 during MIS3.

The existence of a convective zone would affect the average level of δ^{15}N, through the reduction of the diffusive zone, but not the modeled Δdepth that is a function of the total firn thickness (LID), itself dependant of surface temperature and accumulation. For NEEM, to reproduce both the measured Δdepth and δ^{15}N values, using the original DJ accumulation rate, we need to reduce the temperature scenario d3 by 9 °C everywhere and use a 50 m convective zone (not shown). The obtained system of temperature-accumulation-convective zone is inconsistent with present-day observations
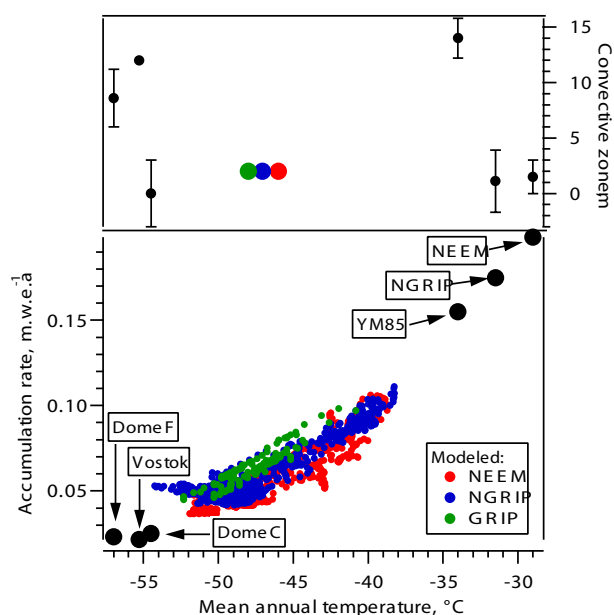

Fig. A2. Bottom: accumulation rate (m.w.e.a^{-1}) vs. temperature (°C). NEEM (red), NGRIP (blue) and GRIP (green), modeled during MIS3. Black dots: measured for different present-day sites. Top: convective zone (m) vs. temperature.

in Greenland and Antarctica (accumulation rate much too large compared to the temperature and convective zone).

As a sensitivity test, we have made simulations with the Goujon model using a constant convective zone of 12 m during MIS3 for NEEM (Fig. 3) and NGRIP (not shown), where we still need to reduce the accumulation rate to match the measured δ^{15}N profile (by 28 % for NEEM and 19 % for NGRIP).

Appendix B

Uncertainties quantification

B1   Temperature increase

The uncertainty associated with temperature reconstruction arises from the contribution of several sources of uncertainties: analytical uncertainties associated with δ^{15}N measurements, uncertainty associated with the estimation of the δ^{15}N temperature sensitivity (Ω parameter), uncertainty related to modeling of firn heat diffusion and firnification. In a simple way, based on Eq. (2), we can write the temperature increase ΔT as

$$\Delta T = \frac{\Delta \delta^{15} N_{therm}}{D\Omega}, \tag{B1}$$

where $\Delta \delta^{15} N_{therm}$ is the difference in $\delta^{15} N_{therm}$ between GS and GI, D is a coefficient for the heat diffusion

M. Guillevic et al.: Past spatial gradients of temperature, accumulation and δ^{18}O in Greenland   **1043**
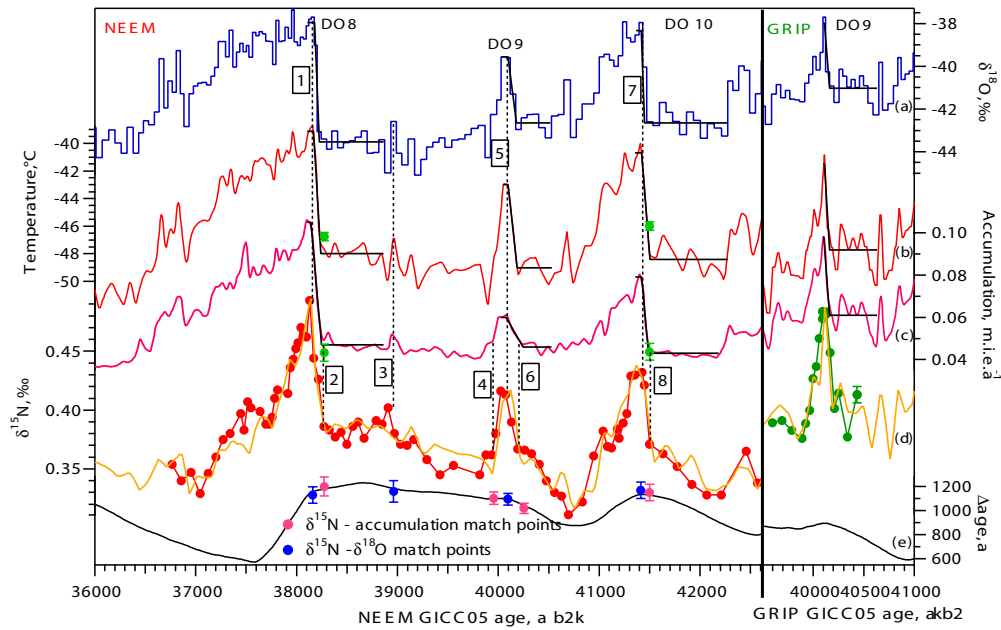

Fig. A3. δ^{15}N reconstruction for NEEM (left) and GRIP (right). **(a)** δ^{18}O profile used to reconstruct the surface temperature profile. **(b)** Surface temperature scenario used in the Goujon model (red line) and in the Herron Langway model (NEEM, 2 green dots). **(c)** Accumulation scenario for the Goujon model (pink line) and the HL model (NEEM, 2 green dots). **(d)** δ^{15}N data measured at LSCE, this study (red (NEEM) and green (GRIP) line and markers) and modeled δ^{15}N by the Goujon model (orange line), using temperature and accumulation scenario shown in **(b)** and **(c)**, plotted on the ice age scale using the Δage produced by the Goujon model (e, black line). Δage tie points are numbered as in Table 2. **(e)** Markers: tie points between δ^{15}N and δ^{18}O (blue markers) or accumulation (pink markers), used to constrain the firnification models. Black line: Δage modeled by the Goujon model. Subplots **(a)**, **(b)** and **(c)**, in black: GS and GI mean states calculated by the rampfit method.

in the ice, and Ω is the thermal diffusion sensitivity (Grachev and Severinghaus, 2003).

To sum the uncertainties we use the general formula (Press et al., 2007):

$$\sigma_x = \sqrt{\sigma_a^2 \left(\frac{\partial x}{\partial a}\right)^2 + \sigma_b^2 \left(\frac{\partial x}{\partial b}\right)^2 + \sigma_c^2 \left(\frac{\partial x}{\partial c}\right)^2} \quad \text{(B2)}$$

where x is a function of a, b, and c associated with, respectively, σ_a, σ_b, and σ_c as standard errors. We can thus sum the uncertainties associated to the temperature increase:

$$\sigma_{\Delta T} = \sqrt{ \sigma_{\Delta \delta^{15}N_{therm}}^2 \left(\frac{1}{D\Omega}\right)^2 + \sigma_\Omega^2 \left(\frac{-\Delta \delta^{15}N_{therm}}{\Omega^2 D}\right)^2 }$$
$$\overline{ + \sigma_D^2 \left(\frac{-\Delta \delta^{15}N_{therm}}{\Omega D^2}\right)^2 } \quad \text{(B3)}$$

or $\sigma_{\Delta T} = \sqrt{\sigma_{\Delta T, \Delta \delta^{15}N_{therm}}^2 + \sigma_{\Delta T, \Omega}^2 + \sigma_{\Delta T, D}^2}.$ (B4)

$\sigma_{\Delta T, \Delta \delta^{15}N_{therm}}$: this uncertainty results from the analytical uncertainty for δ^{15}N measurements and from firnification modeling uncertainty. The pooled standard deviation of our

NEEM δ^{15}N measurement is 0.006 ‰. We use n_{GI} points to define the GI value (respectively 1, 2, and 3 points for DO 8, 9, and 10) and n_{GS} points for the GS value (respectively 9, 3, and 6 points). For a GS to GI increase, the $\Delta \delta^{15}$N uncertainty is thus:

$$\sigma_{\Delta \delta^{15}N} = \sqrt{\frac{\sigma_{\delta^{15}N}^2}{n_{GS}} + \frac{\sigma_{\delta^{15}N}^2}{n_{GI}}} \quad \text{(B5)}$$

which gives, respectively, 0.006, 0.006, and 0.004 ‰ for DO 8, 9, and 10. We run the firnification model with a modified temperature scenario in order to exceed the δ^{15}N peak value by 0.006 ‰ maximum, for each DO event. The accumulation scenario is kept unchanged. The obtained temperature increase is 0.58 °C larger. If we calculate $\sigma_{\Delta T, \Delta \delta^{15}N}$ as given by Eq. (B3) we obtain 0.52 °C. We conclude that the maximum associated temperature uncertainty is 0.58 °C. Concerning the validity of the firnification modeling, we have already shown in Sect. 3.1 that numerous tuning tests performed with the Goujon model do not modify the estimated temperature increase. When using different firnification models (Schwander or Goujon) with similar inputs scenarios, the modeled δ^{15}N profiles are similar. Moreover, the duration of temperature increase is well constrained by the GICC05 chronology

4.2. Spatial gradients of temperature, accumulation and δ^{18}O-ice in Greenland over a series of Dansgaard - Oeschger events

111

and the high resolution δ^{18}O data. The GICC05 dating and the identification of numerous Δage tie points (Table 2) between gas- and ice phases gives strong constrains on the accumulation scenario. We are thus quite confident in the validity of our firnification model to reconstruct past surface temperature and accumulation variations.

$\sigma_{\Delta T, D}$: since the duration of the temperature increase is very well known, the uncertainty on the heat diffusion effect is thus rather small. In our case, it decreases the firn temperature gradient by 1.66 °C with respect to a surface temperature increase of 9.02 °C for DO 8 for NEEM. The major uncertainty in the heat diffusion model is linked to snow/ice conductivity modelisation. For the snow conductivity, we use the formulation from Schwander et al. (1997) where it is a function of the ice conductivity. We have tried different formulations for the ice conductivity (Weller and Schwerdtfeger, 1971; Yen, 1981) and modeled δ^{15}N are very similar.

$\sigma_{\Delta T, \Omega}$: we calculate the uncertainty linked to Ω uncertainty (± 3 %, Grachev and Severinghaus, 2003) to be 0.22, 0.13, and 0.17 °C for DO 8, 9, and 10 respectively for the NEEM core. This uncertainty increases with the estimated temperature increase and is therefore higher for DO 8.

Summing up all these uncertainties, we estimate the error on the reconstructed NEEM temperature increase for each DO event to be ~ 0.6 °C (1σ). Following the same approach, we estimate the uncertainty to be ~ 1.5 °C (1σ) for NGRIP and ~ 0.6 °C for GRIP. For GISP2, we also add an uncertainty of 0.07 °C linked to the amplitude of the accumulation increase (Orsi et al., 2013) and obtain 0.6 °C. The larger uncertainty at NGRIP is mainly caused by the larger analytical uncertainty (0.006 ‰ for NEEM and GRIP δ^{15}N data, 0.02 ‰ for NGRIP δ^{15}N data).

B2 δ^{18}O ice temperature sensitivity

The temperature sensitivity of δ^{18}O measured in the ice is defined by the parameter $\alpha = \Delta\delta^{18}O/\Delta T$. For NEEM, δ^{18}O data are measured with an accuracy of 0.07 ‰. We use 2 δ^{18}O points to estimate the GI value and 12 (DO 8 and 10) or 9 (DO 9) data points to estimate the GS δ^{18}O value. The uncertainty associated with the δ^{18}O increase is

$$\sigma_{\Delta\delta^{18}O} = \sqrt{\frac{\sigma^2_{\delta^{18}O}}{n_{GS}} + \frac{\sigma^2_{\delta^{18}O}}{n_{GI}}} \tag{B6}$$

which gives 0.05 ‰ for DO 8, 9, and 10. Following the same approach, we obtain uncertainties for, respectively, DO 8, 9, and 10 of 0.04, 0.05, and 0.04 ‰ for the NGRIP ice core, and 0.04, 0.08, and 0.06 ‰ for the GRIP ice core. We obtain 0.02 ‰ for the GISP2 core.

For NEEM, temperature and δ^{18}O increases uncertainties result in a 0.05 ‰ °C^{-1} uncertainty for α. We obtain 0.08, 0.12, and 0.06 ‰ °C^{-1} for DO 8, 9, and 10 for NGRIP and 0.05 ‰ °C^{-1} for GISP2 and GRIP following the same approach.

B3   Confidence intervals

We propose here two different approaches to determine whether two increases (δ^{18}O or temperature), Δi and Δj, are different from each other.

First approach: for each calculated Δi we have calculated an associated error estimate σ_i (see previous section). Assuming a Gaussian distribution, each Δi can be defined by a Gaussian distribution function centered in Δi:

$$f(x) = \frac{1}{\sigma_i \sqrt{2\pi}} \exp\left(\frac{-(x - \Delta i)^2}{2\sigma_i}\right). \tag{B7}$$

The probability to get a value $x \pm a_i$ for this Δi is the corresponding integral:

$$p_i = \int_{-a_i}^{a_i} f(x) = \text{erf}\left(\frac{x - \Delta i}{\sigma_i \sqrt{2}}\right). \tag{B8}$$

The integral from $-\infty$ to $+\infty$ equals one. For each pair of increases Δi and Δj, we calculate the respective maximum confidence intervals $[-a_i; a_i]$ and $[-a_j; a_j]$ in a way that these two intervals do not overlap and that $\int_{-a_i}^{a_i} f(x) = \int_{-a_j}^{a_j} g(x)$. The integrals $p_i = p_j$ correspond to the probability to have the value $\Delta i \pm a_i$ and $\Delta j \pm a_j$. We consider that if $p_i = p_j \geq 0.9$, the two increases are significantly different from each other.

Second approach: we take a couple of temperatures increases ΔT_i and ΔT_j, assume both to have Gaussian distribution, and calculate the probability of the difference ΔT_i-ΔT_j to have a value X:

$$\Delta T_i - \Delta T_j = X \tag{B9}$$

$$p(X = x) = \int d\tilde{x} \; p(\Delta T_i = \tilde{x}) \; p(\Delta T_j = \tilde{x} - x) \tag{B10}$$

$$p(X = x) = \frac{1}{\sqrt{2\pi}\sqrt{\sigma_i^2 + \sigma_j^2}}$$
$$\int \exp\left(-\frac{(x - (\Delta T_i - \Delta T_j))^2}{2(\sigma_i^2 + \sigma_j^2)}\right) dx. \tag{B11}$$

Equation (B11) can then be used to find the probability that $X = 0$, hence that $\Delta T_i = \Delta T_j$. The probability that ΔT_i is exactly equal to ΔT_j is nil by definition and we have to define the depth interval over which to integrate Eq. (B11). We will thus calculate the probability that $\Delta T_i = \Delta T_j \pm a$ by assigning the integration range for Eq. (B11) to $[-a; a]$. There is a necessary subjectivity in the choice of this interval. We have chosen to base this estimate of a on the uncertainty

associated with our data so that we take $a = \sqrt{\sigma_i^2 + \sigma_j^2}$:

$$p(-\sqrt{\sigma_i^2 + \sigma_j^2} < x < \sqrt{\sigma_i^2 + \sigma_j^2})$$

$$= \int_{-\sqrt{\sigma_i^2 + \sigma_j^2}}^{\sqrt{\sigma_i^2 + \sigma_j^2}} p(X = x) \, dx \qquad (B12)$$

$$= \frac{1}{\sqrt{2\pi}\sqrt{\sigma_i^2 + \sigma_j^2}}$$

$$\int_{-\sqrt{\sigma_i^2 + \sigma_j^2}}^{\sqrt{\sigma_i^2 + \sigma_j^2}} \exp\left(-\frac{(x - (\Delta T_i - \Delta T_j))^2}{2(\sigma_i^2 + \sigma_j^2)}\right) dx \qquad (B13)$$

$$= \frac{1}{2}\left(\mathrm{erf}\left(\frac{x - (\Delta T_i - \Delta T_j)}{\sqrt{\sigma_i^2 + \sigma_j^2}\sqrt{2}}\right)\right.$$

$$\left. - \mathrm{erf}\left(\frac{-x - (\Delta T_i - \Delta T_j)}{\sqrt{\sigma_i^2 + \sigma_j^2}\sqrt{2}}\right)\right). \qquad (B14)$$

Finally, we consider ΔT_i and ΔT_j to be significantly different when $p(-\sqrt{\sigma_i + \sigma_j} < x < \sqrt{\sigma_i + \sigma_j})$ is equal or less than 0.1.

We now apply this probability calculation for DO 8 for the following comparison:

– NEEM vs. NGRIP: $a = 1.6\,°C$, ΔT_{NEEM}-$\Delta T_{\mathrm{NGRIP}} = 1.6\,°C$ so that the probability that $\Delta T_{\mathrm{NEEM}} = \Delta T_{\mathrm{NGRIP}} \pm 1.6$ is calculated with Eq. (B14) as $p = 0.48$.

– NGRIP vs. GISP2: $a = 1.6\,°C$, $\Delta T_{\mathrm{NGRIP}}$-$\Delta T_{\mathrm{GISP2}} = 0.7\,°C$ so that the probability that $\Delta T_{\mathrm{NGRIP}} = \Delta T_{\mathrm{GISP2}} \pm 1.6$ is calculated with Eq. (B14) as $p = 0.62$.

– NEEM vs. GISP2: $a = 0.85\,°C$, ΔT_{NEEM}-$\Delta T_{\mathrm{GISP2}} = 2.25\,°C$ so that the probability that $\Delta T_{\mathrm{NEEM}} = \Delta T_{\mathrm{GISP2}} \pm 0.85$ is calculated with Eq. (B14) as $p = 0.05$.

These calculations give the same conclusion as obtained from approach 1: for DO 8, ΔT_{NEEM} is significantly different from $\Delta T_{\mathrm{GISP2}}$ with 94 % confidence (first approach) or, according to approach 2, these two temperature increases are significantly equal with 5 % confidence.

The results are reported in Table 3 in the following way: for each DO event, if two values are written in two different colors, they are significantly different from each other. A value written in italic is not significantly different from all the others.

Appendix C

NEEM firn modelisation with the Herron Langway model

The Herron Langway model (hereafter HL) is an empirical firnification model where the density profile and the ice age in the firn are calculated based on surface temperature and accumulation (Herron and Langway, 1980). We use a surface snow density of $0.350\,\mathrm{g\,cm}^{-3}$, as in the Goujon firnification model. Based on the HL density profile in the firn, we calculate the ratio closed to total porosity along the firn column (Goujon et al., 2003). To allow comparison with the Goujon model, we use the same definition for the LID: the depth where the ratio close to total porosity reaches 0.13. At this depth, the HL model gives us the ice age, that we use as a Δage estimate, and we calculate $\delta^{15}N_{\mathrm{grav}}$ assuming a convective zone of 2 m. This model has no heat diffusion component and we thus use it on periods where the Goujon model shows negligible thermal fractionation for $\delta^{15}N$ (within the $\delta^{15}N$ measurement uncertainty), meaning where the surface temperature is stable, without temperature gradient in the firn. We thus can use $\delta^{15}N_{\mathrm{grav}}$ as an estimate for $\delta^{15}N_{\mathrm{tot}}$.

Here, we apply this model on the stadial periods at NEEM to investigate the surface temperature and accumulation scenarios that match the right $\delta^{15}N$ level and Δage. We use the $\delta^{15}N$ and Δage values just preceding the DO events (see Table 2) as target values and tune the surface temperature and accumulation.

For DO 8, we use a target $\delta^{15}N$ value of 0.382 ± 0.006 ‰ and Δage value of 1198 ± 79 a (Table 2, NEEM tie point n. 2). The HL model can reproduce these values using a surface temperature of $-46.76 \pm 0.3\,°C$ and an accumulation rate of $0.043 \pm 0.004\,\mathrm{m.i.e.a}^{-1}$ (58 % reduction of the one determined by the DJ ice flow model). The LID is at 76 real meters depth (or 52.8 m.i.e. meters ice equivalent).

For DO 10, we use the NEEM tie point n. 9, where $\delta^{15}N = 0.371 \pm 0.006$ ‰ and Δage $= 1149 \pm 69$ a. These values are reproduced using as surface temperature $-46.0 \pm 0.3\,°C$ and as accumulation rate $0.044 \pm 0.004\,\mathrm{m.i.e.a}^{-1}$ (51 % reduction). The LID is at 73.5 real meters depth (51.0 m.i.e.).

Modeled surface temperature and accumulation for the onset of DO 8 and 10 are plotted in Fig. A3 with green dots. For DO 8, the HL and Goujon models produce very similar surface temperature scenarios but the HL accumulation rate is lower. For DO 10, the HL and Goujon accumulation rates are similar but the HL temperature is much higher. It is very likely that the differences are due to the strong assumption of no thermal gradient in the firn for the HL model. In order to fit the measured GS level of $\delta^{15}N$ and the Δage at the onset of DO 8 and 10 with the HL model, we need to use a reduced accumulation rate by 58 and 51 %, respectively. We here confirm the finding from the Goujon model: decreasing significantly the accumulation rate estimated by the DJ ice flow model is necessary to match both $\delta^{15}N$ and Δage data.
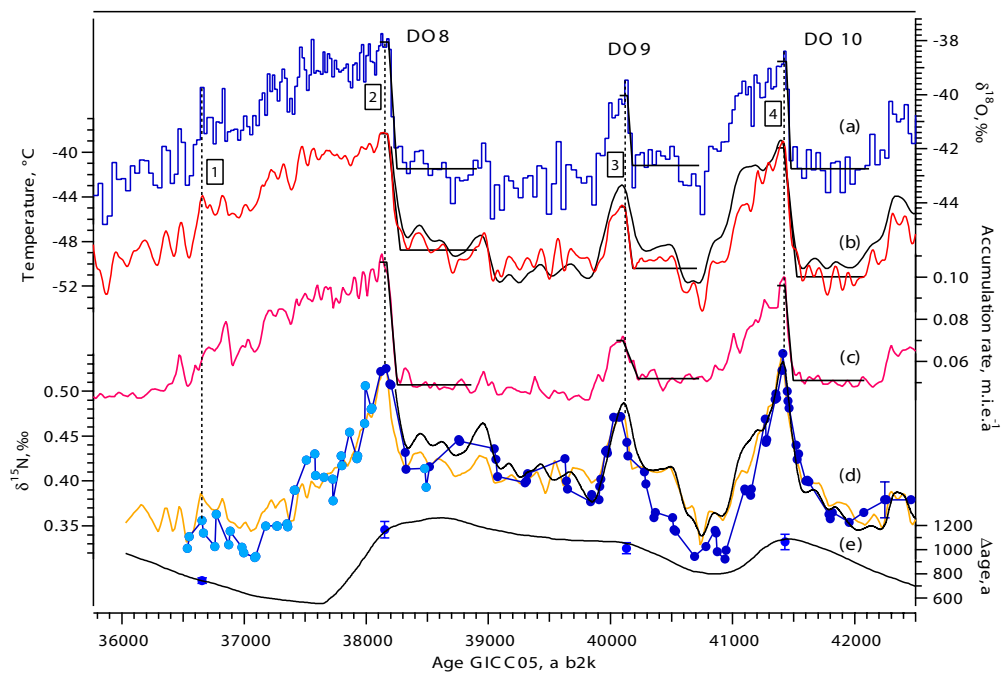
Fig. D1 δ^{15}N reconstruction for NGRIP. **(a)**, δ^{18}O profile used to reconstruct the surface temperature profile, NGRIP members (2004). **(b)** Surface temperature scenario used in the Goujon model (red line, this study) and in Huber et al. (2006), black line. Note that the temperature reconstruction covering DO 8 was missing at that time. **(c)** Accumulation scenario for the Goujon model. **(d)** Measured δ^{15}N data at the University of Bern, Switzerland, with error bar shown on the last point to the right (dark blue dots Huber et al. (2006), new points in light blue dots). Modeled δ^{15}N by the Goujon model (orange line), using temperature and accumulation scenario shown in **(b)** and **(c)**. Measured and modeled δ^{15}N are plotted on the ice age scale using the Δage produced by the Goujon model (**e**, black line). Δage tie points are numbered as in Table 2. Black line: modeled δ^{15}N from Huber et al. (2006) using the temperature scenario in **(b)**, black line. **(e)** Blue markers: tie points between δ^{15}N and δ^{18}O, used to constrain the firnification models. Black line: Δage modeled by the Goujon model. Subplots **(a)**, **(b)** and **(c)**, in black: stadial and interstatial mean states calculated by the rampfit method.

Appendix D

Reprocessing NGRIP δ^{15}N data

To allow the comparison between NEEM and NGRIP, we reconstruct here past temperature and accumulation at NGRIP following the same approach as for the NEEM site. We use the Goujon firnification model adapted to the NGRIP site. To constrain the model, we minimize the distance between the measured δ^{15}N and the modeled one (Fig. D1, c). The corresponding temperature and accumulation scenarios are reported in Fig. D1. For comparison, we also report here the temperature reconstruction from Huber et al. (2006), using the firnification model from Schwander et al. (1997) and the ss09sea06bm timescale. Direct comparison is possible because over DO 8, 9, and 10 (2020 to 2140 m depth), durations proposed by the GICC05 and the ss09sea06bm timescales agree with each other with 5 % difference. Note that the two reconstructions agree well with each other, both for absolute temperature level and temperature variations with time. We use an accumulation rate reduced by 26 % (20 % for Huber

et al., 2006) and thus need to reduce the mean temperature level slightly more than Huber et al. (2006) to still match the δ^{15}N data.

M. Guillevic et al.: Past spatial gradients of temperature, accumulation and δ^{18}O in Greenland   **1047**

References

Ahn, J., Brook, E., Schmittner, A., and Kreutz, K.: Abrupt change in atmospheric CO_2 during the last ice age, Geophys. Res. Lett., 39, L18711, doi:10.1029/2012GL053018, 2012.

Alley, R. B., Meese, D. A., Shuman, C. A., Gow, A. J., Taylor, K. C., Grootes, P. M., White, J. W. C., Ram, M., Waddington, E. D., Mayewski, P. A., and Zielinski, G. A.: Abrupt increase in Greenland snow accumulation at the end of the Younger Dryas event, Nature, 362, 527–529, doi:10.1038/362527a0, 1993.

Andersen, K. K., Svensson, A., Johnsen, S. J., Rasmussen, S. O., Bigler, M., Röthlisberger, R., Ruth, U., Siggaard-Andersen, M.-L., Steffensen, J. P., Dahl-Jensen, D., Vinther, B. M., and Clausen, H. B.: The Greenland Ice Core Chronology 2005, 15–42 ka. Part 1: constructing the time scale, Quaternary Sci. Rev., 25, 3246–3257, doi:10.1016/j.quascirev.2006.08.002, 2006.

Arnaud, L., Barnola, J.-M., and Duval, P.: Physical modeling of of the densification of snow/firn and ice in the upper part of polar ice sheets, Hokkaido University Press, Sapporo, Japan, 2000.

Barlow, L. K., White, J. W. C., Barry, R. G., Rogers, J. C., and Grootes, P. M.: The North Atlantic Oscillation signature in deuterium and deuterium excess signals in the Greenland Ice Sheet Project 2 Ice Core, 1840–1970, Geophys. Res. Lett., 20, 2901–2904, doi:10.1029/93GL03305, 1993.

Bender, M., Sowers, T., Barnola, J.-M., and Chappellaz, J.: Changes in the O_2/N_2 ratio of the atmosphere during recent decades reflected in the composition of air in the firn at Vostok Station, Antarctica, Geophys. Res. Lett., 21, 189–192, 1994a.

Bender, M. L., Tans, P. P., Ellis, T., Orchardo, J., and Habfast, K.: A high precision isotope ratio mass spectrometry method for measuring the O_2/N_2 ratio of air, Geochim. Cosmochim. Ac., 58, 4751–4758, 1994b.

Bereiter, B., Lüthi, D., Siegrist, M., Schüpbach, S., Stocker, T. F., and Fischer, H.: Mode change of millennial CO_2 variability during the last glacial cycle associated with a bipolar marine carbon seesaw, Proc. Natl. Acad. Sci. USA, 109, 9755–9760, 2012.

Bintanja, R., van de Wal, R. S. W., and Oerlemans, J.: Modelled atmospheric temperatures and global sea levels over the past million years, Nature, 437, 125–128, doi:10.1038/nature03975, 2005.

Blunier, T. and Brook, E. J.: Timing of Millennial-Scale Climate Change in Antarctica and Greenland During the Last Glacial Period, Science, 291, 109–112, doi:10.1126/science.291.5501.109, 2001.

Bond, G., Broecher, W., Johnsen, S. J., MacManus, J., Laberie, L., Jouzel, J., and Bonani, G.: Correlations between climate records from North Atlantic sediments and Greenland ice, Nature, 365, 143–147, 1993.

Boyle, E. A.: Cool tropical temperatures shift the global δ^{18}O-T relationship: An explanation for the ice core δ^{18}O – borehole thermometry conflict?, Geophys. Res. Lett., 24, 273–276, doi:10.1029/97GL00081, 1997.

Buchardt, S. L.: Basal melting and Eemian ice along the main ice ridge in northern Greenland, Ph.D. Thesis, Niels Bohr Institute, Faculty of Science, University of Copenhagen, 2009.

Buchardt, S. L., Clausen, H. B., Vinther, B. M., and Dahl-Jensen, D.: Investigating the past and recent δ^{18}O-accumulation relationship seen in Greenland ice cores, Clim. Past, 8, 2053–2059, doi:10.5194/cp-8-2053-2012, 2012.

Buiron, D., Stenni, B., Chappellaz, J., Landais, A., Baumgartner, M., Bonazza, M., Capron, E., Frezzotti, M., Kageyama, M., Lemieux-Dudon, B., Masson-Delmotte, V., Parrenin, F., Schilt, A., Selmo, E., Severi, M., Swingedouw, D., and Udisti, R.: Regional imprints of millennial variability during the MIS 3 period around Antarctica, Quaternary Sci. Rev., 48, 99–112, 2012.

Buizert, C., Martinerie, P., Petrenko, V. V., Severinghaus, J. P., Trudinger, C. M., E.Witrant, Rosen, J. L., Orsi, A. J., Rubino, M., Etheridge, D. M., Steele, L. P., Hogan, C., Laube, J. C., Sturges, W. T., Levchenko, V. A., Smith, A. M., Levin, I., Conway, T. J., Dlugokencky, E. J., Lang, P. M., Kawamura, K., Jenk, T. M., White, J. W. C., Sowers, T., Schwander, J., and Blunier, T.: Gas transport in firn: multiple-tracer characterisation and model intercomparison for NEEM, Northern Greenland, Atmos. Chem. Phys., 12, 4259–4277, doi:10.5194/acp-12-4259-2012, 2012.

Capron, E., Landais, A., Chappellaz, J., Schilt, A., Buiron, D., Dahl-Jensen, D., Johnsen, S. J., Jouzel, J., Lemieux-Dudon, B., Loulergue, L., Leuenberger, M., Masson-Delmotte, V., Meyer, H., Oerter, H., and Stenni, B.: Millennial and sub-millennial scale climatic variations recorded in polar ice cores over the last glacial period, Clim. Past, 6, 345–365, doi:10.5194/cp-6-345-2010, 2010.

Charles, C. D., Rind, D., Healy, R., and Webb, R.: Tropical cooling and the isotopic composition of precipitation in general circulation model simulations of the ice age climate, Clim. Dynam., 17, 489–502, 2001.

Chiang, J. C. H., Cheng, W., and Bitz, C. M.: Fast teleconnections to the tropical Atlantic sector from Atlantic thermohaline adjustment, Geophys. Res. Lett., 35, L07704, doi:10.1029/2008GL033292, 2008.

Craig, H., Horibe, Y., and Sowers, T.: Gravitational separation of gases and isotopes in polar ice caps, Science, 242, 1675–1678, 1988.

Cuffey, K. M. and Clow, G. D.: Temperature, accumulation, and ice sheet elevation in central Greenland through the last deglacial transition, J. Geophys. Res., 102, 26383–26396, 1997.

Cuffey, K. M. and Paterson, W. S. B.: The physics of glaciers, Elsevier, 4th Edn., 2010.

Cuffey, K. M., Clow, G. D., Alley, R. B., Stuiver, M., Waddington, E. D., and Saltus, R. W.: Large Arctic Temperature Change at the Wisconsin-Holocene Glacial Transition, Science, 270, 455–458, doi:10.1126/science.270.5235.455, 1995.

Cutler, N., Raymond, C., Waddington, E., Meese, D., and Alley, R.: The effect of ice-sheet thickness change on the accumulation history inferred from GISP2 layer thickness, Ann. Glaciol., 21, 26–32, 1995.

Dahl-Jensen, D., Mosegaard, K., Gundestrup, N., Clow, G. D., Johnsen, S. J., Hansen, A. W., and Balling, N.: Past Temperatures Directly from the Greenland Ice Sheet, Science, 282, 268–271, doi:10.1126/science.282.5387.268, 1998.

Dahl-Jensen, D. and NEEM community members: Eemian interglacial reconstructed from a Greenland folded ice core, Nature,

493, 489–494, 2013.

Dansgaard, W.: Stable isotopes in precipitation, Tellus, 16, 436–468, 1964.

Dansgaard, W. and Johnsen, S. J.: A flow model and a time scale for the ice core from Camp Century, Greenland, J. Glaciol., 8, 215–223, 1969.

Elliot, M., Labeyrie, L., Dokken, T., and Manthé, S.: Coherent patterns of ice rafted debris deposits in the Nordic regions during the last glacial, Earth Planet. Sci. Lett., 194, 151–163, 2001.

Elliot, M., Labeyrie, L., and Duplessy, J.-C.: Changes in North Atlantic deep-water formation associated with the Dansgaard-Oeschger temperature oscillations (60–10 ka), Quaternary Sci. Rev., 21, 1153–1165, 2002.

EPICA community members: One-to-one coupling of glacial climate variability in Greenland and Antarctica, Nature, 444, 195–198, doi:10.1038/nature05301, 2006.

Fawcett, P. J., Agustdóttir, A. M., Alley, R. B., and Shuman, C. A.: The Younger Dryas termination and North Atlantic deepwater formation: insights from climate model simulations and greenland ice data, Paleoceanography, 12, 23–38, doi:10.1029/96PA02711, 1997.

Ganopolski, A. and Rahmstorf, S.: Rapid changes of glacial climate simulated in a coupled climate model, Nature, 409, 153–158, 2001.

Goujon, C., Barnola, J.-M., and Ritz, C.: Modeling the densification of polar firn including heat diffusion: Application to close-off characteristics and gas isotopic fractionation for Antarctica and Greenland sites, J. Geophys. Res., 108, D24, doi:10.1029/2002JD003319, 2003.

Grachev, A. M. and Severinghaus, J. P.: Laboratory determination of thermal diffusion constants for $^{29}N_2/^{28}N_2$ in air at temperatures from -60 to $0\,^{\circ}$CC for reconstruction of magnitudes of abrupt climate changes using the ice core fossil-air paleothermometer, Geochim. Cosmochim. Ac., 67, 345–360, 2003.

Grachev, A. M. and Severinghaus, J. P.: A revised $+10+/-4$ C magnitude of the abrupt change in Greenland temperature at the Younger Dryas termination using published GISP2 gas isotope data and air thermal diffusion constants, Quaternary Sci. Rev., 24, 513–519, 2005.

Grinsted, A. and Dahl-Jensen, D.: A Monte Carlo tuned model of the flow in the NorthGRIP area, J. Glaciol., 35, 527–530, doi:10.3189/172756402781817130, 2002.

Grootes, P. M. and Stuiver, M.: Oxygen 18/16 variability in Greenland snow and ice with 10^{-3} to 10^5-year time resolution, J. Geophys. Res., 102, 26455–26470, doi:10.1029/97JC00880, 1997.

Grootes, P. M., Stuiver, M., White, J. W. C., Johnsen, S. J., and Jouzel, J.: Comparison of oxygen isotope records from the GISP2 and GRIP Greenland ice cores, Nature, 366, 552–554, doi:10.1038/366552a0, 1993.

Gundestrup, N., Clausen, H., and Hansen, B.: The UCPH borehole logger in Ice drilling technology, NIPR, Japan, 1994.

Heinrich, H.: Origin and consequences of cyclic ice rafting in the Northeast Atlantic Ocean during the past 130,000 years, Quaternary Res., 29, 142–152, doi:10.1016/0033-5894(88)90057-9, 1988.

Herron, M. M. and Langway, C. C.: Firn densification: an empirical model, J. Glaciol., 25, 373–385, 1980.

Hörhold, M., Laepple, T., Freitag, J., Bigler, M., Fischer, H., and Kipfstuhl, S.: On the impact of impurities on the densification of polar firn, Earth Planet. Sc. Lett., 325–326, 93–99, doi:10.1016/j.epsl.2011.12.022, 2012.

Huber, C. and Leuenberger, M.: Measurements of isotope and elemental ratios of air from polar ice with a new on-line extraction method, Geochem. Geophy. Geosy., 5, 10, doi:10.1029/2004GC000766, 2004.

Huber, C., Leuenberger, M., Spahni, R., Flückiger, J., Schwander, J., Stocker, T. F., Johnsen, S. J., Landais, A., and Jouzel, J.: Isotope calibrated Greenland temperature record over Marine Isotope Stage 3 and its relation to CH_4, Earth Planet. Sci. Lett., 243, 504–519, 2006.

Indermühle, A., Monnin, E., Stauffer, B., Stocker, T., and Wahlen, M.: Atmospheric CO_2 concentration from 60 to 20 kyr BP from the Taylor Dome ice core, Antarctica, Geophys. Res. Lett., 27, 735–738, 2000.

Johnsen, S. J., Dansgaard, W., and White, J. W. C.: The origin of Arctic precipitation under present and glacial climate, Tellus, 41B, 452–468, 1989.

Johnsen, S. J., Clausen, H. B., Dansgaard, W., Fuhrer, K., Gundestrup, N., Hammer, C. U., Iversen, P., Jouzel, J., Stauffer, B., and Steffensen, J. P.: Irregular glacial interstadials recorded in a new Greenland ice core, Nature, 359, 311–313, doi:10.1038/359311a0, 1992.

Johnsen, S., Dahl-Jensen, D., Dansgaard, W., and Gundestrup, N.: Greenland paleotemperatures derived from GRIP borehole temperature and ice core isotope profiles, Tellus, 47B, 624–629, 1995.

Johnsen, S. J., Dahl-Jensen, D., Gundestrup, N., Steffensen, J. P., Clausen, H. B., Miller, H., Masson-Delmotte, V., Sveinbjörnsdóttir, A., and White, J.: Oxygen isotope and palaeotemperature records from six Greenland ice-core stations: Camp Century, Dye-3, GRIP, GISP2, Renland and NorthGRIP, J. Quaternary Sci., 16, 299–307, doi:10.1002/jqs.622, 2001.

Jouzel, J., Alley, R., Cuffey, K., Dansgaard, W., Grootes, P., Hoffmann, G., Johnsen, S., Koster, R., Peel, D., Shuman, C., Stievenard, M., Stuiver, M., and White, J.: Validity of the temperature reconstruction from water isotopes in ice cores, J. Geophys. Res., 102, 21471–26487, 1997.

Jouzel, J., Stiévenard, N., Johnsen, S., Landais, A., Masson-Delmotte, V., Sveinbjörnsdóttir, A., Vimeux, F., von Grafenstein, U., and White, J.: The GRIP deuterium-excess record, Quaternary Sci. Rev., 26, 1–17, 2007.

Kageyama, M. and Valdes, P. J.: Impact of the North American ice-sheet orography on the Last Glacial Maximum eddies and snowfall, Geophys. Res. Lett., 27, 1515–1518, 2000.

Kageyama, M., Paul, A., Roche, D. M., and van Meerbeeck, C. J.: Modelling glacial climatic millennial-scale variability related to changes in the Atlantic meridional overturning circulation: a review, Quaternary Sci. Rev., 29, 2931–2956, doi:10.1016/j.quascirev.2010.05.029, 2010.

Kawamura, K., Severinghaus, J. P., Ishidoya, S., Sugawara, S., Hashida, G., Motoyama, H., Fujii, Y., Aoki, S., and Nakazawa, T.: Convective mixing of air in firn at four polar sites, Earth Planet. Sci. Lett., 244, 672–682, 2006.

Kissel, C., Laj, C., Piotrowski, A., Goldstein, S., and Hemming, S.: Millennial-scale propagation of Atlantic deep waters to the glacial Southern Ocean, Paleoceanography, 23, PA2102, doi:10.1029/2008PA001624, 2008.

M. Guillevic et al.: Past spatial gradients of temperature, accumulation and δ^{18}O in Greenland   **1049**

Kobashi, T., Kawamura, K., Severinghaus, J. P., Barnola, J.-M., Nakaegawa, T., Vinther, B. M., Johnsen, S. J., and Box, J. E.: High variability of Greenland surface temperature over the past 4000 years estimated from trapped air in an ice core, Geophys. Res. Lett., 38, L21501, doi:10.1029/2011GL049444, 2011.

Krinner, G., Genthon, C., and Jouzel, J.: GCM analysis of local influences on ice core δ signals, Geophys. Res. Lett., 24, 2825–2828, doi:10.1029/97GL52891, 1997.

Landais, A., Barnola, J.-M., Masson-Delmotte, V., Jouzel, J., Chappellaz, J., Caillon, N., Huber, C., Leuenberger, M., and Johnsen, S. J.: A continuous record of temperature evolution over a sequence of Dansgaard-Oeschger events during Marine Isotopic Stage 4 (76 to 62 kyr BP), Geophys. Res. Lett., 31, L22211, doi:10.1029/2004GL021193, 2004a.

Landais, A., Caillon, N., Severinghaus, J., Barnola, J.-M., Goujon, C., Jouzel, J., and Masson-Delmotte, V.: Isotopic measurements of air trapped in ice to quantify temperature changes, CR Geosci., 336, 963–970, 2004b.

Landais, A., Masson-Delmotte, V., Jouzel, J., Raynaud, D., Johnsen, S. J., Huber, C., Leuenberger, M., Schwander, J., and Minster, B.: The glacial inception as recorded in the NorthGRIP Greenland ice core: timing, structure and associated abrupt temperature changes, Clim. Dynam., 26, 273–284, doi:10.1007/s00382-005-0063-y, 2005.

Landais, A., Barnola, J., Kawamura, K., Caillon, N., Delmotte, M., Ommen, T. V., Dreyfus, G., Jouzel, J., Masson-Delmotte, V., Minster, B., Freitag, J., Leuenberger, M., Schwander, J., Huber, C., Etheridge, D., and Morgan, V.: Firn-air δ^{15}N in modern polar sites and glacial-interglacial ice: a model-data mismatch during glacial periods in Antarctica?, Quaternary Sci. Rev., 25, 49–62, doi:10.1016/j.quascirev.2005.06.007, 2006.

Lang, C., Leuenberger, M., Schwander, J., and Johnsen, S.: 16°C Rapid Temperature Variation in Central Greenland 70,000 Years Ago, Science, 286, 934–937, doi:10.1126/science.286.5441.934, 1999.

Laskar, J., Robutel, P., Joutel, F., Gastineau, M., Correia, A. C. M., and Levrard, B.: A long-term numerical solution for the insolation quantities of the Earth, Astron. Astrophys., 428, 261–285, doi:10.1051/0004-6361:20041335, 2004.

Li, C., Battisti, D. S., Schrag, D. P., and Tziperman, E.: Abrupt climate shifts in Greenland due to displacements of the sea ice edge, Geophys. Res. Lett., 32, L19702, doi:10.1029/2005GL023492, 2005.

Li, C., Battisti, D., and Bitz, C.: Can North Atlantic sea ice anomalies account for Dansgaard-Oeschger climate signals?, J. Climate, 23, 5457–5475, 2010.

Liu, Z., Otto-Bliesner, B. L., He, F., Brady, E. C., Tomas, R., Clark, P. U., Carlson, A. E., Lynch-Stieglitz, J., Curry, W., Brook, E., Erickson, D., Jacob, R., Kutzbach, J., and Cheng, J.: Transient Simulation of Last Deglaciation with a New Mechanism for Bølling-Allerød Warming, Science, 235, 310–314, doi:10.1126/science.1171041, 2009.

Lliboutry, L.: A critical review of analytical approximate solutions for steady stade velocities and temperature in cold ice-sheets, Z. Gletscherkd. Glazialgeol., 15, 135–148, 1979.

Marshall, S. J. and Koutnik, M. R.: Ice sheet action versus reaction: distinguishing between Heinrich events and Dansgaard-Oeschger cycles in the North Atlantic, Paleoceanography, 21, PA2021, doi:10.1029/2005PA001247, 2006.

Masson-Delmotte, V., Jouzel, J., Landais, A., Stiévenard, M., Johnsen, S. J., White, J. W. C., Werner, M., Sveinbjörnsdóttir, A., and Fuhrer, K.: GRIP Deuterium Excess Reveals Rapid and Orbital-Scale Changes in Greenland Moisture Origin, Science, 309, 118–121, doi:10.1126/science.1108575, 2005.

Masson-Delmotte, V., Braconnot, P., Hoffmann, G., Jouzel, J., Kageyama, M., Landais, A., Lejeune, Q., Risi, C., Sime, L., Sjolte, J., Swingedouw, D., and Vinther, B.: Sensitivity of interglacial Greenland temperature and δ^{18}O: ice core data, orbital and increased CO_2 climate simulations, Clim. Past, 7, 1041–1059, doi:10.5194/cp-7-1041-2011, 2011.

Mayewski, P. A., Meeker, L. D., Twickler, M. S., Whitlow, S., Yang, Q., Lyons, W. B., and Prentice, M.: Major features and forcing of high-latitude northern hemisphere atmospheric circulation using a 110,000-year-long glaciochemical series, J. Geophys. Res., 102, 26345–26366, doi:10.1029/96JC03365, 1997.

McManus, J. F., Bond, G. C., Broecker, W. S., Johnsen, S., Labeyrie, L., and Higgins, S.: High resolution climate records from the North Atlantic during the last interglacial, Nature, 371, 326–329, 1994.

Meese, D. A., Gow, A. J., Grootes, P., Stuiver, M., Mayewski, P. A., Zielinski, G. A., Ram, M., Taylor, K. C., and Waddington, E. D.: The accumulation record from the GISP2 core as an indicator of climate change throughout the Holocene, Science, 266, 1680–1682, doi:10.1126/science.266.5191.1680, 1994.

Meese, D. A., Gow, A. J., Alley, R. B., Zielinski, G. A., Grootes, P. M., Ram, M., Taylor, K. C., Mayewski, P. A., and Bolzan, J. F.: The Greenland Ice Sheet Project 2 depth-age scale: methods and results, J. Geophys. Res., 102, 26411–26423, 1997.

Merlivat, L. and Jouzel, J.: Global climatic interpretation of the deuterium-oxygen 18 relationship for precipitation, J. Geophys. Res., 84, 5029–5033, 1979.

Mudelsee, M.: Ramp function regression: a tool for quantifying climate transitions, Comput. Geosci., 26, 293–307, 2000.

NGRIP members: High-resolution record of Northern Hemisphere climate extending into the last interglacial period, Nature, 431, 147–151, doi:10.1038/nature02805, 2004.

Orsi, A., Cornuelle, B., and Severinghaus, J.: Magnitude and temporal evolution of interstadial 8 abrupt temperature change inferred from nitrogen and argon isotopes in GISP2 ice using a new least-squares inversion, submitted, 2013.

Otto-Bliesner, B. L. and Brady, E. C.: The sensitivity of the climate response to the magnitude and location of freshwater forcing: last glacial maximum experiments, Quaternary Sci. Rev., 29, 56–73, doi:10.1016/j.quascirev.2009.07.004, 2010.

Persson, A., Langen, P. L., Ditlevsen, P., and Vinther, B. M.: The influence of precipitation weighting on interannual variability of stable water isotopes in Greenland, J. Geophys. Res., 116, D20120, doi:10.1029/2010JD015517, 2011.

Press, W. H., Teukolsky, S. A., Wetterling, W. T., and Flannery, B. P.: Numerical recipes: the art of scientific computing, Cambridge University Press, 3rd Edn., 2007.

Rasmussen, S. O., Andersen, K. K., Svensson, A. M., Steffensen, J. P., Vinther, B. M., Clausen, H. B., Siggaard-Andersen, M.-L., Johnsen, S. J., Larsen, L. B., Dahl-Jensen, D., Bigler, M., Röthlisberger, R., Fischer, H., Goto-Azuma, K., Hansson, M. E., and Ruth, U.: A new Greenland ice core chronology for the last glacial termination, J. Geophys. Res., 111, doi:10.1029/2005JD006079, submitted, 2013.

Rasmussen, S. O., Seierstad, I., Andersen, K., Bigler, M., Dahl-Jensen, D., and Johnsen, S.: Synchronization of the NGRIP, GRIP, and GISP2 ice cores across MIS 2 and palaeoclimatic implications, Quaternary Sci. Rev., 27, 18–28, 2008.

Rasmussen, T. L. and Thomsen, E.: The role of the North Atlantic Drift in the millennial timescale glacial climate fluctuations, Palaeogeogr. Palaeocl., 210, 101–116, 2004.

Ritz, C.: Un modèle thermomécanique d'évolution pour le bassin glaciaire antarctique Vostok – Glacier Bird: Sensibilité aux valeurs des paramètres mal connus, Ph.D. Thesis, Université Joseph Fourier, Grenoble, France, 1992.

Roche, D., Wiersma, A., and Renssen, H.: A systematic study of the impact of freshwater pulses with respect to different geographical locations, Clim. Dyn., 34, 997–1013, 2010.

Ruth, U., Wagenbach, D., Steffensen, J. P., and Bigler, M.: Continuous record of microparticle concentration and size distribution in the central Greenland NGRIP ice core during the last glacial period, J. Geophys. Res., 108, D06102, doi:10.1029/2002JD002376, 2003.

Ruth, U., Bigler, M., Röthlisberger, R., Siggaard-Andersen, M.-L., Kipfstuhl, S., Goto-Azuma, K., Hansson, M. E., Johnsen, S. J., Lu, H., and Steffensen, J. P.: Ice core evidence for a very tight link between North Atlantic and east Asian glacial climate, Geophys. Res. Lett., 34, L03706, doi:10.1029/2006GL027876, 2007.

Schilt, A., Baumgartner, M., Blunier, T., Schwander, J., Spahni, R., Fischer, H., and Stocker, T. F.: Glacial-interglacial and millennial-scale variations in the atmospheric nitrous oxide concentration during the last 800,000 years, Quaternary Sci. Rev., 29, 182–192, doi:10.1016/j.quascirev.2009.03.011, 2010.

Schwander, J.: The transformation of snow to ice and the occlusion of gases, New York, 1989.

Schwander, J., Sowers, T., Barnola, J.-M., Blunier, T., Fuchs, A., and Malaizé, B.: Age scale of the air in the Summit ice: Implication for glacial-interglacial temperature change, J. Geophys. Res., 102, 19483–19493, 1997.

Severinghaus, J. P. and Brook, E. J.: Abrupt climate change at the end of the Last Glacial Period inferred from trapped air in polar ice, Science, 286, 930–934, doi:10.1126/science.286.5441.930, 1999.

Severinghaus, J. P., Sowers, T., Brook, E. J., Alley, R. B., and Bender, M. L.: Timing of abrupt climate change at the end of the Younger Dryas interval from thermally fractionated gases in polar ice, Nature, 391, 141–146, 1998.

Severinghaus, J. P., Grachev, A., Luz, B., and Caillon, N.: A method for precise measurement of argon 40/36 and krypton/argon ratios in trapped air in polar ice with applications to past firn thickness and abrupt climate change in Greenland and at Siple Dome, Antarctica, Geochim. Cosmochim. Ac., 67, 325–343, 2003.

Severinghaus, J., Albert, M. R., Courville, Z. R., Fahnestock, M. A., Kawamura, K., Montzka, S. A., Mühle, J., Scambos, T. A., Shields, E., Shuman, C. A., Suwa, M., Tans, P., and Weiss, R. F.: Deep air convection in the firn at a zero-accumulation site, central Antarctica, Earth Planet. Sci. Lett., 293, 359–357, 2010.

Shuman, C., Alley, R., Anandakrishnan, S., White, J., Grootes, P., and Stearns, C.: Temperature and accumulation at the Greenland Summit: comparison of high-resolution isotope profiles and satellite passive microwave brightness temperature trends, J. Geophys. Res., 100, 9165–9177, 1995.

Shuman, C., Bromwich, D., Kipfstuhl, J., and Schwager, M.: Multiyear accumulation and temperature history near the North Greenland Ice Core Project site, north central Greenland, J. Geophys. Res., 106, 33853–33856, 2001.

Sjolte, J., Hoffmann, G., Johnsen, S. J., Vinther, B. M., Masson-Delmotte, V., and Sturm, C.: Modeling the water isotopes in Greenland precipitation 1959–2001 with the mesoscale model REMO-iso, J. Geophys. Res., 116, D18105, doi:10.1029/2010JD015287, 2011.

Sowers, T., Bender, M., and Raynaud, D.: Elemental and isotopic composition of accluded O_2 and N_2 in polar ice, J. Geophys. Res., 94, 5137–5150, doi:10.1029/JD094iD04p05137, 1989.

Steen-Larsen, H. C., Masson-Delmotte, V., Sjolte, J., Johnsen, S. J., Vinther, B. M., Bréon, F.-M., Clausen, H. B., Dahl-Jensen, D., Falourd, S., Fettweis, X., Gallée, H., Jouzel, J., Kageyama, M., Lerche, H., Minster, B., Picard, G., Punge, H. J., Risi, C., Salas, D., Schwander, J., Steffen, K., Sveinbjörnsdóttir, A. E., Svensson, A., and White, J. W. C.: Understanding the climatic signal in the water stable isotope records from the NEEM shallow firn/ice cores in northwest Greenland, J. Geophys. Res., 116, D06108, doi:10.1029/2010JD014311, 2011.

Steffensen, J. P., Andersen, K. K., Bigler, M., Clausen, H. B., Dahl-Jensen, D., Fischer, H., Goto-Azuma, K., Hansson, M., Johnsen, S. J., Jouzel, J., Masson-Delmotte, V., Popp, T., Rasmussen, S. O., Röthlisberger, R., Ruth, U., Stauffer, B., Siggaard-Andersen, M.-L., Sveinbjörnsdóttir, A. E., Svensson, A., and White, J. W. C.: High-Resolution Greenland Ice Core Data Show Abrupt Climate Change Happens in Few Years, Science, 321, 680–684, 2008.

Steig, E., Grootes, P., and Stuiver, M.: Seasonnal precipitation timing and ice core records, Science, 266, 1885–1886, 1994.

Stocker, T. F. and Johnsen, S. J.: A minimum thermodynamic model for the bipolar seesaw, Paleoceanography, 18, 1087, doi:10.1029/2003PA000920, 2003.

Svensson, A., Biscaye, P. E., and Grousset, F. E.: Characterization of late glacial continental dust in the Greenland Ice Core Project ice core, J. Geophys. Res., 105, 4637–4656, 2000.

Svensson, A., Andersen, K., Bigler, M., Clausen, H., Dahl-Jensen, D., Davies, S., Johnsen, S., Muscheler, R., Rasmussen, S., Röthlisberger, R., Steffensen, J., and Vinther, B.: The Greenland Ice Core Chronology 2005, 15–42 ka. Part 2: comparison to other records, Quaternary Sci. Rev., 25, 3258–3267, doi:10.1016/j.quascirev.2006.08.003, 2006.

Svensson, A., Andersen, K. K., Bigler, M., Clausen, H. B., Dahl-Jensen, D., Davies, S. M., Johnsen, S. J., Muscheler, R., Parrenin, F., Rasmussen, S. O., Röthlisberger, R., Seierstad, I., Steffensen, J. P., and Vinther, B. M.: A 60 000 year Greenland stratigraphic ice core chronology, Clim. Past, 4, 47–57, doi:10.5194/cp-4-47-2008, 2008.

Svensson, A., Bigler, M., Kettner, E., Dahl-Jensen, D., Johnsen, S. J., Kipfstuhl, S., Nielsen, M., and Steffensen, J. P.: Annual layering in the NGRIP ice core during the Eemian, Clim. Past, 7, 1427–1437, doi:10.5194/cp-7-1427-2011, 2011.

Thomas, E. R., Wolff, E. W., Mulvaney, R., Johnsen, S. J., Steffensen, J. P., and Arrowsmith, C.: Anatomy of a Dansgaard-Oeschger warming transition: High-resolution analysis of the North Greenland Ice Core Project ice core, J. Geophys. Res., 114, 4098, doi:10.1029/2008JD011215, 2008.

M. Guillevic et al.: Past spatial gradients of temperature, accumulation and δ^{18}O in Greenland   **1051**

Vinther, B. M., Clausen, H. B., Johnsen, S. J., Rasmussen, S. O., Andersen, K. K., Buchardt, S. L., Dahl-Jensen, D., Seierstad, I. K., Siggaard-Andersen, M.-L., Steffensen, J. P., and Svensson, A.: A synchronized dating of three Greenland ice cores throughout the Holocene, J. Geophys. Res., 11, D13, doi:10.1029/2005JD006921, 2006.

Vinther, B. M., Buchardt, S. L., Clausen, H. B., Dahl-Jensen, D., Johnsen, S. J., Fisher, D. A., Koerner, R. M., Raynaud, D., Lipenkov, V., Andersen, K. K., Blunier, T., Rasmussen, S. O., Steffensen, J. P., and Svensson, A. M.: Holocene thinning of the Greenland ice sheet, Nature, 461, 385–388, doi:10.1038/nature08355, 2009.

Voelker, A. H. L.: Global distribution of centennial-scale records for Marine Isotope Stage (MIS) 3: a database, Quaternary Sci. Rev., 21, 1185–1212, 2002.

Weller, G. E. and Schwerdtfeger, P.: New data on the thermal conductivity of natural snow, J. Glaciol., 10, 309–311, 1971.

Werner, M., Mikolajewicz, U., Heimann, M., and Hoffman, G.: Borehole versus isotope temperatures on Greenland: seasonality does matter, Geophys. Res. Lett., 27, 723–725, 2000.

Werner, M., Heimann, M., and Hoffmann, G.: Isotopic composition and origin of polar precipitation in present and glacial climate simulations, Tellus, 53B, 53–71, 2001.

Wolff, E. W., Chappellaz, J., Blunier, T., Rasmussen, S., and Svensson, A.: Millennial-scale variability during the last glacial: The ice core record, Quaternary Sci. Rev., 29, 2828–2838, doi:10.1016/j.quascirev.2009.10.013, 2009.

Yen, Y.-C.: Review of thermal properties of snow, ice, and sea ice, US Army, Corps of Engineers, Cold Regions Research and Engineering Laboratory, 1981.

4.3 Future work: comparison of MIS3 and MIS5 spatial gradients
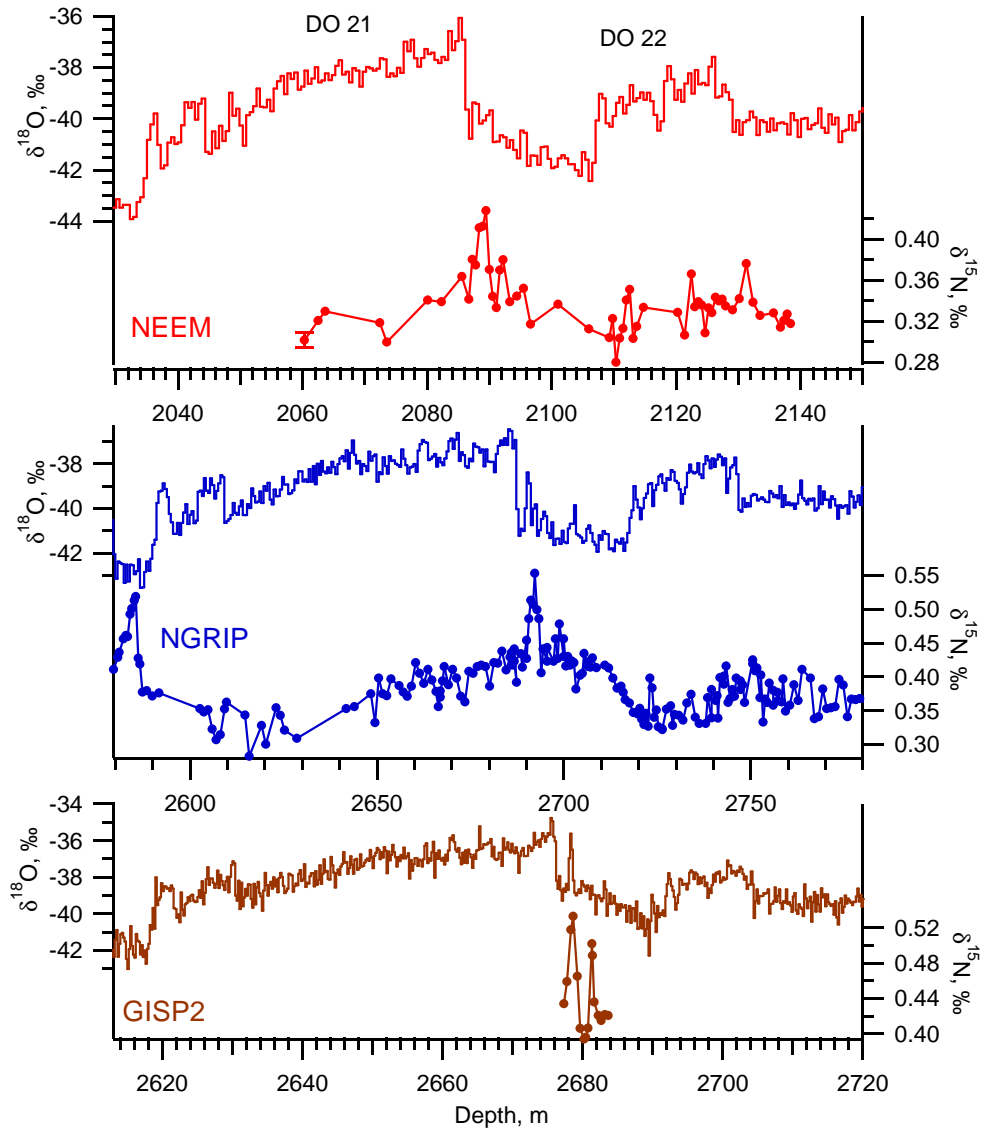
Figure 4.2: DO 21 and 22: $\delta^{18}O$ and $\delta^{15}N$ measured in the GISP2, NGRIP and NEEM ice core. NEEM $\delta^{18}O$: NEEM water isotope consortium, pers. com. NEEM $\delta^{15}N$: new data measured at LSCE, this study. NGRIP $\delta^{18}O$: NGRIP members (2004). NGRIP $\delta^{15}N$: Capron et al. (2010a,b); Kindler et al. (2014). GISP2 $\delta^{18}O$: Grootes and Stuiver (1997). GISP2 $\delta^{15}N$: Grachev et al. (2007).

In the previous section we have reconstructed the spatial gradients of water isotopes, temperature and accumulation rate during a sequence of DO events of MIS3. We have shown that the temperature sensitivity of water isotopes (α) varies for each DO event and for each ice core site in Greenland. In the next section, we will see that the NGRIP α varies also at orbital timescales.

The extension of such spatial reconstructions for different past periods is needed in order to test their robustness along different climate backgrounds, and for comparisons with climate model results. Climate models equipped with water isotopes, $\delta^{15}N$-based tempera-

ture reconstructions and water isotope data will allow to fully understand the mechanisms driving changing patterns of $\delta^{18}O$ (precipitation intermittency, moisture source effects) with different ice sheet and orbital configurations. The information on past spatial patterns of accumulation rates is also critical for simulations of the Greenland ice sheet.

In this section, we only present new NEEM $\delta^{15}N$ data, together with published NGRIP and GISP2 $\delta^{15}N$ data, that would allow to reconstruct spatial gradients of temperature and accumulation rate over DO 21 and DO 22. This period corresponds to an intermediate climate configuration compared to Interglacials or the LGM, in terms of ice sheet size, CO_2 mixing ratio, sea-level and constitutes therefore a time slice complementary to MIS3 for model-data comparison.

4.3.1 Data

Water isotopes NEEM water isotopes are available as average over 55 cm sample length. This corresponds to an average time resolution of 73 a for DO 21 to DO 22. The samples have been measured at LSCE and CIC by the respective water isotope laboratories. The uncertainty is 0.07 ‰. NGRIP and GRIP water isotopes were measured at CIC, also available as 55 cm averages (uncertainty of 0.07 ‰ NGRIP members, 2004; Johnsen et al., 1992). GISP2 water isotopes have been measured at the University of Washington's Quaternary Isotope Laboratory (Grootes and Stuiver, 1997), and available as 20 cm averages. The uncertainty is 0.05 to 0.1 ‰.

Nitrogen isotopes For the NEEM ice core, new $\delta^{15}N$ data have been measured during my PhD at LSCE by F. Prié, A. Landais and myself, using the melt-refreeze technique described in Landais et al. (2004c). For NGRIP, $\delta^{15}N$ data have been measured at LSCE and published in Capron et al. (2010a,b) and Kindler et al. (2014). The pooled standard deviation is 0.006 ‰ for all LSCE data. The GISP2 $\delta^{15}N$ data covering DO 21 have been measured by Grachev et al. (2007) with a pooled standard deviation of 0.005 ‰ (Petrenko et al., 2006).

4.3.2 Future work

The same methodology as in Guillevic et al. (2013) will be applied to reconstruct the temperature and accumulation rate at NEEM, NGRIP and GISP2 using the available $\delta^{15}N$ data and the Goujon firn model, on the AICC2012 timescale. These reconstructions will be compared with the ones performed by Kindler et al. (2014) using the Schwander firn model and the ss09sea06bm timescale. As shown in Sect. 3.4.4, the timescale used has an effect on the reconstruction of temperature and accumulation rate. We will test the effect of using the duration of GS-22 as proposed by Vallelonga et al. (2012), which is slightly longer than the AICC2012 duration. The obtained spatial gradients of water isotope, temperature and accumulation rate for MIS5 will be compared to the one previously obtained for MIS3.

A first look at the water isotope profiles from the NEEM, NGRIP and GISP2 ice cores seems to confirm the spatial pattern of $\delta^{18}O$ observed during MIS3: at the onset of DO events 21 and 22, the increase in $\delta^{18}O$ is small at GISP2 compared to the more northern sites NEEM and NGRIP.

4.4   Temperature reconstruction from 10 to 120 kyr b2k from the NGRIP ice core

In this section is reported the article accepted 19th Jan. 2014 in *Clim. Past* as Kindler et al., 2014. All measurements and climatic reconstructions (temperature, accumulation rate) have been made by Ph. Kindler. Two stays at the University of Bern of nearly two months in total really made possible to have developed scientific discussion on the obtained datasets. I contributed to the analyses and interpretation of the climatic reconstructions. The article writing was done by Ph. Kindler.

Temperature reconstruction from 10 to 120 kyr b2k from the NGRIP ice core

P. Kindler[1], M. Guillevic[2,3], M. Baumgartner[1], J. Schwander[1], A. Landais[2], and M. Leuenberger[1]

[1]Climate and Environmental Physics, Physics Institute and Oeschger Centre for Climate Change Research, University of Bern, 3012 Bern, Switzerland

[2]Institut Pierre-Simon Laplace/ Laboratoire des Sciences du Climat et de l'Environnement, Gif-sur-Yvette, France

[3]Centre for Ice and Climate, Niels Bohr Institute, Universtity of Copenhagen, Copenhagen, Denmark

Abstract. In order to reconstruct the temperature of the North Greenland Ice Core Project (NGRIP) site, new measurements of δ^{15}N have been performed covering the time period from the beginning of the Holocene to Dansgaard–Oeschger (DO) event 8. Together with previously measured and mostly published δ^{15}N data, we present for the first time a NGRIP temperature reconstruction for the whole last glacial period from 10 to 120 kyr b2k (years before 2000 AD) including every DO event based on δ^{15}N isotope measurements combined with a firn densification and heat diffusion model. The detected temperature rises at the onset of DO events range from 5 °C (DO 25) up to 16.5 °C (DO 11) with an uncertainty of ±3°C. To bring measured and modelled data into agreement, we had to reduce the accumulation rate given by the NGRIP ss09sea06bm time scale in some periods by 30 to 35%, especially during the last glacial maximum. A comparison between reconstructed temperature and δ^{18}O$_{ice}$ data confirms that the isotopic composition of the stadial was strongly influenced by seasonality. We evidence an anticorrelation between the variations of the δ^{18}O$_{ice}$ sensitivity to temperature (referred to as α) and obliquity in agreement with a simple Rayleigh distillation model. Finally, we suggest that α might be influenced by the Northern Hemisphere ice sheet volume.

1   Introduction

Deep ice core drillings in Greenland revealed large millennial scale variability in the water isotopic composition δ^{18}O$_{ice}$ during the last glacial, reflecting local temperature variations (Johnsen et al., 1972; Dansgaard et al., 1982), known today as Dansgaard–Oeschger (DO) events. The 25 DO events identified in the North Greenland Ice Core Project (NGRIP) ice core (NGRIP members, 2004) are characterised by a rapid temperature increase followed by a gradual cooling back to stadial conditions. These rapid temperature variations are at least of northern hemispheric extent (Voelker, 2002) and can be clearly traced in different ice core climate proxies, like δ^{18}O$_{ice}$ (Dansgaard et al., 1993), dust content (Ruth et al., 2003) and other aerosol contents (Mayewski et al., 1997), greenhouse gas concentrations (Huber et al., 2006b; Schilt et al., 2010), as well as in other climate proxies such as sea sediments (Bond et al., 1993; Deplazes et al., 2013) and speleothems (Fleitmann et al., 2009; Kanner et al., 2012; Wang et al., 2001).

It is widely assumed that DO events are linked to reorganisations and/or variations in the strength of the Atlantic Meridional Overturning Circulation (AMOC) (Broecker et al., 1990). In addition, a southward shift of the Intertropical Convergence Zone (ITCZ) during Greenland cold (stadials and Heinrich) events is suggested to explain the similar DO pattern seen in Greenland ice cores and in tropical records (Chiang and Bitz, 2005). While the actual trigger and the detailed mechanisms involved in DO events remain unclear, recent work underlines the role of sea ice cover in the Arctic and especially in the Nordic Seas (Li et al., 2010; Dokken et al., 2013; Petersen et al., 2013) where its rapid retreat and regrowth would be able to alter Greenland's temperature on decadal or even shorter time scale.

Most of the DO events have an Antarctic analogue called Antarctic Isotopic Maximum (AIM) (EPICA community members, 2006; Blunier and Brook, 2001; Capron et al., 2010a; Wolff et al., 2010). The slow and quite smooth AIM temperature increases precede the rapid Greenland warmings by several hundreds to thousands of years (Capron et al., 2010b). These findings are in line with the concept of the 'thermal bipolar seesaw' where the Southern Ocean is considered as a heat reservoir which delivers heat via the AMOC to the North Atlantic and the Northern Sea (Stocker and Johnsen, 2003).

A first qualitative Greenland temperature reconstruction

Correspondence to: P. Kindler (kindler@climate.unibe.ch)

Table 1. Overview of the δ^{15}N measurements performed on the NGRIP ice core. GS and GI denote Greenland stadial and interstadial, respectively.

period	NGRIP depth, m	measured at	references
Holocene to DO 8	1391.11 – 2092.52	KUP	this work
DO 8 to DO 17	2085.50 – 2463.83	KUP	Huber et al. (2006b)
DO 18, 19, 20	2464.09 – 2620.24	LSCE	Landais et al. (2004a)
GI-21	2623.07 – 2649.47	LSCE	this work
GS-22, GI-21	2650.45 – 2743.95	LSCE	Capron et al. (2010b)
GS-23, GI-22	2744.5 – 2796.65	LSCE	Capron et al. (2010a)
GS-23	2800.72 – 2873.87	LSCE	this work
DO 23 to 25	2875.44 – 3083.33	LSCE	Landais et al. (2005)
			Capron et al. (2012)

for the last glacial has been obtained using $\delta^{18}O_{ice}$ and the present-day spatial relationship between temperature and water isotopes of $0.67\,‰\,°C^{-1}$ (Johnsen et al., 1989), leading to DO temperature amplitudes of $\sim7\,°C$ (Johnsen et al., 1992). However, temperature reconstructions based on the deconvolution of the borehole temperature (Johnsen et al., 1995; Cuffey et al., 1995) made clear that the present-day spatial gradient cannot be applied to the past. An alternative quantitative method is provided by nitrogen isotopes of the entrapped air. This proxy is sensitive to local firn processes only: firn thickness, temperature and temperature gradient as well as air entrapping processes (Schwander, 1989; Severinghaus et al., 1998; Severinghaus and Battle, 2006; Huber et al., 2006a). The obtained temperature variations of 3 to $16\,°C$ within decades (Capron et al., 2012; Huber et al., 2006b; Landais et al., 2005; Lang et al., 1999; Severinghaus et al., 1998) are in general larger than the ones obtained by climate model simulations (up to $7.5\,°C$, e.g., review by Kageyama et al., 2013). Kageyama et al. (2013) underline the varying response of the oceanic circulation and the sea ice cover to the fresh water hosing between models used to simulate a stadial period, explaining the diversity of modelled temperature difference between stadials and interstadials. A complete Greenland temperature record covering the last glacial may help to investigate this model-data discrepancy. Moreover, while a clear relationship between the Greenland stadial durations and the AIM warming events has been established (e.g., EPICA community members, 2006), a possible relationship between Antarctic and subsequent Greenland warming amplitudes has not been tested for the full glacial period yet.

The aim of this paper is first to quantitatively reconstruct the NGRIP temperature over the full last glacial based on δ^{15}N data. To do so, we present the first NGRIP δ^{15}N data covering the period from the beginning of the Holocene back to DO 8, completing the already existing δ^{15}N records (Table 1). The combined δ^{15}N records together with firn modelling are used to reconstruct the past NGRIP temperature and accumulation rate from 10 to 120 kyr. Then, we investigate the sensitivity of Greenland water isotopes to the reconstructed temperature changes at millennial and orbital time

scales and its possible relation to the ice sheet size.

2   Method and data

2.1   Paleothermometry method based on air δ^{15}N measurements

To reconstruct the surface temperature evolution at the NGRIP site, we combine air δ^{15}N measurements with simulations performed with a firn densification and heat diffusion model (Severinghaus et al., 1998; Leuenberger et al., 1999; Lang et al., 1999; Huber et al., 2006b; Schwander et al., 1997).

The upper most 50 to 100 m of an ice sheet, where the air in the still open pores can exchange with the atmosphere, are called firn. In this layer the snow is gradually transformed to ice and at its bottom, the air is enclosed into bubbles. The processes relevant for the results presented here occur in the firn. With respect to the air molecule mobility, one can divide the firn into three parts: convective, diffusive and non-diffusive zones. In the generally small upper convective zone the composition of the air remains nearly unchanged compared to ambient air whereas a gradual enrichment occures in heavy molecules within the diffusive zone due to gravitation, i.e. ^{15}N/^{14}N ratio is increased. The enrichment stops at the lower end of the diffusive zone, at the lock in depth (LID). With the barometric formula (Craig et al., 1988; Schwander, 1989) one finds (in delta-notation):

$$\delta^{15}N_{grav}(z) = (e^{\frac{\Delta m g z}{RT}} - 1) \cdot 1000 \approx \frac{\Delta m \cdot g \cdot z}{R \cdot T} \cdot 1000 \qquad (1)$$

where z is the depth of the diffusive zone, g the acceleration constant, Δm the mass difference between the isotopes, R the ideal gas constant and T the mean firn temperature. Present-day δ^{15}N measurements in firns show that no further gravitational enrichment occurs below the LID (Landais et al., 2006; Buizert et al., 2012). A temperature gradient in the firn causes a second important process called thermal diffusion, which leads, for example during a surface warming, to an additional enrichment of the ^{15}N/^{14}N ratio towards the bottom of the firn. Because gas diffuses about ten times faster

than heat through the firn (Paterson, 1994), the thermal diffusion signal of a rapid temperature increase at the beginning of DO events can fully develop before the warmer temperatures propagate through the firn column and therefore slowly diminish the thermal signal. Thermal diffusion can be characterised as (Severinghaus et al., 1998):

$$\delta^{15}N_{therm} = \left[\left(\frac{T_t}{T_b}\right)^{\alpha_T} - 1\right] \cdot 1000 \approx \Omega \cdot \Delta T \qquad (2)$$

where T_t and T_b stand for the temperature at the top and the bottom of the firn, α_T for the thermal diffusion constant ($\alpha_T = 4.61198 \cdot 10^{-3} \cdot ln(\overline{T}/113.65\mathrm{K})$, $\overline{T}$ stands for the average firn temperature (Leuenberger et al., 1999)), Ω for the thermal diffusion sensitivity and ΔT for the temperature difference (T_t-T_b). After several hundreds of years, when the temperature distribution in the firn is uniform again (neglecting geothermal influences), the thermal diffusion effect disappears but the signal of rapid warming is preserved by the $^{15}N/^{14}N$ ratio in air enclosed in bubbles.

As the air is able to diffuse down into the firn, a climatic signal will be registered in the gas phase deeper down in the ice core than in the ice phase. The resulting difference in depth is called Δdepth and the age difference of the ice and the gas at a certain depth called Δage.

2.2 New and published $\delta^{15}N$ measurements

The $\delta^{15}N$ dataset used for this work is a composite of measurements of two laboratories, Laboratoire des Sciences du Climat et de l'Environnement (LSCE), Gif-sur-Yvette and the Climate and Environmental Physics Division (KUP) of the Physics Institute of the University of Bern (Tab. 1). The data from KUP (Holocene to DO 17) has been measured with an online setup with an uncertainty of $\pm 0.02\,\%o$ in $\delta^{15}N$ (Huber et al., 2003; Huber and Leuenberger, 2004). For the new dataset, 384 ice samples (up to 45 cm long) have been measured covering the period from the beginning of the Holocene to DO 8. 11 samples have been rejected due to a failure of the system. The remaining 373 measurements have been divided into 600 data points, each representing 10 to 25 cm of ice depending on the original sample length which is influenced by the ice availability and ice quality. The ice samples investigated at LSCE (DO 18 to 25) have been measured with a melt-refreeze technique with a precision of $\pm 0.006\,\%o$ (Landais et al., 2003, 2004c). Additional LSCE $\delta^{15}N$ data between DO 21 and DO 23 is published here for the first time (Tab. 1).

2.3 Strategy for surface temperature reconstruction

The temperature reconstruction was done with the firn densification and heat diffusion model from Schwander et al. (1997) by using the NGRIP ss09sea06bm age scale (in years before 2000 AD or yr b2k) (NGRIP members, 2004; Johnsen et al., 2001; Andersen et al., 2006). The ss09sea06bm
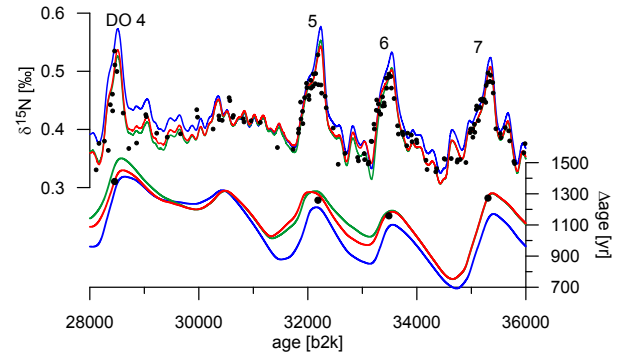

Fig. 1. The effects of the three steps of the temperature reconstruction on the modelled $\delta^{15}N$ and Δage are marked with three different colours on a gas age scale: step (i) (α adjustment) in blue, step (ii) (accumulation and temperature adjustment) in green and step (iii) (manual adjustment where needed) in red. Black dots are $\delta^{15}N$ and Δage measurements.

timescale is the most appropriate since it is the only age scale with accumulation rate reconstructions over the entire studied time period. Transferring our final model input to the GICC05 age scale leads only to minor changes within the uncertainties in the model output compared to the used ss09sea06bm age scale, so we are confident that our results are valid for both age scales.

The input parameters of the model are age, accumulation rate and temperature. The temperature is calculated according to

$$T = (\delta^{18}O_{ice} + 35.1[\mathrm{permil}])/\alpha_{fit} + 241.6\mathrm{K} + \beta_{fit} \qquad (3)$$

which expresses the qualitative similarity between the temperature and $\delta^{18}O_{ice}$. 35.1‰ and 241.6 K stand for NGRIP Holocene values (NGRIP members, 2004), α_{fit} and β_{fit} denote scaling parameters to take into account the changing sensitivity between temperature and $\delta^{18}O_{ice}$ as outlined in detail below. The used accumulation and $\delta^{18}O_{ice}$ data from the NGRIP ss09sea06bm time scale has been splined with a cut-off-period (COP) of 200 yr in order to match the observed variability in $\delta^{15}N$ with the model. The basic idea is to vary the temperature (α_{fit} and β_{fit}) and the accumulation rate in such a way that the model is able to reproduce the measured $\delta^{15}N$ data. Note that the use of Eq. 3 to find this best fit is not compelling but it is technically meaningful because it expresses a first order relation between temperature and isotopes. The fitted values of α_{fit} and β_{fit} is only in rough agreement with the α-sensitivity discussed later. Three steps are followed to infer the NGRIP surface temperature: (i) rough adjustment of the temperature-$\delta^{18}O_{ice}$-sensitivity (α_{fit}) to approximate the shape of the modelled $\delta^{15}N$, (ii) refinement of the adjustment by varying the accumulation rate and a temperature shift (β_{fit}) for best fitting the Δage

and (iii) final manual tuning where needed. The effect of each step on the modelled δ^{15}N and Δage can be seen for the time period DO 4 to 7 in Fig. 1.

In the first step, 19 different α_{fit}-scenarios have been calculated by varying the α_{fit} value in 0.02 steps from 0.24 to 0.60 ‰/°C. As in Huber et al. (2006b) the initial accumulation rate was reduced by 20% and a constant temperature shift of β_{fit}= +4 K was introduced to match approximately the measured Δage. Without these corrections the modelled Δage is underestimated by up to 400 yr in some parts, especially in the time period from 60 to 10 kyr (Fig. 7). In order to find the best α_{fit} in a 2 kyr time window, the sum of the squared differences between the δ^{15}N model-output of a scenario and the spline through the measured data was calculated and the scenario with the smallest sum was determined. Thereafter the time window was shifted continuously by 250 yr and the same procedure was applied until all data points were covered. At the end of step one, we obtain a best α_{fit} value every 250 yr, these values are splined for further calculations with a COP of 2 kyr. With these values, which vary roughly between 0.28 and 0.42 ‰/°C, the model is able to coarsely reproduce the measured δ^{15}N data (Fig. 1, blue lines).

To further refine the adjustment in a second step, the accumulation rate is varied from 60 to 100% in 5% steps and the temperature offset β_{fit} from +0 to +8 K in 1 K steps while retaining the α_{fit} values from step one. This yields 81 different combinations and we proceed in the same way as in step one to find the best accumulation rate and temperature shift to match the measured δ^{15}N data. The time dependent temperature shift β_{fit} varies within 2 K around +4 K. With these three tuned parameters (α_{fit}, β_{fit} and accumulation) the model is able to reproduce the measured δ^{15}N data generally well, both the amplitudes as well as the timing of the DO events. The Δage output of the model and the calculated Δdepth are also in agreement with the measured data (Fig. 1, green lines).

The parts of the reconstruction which do not yet match are now tuned manually (using parameters β_{fit} and accumulation) on short periods (centuries) in a third step so that the model reproduces the measured data within their uncertainty (Fig. 1, red lines). Manual adjustment was necessary especially in the Bølling Allerød-Younger Dryas-transition and in the periods of DO 16 and 17, DO 19 and 20 and DO 23 to 25. The tuning was done by a linear adjustment of the temperature evolution between two selected time points in a given time period (e.g. a DO event). In addition, the accumulation rate was enhanced or lowered slightly in parts where the timing was not yet satisfactory. After step three, modelled δ^{15}N as well as Δage and Δdepth are in agreement with the measured data.

The 2σ uncertainty of the temperature amplitudes of DO events amounts to ±3°C (Huber et al., 2006b). Deviations (e.g. amplitude and timing) of our temperature reconstruction compared to other studies using the δ^{15}N method

can be explained by the fact that other investigators have used different models (e.g. Goujon model (Goujon et al., 2003)) and data-adjustment methods or by using a different approach, e.g. the combined use of δ^{15}N and δ^{40}Ar (Severinghaus et al., 1998; Landais et al., 2004b; Kobashi et al., 2011).

2.4 Damping of the δ^{15}N signal in the firn

High-resolution (20 mm) NGRIP δ^{18}O$_{ice}$ data has shown that stadial-interstadial transitions can occur within a few years, e.g. the transition at DO 8 occurred within 21 yr (Thomas et al., 2009; Steffensen et al., 2008). We cannot observe such a rapid increase at the onset of DO 8 in the NGRIP δ^{15}N record (1.1 m data resolution) nor in the NEEM record (0.55 m data resolution, Fig. 2a). Also the duration of the temperature increase at DO 8 (roughly 200 yr) of our reconstructed temperature is in contrast to the duration suggested by the high-resolution δ^{18}O$_{ice}$ data.

In addition to the lower δ^{15}N resolution, two reasons could explain the discrepancy of the longer duration observed in the measured δ^{15}N data as well as in the reconstructed temperature: (i) during extremely rapid events (decades), the δ^{15}N (especially the δ^{15}N$_{therm}$) formed at the LID is damped by gas diffusion in the firn and mostly during the bubble close-off process that occurs over a depth interval of more than 10 m (Spahni et al., 2003), resulting in a smoother δ^{15}N signal in the ice. The attenuation effect on the gas signal during the enclosure process at the bottom of the firn is included neither in the Schwander nor in the Goujon model (Schwander et al., 1997; Goujon et al., 2003). To our knowledge, only Grachev and Severinghaus (2005) have studied such an effect on δ^{15}N variations and thus on surface temperature reconstruction. (ii) as it is explained in Sect. 2.3, the δ^{18}O$_{ice}$ data, which is used in the model input for a first temperature estimate, has a resolution of 55 cm (corresponding to 10 to 100 yr) and is splined with a COP of 200 yr in order to reduce the signal variability in the firn densification and heat diffusion model to a level, which is in agreement with the measured δ^{15}N profile.

To investigate possibility (i), we model a highly simplified scenario to mimic DO 8, where the temperature is increased by +10°C (from −46 to −36°C) with a concomitant accumulation increase from 0.06 to 0.10 meters ice equivalent (m i.e.) within 20 yr, according to the timing proposed by Thomas et al. (2009) for DO 8. Hereby we first calculate with the Schwander model the corresponding δ^{15}N signal (without the proposed damping, dark blue dotted line in Fig. 2a) which is then used as an input for the firn model of Spahni et al. (2003). The Spahni model calculates the smoothing of an initial surface signal at the LID with respect to gas diffusion and the additional gradual bubble enclosure. The dashed (effect of diffusion) and the solid line (diffusion and gradual gas enclosure) scenarios in Fig. 2a are calculated by folding the original δ^{15}N signal (dotted line) with the characteris-
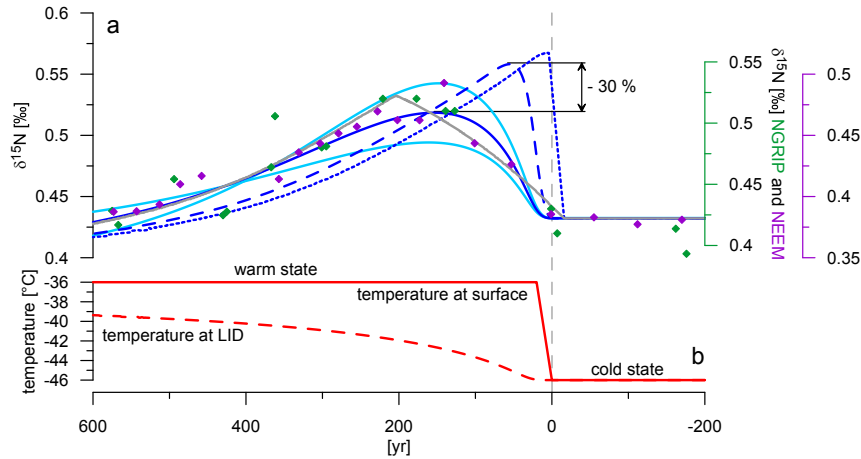
Fig. 2. Simplified model calculation for a possible δ^{15}N damping in the firn due to the gradual bubble enclosure. (a) The dark blue lines represent a scenario where a +10°C temperature increase (from -46 to -36°C) within 20 yr is assumed. The dotted line corresponds to the δ^{15}N signal as calculated by the Schwander model (Schwander et al., 1997) which then serves as an input for the firn model from Spahni et al. (2003) to calculate the damping caused by diffusion (dashed line) and additional gradual bubble enclosure (dark blue solid line). The light blue lines show a δ^{15}N signal smoothed by gradual bubble enclosure of a +7 and +13°C temperature increase which corresponds to the uncertainty interval of the temperature amplitude. The grey line shows a δ^{15}N signal as calculated by the Schwander model where the input data of a temperature increase is splined with 200 yr. Diamonds represent δ^{15}N measurements for DO 8 from NGRIP (green, uncertainty: ± 0.02‰, this study) and NEEM (violet, uncertainty: ± 0.006‰, from Guillevic et al. (2013)). The scale on the x-axis is chosen in a way that 0 yr corresponds to the beginning of the surface warming, marked by the grey dashed line. δ^{15}N data is plotted on a gas age scale. (b) Surface (solid line) and LID temperature (dotted line) are given for the +10°C temperature increase as calculated by the Schwander model.

tic age distribution of the initial cold state. This approach is physically not fully correct. On the one hand, the used δ^{15}N signal input for the Spahni model is not a surface signal but is generated in the firn itself. On the other hand, using a constant age distribution is not correct either: after a certain time period the surface warming penetrates to depths where the bubbles are enclosed (Fig. 2b, dashed line), altering the snow structure and modifying the age distribution. To allow for a small temperature rise at the LID, we use an age distribution corresponding to -45°C, slightly higher than the initial temperature of -46°C.

In Fig. 2a, the results of our simplified model calculations are compared to the measured δ^{15}N values of DO 8 from NGRIP (green diamonds) and NEEM (violet diamonds), where a temperature increase of 8.8$\pm$1.2°C has been estimated (Guillevic et al., 2013). As the shape of the measured data and the modelled dark blue solid line agrees well, our simplified calculations indeed suggest for the considered scenario (+10°C in 20 yr) a significant damping of the signal amplitude of roughly -30% due to gradual bubble enclosure compared to diffusion only. We refrain from calculating the damping of longer temperature increases because the LID-temperature would be affected significantly by the surface temperature increase, complicating the estimation of a unique and appropriate age distribution. In general, the damping decreases with increasing duration of a temperature

rise as well as with a smaller temperature amplitude and vice versa (Spahni et al., 2003).

Following possibility (ii), we spline the initial temperature scenario (+10°C in 20 yr) with 200 yr and use this data to calculate a δ^{15}N signal with the Schwander model (Fig. 2a, grey line). Figure 2a shows that the effect of this initial smoothing of the input data is of similar magnitude regarding the signal amplitude as the effect arising from the signal damping calculated by the Spahni model.

While the duration of temperature increases may be overestimated in our reconstruction, we are confident that our calculated temperature amplitudes at DO events using approach (ii) should be valid within the given uncertainty. Remaining local disagreements between modelled and measured data can be cleared by manual tuning as described in Sect. 2.3. These arguments also provide confidence in other studies which used δ^{18}O$_{ice}$ data smoothed up to 70 yr or more to estimate the corresponding site temperature (Capron et al., 2010a; Guillevic et al., 2013; Huber et al., 2006b; Landais et al., 2005).

For future work it is advisable to investigate the δ^{15}N damping in the firn in more detail with transient models and a highly resolved measurement of an exemplary DO event (e.g. DO 1, 5, 8 or 19). Additionally, it would make sense to implement a gradual bubble enclosure process in firn densification and heat diffusion models which are currently used to

reconstruct the temperature evolution of a specific site. Also the calculations for $\delta^{15}N_{therm}$ should be further refined in these models. Currently, an instantaneous signal during a surface warming is assumed at the bottom of the firn and the temperature gradient, which is important for the determination of the $\delta^{15}N_{therm}$, depends only on two temperature points (top and bottom). As these two assumptions do not take into account the time lag of the signal due to diffusion nor the actual temperature profile in the firn, the model may slightly overestimate the $\delta^{15}N_{therm}$ at the beginning of a temperature increase.

3 Results and discussion

The results are divided into 3 sections. First we will discuss the new temperature reconstruction (Sect. 3.1), followed by a comparison between the NGRIP $\delta^{18}O_{ice}$ to temperature relationship on millennial, glacial and orbital time scales (Sect. 3.2). Finally, we discuss the inferred accumulation rate (Sect. 3.3).

3.1 NGRIP surface temperature reconstruction

The reconstructed NGRIP temperature evolution from 10 to 120 kyr b2k, together with the used $\delta^{18}O_{ice}$ data and the measured and modelled $\delta^{15}N$ data, is shown in Fig. 3. The temperature evolution for the period Younger Dryas-Holocene (DO 0) to DO 8 is presented here the first time whereas the temperature evolution for DO 9 to DO 25 is a reanalysis of existing data.

To define the temperature amplitude of a DO event we specify the onset and the end of the event based on the following criteria. The DO event onset corresponds to the difference quotient exceeding $0.25°C/50\,yr$ ($0.05°C\,decade^{-1}$), which is equivalent to about one-tenth of the increase rates for DO 9 to 17 found by Huber et al. (2006b). The end of the event was determined likewise, i.e. when the temperature increase rate became smaller than $0.05°C\,decade^{-1}$. The 50 yr time interval was chosen because it is long enough to overcome small-scale temperature variations. When one would use a longer time interval of 100 yr or longer, the durations of the temperature increases tend to be prolonged in an unrealistic way and the corresponding temperature amplitudes are in general slightly reduced.

Generally, the DO events feature temperature amplitudes between 9 and 13°C which are independent of the background of the climate state (different marine isotope stages (MIS)). The smallest temperature amplitude of 5°C is obtained for DO 25. This is 2 degrees more than the result from Capron et al. (2012) but within their uncertainty of $\pm2.5°C$. On the other hand the largest amplitude of our temperature reconstruction is DO 11 with 16.5°C, where Huber et al.

(2006b) found a slightly smaller rise of 15°C but still within the given uncertainty.

DO events 2, 7 (Fig. 3c), 11 and 18 feature a temperature increase in two steps which is different from the three DO types found by Capron et al. (2010a). The duration of the small drop between the two increases in temperature generally lasts for less than 100 yr with amplitudes of less than 1°C. As both sections of such a split temperature increase exhibit about the same temperature increase rate they were treated as one increase. Also DO 9 features basically a stop (Fig. 3d). As the temperature plateau in this reconstruction is of longer duration (about 300 yr) than the following temperature increase (140 yr), the temperature plateau was not taken into account which leads to ΔT=6.5°C. This is lower in amplitude than the findings from Huber et al. (2006b) (ΔT=9°C), which would be better in line when one includes both temperature rises resulting in ΔT=8°C. DO 5 (Fig. 3b) may also be considered to have a small temperature reversal at the beginning. When the 2°C temperature drop just before the onset of the DO event is included, we obtain ΔT=14.5°C. As the second (main) temperature increase starts more gradually which is not the case for the DO events which feature a two-step temperature increase mentioned above, we exclude the small temperature drop before DO 5 from our temperature increase calculations.

Another type of temperature increase can be observed for DO 8, 12, 22 and maybe 17 where a slight long-term warming occurs before the start of the rapid temperature increase. They are roughly 3.5°C in 950 yr (DO 8), 3°C in 1300 yr (DO 12), 1°C in 3500 yr (DO 17) and 1°C in 2800 yr (DO 22). The long term warming before DO 8 is comparable to the findings of Huber et al. (2006b) whereas they find a more pronounced long term warming of about 3 to 4°C for DO 17. Looking at MIS 3, each stadial where a Heinrich (H) event took place (Heinrich stadial) exhibits a long term warming (Fig. 3a, orange shaded stadials). The yellow shaded stadials in Fig. 3a, situated around the last glacial maximum, experience H events but do not manifest any obvious long term warming before a DO event. The warming at the NGRIP site during H stadial 4 (GS-9) could be of larger spatial extent as Guillevic et al. (2013) found also a slight long term warming at the NEEM site.

Based on pollen records, Genty et al. (2010); Sánchez Goñi et al. (2000) demonstrated that Europe featured a colder climate during periods of H events. In contrast, our NGRIP temperature reconstruction does not show particularly cold temperatures during these stadials.

The finding of the linear relationship between the duration of the Greenland stadial and the corresponding AIM temperature amplitude is explained by the bipolar seesaw mechanism (EPICA community members, 2006; Capron et al., 2010a; Vallelonga et al., 2012; Stocker and Johnsen, 2003). We see no correlation between the NGRIP DO temperature amplitudes and the corresponding Greenland stadial durations (Fig. 4a) nor the AIM temperature amplitudes (Fig. 4b).
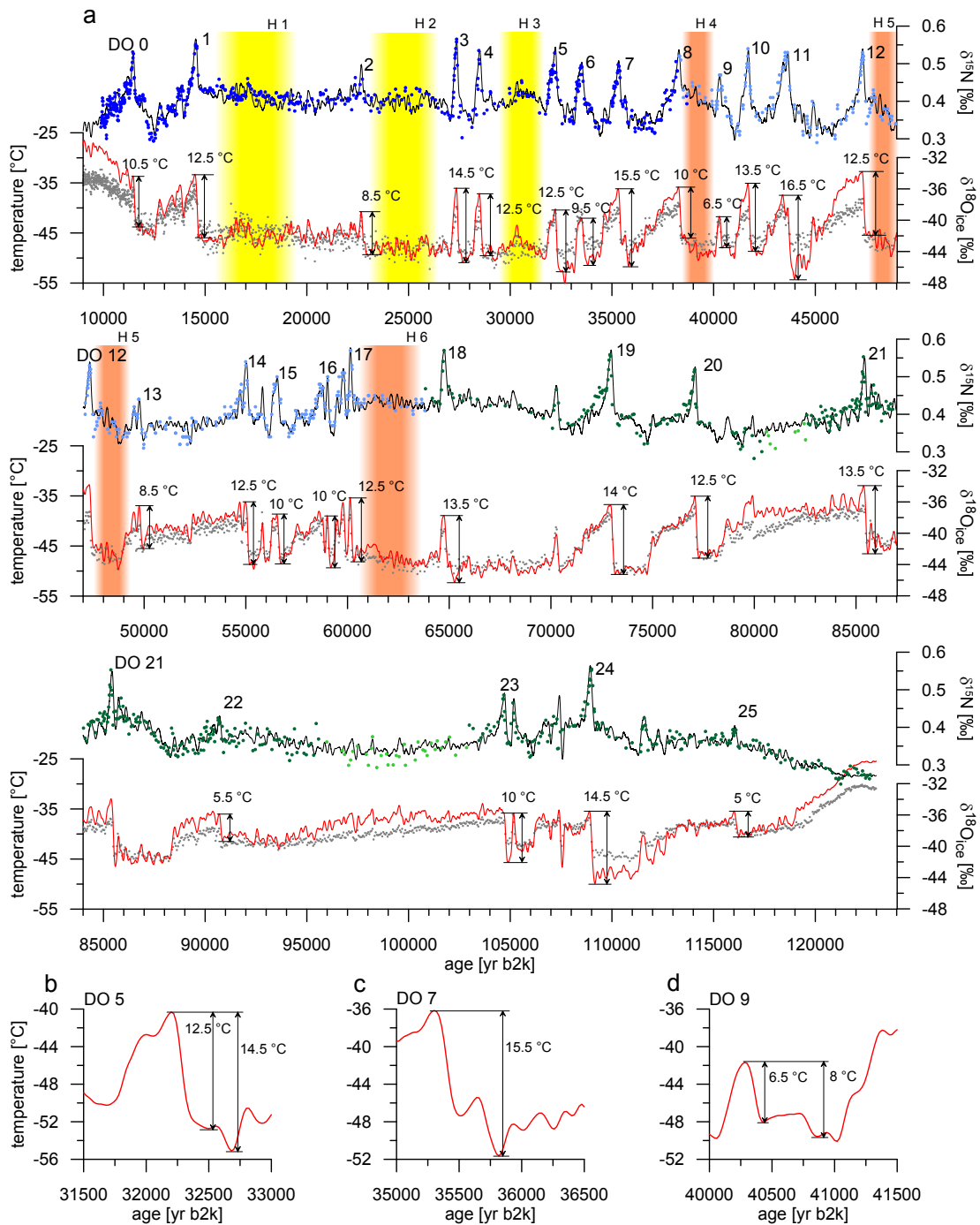
Fig. 3. (a) NGRIP temperature reconstruction from 10 to 120 kyr b2k on the ss09sea06bm time scale. Red line: temperature reconstruction, grey points: $\delta^{18}O_{ice}$ (0.55m mean data, (NGRIP members, 2004)) on ice age scale, dark blue points: new $\delta^{15}N$ measurements, this study, light blue points: measurements from Huber et al. (2006b), dark green points: published $\delta^{15}N$ measurements from LSCE (Landais et al., 2004a, 2005; Capron et al., 2010a,b, 2012), light green points: unpublished $\delta^{15}N$ measurements from LSCE, black line: modelled $\delta^{15}N$, all $\delta^{15}N$ data is plotted on the gas age scale. Because there is no exact agreement in the literature about the timing and the duration of H events (Hemming, 2004; Sánchez Goñi and Harrison, 2010; Jonkers et al., 2010; Roche et al., 2004), we do not explicitly indicate the H events themselves but the stadials in which they took place by colouring the corresponding time period in yellow (no long term warming observed in the stadial with a H event) and orange (a long term warming is observed). (b) to (d): Focus on the temperature evolution of DO 5, 7 and 9.
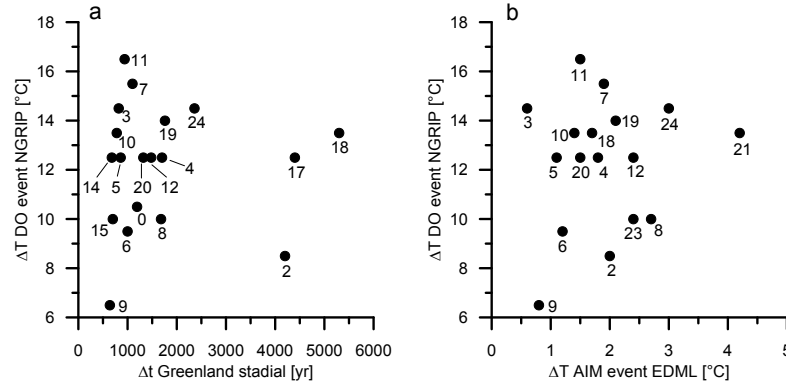
Fig. 4. Comparison of the NGRIP DO temperature amplitudes to (a) the preceding Greenland stadial durations (Rasmussen et al., 2013) and (b) EDML AIM temperature amplitudes (EPICA community members, 2006; Capron et al., 2010a), respectively. Numbers indicate DO events.

Therefore, the different temperature amplitudes at the onset of DO events may not be primarily influenced by the seesaw mechanism nor by different AMOC strengths but rather by regional amplification mechanisms such as sea-ice changes (Gildor and Tziperman, 2003; Li et al., 2010; Petersen et al., 2013; Dokken et al., 2013). This is in line with a comparison of model simulations of different complexities (Kageyama et al., 2013), where the largest Arctic warming is produced by the AMOC restart associated with the largest sea-ice retreat.

3.2 $\delta^{18}O_{ice}$-temperature relationship

In this section we will investigate the relationship between $\delta^{18}O_{ice}$ and temperature, referred to as α, on different time scales. In general $\delta^{18}O_{ice}$ follows temperature (Fig. 3a) but the sensitivity is changing with time (Landais et al., 2004a). While a rather similar evolution of variations between temperature and $\delta^{18}O_{ice}$ can be observed during DO 20 to 14, a significant deviation occurs e.g. during DO 8. The interstadials of DO 21 (80 to 85 kyr) and 23 (98 to 105 kyr) feature even a slight decoupling of temperature and $\delta^{18}O_{ice}$; the temperature seems to be constant while the $\delta^{18}O_{ice}$ has a decreasing trend. The modelling of the temperature in these periods was more delicate due to rare Δage match points (Fig. 7). If the reconstructed temperature evolution for DO 21 and 23 is correct, the observed decoupling between temperature and $\delta^{18}O_{ice}$ may indicate a changing atmospheric circulation during longer interstadials. On the other hand, we observe also a divergence during the stadial preceding DO 24; temperature has a decreasing, $\delta^{18}O_{ice}$ an increasing trend. As the measured Δage could not be matched well by the model, caution should be taken in interpreting this period.

In the following two sections, the $\delta^{18}O_{ice}$-temperature relationship will be discussed on glacial and orbital time scales. Note, that α is defined here as the actual slope between the reconstructed temperature and $\delta^{18}O_{ice}$ within a certain time period, as outlined below, and not in relation to the Holocene condition as expressed in Eq. 3. To calculate α, we use the 200 yr splined $\delta^{18}O_{ice}$ data which served as an initial temperature estimation (Sect. 2.3).

3.2.1 $\delta^{18}O_{ice}$-temperature relationship of the last glacial

Before comparing the $\delta^{18}O_{ice}$ data with our reconstructed temperature, the $\delta^{18}O_{ice}$ data has been corrected for the influence of the increased isotopic composition of the ocean during the glacial stage after Jouzel et al. (2003): $\delta^{18}O_{icecorr} = \delta^{18}O_{ice} - \Delta\delta^{18}O_{sea} \cdot (1 + \delta^{18}O_{ice})/(1 + \Delta\delta^{18}O_{sea})$. $\Delta\delta^{18}O_{sea}$ denotes the isotopic difference of the sea water which is due to the increased ice masses at the poles compared to present conditions (Bintanja et al., 2005; Lisiecki and Raymo, 2005).

Figure 5 shows that the $\delta^{18}O_{icecorr}$ to temperature relationship during the last glacial period (15 to 119 kyr) has a mean value of $0.52\,\%o\,°C^{-1}$ (black line). As there are uncertainties in both variables, the temperature and the $\delta^{18}O_{icecorr}$, we used the geometric mean regression to determine α. The grey line indicates the modern Greenland spatial dependency of $\alpha = 0.80\,\%o\,°C^{-1}$ (Sjolte et al., 2011), the green and the red diamond represent glacial and modern mean values, respectively.

How can the observed data be explained? As described in Huber et al. (2006b) and as we suggest for interstadials, a general precipitation source temperature cooling during the glacial would shift the grey line into the grey dashed line (shown by the blue arrow), which means that less depleted precipitation is expected. This can be understood by means of a simple Rayleigh model: as the source temperature gets colder, the temperature gradient between source and site becomes smaller and therefore the isotopic compo-
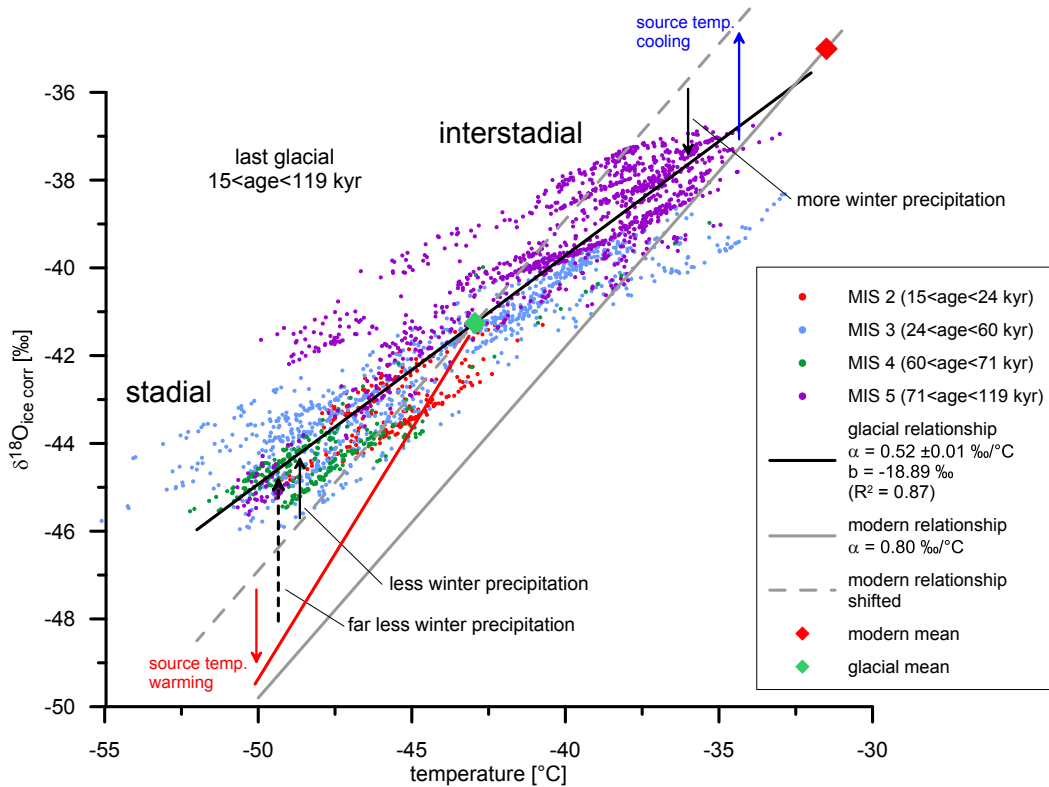
Fig. 5. Relationship between NGRIP $\delta^{18}O_{icecorr}$ (200 yr spline) and $\delta^{15}N$ derived temperature during the glacial. The data is colour-coded according to the different MIS. The glacial relationship is represented by the black line (geometric mean regression), the present-day spatial gradient for Greenland by the grey line (Sjolte et al., 2011). Due to the general source temperature cooling during the glacial, it is shifted into the grey dashed line. The expected lower isotopic values during the stadial as a consequence of the source temperature increase are shown by the red line (Masson-Delmotte et al., 2005). The smaller gradient (black line) during the glacial compared to present-day slope (grey line) is explained by enhanced seasonality (black solid and dashed arrows).

sition is less depleted. Huber et al. (2006b) explained the smaller α (during MIS 3) compared to the present-day value by changes in annual distribution of precipitation; less winter precipitation in the stadial, more winter precipitation in an interstadial, respectively (Fig. 5, black solid arrows). The fact that the $\delta^{18}O_{ice}$ is not only dependent on the mean annual temperature but also amongst others on the seasonality of the precipitation has been discussed in other publications (Steig et al., 1994; Fawcett et al., 1997; Krinner et al., 1997; Masson-Delmotte et al., 2005; Jouzel et al., 2007). For the NGRIP site in particular, at present-day large spatial gradients of precipitation seasonality are observed (Steen-Larsen et al., 2011). Small changes in circulation patterns could therefore be responsible for significant seasonality changes in the vicinity of the NGRIP site.

Compared to Huber et al. (2006b), we suggest an additional explanation for the values of the isotopic precipitation during stadial conditions. It has been proposed (Gildor and Tziperman, 2003; Kaspi et al., 2004) and shown that sea ice

changes around Greenland can have a significant influence on Greenland climate (Li et al., 2005, 2010). As the sea ice extent is enlarged during stadial conditions (Broecker, 2000), the precipitation source location for Greenland precipitation is pushed southwards to warmer ocean conditions which can be traced in the d-excess (Masson-Delmotte et al., 2005). In addition to the expected low stadial $\delta^{18}O_{ice}$ values (grey dashed line) the isotopy should therefore be further depleted because of the increased temperature gradient between precipitation source and the NGRIP site (Rayleigh). This suggested behaviour is shown in Fig. 5 by the qualitative red line. The discrepancy between observed and expected $\delta^{18}O_{ice}$ values is even enlarged compared to the interpretation from Huber et al. (2006b), suggesting that the seasonality effect (black dashed arrow) which is used to explain the mismatch between measured data and the enhanced isotopic sensitivity (red line) is even more pronounced during stadials.
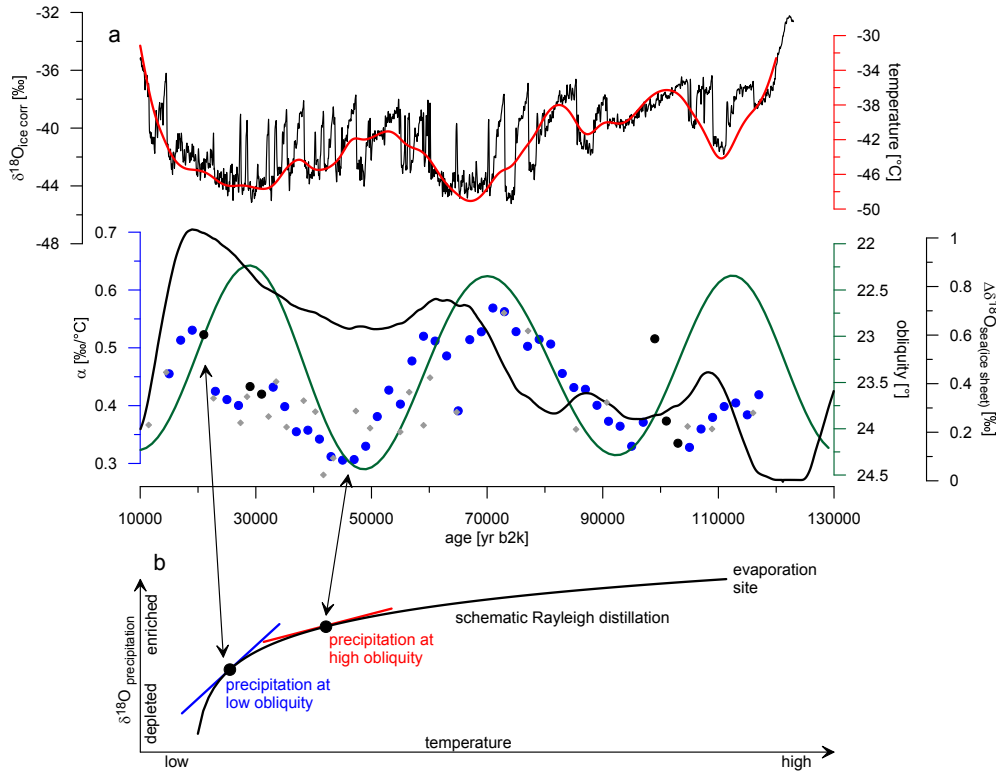
Fig. 6. Comparison between α and obliquity. (a) NGRIP $\delta^{18}O_{icecorr}$ (NGRIP members, 2004; Bintanja et al., 2005) splined with a COP of 200 yr (upper black line); 10 kyr temperature spline (red line); obliquity (green line, Berger and Loutre (1991)); $\Delta\delta^{18}O_{sea}$ as a proxy of ice sheet volume (lower black line, Bintanja et al. (2005)); α values calculated for single DO events in a 1 kyr window (grey diamonds); α calculated over a time period of 10 kyr with a correlation of $0.6 < R^2 < 0.8$ and $0.8 < R^2$, respectively (black and blue dots). α was calculated using the temperature record as shown in Fig. 3 and the NGRIP $\delta^{18}O_{icecorr}$ data splined by 200 yr as shown in this graph. (b) Schematic Rayleigh model to explain the α variations.

3.2.2 $\delta^{18}O_{ice}$-temperature relationship on orbital time scales

Here we investigate the $\delta^{18}O_{ice}$-temperature relationship on orbital time scales. For this, we calculated α on a 10 kyr time window, every 2 kyr (Fig. 6a), together with the corresponding correlation coefficient (R^2). Blue dots correspond to time windows with a robust correlation ($0.8 < R^2$) and black dots to those with a weaker correlation ($0.6 < R^2 < 0.8$), occurring generally in time periods with rare and small abrupt climatic changes. The calculated α variations seem to follow obliquity (Fig. 6a, green line). When looking at single DO events (1 kyr time window ending at the DO peak, small grey diamonds in Fig. 6a), the variations are more scattered and the α-obliquity relationship is almost impossible to detect.

The imprint of obliquity in the source-site temperature gradient has been previously evidenced in the d-excess measurements performed in both Antarctica and Greenland ice cores

(Vimeux et al., 1999; Masson-Delmotte et al., 2005). Indeed, a low obliquity implies an increase of the source temperature and a cooling of the northern latitudes. The NGRIP $\delta^{18}O_{ice}$ record and our reconstructed temperature profile (10 kyr spline, Fig 6a, red line) clearly show that temperature and obliquity minima occur at the same time. Cold Greenland temperature during obliquity minima is most probably further reduced by positive feedbacks such as extending sea ice and albedo effects resulting in a further increase of the source-site temperature gradient.

Our α reconstruction covering the last glacial period shows that also the sensitivity of NGRIP water isotopes is affected by obliquity (Fig 6a); α minima of around $0.3\,\permil\,°C^{-1}$ correspond to obliquity maxima while α values reach up to $0.6\,\permil\,°C^{-1}$ during obliquity minima. This is in qualitative agreement with a schematic Rayleigh distillation model (Fig. 6b), where the $\delta^{18}O$ of precipitation is mainly explained by the source-site temperature gradient. In the case of an obliquity decrease, we move on the Rayleigh precipitation curve

from the right black dot to the left one, which exhibits a steeper gradient (Fig. 6b, blue line). This steeper gradient would produce an enhanced isotopic effect for the same temperature variation in Greenland, therefore increasing α which is in agreement with our observations.

While α and obliquity are roughly anticorrelated from 112 to 70 kyr, the α maximum at 20 kyr appears to be concomitant with the maximum of the ice sheet volume (Fig. 6a, black line, Bintanja et al. (2005)). Note that the time uncertainty related to ice sheet size data is 4 kyr (Lisiecki and Raymo, 2005). Therefore it seems that both obliquity and northern hemisphere ice sheet volume have an impact on the sensitivity of Greenland water isotopes.

Masson-Delmotte et al. (2005) and Landais et al. (2004a) have already proposed that larger ice sheets (favoured by smaller obliquity) would strongly reduce the arrival of precipitation in winter and hence increase the seasonality effect, thus decreasing α. While this suggestion remains valid, our data suggest a counter-acting mechanism; in the period 70 to 115 kyr a concomitant increase of α and ice sheet size can be observed. Bromwich et al. (2004) suggested that the Laurentide ice sheet modified the air mass trajectories, possibly influencing Greenland by very depleted precipitation coming from Pacific sources. Again considering a simple Rayleigh model, these precipitations would (i) lower the $\delta^{18}O$ level and (ii) be likely more sensitive to temperature fluctuations in Greenland. As a consequence, α would increase with the Northern Hemisphere ice sheet volume, which is what we observe here. Our first continuous record of α over a complete glacial-interglacial cycle therefore supports that both obliquity and probably Northern Hemisphere ice sheet volume influences the hydrological cycle and therefore the $\delta^{18}O$ of precipitation.

3.3 Accumulation rate

As mentioned in Sect. 2.3 and illustrated in Fig. 7, we reduced the accumulation rate in some parts substantially to adjust the modelled $\delta^{15}N$ as well as Δdepth and Δage to match the measured data. From 12 to 64 kyr the accumulation was lowered by 20 to 30% with a mean value of 24% and from 64 to 120 kyr by 0 to 20% with a mean value of 4%. During some few periods the accumulation rate was even reduced by 30 to 35%.

A comparison of our temperature reconstruction with reduced accumulation to a scenario with unchanged accumulation is shown in Fig. 7. The red lines show the used reduced accumulation rate and the corresponding modelled Δage values. The blue lines are obtained with an unchanged accumulation rate as described above in Sect. 2.3 but without a final manual adjustment which would lead only to minor changes regarding Δage values. One can clearly see that in the period from 10 to 60 kyr the 100%-accumulation-scenario underestimates the Δage up to 400 yr. Most significant deviations occur during the last glacial maximum. Not shown

is the modelled $\delta^{15}N$ data for the 100% accumulation rate-scenario, for which a substantial disagreement in the timing between measured and modelled data occurs in this period (modelled $\delta^{15}N$ values are shifted to younger ages). According to our data adjustment, the accumulation reduction seems to be smaller in the older half of the record, nevertheless also here our model suggests in some periods (around 99 and 110 kyr) a reduction of 10 to 20%.

A general test to verify the Schwander model (Schwander et al., 1997) regarding accumulation rates and corresponding LID (which influence the Δage and Δdepth) can be performed with modern data from different ice core sites. With the present-day NGRIP accumulation rate of $0.19\,\mathrm{m\,i.e.\,yr^{-1}}$ and a mean surface temperature of -31.5°C (NGRIP members, 2004), the Schwander model (Schwander et al., 1997) calculates a LID of 66.8 m, which is in excellent agreement to measurements of 66 to 68 m (Huber et al., 2006a). Consequently, in absence of any warming event, the model is also able to calculate the $\delta^{15}N_{grav}$. According to Fig. 3 and 7, the coldest temperatures of the reconstruction are around -55°C and the lowest accumulation rates are in the order of $4\,\mathrm{cm\,i.e.\,yr^{-1}}$. These values are similar for Dome C present-day surface climatic conditions: accumulation $2.7\,\mathrm{cm\,i.e.\,yr^{-1}}$ and a temperature of -54.5°C (Landais et al., 2006). So we can consider the Dome C characteristics as a test for the Schwander model for NGRIP lower boundary stadial conditions. When one runs the Schwander model with Dome C present-day surface conditions it is able to reproduce the LID (94.6 m) and the $\delta^{15}N_{grav}$ (0.51‰) in close agreement with observations of LID=98 m and $\delta^{15}N_{grav}$=0.52‰ (Landais et al., 2006). Therefore we are confident that the Schwander model is capable of modelling NGRIP glacial climatic conditions.

The observed necessity for a partial reduction in the accumulation rate in order to reconstruct a $\delta^{15}N$-based temperature with firn densification and heat diffusion models was recognised also in previous studies and therefore support our findings. To reconstruct the temperature evolution from DO 9 to 17 (38 to 64 kyr) Huber et al. (2006b) reduced the accumulation rate from the ss09sea06bm time scale constantly by 20%. The average of our time dependent reduced accumulation rate over the same period is similar (22.5%). To test the validity of their model, Huber et al. (2006b) also modelled $\delta^{15}N$ values of DO 18 to 20 (64 to 79 kyr) measured by Landais et al. (2004a) and found that in this period one can use mostly the unchanged accumulation rate, which is also in line with our findings. Also Guillevic et al. (2013) who reconstructed the NGRIP temperature over DO 8, 9 and 10 (36.5 to 43 kyr on the GICC05 time scale), using the same $\delta^{15}N$ data but the Goujon firnification model (Goujon et al., 2003), had to reduce the accumulation rate by 26% in this section. Again, when averaged we find for the same period a similar accumulation reduction of 29%. Interestingly, Landais et al. (2004a, 2005) and Capron et al. (2010a, 2012) worked with the original accumulation rate to reconstruct the
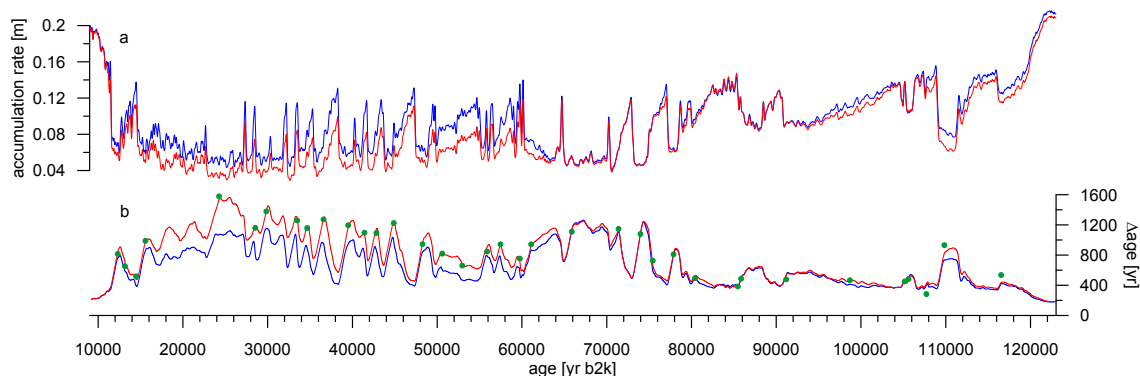
Fig. 7. (a) Accumulation rate from the ss09sea06bm timescale (blue line, NGRIP members (2004); Johnsen et al. (2001)), reduced accumulation rate used for the temperature reconstruction (red line). (b) modelled Δage with original accumulation rate (blue) and reduced accumulation rate (red), Δdepth measurements (green dots).

temperature evolution over DO 18 to 25. These findings are mostly confirmed by our work where we use accumulation rates of approximately 100% around the DO events mentioned above. An exception is DO 24 for which we had to lower the accumulation rate by 10 to 20%.

As the ss09sea06bm time scale has been validated by the GICC05 annual layer counting time scale (Svensson et al., 2008) back to 64 kyr, the accumulation reduction in this period cannot be due to an inaccuracy in the time scale. We therefore confirm that the Dansgaard–Johnsen ice flow model (Dansgaard and Johnsen, 1969; NGRIP members, 2004) which was used to establish the NGRIP accumulation rate probably provides generally too high glacial accumulation rates, especially during the coldest periods. This tendency is likely due to a too simplistic ice flow model (Guillevic et al., 2013).

4   Conclusions

We present for the first time a continuous temperature reconstruction for the whole glacial period (10 to 120 kyr) based on new and published δ^{15}N measurements performed on the trapped air of the NGRIP ice core. In line with previous studies, we find surface temperature rises from +5 to +16.5°C (± 3°C, 2σ) at the onset of abrupt events (Huber et al., 2006b; Landais et al., 2005; Capron et al., 2010a, 2012). Most of the DO events show a one-step temperature increase. In contrast, DO 2, 7, 11 and 18 feature a two-step temperature rise with a small interruption of generally less than 100 yr between stadial and interstadial conditions. No particular cold temperatures characterise stadials associated with H events and a long term warming of about one to three degrees is observed during the Heinrich stadials 4, 5 and 6 of MIS 3.

With a highly simplified model calculation we tried to assess the δ^{15}N smoothing in the firn due to the gradual bubble enclosure and found a damping of roughly -30% for a +10°C temperature increase within 20 yr. Our smoothing of the model input data has an effect which is in the same range. To be able to better quantify the damping in the firn in the future, it would be advantageous to implement this effect in the used firn densification and heat diffusion models.

When comparing the δ^{18}O$_{icecorr}$ data with the corresponding temperatures during the last glacial and taking into account a warmer source temperature for the precipitation during stadials we propose that the seasonality effect of precipitation during stadials is even more pronounced than previously assumed. Our first reconstruction of NGRIP α during the full glacial period shows (i) an anticorrelation between obliquity and a long term (10 kyr) α, supported qualitatively by a simple Rayleigh distillation model, and (ii) a possible influence of the Northern Hemisphere ice sheet size on α which may be explained by enhanced Pacific vapour sources at the NGRIP site when the Laurentide ice sheet volume increases.

Associated with the NGRIP δ^{18}O$_{ice}$ profile, our reconstructed temperature provide useful constraints for future investigations on the parameter α based on water isotope modelling aiming at better quantifying in particular, the respective influences of obliquity on the source-site temperature gradient, and the ice volume.

In order to match measured and modelled δ^{15}N data as well as Δage we had to reduce the accumulation rate given by the ss09sea06bm age scale significantly, particularly in the second half of the last glacial from 12 to 64 kyr where a mean reduction of 24% was applied. This further emphasises the fact that the Dansgaard–Johnsen ice flow model partly overestimates the NGRIP accumulation rate (Dansgaard and Johnsen, 1969; NGRIP members, 2004; Huber et al., 2006b; Guillevic et al., 2013)

References

Andersen, K. K., Svensson, A., Johnsen, S. J., Rasmussen, S. O., Bigler, M., Röthlisberger, R., Ruth, U., Siggaard-Andersen, M.-L., Steffensen, J. P., Dahl-Jensen, D., Vinther, B. M., and Clausen, H. B.: The Greenland Ice Core Chronology 2005, 15-42 ka. Part 1: constructing the time scale, Quaternary Sci. Rev., 25, 3246–3257, doi:{10.1016/j.quascirev.2006.08.002}, 2006.

Berger, A. and Loutre, M.: Insolation Values for the Climate of the last 10 Million Years, Quaternary Sci. Rev., 10, 297–317, doi:{10.1016/0277-3791(91)90033-Q}, 1991.

Bintanja, R., van de Wal, R., and Oerlemans, J.: Modelled atmospheric temperatures and global sea levels over the past million years, Nature, 437, 125–128, doi:{10.1038/nature03975}, 2005.

Blunier, T. and Brook, E.: Timing of millennial-scale climate change in Antarctica and Greenland during the last glacial period, Science, 291, 109–112, doi:{10.1126/science.291.5501.109}, 2001.

Bond, G., Broecher, W., Johnsen, S. J., MacManus, J., Laberie, L., Jouzel, J., and Bonani, G.: Correlations between climate records from North Atlantic sediments and Greenland ice, Nature, 365, 143–147, doi:{10.1038/365143a0}, 1993.

Broecker, W.: Abrupt climate change: causal constraints provided by the paleoclimate record, Earth-Sci. Rev., 51, 137–154, doi:{10.1016/S0012-8252(00)00019-2}, 2000.

Broecker, W. S., Bond, G., Klas, M., Bonani, G., and Wolfli, W.: A salt oscillator in the glacial Atlantic? 1. The concept, Paleoceanography, 5, 469–477, doi:{10.1029/PA005i004p00469}, 1990.

Bromwich, D., Toracinta, E., Wei, H., Oglesby, R., Fastook, J., and Hughes, T.: Polar MM5 simulations of the winter climate of the Laurentide Ice Sheet at the LGM, J. Climate, 17, 3415–3433, doi:{10.1175/1520-0442(2004)017⟨3415:PMSOTW⟩2.0.CO;2}, 2004.

Buizert, C., Martinerie, P., Petrenko, V. V., Severinghaus, J. P., Trudinger, C. M., E.Witrant, Rosen, J. L., Orsi, A. J., Rubino, M., Etheridge, D. M., Steele, L. P., Hogan, C., Laube, J. C., Sturges, W. T., Levchenko, V. A., Smith, A. M., Levin, I., Conway, T. J., Dlugokencky, E. J., Lang, P. M., Kawamura, K., Jenk, T. M., White, J. W. C., Sowers, T., Schwander, J., , and Blunier, T.: Gas transport in firn: multiple-tracer characterisation and model intercomparison for NEEM, Northern Greenland, Atmos. Chem. Phys., 12, 4259–4277, doi:10.5194/acp-12-4259-2012, 2012.

Capron, E., Landais, A., Chappellaz, J., Schilt, A., Buiron, D., Dahl-Jensen, D., Johnsen, S. J., Jouzel, J., Lemieux-Dudon, B., Loulergue, L., Leuenberger, M., Masson-Delmotte, V.,

Meyer, H., Oerter, H., and Stenni, B.: Millennial and sub-millennial scale climatic variations recorded in polar ice cores over the last glacial period, Clim. Past, 6, 345–365, doi:{10.5194/cp-6-345-2010}, 2010a.

Capron, E., Landais, A., Lemieux-Dudon, B., Schilt, A., Masson-Delmotte, V., Buiron, D., Chappellaz, J., Dahl-Jensen, D., Johnsen, S., Leuenberger, M., Loulergue, L., and Oerter, H.: Synchronising EDML and NorthGRIP ice cores using δ^{18}O of atmospheric oxygen (δ^{18}Oatm) and CH4 measurements over MIS5 (80-123 kyr), Quaternary Sci. Rev., 29, 222–234, doi:{10.1016/j.quascirev.2009.07.014}, 2010b.

Capron, E., Landais, A., Chappellaz, J., Buiron, D., Fischer, H., Johnsen, S. J., Jouzel, J., Leuenberger, M., Masson-Delmotte, V., and Stocker, T. F.: A global picture of the first abrupt climatic event occurring during the last glacial inception, Geophys. Res. Lett., 39, doi:{10.1029/2012GL052656}, 2012.

Chiang, J. and Bitz, C.: Influence of high latitude ice cover on the marine Intertropical Convergence Zone, Clim. Dynam., 25, 477–496, doi:{10.1007/s00382-005-0040-5}, 2005.

Craig, H., Horibe, Y., and Sowers, T.: Gravitational Separation of Gases and Isotopes in Polar Ice Caps, Science, 242, 1675–1678, doi:{10.1126/science.242.4886.1675}, 1988.

Cuffey, K., Clow, G., Alley, R., Stuiver, M., Waddington, E., and Saltus, R.: Large arctic temperature change at the Wisconsin-Holocene glacial transition, Science, 270, 455–458, 1995.

Dansgaard, W. and Johnsen, S. J.: A flow model and a time scale for the ice core from Camp Century, Greenland, J. Glaciol., 8, 215–223, 1969.

Dansgaard, W., Clausen, H., Gundestrup, N., Hammer, C., Johnsen, S., Gristinsdottir, P., and Reeh, N.: A New Greenland Deep Ice Core, Science, 218, 1273–1277, doi:{10.1126/science.218.4579.1273}, 1982.

Dansgaard, W., Johnsen, S., Clausen, H., Dahljensen, D., Gundestrup, N., Hammer, C., Hvidberg, C., Steffensen, J., Sveinbjornsdottir, A., Jouzel, J., and Bond, G.: Evidence for general instability of past climate from a 250-kyr ice-core record, Nature, 364, 218–220, doi:{10.1038/364218a0}, 1993.

Deplazes, G., Lückge, A., Peterson, L. C., Timmermann, A., Hamann, Y., Hughen, K. A., Rühl, U., Laj, C., Cane, M. A., Sigman, D. M., and Haug, G. H.: Links between tropical rainfall and North Atlantic climate during the last glacial period, Nat. Geosci., 6, 213–217, doi:{10.1038/NGEO1712}, 2013.

Dokken, T. M., Nisancioglu, K. H., Li, C., Battisti, D. S., and Kissel, C.: Dansgaard-Oeschger cycles: Interactions between ocean and sea ice intrinsic to the Nordic seas, Paleoceanography, 28, 491–502, doi:10.1002/palo.20042, http://dx.doi.org/10.1002/palo.20042, 2013.

EPICA community members: One-to-one coupling of glacial climate variability in Greenland and Antarctica, Nature, 444, 195–198, doi:{10.1038/nature05301}, 2006.

Fawcett, P. J., Agustdóttir, A. M., Alley, R. B., and Shuman, C. A.: The Younger Dryas termination and North Atlantic Deep Water Formation: Insights from climate model simulations and Greenland ice cores, Paleoceanography, 12, 23–38, doi:{10.1029/96PA02711}, 1997.

Fleitmann, D., Cheng, H., Badertscher, S., Edwards, R. L., Mudelsee, M., Goektuerk, O. M., Fankhauser, A., Pickering, R., Raible, C. C., Matter, A., Kramers, J., and Tuysuz, O.: Timing and climatic impact of Greenland interstadials recorded in

stalagmites from northern Turkey, Geophys. Res. Lett., 36, doi: {10.1029/2009GL040050}, 2009.

Genty, D., Combourieu-Nebout, N., Peyron, O., Blamart, D., Wainer, K., Mansuri, F., Ghaleb, B., Isabello, L., Dormoy, I., von Grafenstein, U., Bonelli, S., Landais, A., and Brauer, A.: Isotopic characterization of rapid climatic events during OIS3 and OIS4 in Villars Cave stalagmites (SW-France) and correlation with Atlantic and Mediterranean pollen records, Quaternary Sci. Rev., 29, 2799–2820, doi:{10.1016/j.quascirev.2010.06.035}, 2010.

Gildor, H. and Tziperman, E.: Sea-ice switches and abrupt climate change, Philos. T. Roy. Soc. A, 361, 1935–1942, doi:{10.1098/rsta.2003.1244}, 2003.

Goujon, C., Barnola, J., and Ritz, C.: Modeling the densification of polar firn including heat diffusion: Application to close-off characteristics and gas isotopic fractionation for Antarctica and Greenland sites, J. Geophys. Res., 108, doi:{10.1029/2002JD003319}, 2003.

Grachev, A. and Severinghaus, J.: A revised $+10 \pm 4$ degrees$^\circ$C magnitude of the abrupt change in Greenland temperature at the Younger Dryas termination using published GISP2 gas isotope data and air thermal diffusion constants, Quaternary Sci. Rev., 24, 513–519, doi:{10.1016/j.quascirev.2004.10.016}, 2005.

Guillevic, M., Bazin, L., Landais, A., Kindler, P., Orsi, A., Masson-Delmotte, V., Blunier, T., Buchardt, S., Capron, E., Leuenberger, M., Martinerie, P., Pri, F., and Vinther, B.: Spatial gradients of temperature, accumulation and δ^{18}O-ice in Greenland over a series of Dansgaard-Oeschger events, Clim. Past, 9, 1029–1051, doi:{10.5194/cp-9-1029-2013}, 2013.

Hemming, S.: Heinrich events: Massive late pleistocene detritus layers of the North Atlantic and their global climate imprint, Review of Geophysics, 42, doi:{10.1029/2003RG000128}, 2004.

Huber, C. and Leuenberger, M.: Measurements of isotope and elemental ratios of air from polar ice with a new on-line extraction method, Geochem. Geophy. Geosy., 5, doi:{10.1029/2004GC000766}, 2004.

Huber, C., Leuenberger, M., and Zumbrunnen, O.: Continuous extraction of trapped air from bubble ice or water for on-line determination of isotope ratios, Anal. Chem., 75, 2324–2332, doi: {10.1021/ac0263972}, 2003.

Huber, C., Beyerle, U., Leuenberger, M., Schwander, J., Kipfer, R., Spahni, R., Severinghaus, J., and Weiler, K.: Evidence for molecular size dependent gas fractionation in firn air derived from noble gases, oxygen, and nitrogen measurements, Earth Planet. Sc. Lett., 243, 61–73, doi:{10.1016/j.epsl.2005.12.036}, 2006a.

Huber, C., Leuenberger, M., Spahni, R., Flückiger, J., Schwander, J., Stocker, T., Johnsen, S., Landals, A., and Jouzel, J.: Isotope calibrated Greenland temperature record over Marine Isotope Stage 3 and its relation to CH_4, Earth Planet. Sc. Lett., 243, 504–519, doi:{10.1016/j.epsl.2006.01.002}, 2006b.

Johnsen, S., Dansgaard, W., Clausen, H., and Langway, C.: Oxygen Isotope Profiles through the Antarctic and Greenland Ice Sheets, Nature, 235, 429–434, 1972.

Johnsen, S. J., Dansgaard, W., and White, J. W. C.: The origin of Arctic precipitation under present and glacial climate, Tellus, 41B, 452–468, 1989.

Johnsen, S. J., Dahl-Jensen, D., Dansgaard, W., and Gundestrup, N.: Greenland paleotemperatures derived from GRIP borehole temperature and ice core isotope profiles, Tellus, 47B, 624–629, 1995.

Johnsen, S. J., Clausen, H. B., Dansgaard, W., Fuhrer, K., Gundestrup, N., Hammer, C. U., Iversen, P., Jouzel, J., Stauffer, B., and Steffensen, J. P.: Irregular glacial interstadials recorded in a new Greenland ice core, Nature, 359, 311–313, doi:{10.1038/359311a0}, 1992.

Johnsen, S. J., Dahl-Jensen, D., Gundestrup, N., Steffensen, J. P., Clausen, H. B., Miller, H., Masson-Delmotte, V., Sveinbjörnsdóttir, A., and White, J.: Oxygen isotope and palaeotemperature records from six Greenland ice-core stations: Camp Century, Dye-3, GRIP, GISP2, Renland and NorthGRIP, J. Quaternary Sci., 16, 299–307, doi:{10.1002/jqs.622}, 2001.

Jonkers, L., Moros, M., Prins, M. A., Dokken, T., Dahl, C. A., Dijkstra, N., Perner, K., and Brummer, G.-J. A.: A reconstruction of sea surface warming in the northern North Atlantic during MIS 3 ice-rafting events, Quaternary Sci. Rev., 29, 1791–1800, doi: {10.1016/j.quascirev.2010.03.014}, 2010.

Jouzel, J., Vimeux, F., Caillon, N., Delaygue, G., Hoffmann, G., Masson-Delmotte, V., and Parrenin, F.: Magnitude of isotope/temperature scaling for interpretation of central Antarctic ice cores, J. Geophys. Res-Atmos., 108, doi:{10.1029/2002JD002677}, 2003.

Jouzel, J., Stiévenard, N., Johnsen, S., Landais, A., Masson-Delmotte, V., Sveinbjörnsdóttir, A., Vimeux, F., von Grafenstein, U., and White, J.: The GRIP deuterium-excess record, Quaternary Sci. Rev., 26, 1–17, doi:{10.1016/j.quascirev.2006.07.015}, 2007.

Kageyama, M., Merkel, U., Otto-Bliesner, B., Prange, M., Abe-Ouchi, A., Lohmann, G., Ohgaito, R., Roche, D. M., Singarayer, J., Swingedouw, D., and Zhang, X.: Climatic impacts of fresh water hosing under Last Glacial Maximum conditions: a multi-model study, Clim. Past, 9, 935–953, doi: 10.5194/cp-9-935-2013, http://www.clim-past.net/9/935/2013/, 2013.

Kanner, L. C., Burns, S. J., Cheng, H., and Edwards, R. L.: High-Latitude Forcing of the South American Summer Monsoon During the Last Glacial, Science, 335, 570–573, doi:{10.1126/science.1213397}, 2012.

Kaspi, Y., Sayag, R., and Tziperman, E.: A 'triple sea-ice state' mechanism for the abrupt warming and synchronous ice sheet collapses during Heinrich events, Paleoceanography, 19, doi: {10.1029/2004PA001009}, 2004.

Kobashi, T., Kawamura, K., Severinghaus, J. P., Barnola, J.-M., Nakaegawa, T., Vinther, B. M., Johnsen, S. J., and Box, J. E.: High variability of Greenland surface temperature over the past 4000 years estimated from trapped air in an ice core, Geophys. Res. Lett., 38, L21 501, doi:10.1029/2011GL049444, 2011.

Krinner, G., Genthon, C., and Jouzel, J.: GCM analysis of local influences on ice core δ signals, Geophys. Res. Lett., 24, 2825–2828, doi:{10.1029/97GL52891}, 1997.

Landais, A., Barnola, J., Kawamura, K., Caillon, N., Delmotte, M., Ommen, T. V., Dreyfus, G., Jouzel, J., Masson-Delmotte, V., Minster, B., Freitag, J., Leuenberger, M., Schwander, J., Huber, C., Etheridge, D., and Morgan, V.: Firn-air δ^{15}N in modern polar sites and glacialinterglacial ice: a model-data mismatch during glacial periods in Antarctica?, Quaternary Sci. Rev., 25, 49–62, doi:10.1016/j.quascirev.2005.06.007, 2006.

Landais, A., Caillon, N., Severinghaus, J., Jouzel, J., and Masson-Delmotte, V.: Analyses isotopiques à haute précision de l'air piégé dans les glaces polaires pour la quantification des varia-

tions rapides de température: méthode et limites, Notes des Activités Instrumentales de l'IPSL, nr.39, 2003.

Landais, A., Barnola, J., Masson-Delmotte, V., Jouzel, J., Chappellaz, J., Caillon, N., Huber, C., Leuenberger, M., and Johnsen, S.: A continuous record of temperature evolution over a sequence of Dansgaard-Oeschger events during Marine Isotopic Stage 4 (76 to 62 kyr BP), Geophys. Res. Lett., 31, doi:{10.1029/2004GL021193}, 2004a.

Landais, A., Caillon, N., Goujon, C., Grachev, A., Barnola, J., Chappellaz, J., Jouzel, J., Masson-Delmotte, V., and Leuenberger, M.: Quantification of rapid temperature change during DO event 12 and phasing with methane inferred from air isotopic measurements, Earth Planet. Sc. Lett., 225, 221–232, doi:{10.1016/j.espl.2004.06.009}, 2004b.

Landais, A., Caillon, N., Severinghaus, J., Barnola, J., Goujon, C., Jouzel, J., and Masson-Delmotte, V.: Isotopic measurements of air trapped in ice to quantify temperature changes., CR Geosci., 336, 963–970, doi:{10.1016/j.crte.2004.03.013}, 2004c.

Landais, A., Jouzel, J., Masson-Delmotte, V., and Caillon, N.: Large temperature variations over rapid climatic events in Greenland: a method based on air isotopic measurements, CR Geosci., 337, 947–956, doi:{10.1016/j.crte.2005.04.003}, 2005.

Lang, C., Leuenberger, M., Schwander, J., and Johnsen, S.: 16°C Rapid Temperature Variation in Central Greenland 70,000 Years Ago, Science, 286, 934–937, doi:10.1126/science.286.5441.934, 1999.

Leuenberger, M. C., Lang, C., and Schwander, J.: Delta ^{15}N measurements as a calibration tool for the paleothermometer and gas-ice age differences: A case study for the 8200 BP event on GRIP ice, J. Geophys. Res-Atmos., 104, 22 163–22 170, doi:{10.1029/1999JD900436}, 1999.

Li, C., Battisti, D., Schrag, D., and Tziperman, E.: Abrupt climate shifts in Greenland due to displacements of the sea ice edge, Geophys. Res. Lett., 32, doi:{10.1029/2005GL023492}, 2005.

Li, C., Battisti, D. S., and Bitz, C. M.: Can North Atlantic Sea Ice Anomalies Account for Dansgaard-Oeschger Climate Signals?, J. Climate, 23, 5457–5475, doi:{10.1175/2010JCLI3409.1}, 2010.

Lisiecki, L. and Raymo, M.: A Pliocene-Pleistocene stack of 57 globally distributed benthic delta O-18 records, Paleoceanography, 20, doi:{10.1029/2004PA001071}, 2005.

Masson-Delmotte, V., Jouzel, J., Landais, A., Stiévenard, M., Johnsen, S. J., White, J. W. C., Werner, M., Sveinbjörnsdóttir, A., and Fuhrer, K.: GRIP deuterium excess reveals rapid and orbital-scale changes in Greenland moisture origin, Science, 309, 118–121, doi:{10.1126/science.1108575}, 2005.

Mayewski, P., Meeker, L., Twickler, M., Whitlow, S., Yang, Q., Lyons, W., and Prentice, M.: Major features and forcing of high-latitude northern hemisphere atmospheric circulation using a 110,000-year-long glaciochemical series, J. Geophys. Res-Oceans, 102, 26 345–26 366, doi:{10.1029/96JC03365}, 1997.

NGRIP members: High-resolution record of Northern Hemisphere climate extending into the last interglacial period, Nature, 10.1038/nature02805, doi:10.1038/nature02805, 2004.

Paterson, W. S. B.: The Physics of Glaciers, Pergamon, Tarrytown, N.Y., 1994.

Petersen, S. V., Schrag, D. P., and Clark, P. U.: A new mechanism for Dansgaard-Oeschger cycles, Paleoceanography, 28, doi:{10.1029/2012PA002364}, 2013.

Rasmussen, S. O., Bigler, M., Blockley, S. P. E., Blunier, T., Buchardt, S. L., Clausen, H. B., Cvijanovic, I., Dahl-Jensen, D., Johnsen, S. J., Fischer, H., Gkinis, V., Guillevic, M., Hoek, W. Z., Lowe, J. J., Pedro, J., Popp, T., Seierstad, I., Steffensen, J. P., Svensson, A. M., Vallelonga, P., Vinther, B. M., Walker, M. J. C., Wheatley, J. J., and Winstrup, M.: A stratigraphic framework for robust naming and correlation of past abrupt climatic changes during the last glacial period based on three synchronized Greenland ice core records, submitted to Quaternary Sci. Rev., 2013.

Roche, D., Paillard, D., and Cortijo, E.: Constraints on the duration and freshwater release of Heinrich event 4 through isotope modelling, Nature, 432, 379–382, doi:{10.1038/nature03059}, 2004.

Ruth, U., Wagenbach, D., Steffensen, J., and Bigler, M.: Continuous record of microparticle concentration and size distribution in the central Greenland NGRIP ice core during the last glacial period, J. Geophys. Res-Atmos., 108, doi:{10.1029/2002JD002376}, 2003.

Sánchez Goñi, M., Turon, J., Eynaud, F., and Gendreau, S.: European climatic response to millennial-scale changes in the atmosphere-ocean system during the last glacial period, Quaternary Res., 54, 394–403, doi:{10.1006/qres.2000.2176}, 2000.

Sánchez Goñi, M. F. and Harrison, S. P.: Millennial-scale climate variability and vegetation changes during the Last Glacial: Concepts and terminology Introduction, Quaternary Sci. Rev., 29, 2823–2827, doi:{10.1016/j.quascirev.2009.11.014}, 2010.

Schilt, A., Baumgartner, M., Blunier, T., Schwander, J., Spahni, R., Fischer, H., and Stocker, T. F.: Glacial-interglacial and millennial-scale variations in the atmospheric nitrous oxide concentration during the last 800,000 years, Quaternary Sci. Rev., 29, 182–192, doi:{10.1016/j.quascirev.2009.03.011}, 2010.

Schwander, J.: The Transformation of Snow to Ice and the Occlusion of Gases, in: The Environmental Record in Glaciers and Ice Sheets, edited by Oeschger, H and Langway, CC, Physical, Chemical, and Earth Sciences Research Reports, pp. 53–67, 1989.

Schwander, J., Sowers, T., Barnola, J., Blunier, T., Fuchs, A., and Malaizé, B.: Age scale of the air in the summit ice: Implication for glacial-interglacial temperature change, J. Geophys. Res-Atmos., 102, 19 483–19 493, doi:{10.1029/97JD01309}, 1997.

Severinghaus, J. P. and Battle, M. O.: Fractionation of gases in polar Ice during bubble close-off: new constraints from firn air Ne, Kr and Xe observations, Earth Planet. Sc. Lett., 244, 474–500, doi:{10.1016/j.epsl.2006.01.032}, 2006.

Severinghaus, J. P., Sowers, T., Brook, E. J., Alley, R. B., and Bender, M. L.: Timing of abrupt climate change at the end of the Younger Dryas interval from thermally fractionated gases in polar ice, Nature, 391, 141–146, doi:{10.1038/34346}, 1998.

Sjolte, J., Hoffmann, G., Johnsen, S. J., Vinther, B. M., Masson-Delmotte, V., and Sturm, C.: Modeling the water isotopes in Greenland precipitation 1959-2001 with the meso-scale model REMO-iso, J. Geophys. Res-Atmos., 116, doi:{10.1029/2010JD015287}, 2011.

Spahni, R., Schwander, J., Flückiger, J., Stauffer, B., Chappellaz, J., and Raynaud, D.: The attenuation of fast atmospheric CH4 variations recorded in polar ice cores, Geophys. Res. Lett., 30, doi:{10.1029/2003GL017093}, 2003.

Steen-Larsen, H. C., Masson-Delmotte, V., Sjolte, J., Johnsen, S. J., Vinther, B. M., Bréon, F.-M., Clausen, H. B., Dahl-Jensen, D.,

Falourd, S., Fettweis, X., Gallée, H., Jouzel, J., Kageyama, M., Lerche, H., Minster, B., Picard, G., Punge, H. J., Risi, C., Salas, D., Schwander, J., Steffen, K., Sveinbjörnsdóttir, A. E., Svensson, A., and White, J. W. C.: Understanding the climatic signal in the water stable isotope records from the NEEM shallow firn/ice cores in northwest Greenland, J. Geophys. Res., 116, D06 108, doi:10.1029/2010JD014311, 2011.

Steffensen, J. P., Andersen, K. K., Bigler, M., Clausen, H. B., Dahl-Jensen, D., Fischer, H., Goto-Azuma, K., Hansson, M., Johnsen, S. J., Jouzel, J., Masson-Delmotte, V., Popp, T., Rasmussen, S. O., Röthlisberger, R., Ruth, U., Stauffer, B., Siggaard-Andersen, M.-L., Sveinbjörnsdóttir, A. E., Svensson, A., and White, J. W. C.: High-resolution Greenland Ice Core data show abrupt climate change happens in few years, Science, 321, 680–684, doi:{10.1126/science.1157707}, 2008.

Steig, E., Grootes, P., and Stuiver, M.: Seasonal Precipitation Timing and Ice Core Records, Science, 266, 1885–1886, doi: {10.1126/science.266.5192.1885}, 1994.

Stocker, T. and Johnsen, S.: A minimum thermodynamic model for the bipolar seesaw, Paleoceanography, 18, doi:{10.1029/2003PA000920}, 2003.

Svensson, A., Andersen, K. K., Bigler, M., Clausen, H. B., Dahl-Jensen, D., Davies, S. M., Johnsen, S. J., Muscheler, R., Parrenin, F., Rasmussen, S. O., Röthlisberger, R., Seierstad, I., Steffensen, J. P., and Vinther, B. M.: A 60 000 year Greenland stratigraphic ice core chronology, Clim. Past, 4, 47–57, doi: {10.5194/cp-4-47-2008}, 2008.

Thomas, E. R., Wolff, E. W., Mulvaney, R., Johnsen, S. J., Steffensen, J. P., and Arrowsmith, C.: Anatomy of a Dansgaard-Oeschger warming transition: High-resolution analysis of the North Greenland Ice Core Project ice core, J. Geophys. Res-Atmos., 114, doi:{10.1029/2008JD011215}, 2009.

Vallelonga, P., Bertagna, G., Blunier, T., Kjaer, H. A., Popp, T. J., Rasmussen, S. O., Steffensen, J. P., Stowasser, C., Svensson, A. S., Warming, E., Winstrup, M., Bigler, M., and Kipfstuhl, S.: Duration of Greenland Stadial 22 and ice-gas Delta age from counting of annual layers in Greenland NGRIP ice core, Clim. Past, 8, 1839–1847, doi:{10.5194/cp-8-1839-2012}, 2012.

Vimeux, F., Masson, V., Jouzel, J., Stievenard, M., and Petit, J.: Glacial-interglacial changes in ocean surface conditions in the southern hemisphere, Nature, 398, 410–413, doi:{10.1038/18860}, 1999.

Voelker, A. H. L.: Global distribution of centennial-scale records for Marine Isotope Stage (MIS) 3: a database, Quaternary Sci. Rev., 21, 1185–1212, doi:{10.1016/S0277-3791(01)00139-1}, 2002.

Wang, Y., Cheng, H., Edwards, R., An, Z., Wu, J., Shen, C., and Dorale, J.: A high-resolution absolute-dated Late Pleistocene monsoon record from Hulu Cave, China, Science, 294, 2345–2348, doi:{10.1126/science.1064618}, 2001.

Wolff, E. W., Chappellaz, J., Blunier, T., Rasmussen, S. O., and Svensson, A.: Millennial-scale variability during the last glacial: The ice core record, Quaternary Sci. Rev., 29, 2828–2838, doi: {10.1016/j.quascirev.2009.10.013}, 2010.

4.5 Conclusions and perspectives of this chapter

The work in this chapter was motivated by the need of a better description of the patterns of changes associated to the Dansgaard-Oeschger events observed in Greenland ice cores, temporally and spatially, in order to better understand the underlying mechanisms. In this chapter, we have reconstructed a more precise picture of DO events in Greenland. We have used δ^{15}N data and firn models, an alternative method to the water isotope thermometer, in order to quantitatively reconstruct the past temperature at different sites in Greenland. This method also gives an estimate of the past accumulation rate. We were then able to compare these quantitative temperature and accumulation rate reconstructions in between different Greenland sites. This has been done for DO-8 to DO-10 for the NEEM, NGRIP, GRIP and GISP2 sites. The temperature reconstructions were also compared to the water isotopes, in order to better quantify the sensitivity of water isotopes to temperature (α factor). A detailed investigation of the temporal changes in α has been conducted for the NGRIP core, from the Holocene to the Eemian. We summarise hereafter our main findings.

At the onset of DO-8 and DO-10, the temperature and accumulation increases are smaller going north, while the water isotope increase is larger (no spatial gradient is detected for the small DO-9 event). These observations are in agreement with a study of spatial Greenland response to reduced sea-ice extent in the Nordic seas (Li et al., 2010). Our results therefore support the suggestion from Li et al. (2010), based on model simulations, as well as Dokken et al. (2013), based on a high resolution marine core from the Nordic Seas, that sea-ice cover in this area does play a role in the Dansgaard-Oeschger mechanisms. Abrupt sea ice retreat at the beginning of a DO event is likely to contribute to the warming and accumulation rate increase in Greenland. Also, this see-ice retreat may allow new moisture sources for Greenland from more local and cold waters than during the stadials. This would be in agreement with reconstructions of vapour source characteristics (temperature, relative humidity) for Greenland based on d-excess data (Johnsen et al., 1989; Masson-Delmotte et al., 2005a).

The amplitude of Greenland warming at the onset of DO events is not related to indicators of the seesaw mechanism. We suggest local Arctic amplification mechanisms. It has been previously shown that the EDML warming is linearly related to the preceding Greenland stadial duration, as predicted by the seesaw mechanism. On the contrary, the continuous temperature reconstruction from the NGRIP ice core has shown that there is no link between the GS duration and the GI temperature increase. In the same way, there is also no link between the preceding EDML warming and the GI temperature increase. This calls for other mechanisms at play in the Arctic, complementing the AMOC restart in order to explain Greenland temperature variations. Again, sea ice retreat in the Nordic Seas is a good candidate, because of marine evidences (Dokken et al., 2013; Zumaque et al., 2012) and model studies (Li et al., 2005, 2010) supported by ice core data (Guillevic et al., 2013).

During MIS3, the sensitivity of NEEM water isotopes to temperature is higher compared to NGRIP, GRIP and GISP2. This may be due to limited changes in precipitation seasonality at NEEM, which today already receives a larger fraction of its precipitation during summer (Steen-Larsen et al., 2011). This finding will also have implications for climate reconstructions based on NEEM water isotope data. To assess the stability of this observation, further paleoclimate reconstructions for different MIS would be needed.

At orbital timescales, a comparison of NGRIP temperature and water isotopes sug-

gests that α is influenced by obliquity and northern hemisphere ice sheet size. The obliquity imprint on α (α increases when the obliquity decreases) can be qualitatively explained by a Rayleigh distillation model. Masson-Delmotte et al. (2005a) already noticed an imprint of obliquity in the source-site temperature gradient for GRIP, which is in agreement with our findings. To explain why α seems to increase with the northern hemisphere ice sheet size is less straightforward. The Laurentide ice sheet may have an effect on the atmospheric circulation, influencing the vapour source location and its trajectory on the way to Greenland (Liu et al., 2012; Bromwich et al., 2004; Langen and Vinther, 2009; Pausata et al., 2011b). A split jet stream due to a massive Laurentide ice sheet may increase the relative proportion in Greenland ice of depleted vapour originating from the Pacific, explaining our observations. Note also that for the last interglacial warmer than today, Sime et al. (2013) have shown that Greenland isotopes as reconstructed by AGCMs strongly depend on the patterns of sea surface temperature (SST) and sea ice changes in the Arctic. A future study combining the Greenland temperature reconstructions presented in this chapter together with databases of past sea-ice cover and SST would be highly valuable.

Further investigations of possible source effects on Greenland water isotopes (using deuterium excess and ^{17}O excess), and an improved characterisation of atmospheric circulation patterns would be required to better explain the causes of the regional isotope and temperature gradients in Greenland. We hope that the new information we have provided in this chapter will motivate higher resolution simulations of the Greenland climate.

Chapter 5

Heinrich events signature in high resolution ice core proxies

5.1 Motivations and organisation of this chapter

Heinrich events (HE) are defined as sediment layers in North Atlantic marine cores with a high percentage of ice rafted detritus (IRD), created by the melting of icebergs. Six sediment layers fulfilling this definition have been clearly identified in many marine cores from the North Atlantic during the last glacial period (Heinrich, 1988; Bond et al., 1992; Broecker et al., 1992), numbered H1 (the most recent one) to H6, Fig. 5.6 p. 150. While the signature of Heinrich events has been identified in surface temperature and salinity proxies from North Atlantic marine cores, no consensus exists up to now to robustly identify the signature of HE in ice cores.

The aim of this chapter is to investigate multiple climate proxies registered in Greenland ice cores, giving information about the local as well as the remote climate on exactly the same timescale, during the major Heinrich Events 4 and 5, occurring during MIS3. Once the fingerprints registered in ice core proxies of the icebergs delivery are placed on the same chronology, it is possible to reconstruct the sequence of events surrounding H4 and H5 at low and high latitudes.

In a first section, we present the state of the art on what is known about Heinrich events, their possible trigger and their (absence of) signature in different proxies from different places. We then present our multi-proxy study based on Greenland ice cores, where we aim at identifying the fingerprint of Heinrich event 4 and 5. This identification makes possible to propose a precise timing of the iceberg delivery compared to the Greenland Dansgaard-Oeschger events.

5.2 What do we know about Heinrich events?

5.2.1 Identification of Heinrich events in marine cores from the North Atlantic

According to Hemming (2004), IRD are "*sediment that was entrained in floating ice, either ice-bergs or sea ice, and that settled to the seafloor when the enclosing ice melted*". Six such layers have been identified in multiple marine cores from the North Atlantic, numbered H1 to H6 (Fig. 5.6 p. 150), and originating from northern hemisphere ice sheets (map Fig. 2 p. 2). The

Younger Dryas is sometimes considered as H0. Other minor HE have been reported, for example H5a before DO 14 (Rashid et al., 2003), and H7a, 7b, 8, 9 and 10 before DO 19, 20, 21, 22 and 23 (Rasmussen et al., 2003), Fig. 5.6 p. 150. For these minor IRD layers, the alternative nomenclature C-i can be used, e.g. Chapman and Shackleton (1999), with *i* being the number of the GI chronologically following the IRD layer.

Heinrich events are accompanied by a lowering of $\delta^{18}O$ from the carbonate shell of planktonic foraminifers, which is a proxy for local temperature, salinity and oceanic $\delta^{18}O$ isotopic composition. Because of the icebergs delivery, the North Atlantic surface waters cool down, the salinity decreases, as well as the surface water isotopic composition. A regional study from Cortijo et al. (1997) for H4 showed that the salinity reduction spreads between 40 and 50°N, in agreement with the spatial distribution of IRD in the North Atlantic, while latitudes up to 60°N are affected by a temperature reduction.

Other archives from remote places compared to the North Atlantic Ocean record climatic anomalies at times of Heinrich events, in the mid Northern latitudes and in the tropics (see Sect. 5.2.5). On the contrary, Greenland water isotopes from ice cores, a proxy for local temperature, do not show particularly low values during the stadials when Heinrich events occur; this is observed for all Greenland ice cores (Johnsen et al., 2001; NGRIP members, 2004). The same finding is obtained when considering Greenland temperature reconstructions based on gas isotopes from the air entrapped in the ice, an alternative proxy to reconstruct Greenland temperature (e.g., Kindler et al., 2014). Antarctica experiences pronounced warming at time of Heinrich events; however, this warming is believed to be due to the particularly long duration of the stadials encompassing a HE (EPICA community members, 2006; Capron et al., 2010a), "giving time" to accumulate heat in the southern ocean according to the bipolar seesaw mechanism (Stocker and Johnsen, 2003), as opposed to the HE itself.

5.2.2 Construction of marine timescales

Marine cores usually contain a sufficient amount of organic material to be dated by ^{14}C dating. However, a large uncertainty of this method is the estimation of the reservoir age (Waelbroeck et al., 2001): "*the ^{14}C dates are measured on foraminifera preserved in the sediments and hence reflect the $^{14}C/^{12}C$ ratio of the water in which the foraminifera calcified. The surface-water $^{14}C/^{12}C$ ratio is different from that of the contemporaneous atmosphere, reflecting the balance between the input of atmospheric ^{14}C and its removal by transport and radiodecay in the water column. This difference in $^{14}C/^{12}C$ ratio is usually expressed as the apparent or reservoir age of the water mass.*" Earlier studies generally assumed that this age was constant over time and equal to its present-day value of 400±100 a. On the contrary, Waelbroeck et al. (2001) evidenced that this reservoir age varied in the past, being around 1200 to 1900±700 a at the end of H1 in the North Atlantic, depending on the precise location of the core. Changes in the reservoir age can be due to the shutdown of the NADW circulation during Heinrich events, to the continental water release by icebergs discharges from ice sheets during HEs, or to change of the atmospheric radiocarbon age, further influencing the reservoir radiocarbon age (Hemming, 2004; Yokoyama et al., 2000).

Alternatively, marine cores from the North Atlantic can be tied to ice core chronologies, which is very tempting since both display the similar millennial scale variations known as Dansgaard-Oeschger events (Shackleton et al., 2004; Skinner, 2008, Fig. 5.1). This has been
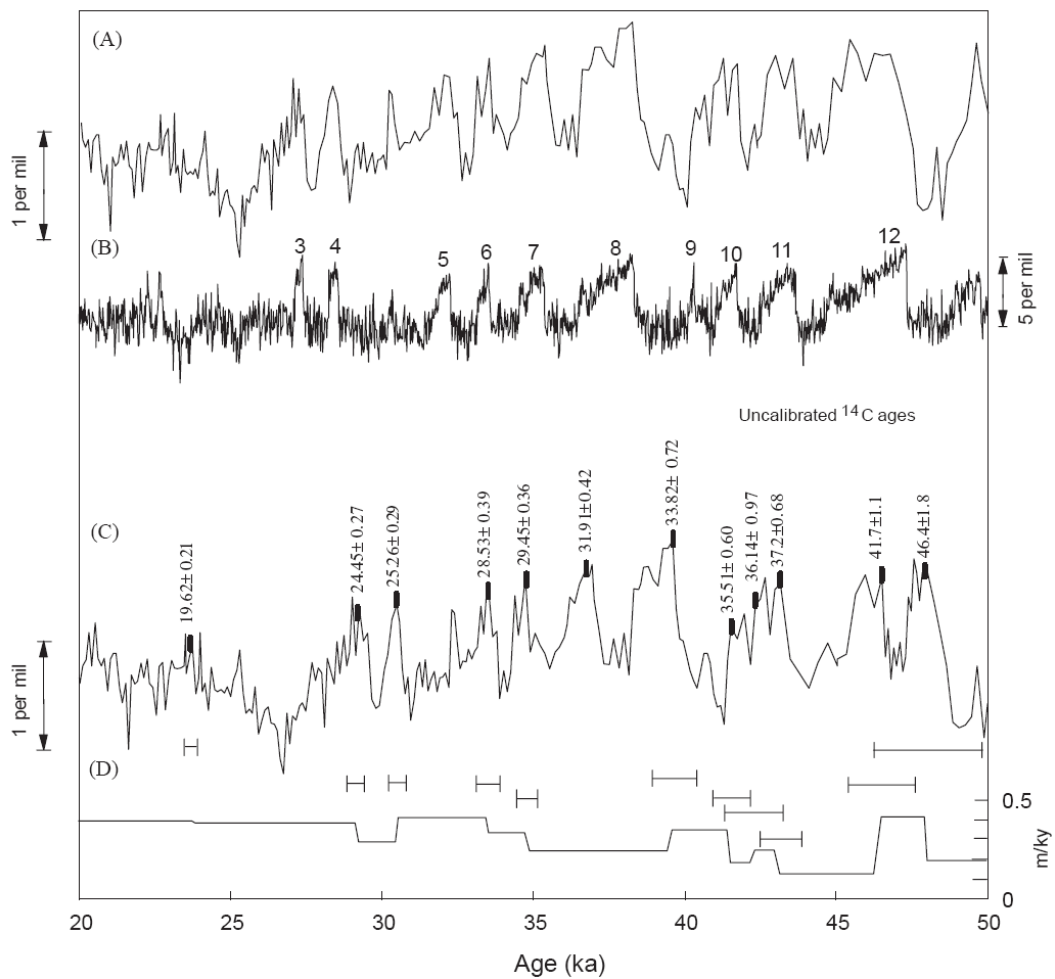
Figure 5.1: Shackleton et al. (2004), Fig. 1.: construction of the marine core MD95-2042 chronology by matching to the GRIP ice core. Original caption: *(A) δ^{18}O in Globigerina bulloides, core MD95-2042, time scale based on a correlation to GRIP on the SS09sea time scale. (B) δ^{18}O in GRIP ice core, time scale SS09sea of Johnsen et al. (2001). (C) δ^{18}O in Globigerina bulloides, core MD95-2042, time scale using as controls only the ^{14}C measurements shown, calibrated as in Table 1. (D) Sediment accumulation rates implied by (C) with above, analytical error (1 σ) on age controls.*

for example proposed by Bond et al. (1993): "*That alignment is justified by the fact that at the latitudes of our cores (50–54°N), shifts in sea surface temperature must be in phase with air temperature changes above Greenland, especially at the sharp terminations of Dansgaard-Oeschger cycles*". This matching strategy is still widely applied and recommended by the INTIMATE working group (Integration of ice cores, marine and terrestrial records of the North Atlantic) for the period 0-60 ka b2k, in the absence of independent chronological match points as tephra layers, as reviewed by Austin and Hibbert (2012). The relatively good correspondence between the DO climate shape in Greenland ice and oceanic sea surface temperature variations as recorded in marine cores from the North Atlantic is so far used as the reason why cold and warm phases in ice and marines cores are assumed to be equivalent in duration.

However, temperature reconstructions from Greenland ice cores are not particularly colder during the GS when a Heinrich event occurred compared to the GS without Heinrich event, as mentioned before: Greenland climate appears to be insensitive to Heinrich events.

This remains so far unexplained. This strongly limits the investigation of phase relationships between Greenland temperature and North Atlantic Ocean surface temperature.

5.2.3   Heinrich events and oceanic circulation

As reviewed by Hemming (2004), different proxies for oceanic circulation point to a drastically reduced North Atlantic Deep Water (NADW) concomitant with the massive icebergs delivery of Heinrich events. Remarkable reduction in benthic $\delta^{13}C$ (Keigwin and Lehman, 1994; Vidal et al., 1997, 1998; Zahn et al., 1997; Willamowski and Zahn, 2000; Elliot et al., 2002) as well as excess Pa/Th ratios from Bermuda rise sediments (McManus et al., 2002) are both in agreement with drastic reduction of the NADW formation. Looking more into details, core ODP 1060 off Florida records $\delta^{13}C$ values similar during both GS and Heinrich events (Vautravers et al., 2004). On the contrary, marine cores from the Irminger Basin and Rockall Plateau, Northern Atlantic, register significantly lower $\delta^{13}C$ during Heinrich events compared to GS (Elliot et al., 2002). These authors underline that "*equivalent degree of cooling over Greenland is obtained with different perturbations of deep-water formation. Our results either question the role of the THC as the unique explanation for these millennial scale climate oscillations, or call upon an amplifying mechanism not yet taken into account*". The re-start of the AMOC and NADW formation after Heinrich events, corresponding to warm phases in Greenland, is also evidenced (e.g. for H4, Gutjahr et al., 2010).

Several climate models produce such an NADW shut off when injecting a sufficient amount of fresh water in the Ruddiman belt (the North Atlantic area where IRD layers are present) (Manabe and Stouffer, 1995; Paillard and Cortijo, 1999; Kageyama et al., 2010), suggesting that the NADW reduction is a response to H events and not its trigger. The NADW reduction would then block the arrival of surface warm waters (the Atlantic Meridional Overturning Circulation) into the North Atlantic, further cooling the North Atlantic. The amount of fresh water that has to be injected to shut off the thermohaline circulation is model dependent and also varies with the location of the input (e.g., Roche et al., 2010; Otto-Bliesner and Brady, 2010).

5.2.4   The Nordic Seas during Heinrich events: a sub-surface warming?

During Heinrich events and stadials, different climate proxies from marine cores drilled in the Nordic Seas point to either a warming or a larger sea-ice cover in this area, which seems contradictory (e.g., Eynaud et al., 2002). This has been reviewed and tentatively explained for the LGM by de Vernal et al. (2006), Fig. 5.2. To explain the coexistence of warm water and cold water proxies, Rasmussen and Thomsen (2004) proposed that "*during the stadials, a halocline was established in the Nordic Seas and in the northernmost part of the North Atlantic and the outflow from the Nordic Seas stopped. However, below the cold, light surface layer, the relatively warm water of the North Atlantic Drift continued to flow across the North Atlantic and into the Nordic Seas, here warming up the deep-water masses.*" More recently, Jonkers et al. (2010) even recorded a subsurface warming during Heinrich events, and in particular H4, in two marines cores from the Eastern flank of the Reykjanes Ridge ($\sim$58.57°N, $\sim$30.30°W), together with a decrease of the water mass ventilation. They suggested that sea-ice cover causes the ventilation decrease, and creates an insulation lid between the ocean and the cold atmosphere, facilitating a warming of the subsurface by the North Atlantic Drift.
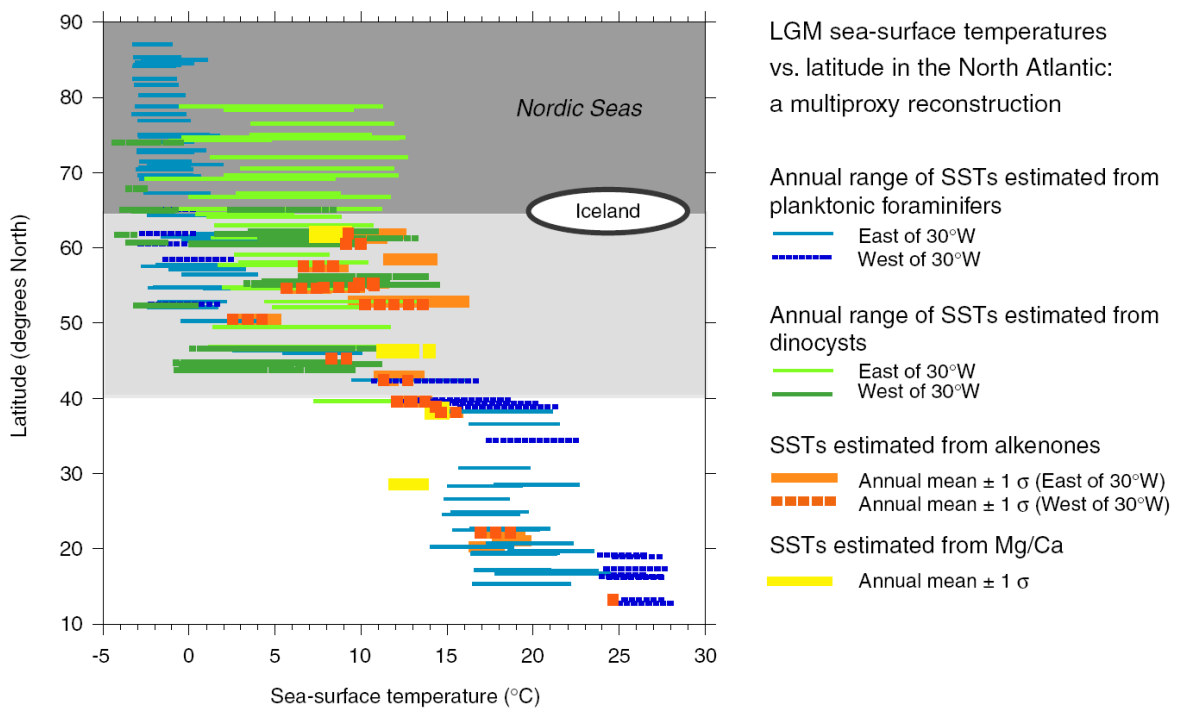
Figure 5.2: de Vernal et al. (2006), Fig.3. Original caption: *The latitudinal distribution of LGM SSTs in the North Atlantic based on reconstructions using foraminifers (Weinelt, 2004; Kucera et al., 2005), alkenones (Lee, 2004), dinocysts (de Vernal et al., 2005) and Mg/Ca measurements in epipelagic foraminifers (Barker et al., 2005). The annual range of estimated temperatures is shown based on planktonic foraminifer and dinocysts data. A distinction between the eastern and western sites has been made to illustrate the regional pattern that seems to characterise the North Atlantic at LGM.*

5.2.5 Atmospheric circulation changes associated with Heinrich events

Different climate proxies from middle to low latitudes around the globe point to atmospheric circulation reorganisations associated with Heinrich events (e.g., Clement et al., 2004; Boyle, 2000; Lewis et al., 2010). In Europe, speleothems from the Villars cave, South West France, show an increase in δ^{13}C, associated with reduced soil biological activity, or a hiatus during the coldest HE, when the soil was frozen. The calcite δ^{18}O records from this cave do not show any particular trend, maybe due to counteracting effects of precipitation isotopic composition and cave temperature (Genty et al., 2006). Pollen records indicate colder temperatures and possibly drier conditions in South of France, Italy, Iberia and in the Alps (Genty et al., 2010; Pérez-Folgado et al., 2003; Moreno et al., 2005). The same climatic patterns can be reconstructed from the Sofular speleothem records, Turkey (Fleitmann et al., 2009).

In the Cariaco Basin, Central America, sediment cores indicate decreased precipitation and riverine discharges, and generally drier and colder conditions (Peterson et al., 2000; Deplazes et al., 2013; Gonzalez et al., 2008). In South America, speleothems from different caves show increased growth (Wang et al., 2004) and lighter precipitation, interpreted as markers of increased rainfall amount (Kanner et al., 2012; Wang et al., 2007; Mosblech et al., 2012). Glaciological evidence of glacier advance are present in the Andes, again because of increased precipitation (Smith and Rodbell, 2010).

All these proxies suggest a southwards displacement of the intertropical convergence

zone (ITCZ) during stadials with Heinrich event, clearly more pronounced than during stadials without Heinrich event. Model simulations (e.g. Chiang et al., 2008; Cvijanovic and Chiang, 2013) indeed produce in a few years a southwards displacement of the ITCZ over the Atlantic Ocean and its margins, in response to North Atlantic cooling, clearly pointing to an atmospheric teleconnection between North Atlantic and tropical climate. Other model studies (Lewis et al., 2010; Pausata et al., 2011a), supported by speleothem data (Wang et al., 2001) show that the African and East-Asian monsoon systems are also affected by Heinrich events, again through fast atmospheric teleconnections. The changes in sea surface temperature and ITCZ position are also thought to modify the isotopic composition of the precipitation in the Northern Hemisphere and in the tropics. This is imprinted on speleothems $\delta^{18}O$ records from Brazil caves, India, China, as well as δD of plant wax in lake sediments from Africa (e.g., review by Lewis et al., 2010).

Along the coast of Chile, at the onset of the last deglaciation, pollen records (Montade et al., 2013, and references therein), marine productivity reconstructions (Romero et al., 2006; Mohtadi et al., 2008; Anderson et al., 2009), and model simulations (Toggweiler et al., 2006) suggest a polewards shift of the mean position of the westerlies, locally increasing SST and upwelling, the latter leading to degassing of CO_2 into the atmosphere. For at least H1 (Anderson et al., 2009), this scenario is supported by the synchronous atmospheric CO_2 and Antarctic temperature rises registered in Antarctic ice cores, suggesting that H1, through atmospheric teleconnections, might be the trigger of the westerlies polewards shift. Lamy et al. (2007) also suggest that oceanic circulation changes might be transferred from the North Atlantic to the Southern Ocean through a seesaw mechanism, with the same consequences. Finally, based on their marine records off Chile that register periods of increased productivity at around the same time of Heinrich events during the glacial period, Anderson et al. (2009) suggest that each HE might trigger such a sequence of events. Such an outgassing of old CO_2, poor in ^{14}C, may also change the atmospheric and oceanic radiocarbon ages (e.g., Muscheler et al., 2008).

5.2.6   What is the trigger of Heinrich events?

So far, there is no consensus on the trigger of Heinrich events. Several hypotheses exist and constitute two categories: internal and external causes. The internal causes support that the Laurentide ice sheet may itself trigger its instability. Different ice sheet models indeed propose "*purging of the Laurentide ice sheet, episodic activity of an ice stream in Hudson Strait, jökulhlaup activity and ice shelf building/collapse*", as reviewed by Hemming (2004).

External causes propose a external trigger as responsible for the Laurentide ice sheet collapse. For example Braun et al. (2005) invoke solar activity. Scourse et al. (2000), based on the origin identification of IRD within a IRD layer, propose a role of the European ice-sheets as precursor of H2. This is however debated, since more recent studies underline the presence of European IRD at many periods of MIS3 and MIS2, followed or not by a HE (Peters et al., 2008; Haapaniemi et al., 2010). More recently, sub-surface warming at the base of ice streams causing their collapse, leading to a destabilisation of the Laurentide is suggested by Alvarez-Solas et al. (2010); Marcott et al. (2011).

One of the major limitations when studying Heinrich events (e.g. to infer a triggering mechanism) is the timing uncertainty. Low sedimentation rates limit the possible sampling resolution when analysing marine records. As a consequence, changes in e.g. IRD con-

tent and foraminifers assemblages may seem synchronous at the resolution allowed by the sampling, but leads or lags up to a couple of hundred years, depending on the sampling resolution, may be difficult to ascertain. Dating methods uncertainties and modification of the sedimentation rates due to Heinrich events make any absolute dating and duration of the iceberg delivery hard to estimate. Matching to other archives often use the assumption that changes in different archives are synchronous, which may not be the case.

Until now, it is actually not certain what was the climate state (GS/GI) in Greenland, in the North Atlantic and in the mid-latitudes when a given IRD delivery from a given ice sheet started, making the trigger for Heinrich events difficult to identify. For example, Heinrich simulations by Alvarez-Solas et al. (2010) need a subsurface oceanic warming to destabilise an ice shelf, initiating the ice sheet collapse. This climatic context of reduced AMOC and subsurface warming in the North West Atlantic preceding Heinrich events by up to 1 ka is suggested by Marcott et al. (2011), based on data from a marine core (EW9302-2JPC, 48.47.70°N, 45.05.09°W) and model simulations.

5.2.7 Origin and timing of IRD during Heinrich event 4
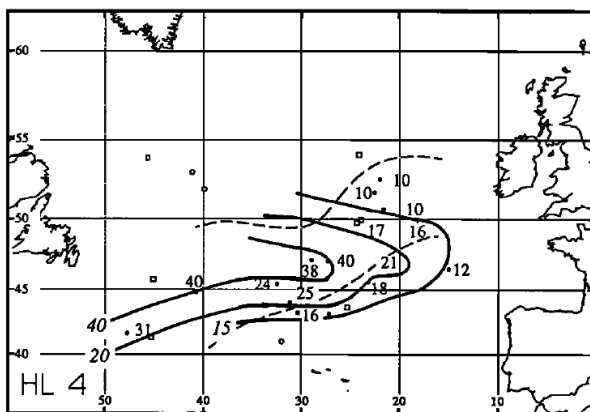
Figure 5.3: Grousset et al. (1993), Fig. 6, H4. Original caption: *Patterns of Heinrich layer thickness (in cm); ice-rafter detritus belt [after Ruddiman, 1977] is shown in dashed lines. Open symbols represent cores in which Heinrich layers are not present.*

We report here characteristics of Heinrich event 4, a major iceberg delivery well registered in the Ruddiman belt. This event occurred during MIS3, a period of high climatic instability, with short lived and frequent Dansggard-Oeschger events (NGRIP members, 2004; Capron et al., 2010b). Later in this chapter we will look for fingerprints of this event in Greenland ice cores.

Different analyses of the chemical characteristics of the IRD constitutive of Heinrich Event 4 point to a main Canadian origin, meaning that these IRD are transported by icebergs originating from the Laurentide ice sheet (LIS) (see Table 5.1, Fig. 5.4 and also Grousset et al., 1993, 2000; Rashid et al., 2003; Rashid and Grosjean, 2006; Hemming, 2004; Walden et al., 2007; Peck et al., 2007; Peters et al., 2008). This is true for all the IRD in the Ruddiman belt and as far south as the Iberian margin (Thouveny et al., 2000). The geographical pattern of IRD layer thickness also points to a LIS origin, and moreover shows that the majority of the icebergs melt between 45 and 50°N and 50 to 30°W (Fig. 5.3 and Grousset et al., 1993). Grousset et al. (1993) showed that at least in the Ruddiman belt, the presence of IRD in marine cores is associated with a synchronous increase of magnetic susceptibility (see also Fig. 5.4).

The timing of IRD registered in marine cores compared to the surface temperature sig-

Core	location	Lat., °N	Long., °W	Temperature	IRD origin	IRD vs cold state	Reference
SU 90-24	Irminger Basin	62.40	37.22	foram. count	mainly Iceland not LIS	after	Elliot et al. (1998)
MD99-2281	Faeroe Bank	60.21	09.27	% N.p., dynocysts		after	Zumaque et al. (2012)
LO09-18	Reykjanes Ridge	58.58.04	30.40.99	foram. assemblages		after	Jonkers et al. (2010)
MD95-2006	East of Scotland	57.01.82	10.03.48	% N.p.	LIS	after	Peters et al. (2008)
MD95-2002	Celtic margin	47.27.12	8.27.03	% N.p.	LIS	after	Auffret et al. (2002)
MD04-2845	Bay of Biscay	45.21	5.13	% N.p.		after?	Sánchez-Goñi et al. (2008)
MD04-2845				foram. assemblages		synchronous	
SU 90-11	NW Atlantic	44.04	40.20	% N.p.	LIS	synchronous	Cortijo et al. (1997); Jullien et al. (2006)
MD99-2331	Iberian margin	42.09.00	9.40.90	% N.p.		synchronous?	Naughton et al. (2009)
				foram. assemblages		up to 700 a after	Sánchez-Goñi et al. (2008)
MD95-2040	Iberian margin	40.34.91	9.51.67	% N.p.		200 a after or synchronous	Schönfeld et al. (2003) de Abreu et al. (2003)
SU 90-03	Central N Atl.	40.03	32.00	% N.p.		synchronous	Chapman and Shackleton (1998)
MD95-2042	Iberian margin	37.48	10.10	% N.p., foram. assemblages	mainly LIS	synchronous	Thouveny et al. (2000) Sánchez-Goñi et al. (2000, 2008)
ODP 1060	off Florida	30.46	74.28	faunal assemblages	synchronous	synchronous	(Vautravers et al., 2004; Gut-jahr et al., 2010)

Table 5.1: Heinrich event 4: timing of the onset of the IRD delivery compared to the beginning of the cold period, in different marine cores from the North Atlantic. Column 5 indicates which proxy is used to characterise the temperature (warm/cold). Methods are :% N.p., percentage of *Neogloboquadrina pachyderma*; foraminifers (foram.) or faunal assemblages; foraminifers count: number of present foraminifers. Column 6: origin of the IRD. LIS: Laurentide Ice Sheet; blank: undetermined. Column 7: timing of IRD onset vs cold period onset. A question mark indicates that the resolution of the core is too low to draw a clear conclusion on the timing.
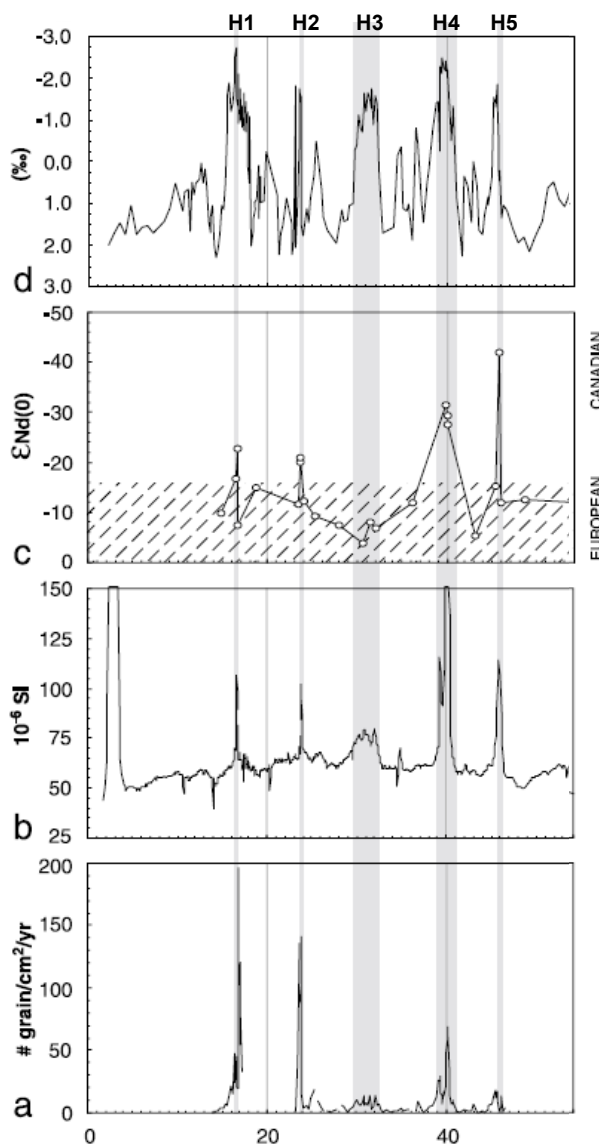
Figure 5.4: Auffret et al. (2002), detail of Fig. 9. Original caption: *(a) LLG (lithic grains larger than 150 μm) fluxes in core MD95-2002; (b) magnetic susceptibility; (c) $\epsilon_{Nd}(o)$ of the non-carbonate lithic fraction coarser than 150 μm; (d) sea surface salinity anomaly. x axis: calendar ages, ka BP. Note that H4 is characterised by a double peak in lithic grains and magnetic susceptibility.*

nal is not the same everywhere. On the northern side of the Ruddiman belt, the IRD do not originate from the LIS and therefore the timing of LIS collapse vs surface temperature drop is impossible to establish (e.g., core SU 90-24 in the Irminger Basin, Elliot et al., 1998). From approximately 57 to 45°N, the IRD input originating from Canada seems to be registered in marine cores after the onset of a cold period, and possibly produces a further cooling (e.g. core MD95-2002, Table 5.1). However, given the limited resolution of marine cores (∼200 to 400 a) compared to ice cores (down to ∼20 a for NGRIP) and the lack of temperature-independent match points (like tephra or paleomagnetic excursions) in between these two archives, it is not always clear if this cold period in marine cores is a cold GI-9 or already the onset of GS-9. A high resolution picture of H4 can be found in core MD95-2006 East of Scotland: GS-9 is clearly identified, marked by a high percentage of *N. Pachyderma*, indicating a polar climate at 57°N (Dickson et al., 2008). The IRD layer from the Laurentide is clearly registered (up to 700 a) after the beginning of GS-9 (Fig. 5.5 and Leigh, 2006; Peters et al., 2008).

On the southern side of the IRD belt, from 44 to 30°N, in general the onset of IRD deposition is synchronous with the onset of the cold phase, within data resolution (e.g., core
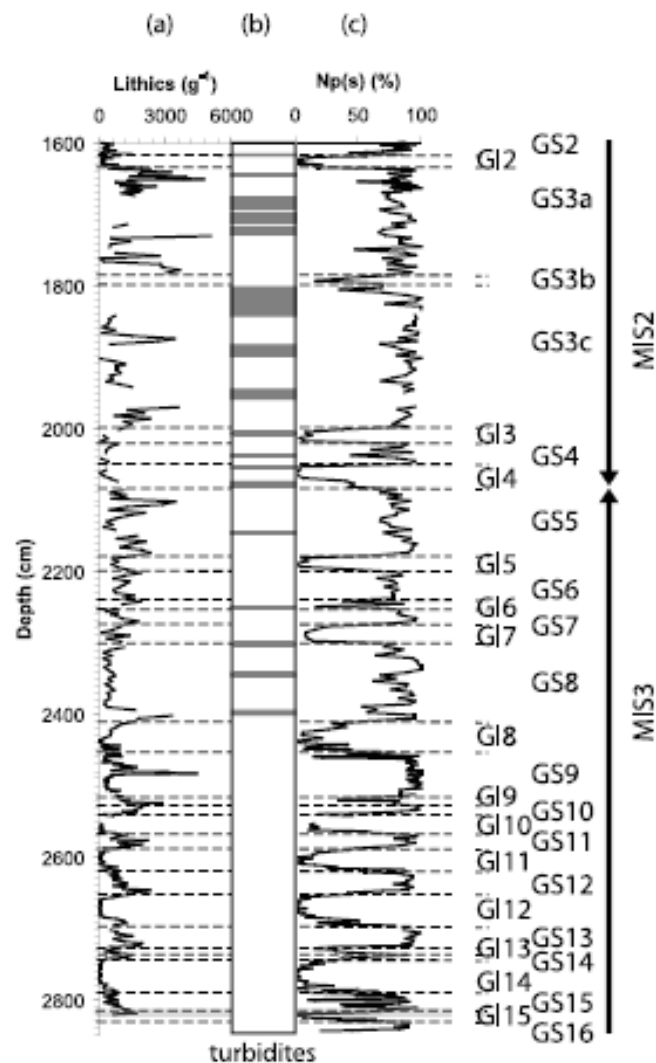
Figure 5.5: Peters et al. (2008), Fig. 2.a.b.c. Original caption: *Profiles spanning GS-16 to GS-2. The lithic counts and Np(s) data (data compiled from Austin et al. [2004], Dickson [2004], and Leigh [2006]) were used to define the stadial/interstadial sequence. The shaded band at ∼2817 cm represents the North Atlantic Ash Zone II. Eight magnetic parameters and ratios are shown reflecting IRD input and climatic variation.*

MD95-2040, de Abreu et al., 2003). However, this is clearly not the case for core MD99-2331 at 42°N, where on a depth scale the IRD are registered after the onset of the cold phase, and where the timescale suggests a delay of up to 700 a (Sánchez-Goñi et al., 2008). Comparing magnetic susceptibility and IRD in cores along the Iberian coast, Naughton et al. (2009) noticed the presence of high magnetic susceptibility at the time of sea surface temperature cooling, even though IRD are absent, and suggested that IRD delivery in the Ruddiman belt is synchronous with the temperature drop registered along the Iberian margin (Bard et al., 2000; Moreno et al., 2002). A modelling study of iceberg delivery to the North Atlantic (Jongma et al., 2013) showed that icebergs preferentially migrate along the North Atlantic Drift, while few icebergs actually melt at the Iberian Margin. This can explain why IRD may be absent or apparently delayed in-between different marines cores off the Iberian Margin.

Based on these observations, it seems that the cold phase (GS-9) may start before the IRD delivery on the northern edge of the Ruddiman belt, while the cooling may be synchronous

to the IRD delivery along the Iberian margin.

Interestingly, a couple of marine cores with high resolution data register the IRD of H4 as 2 distinct sub-events (MD95-2002 in Fig. 5.4, ODP 1060). In a similar way, core MD95-2042 displays 2 sub-cooling during H4 (Fig. 5.1 Pailler and Bard, 2002; Shackleton et al., 2004).

All these observations based on marine core proxies will be compared to ice core proxies in the next section.

5.3   Multi-proxy fingerprint of Heinrich Event 4 in Greenland ice core records

This section is a draft of an article from M. Guillevic, L. Bazin, C. Stowasser, A. Landais, V. Masson-Delmotte, T. Blunier, F. Eynaud, S. Falourd, E. Michel, B. Minster, T. Popp, F. Prié and B.M. Vinther. I did most of the writing with help from all co-authors. The new ^{17}O excess and δ^{18}O$_{atm}$ presented here were measured at LSCE by L. Bazin, F. Prié, A. Landais and myself. The NEEM methane data were measured by C. Stowasser and T. Blunier and are now published in Chappellaz et al. (2013). The NEEM δ^{18}O and d-excess were measured at LSCE and CIC by the respective stable water isotope laboratories.

Abstract Glacial climate was characterised by two types of abrupt events. Greenland ice cores document Dansgaard-Oeschger events, marked by abrupt warming in-between cold, stadial phases. Six of these stadials coincide with major Heinrich events (HE) (Bond et al., 1992; Hemming, 2004), identified from Iceberg Rafted Debris (IRD) in North Atlantic deep sea sediments, documenting major inflows of melt water from ice sheets. This finding has led to the paradigm that glacial cold events are induced by the response of the Atlantic Meridional Overturning Circulation to massive freshwater inputs, supported by sensitivity studies conducted with climate models of various complexity (Kageyama et al., 2013). This mechanism could however never be confirmed or infirmed because the exact timing of Heinrich events and associated low latitude hydrological cycle changes (Clement and Peterson, 2008) with respect to Greenland stadials has so far remained elusive. Here, we provide the first multi-proxy fingerprint of H4 in Greenland ice cores through ice and air proxies of low latitude climate and water cycle changes. Our new dataset demonstrates that stadial 9 consists of three phases, characterised first by Greenland cooling during 540±50 years, followed by the fingerprint of Heinrich Event 4 as identified from subtropical Atlantic proxy records, lasting 740±50 years, itself ending approximately 370±50 years prior to abrupt Greenland warming. The decoupling between stable cold Greenland temperature and low latitude HE imprints provides new targets for benchmarking climate model simulations and testing mechanisms associated with millennial variability.

5.3.1   Introduction

Glacial climate is characterised by millennial variability, recorded with specific expressions in different archives and at different latitudes (Clement and Peterson, 2008). Greenland ice core records of ice δ^{18}O, a qualitative proxy of air temperature, have unveiled with high resolution the succession of cold phases (Greenland Stadials, GS) and warm phases (Greenland Interstadials, GI) forming the 25 Dansgaard-Oeschger events (DO) of the last glacial
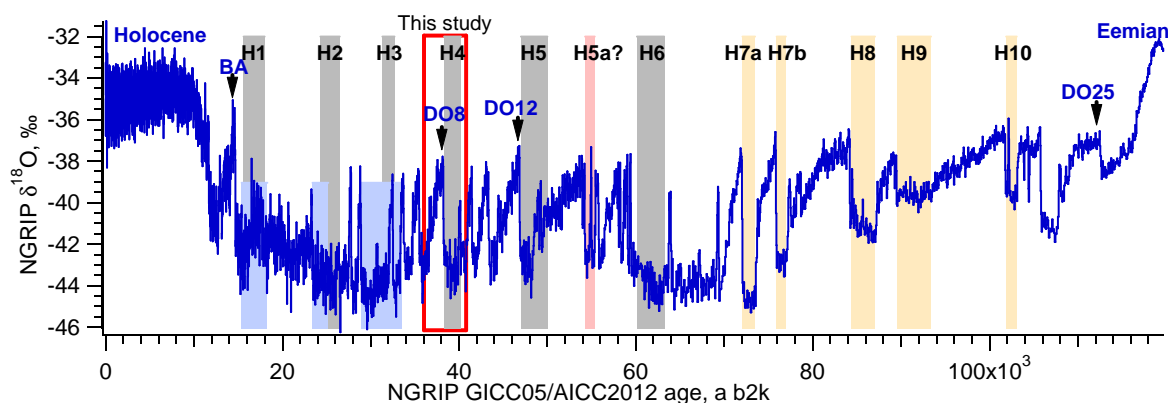
Figure 5.6: Dansgaard-Oeschger (DO) and Heinrich (H) events during the last glacial period. NGRIP $\delta^{18}O$ (‰) (NGRIP members, 2004), blue line, on the GICC05 timescale (Supplementary Information). BA: Bølling Allerød. Grey areas: position and duration of H1 to H6, major Heinrich events recorded in marine cores from the North Atlantic (Sánchez Goñi and Harrison, 2010). Blue areas: periods of low salinity corresponding to fresh water input on the Celtic Margin. H5a (pink) and H7 to H10 (yellow) are minor IRD events, recorded in the West Atlantic (references in Supplementary Information).

period (NGRIP members, 2004). Continental and marine archives from lower latitudes also exhibit millennial variability for e.g. temperature, monsoon strength and vegetation cover (Clement and Peterson, 2008).

A prominent feature identified in North Atlantic deep cores is the occurrence of Ice Rafted Debris (IRD). These Heinrich events (HE) evidence strong iceberg discharges during 6 of the cold phases (stadials) of the last glacial period (Fig. 5.6) (Bond et al., 1992; Hemming, 2004). Several lines of evidence suggest that HE are shorter than the corresponding GS (Peters et al., 2008; Roche et al., 2004). However, the timescale accuracy for both marine and ice records so far prevents the exact timing of Heinrich events with respect to GS. Therefore the mechanisms relating iceberg discharge, low latitude climatic change and Greenland temperature change during stadials remains debated (Sánchez Goñi and Harrison, 2010; Austin and Hibbert, 2012).

Here, we focus on GS-9, 38,220-39,920 a b2k (years before 2,000 AD on the GICC05 timescale, Supplementary Information), between GI-8 and GI-9, characterised by the occurrence of the major H4 IRD event of mostly Laurentide ice sheet origin (Hemming, 2004).This event occurs during Marine Isotope Stage 3, a period consisting of short-lived and frequent DO events (NGRIP members, 2004). In the following we will argue that the climatic fingerprint of H4 can be identified in multiple proxy records sensitive to climate and environmental changes at high, mid and low latitudes, archived in the ice and air of Greenland ice cores. All these records are reported here on the GICC05 chronology (Supplementary information).

5.3.2 Data and discussion

Precious information on the sequence between mid and high latitude climate arises from the combination of all stable water isotopologues in Greenland ice cores. $\delta^{18}O$ is a qualitative proxy of local Greenland temperature showing the well-known GS-GI pattern. Deuterium excess (d-excess) is influenced by the vapour source temperature and relative humidity,
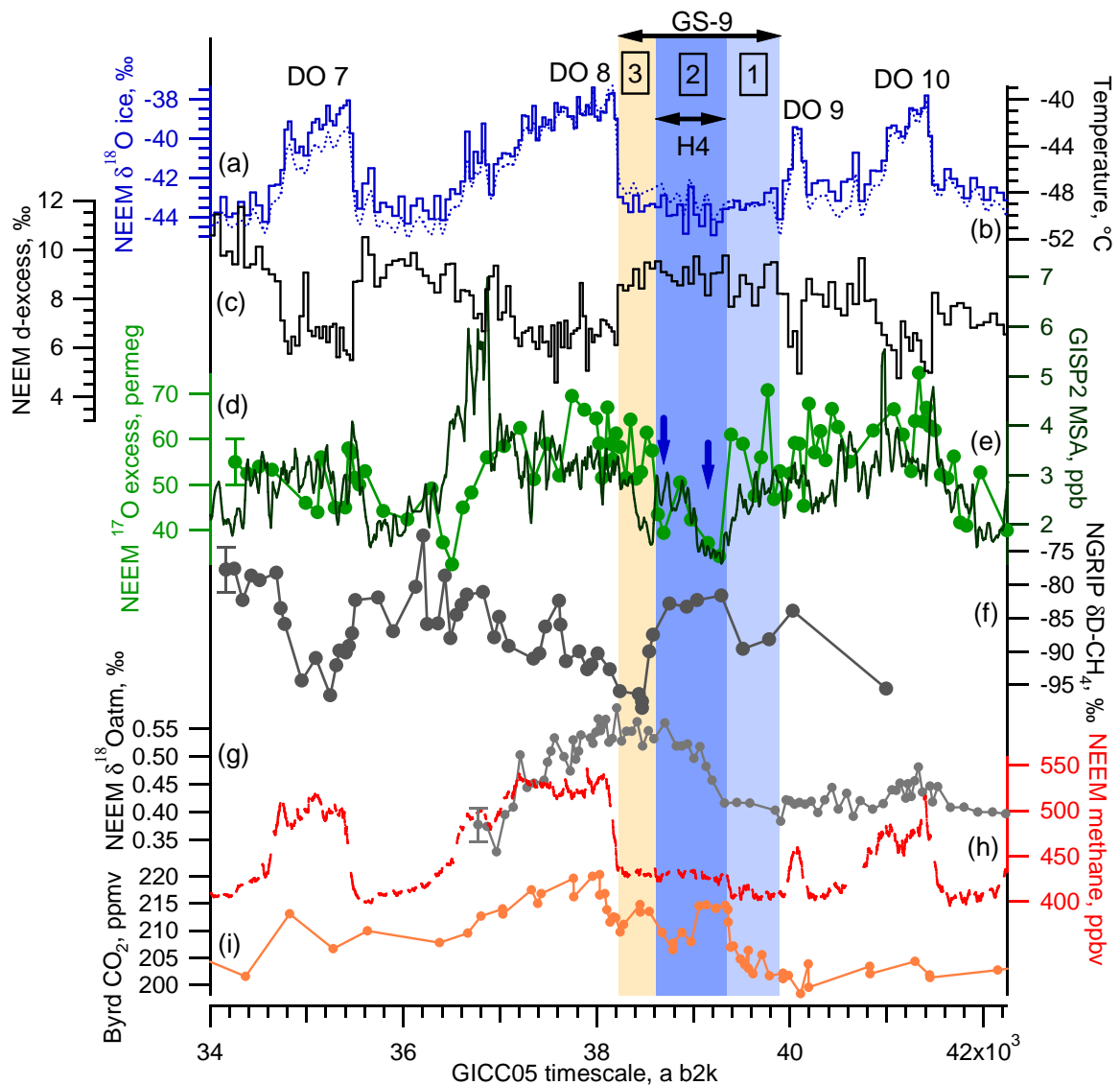
Figure 5.7: Greenland and Antarctic ice core records surrounding Heinrich event 4, synchronised to the GICC05 timescale (Supplementary Information). Light blue area, phase 1: 39,890-39,350 a b2k. Blue area, phase 2 (H4): 39,350-38,610 a b2k. Yellow area, phase 3: 38,610-38,230 a b2k.

(a) Blue line: δ^{18}O ice, ‰ (precision: 0.07 ‰), NEEM ice core, Greenland (Guillevic et al., 2013).

(b) Blue dotted line: NEEM temperature reconstructed using δ^{15}N data and firn modeling (Guillevic et al., 2013).

(c) Black: NEEM deuterium excess, ‰ (±0.7 ‰), this study, measured at LSCE (France).

(d) Green dots: NEEM ^{17}O excess, permeg (±5 permeg), this study. Measured at LSCE Landais et al. (2012b). Each dot corresponds to the average over 55 cm of ice.

(e) Dark green: GISP2 MSA concentration data (Saltzman et al., 1997), ppb, 50 a running average.

(f) Dark grey: NGRIP δD-CH$_4$, ‰ (±3.4‰) (Bock et al., 2010).

(g) Light grey: NEEM δ^{18}O$_{atm}$, ‰ (±0.03‰), this study, measured at LSCE.

(h) Red: NEEM methane mixing ratio, ppbv (±5 ppbv), record measured by the Picarro instrument (Chappellaz et al., 2013).

(i) Orange: CO$_2$ mixing ratio, ppmv (±1 ppmv), from the Byrd ice core, Antarctica (Ahn et al., 2012).

as well as the condensation temperature of precipitation Masson-Delmotte et al. (2005a). ^{17}O excess (^{17}O excess = ln(δ^{17}O) - 0.528 ln(δ^{18}O)) is a new parameter reflecting variations in the relative humidity of Greenland moisture source, situated at mid-latitudes Masson-Delmotte et al. (2005a); Landais et al. (2012b).

We have performed on the NEEM ice core (Dahl-Jensen and NEEM community members, 2013) the first measurements of ^{17}O excess, spanning a sequence of 3 DO and encompassing GS-9 (Supplementary Information). Within GS-9 of constantly low δ^{18}O and high d-excess values, three distinct phases are inferred from ^{17}O excess variations (Fig. 5.7d): phase 1 (39,890-39,350 a b2k), corresponding to the beginning of GS-9, is marked by high ^{17}O excess values (mean=56 permeg); phase 2 (39,350-38,610 a b2k) corresponds to low ^{17}O excess values (down to 34 permeg); finally during phase 3 (38,610-38,230 a b2k) ^{17}O excess reaches high interstadial levels again (mean=57 permeg). The cold and stable Greenland temperature during the entire GS-9 is further confirmed by an independent temperature reconstruction based on firn gas fractionation (δ^{15}N, Fig. 5.7b and Guillevic et al., 2013). Our new data therefore suggest a decoupling between stable, cold Greenland temperatures and changes in the climate of the mid latitude source region for Greenland precipitation.

Using high resolution measurements of δ^{18}O of O$_2$ (δ^{18}O$_{atm}$) trapped in the NEEM ice core over the same sequence of events, we are able to evidence a global signature for this three phase sequence of GS-9 at mid-latitudes. Indeed, earlier studies have shown that millennial δ^{18}O$_{atm}$ variations are global responses to water cycle changes in the northern tropics (Severinghaus et al., 2009; Landais et al., 2010), where ITCZ shifts drive changes in precipitation isotopic composition (Lewis et al., 2010; Pausata et al., 2011a). Our 95 new measurements of δ^{18}O$_{atm}$ depict a stable, low δ^{18}O$_{atm}$ during phase 1, followed by an increase over phase 2 (+0.14 ‰), and finally a stable high plateau during phase 3 (Fig. 5.7g). The onsets of changes of δ^{18}O$_{atm}$ and ^{17}O excess occur synchronously at the beginning of phase 2, but the increase of δ^{18}O$_{atm}$ is much slower than the observed changes in ^{17}O excess; this is expected because of the long residence time of oxygen in the atmosphere (1000 - 2000 a) (Severinghaus et al., 2009).

Additionally, MSA (methyl sulfonic acid) and methane from ice cores evidence the same tree phase structure during GS-9. First, in the ice phase, the high resolution MSA data from the GISP2 Greenland ice core (Fig. 5.7e and Saltzman et al., 1997), a proxy of sea-ice extent (Abram et al., 2013) suggests that the onset of phase 2 is marked by a large sea-ice expansion in the North Atlantic. Such a sea-ice expansion is likely associated with a southwards shift of storm tracks and, hence, Greenland moisture sources, leading to more recycling of the vapour on the way to Greenland without necessary source temperature changes, therefore explaining the low ^{17}O excess signal and the constant d-excess during phase 2 (Fig. 5.7c, d). Southward shifts of ITCZ simulated in response to increased North Atlantic sea ice cover (Chiang et al., 2008) could also explain the simultaneous δ^{18}O$_{atm}$ signal.

Second, in the gas phase, the global expression of the three phase sequence is imprinted in the records of CH$_4$ and its hydrogen isotopic composition (δD-CH$_4$) (Fig. 5.7h and 5.7f, respectively). Phase 1 is characterised by a minimum in methane mixing ratio, whereas the onset of phase 2 is marked by a 20 ppb abrupt increase (Fig. 5.7h and Chappellaz et al., 2013) accompanied by a 8 ‰ ±4.8 ‰ increase in δD-CH$_4$ (Bock et al., 2010). Such a shift would be in agreement with clathrate release, but is not supported by the following stable plateau of methane mixing ratio throughout phase 2 and 3. We rather favour a source mix change or/and heavier isotopic composition of tropical precipitation (Möller et al., 2013)

at the onset of phase 2. The mixing ratio increase is consistent with the activation of new methane sources, in e.g. South America (Hopcroft et al., 2011), associated with a southward ITCZ shift at the onset of phase 2. Moreover, such southward ITCZ shift is expected to produce more depleted precipitation in the SH tropics and heavier precipitation in the NH tropics (Pausata et al., 2011a; Lewis et al., 2010). The increase in both δD-CH$_4$ and δ^{18}O$_{atm}$ at the onset of phase 2 are consistent with this mechanism, provided that NH tropics remain the main source of methane and oxygen. A minor part of the δD-CH$_4$ increase can be due to oxidation of methane in the troposphere, consuming preferentially the light methane isotopologues because of the globally lower mean atmospheric temperature at the onset of phase 2 (Lewis et al., 2010; Bock et al., 2010).

Finally, two abrupt $\sim$20 ppm increases in the atmospheric CO$_2$ concentration recently unveiled from high resolution Antarctic ice core records occur at the onsets of phase 2 and phase 3 (Fig. 5.7i). This finding arises from our fine synchronisation of Antarctic and Greenland ice core records (Supplementary Information). The current interpretation of these CO$_2$ rises is changes in upwelling and/or shifts of the mean position of the SH westerlies, two features which could be related to ITCZ shifts (Toggweiler et al., 2006; Anderson et al., 2009).

The proposed sequence of events is summarised in Fig. 5.8. Altogether, our multi-proxy ice core dataset reveals a 740 a long period beginning 540 a after the beginning of GS-9 (phase 2) which is marked by N Atlantic sea ice expansion and southward shifts in N Atlantic storm tracks and ITCZ. The transition to phase 3 is characterised by reversed variations, with ^{17}O excess, MSA and δD-CH$_4$ reaching interstadial values 200 to 400 a prior to the increase in δ^{18}O marking the onset of GI-8. We explain this pattern by a gradual northward ITCZ and sea-ice cover shift, associated with lighter precipitation in the NH tropics and heavier precipitation in the SH tropics. The flat methane and δ^{18}O$_{atm}$ records suggest globally stable methane budget and biosphere productivity, possibly due to compensating effects at different latitudes.

The three phase sequence identified in low to mid-latitude proxies in Greenland ice cores during GS-9 is also found in low to mid-latitude climatic archives. Indeed, combining North Atlantic marine cores from different latitudes, stadial 9 can also be subdivided into 3 phases (Peters et al., 2008; Naughton et al., 2009): (i) prior to the Laurentide ice sheet IRD delivery, cold conditions are already depicted at 45-55°N while interstadial conditions persist in the Iberian Peninsula (35-42°N). (ii) The onset of the Laurentide IRD delivery coincides with a possible further cooling at high latitudes, while Iberia enters into cold and dry stadial conditions. (iii) Once low IRD levels are registered again, interstadial conditions are recorded in the Iberian Peninsula, while cold temperatures persist at 45-55°N.

We previously argued for a southward shift of the ITCZ at the onset of phase 2 of our Greenland ice core sequence with signals in CH$_4$, δD-CH$_4$, ^{17}O excess and δ^{18}O$_{atm}$. Bringing together marine cores and our ice core records, we suggest that this ITCZ shift coincides with the onset of colder and drier conditions in the Iberian Peninsula and also corresponds to the purge of the LIS, i.e. the beginning of H4. If true the inferred date of H4 is 39,350 $\pm$1,500 a b2k on the GICC05 chronology. This iceberg discharge would lead to North Atlantic cooling, southward expansion of North Atlantic sea-ice cover and southward ITCZ shift, as simulated by climate models (Chiang et al., 2008). Within phase 2, the secondary minima in ^{17}O excess and MSA data at $\sim$38,600 a b2k (blue arrows, Fig. fig-H4diagram) could reflect another massive iceberg delivery.

Why did Greenland temperature not respond to these low latitude changes? Atmospheric simulations (Li et al., 2010) suggest that Greenland temperature is sensitive to changes in sea ice cover anomalies in the Nordic Seas but not in the NW Atlantic. While we suggest large changes in the North Atlantic sea ice extent during H4, no specific sea ice change is depicted during this period from deep sea core records obtained in the Irminger Sea and around the Faeroe Islands (Cortijo et al., 2005; Zumaque et al., 2012). The lack of specific sea ice anomaly in the Nordic Seas may explain why no cold anomaly is recorded in Greenland during H4.

5.3.3 Summary and perspectives
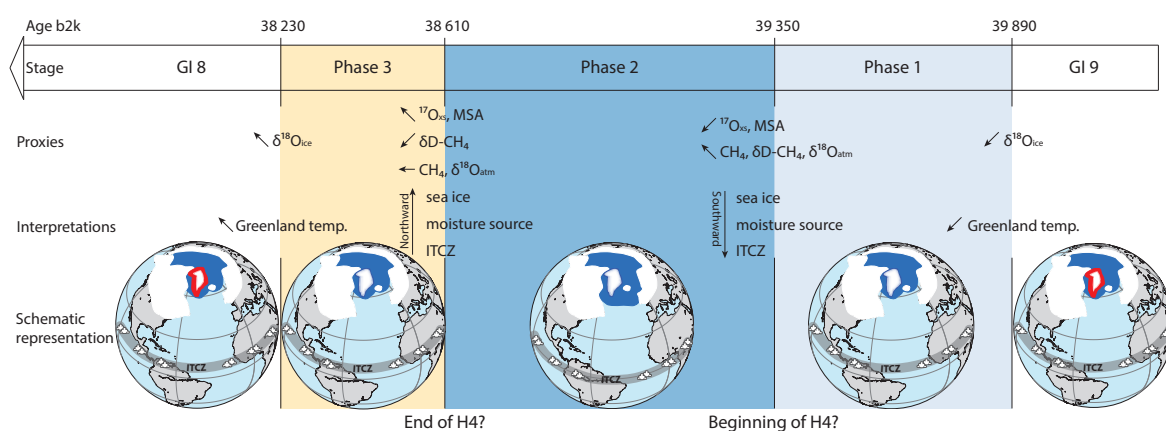
Figure 5.8: Sequence of events indicated by the proxy records and our climatic interpretation. The globes give a schematic representation of the sea ice extent (in dark blue), the position of the ITCZ, and Greenland temperature (red representing warm conditions).

In summary, our new multi-proxy record from Greenland ice cores has revealed a 3-phase sequence of GS-9. While Greenland temperature remains uniformly cold along GS-9, synchronous changes in ^{17}O excess, MSA, δ^{18}O$_{atm}$, δD-CH$_4$, methane and CO$_2$ are interpreted as a polar ice core fingerprint of the low to mid latitude climatic impacts that we associate with H4. Following this interpretation, the beginning of the H4 impact on mid to low latitudes is dated at 39,350 a b2k, 540±50 a after the end of GI-9. It ends 740±50 a later, when ^{17}O excess, MSA, δ^{18}O$_{atm}$ and δD-CH$_4$ have shifted back to interstadial values, 370±50 a before the onset of GI-8.

Preliminary investigations on GS-13 encompassing H5, based on ice core δ^{18}O, MSA, δ^{18}O$_{atm}$, CH$_4$ and CO$_2$ data also reveal a 3 phase structure, as well as the same sequence of events (Supplementary Information, Fig. 5.12). Our findings obviously call for systematic investigations of the ice core multi-proxy fingerprints of other Heinrich events, to assess the robustness of our results for H4 and H5, mainly due to the LIS, with respect to H3 and H6, due to European ice sheets mainly (Hemming, 2004).

The decoupling between the flat Greenland temperature during GS-9 and the climate variability associated with H4 at lower latitudes challenges the use of Greenland ice core temperatures as a single target for benchmarking climate simulations focused on HE. Our multi-proxy study opens new paths for parallel investigations of different marine, terrestrial and ice core climate archives.

5.4 Supplementary informations

5.4.1 Heinrich events of the last glacial period as registered in North Atlantic deep sea cores

Deep sea cores from the North Atlantic document layers of ice rafted debris (IRD) of various importance and origin (Bond et al., 1992; Hemming, 2004). Six major IRD layers (H1 to H4, H5 and H6) are well identified in numerous marine cores, and minor events identified in one or a few cores are additionally reported (H5a (Rashid et al., 2003), H7a, H7b, H8 to H10 (Rasmussen et al., 2003), Fig. 5.6 in the main text). In addition to the IRD layers, periods of low surface salinity likely due to fresh water fluxes are evidenced in a deep core from the Celtic margin (Fig. 5.6 in the main text, blue areas Eynaud et al., 2012). Studies on the composition of each IRD layer have now well established the mostly Laurentide origin of H2, H4 and H5, while H3 and H6 are mainly due to icebergs delivery from European ice sheets (Grousset et al., 1993; Gwiazda et al., 1996; Hemming et al., 1998; Snoeckx et al., 1999; Grousset et al., 2001; Jullien et al., 2006). H1 results from the collapse of several ice sheets (Stanford et al., 2011). Some marine cores depict the H4 IRD layer as 2 distinct sub-events accompanied by 2 episodes of cooling (Auffret et al., 2002; Shackleton et al., 2004; Jonkers et al., 2010); interestingly, two episodes of low ^{17}O excess and MSA are identified during phase 2 of GS-9 (main text Fig. 5.7, blue arrows).

Each HE has unique characteristics (origin, duration, climatic context) and the climate response that we identify for the similar H4 and H5 events may not be applied to the other Heinrich Events. The identification in ice core proxies of the imprint of the geomagnetic events Laschamp and Mono Lake, occurring respectively before and after H4, may help future parallel investigations of ice and marine records around GS-9 (Svensson et al., 2008; Singer et al., 2009).

5.4.2 ^{17}O excess measurements: method

^{17}O excess measurements were performed following the method first described by Luz and Barkan in 2005 (Luz and Barkan, 2005). 2 microlitres of water are fluorinated under a helium flow and the resulting oxygen is purified on molecular sieve before being trapped in a manifold immersed in liquid helium. Converted oxygen is then measured by dual inlet mass spectrometry on a DELTA V versus pure oxygen. Dual inlet measurement last 75 minutes for each converted oxygen sample. Each water sample has been converted and measured at least twice. Every day, we use 2 homemade water standards in our fluorination line to check the stability of the measurements and perform calibration. The resulting pooled standard deviation for ^{17}O excess measurements is 5 permeg.

For this study with δ^{18}O varying between -43 and -38‰, we have mainly used 3 homemade standards at around -32‰, -40‰ and -58‰. These homemade standards are calibrated vs V-SMOW (δ^{18}O $=0$‰; ^{17}O excess $= 0$ permeg) and SLAP (δ^{18}O $=-55.5$‰; ^{17}O excess $= 0$ permeg, Luz et al., 2009; Schoenemann et al., 2013). The calibration of our raw ^{17}O excess data can then be done in two different ways. In a first attempt, we have simply subtracted to all raw ^{17}O excess data the ^{17}O excess difference between the measured and the calibrated standard at -40‰. In a second attempt, we have used a 2 points calibration between measured and accepted values of V-SMOW and SLAP so that the ^{17}O excess correction increases with the δ^{18}O difference between O_2 obtained from the sample con-
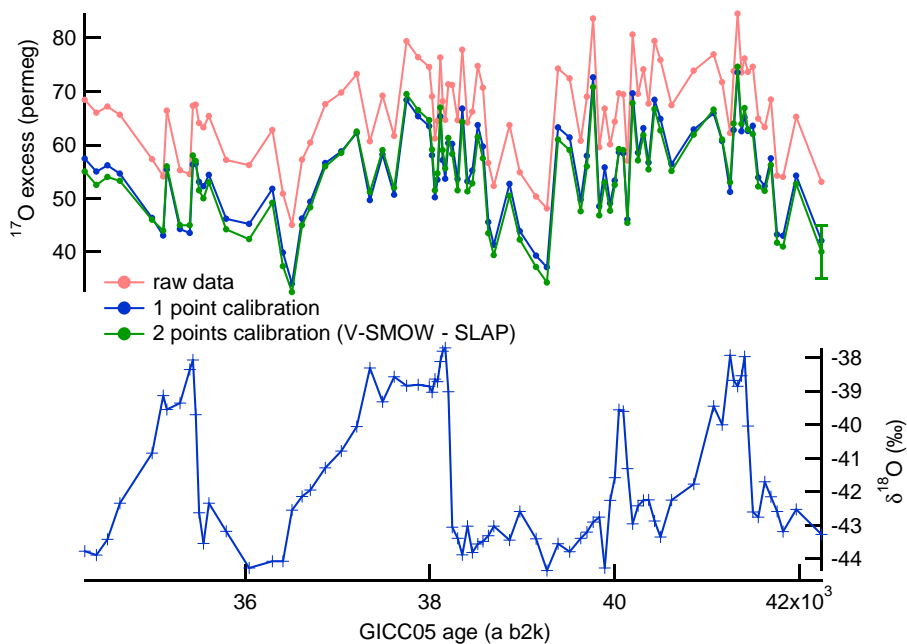
Figure 5.9: NEEM ^{17}O excess (permeg, top) and δ^{18}O (‰, bottom) data. Top: one point (blue dots) and two points (green dots) calibrations of the measured ^{17}O excess data.

version and O_2 obtained from V-SMOW conversion. We show in Fig. 5.9 the comparison of ^{17}O excess evolution after these two corrections as well as the raw data. The general evolution of the ^{17}O excess profile and the particular separation in phases over GS-9 is not affected by the different corrections.

Finally, note that the measurements were done in two rounds, with a first series measured in Spring 2011 and a second one at the beginning of 2012. Comparisons of the profiles are displayed in Fig. 5.10 after correction with a two points (V-SMOW vs SLAP) calibration. Note that for samples before 39.5 ka, the measurements were not necessary performed over the same exact depth levels which makes the inter-comparison less accurate. Both the mean levels and the variability are very coherent between the two ^{17}O excess profiles.

5.4.3 Synchronisation of the used ice cores to the GICC05 chronology

Ice age scales

The GICC05 (Greenland Ice Core Chronology 2005) has been constructed for the NGRIP ice core from present back to 60 ka b2k based on annual layer counting in ice cores of parameters featuring seasonal scale variations (Vinther et al., 2006; Andersen et al., 2006; Rasmussen et al., 2006; Svensson et al., 2008). The GRIP, GISP2 (I. Seierstad, pers. com.) and NEEM ice cores (Rasmussen et al., 2013) have been synchronised to the NGRIP ice core using match points based on peaks of electrical conductivity and dielectrical properties of the ice. The synchronisation uncertainty between NGRIP, NEEM, GRIP and GISP2 is estimated to be ~10 cm (1 sigma, Rasmussen et al., 2013), resulting in ~10 a synchronisation uncertainty for GS-9. The GICC05 uncertainty is estimated by the maximum counting error in years (Rasmussen et al., 2006), with each uncertain year counted as 0.5 ± 0.5 a. This can be considered as a 2σ uncertainty. We give the duration uncertainty of each of the phases of GS-9 and GS-13 as the sum of the uncertain years counted within each phase.
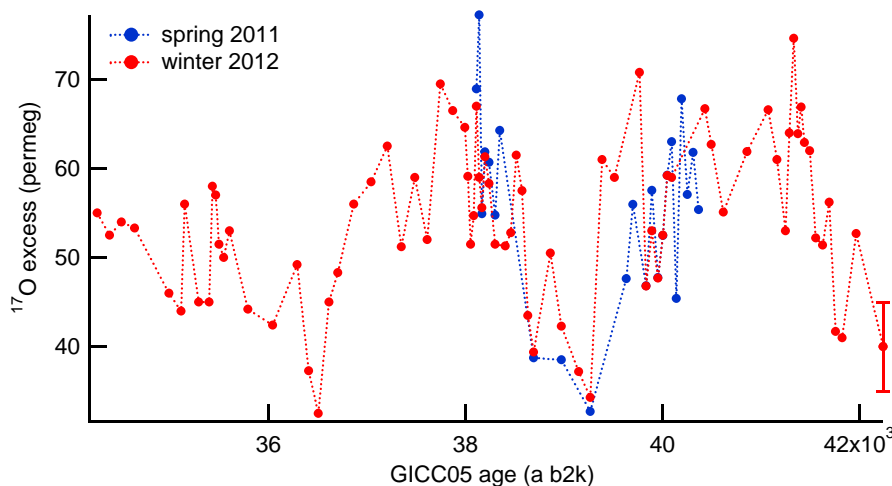
Figure 5.10: Comparison of the ^{17}O excess data measured in spring 2011 (blue dots) and winter 2012 (red dots).

Gas age scales

Byrd depth, m	NEEM methane gas age, a b2k
1617.15	33716
1654.05	35435
1691.10	36901
1716.10	38125
1743.55	39372
1759.20	40121
1780.30	41467
1807.95	43351

Table 5.2: Match points between methane depths from the Byrd ice core (Ahn and Brook, 2008; Ahn et al., 2012) and NEEM methane (Chappellaz et al., 2013) gas age according to the GICC05 chronology (Rasmussen et al., 2013).

For the NGRIP gas records (δD-CH$_4$, δ^{18}O$_{\text{atm}}$), we use the gas age scale from Kindler et al. (2014), initially constructed on the NGRIP ss09sea06bm timescale (NGRIP members, 2004; Wolff et al., 2010), and we transfer it to the GICC05 chronology. We use the NEEM gas age scale from Rasmussen et al. (2013). The NGRIP and NEEM gas age scale covering GS-9 are well constrained (uncertainty of the gas age scale compared to the ice age scale: $\sim$100 years) thanks to numerous measured δ^{15}N data (Kindler et al., 2014; Guillevic et al., 2013).

To synchronise the Byrd gas records to the NEEM ice core, we use a traditional approach consisting in matching methane records from both ice cores (Blunier et al., 1998). We first use the high resolution NEEM methane record on its GICC05 gas age scale (Rasmussen et al., 2013). We then match the Byrd methane record (Ahn et al., 2012) to the NEEM methane record, using as match points the mid-slope of each GI onset (Fig. 5.11 and Table 5.2). We perform a linear interpolation in between the match points. We then apply the obtain depth-gas age scale for Byrd to the Byrd CO$_2$ record.

Figure 5.11: Construction of a gas age scale for the Byrd ice core. (a) NEEM methane data (Chappellaz et al., 2013) on the NEEM GICC05 gas age scale (Rasmussen et al., 2013). **(b)** CH_4 and **(c)** CO_2 data from the Byrd ice core on a depth scale (Ahn et al., 2012). The dotted black lines indicate the match points used to tie the Byrd record to the NEEM GICC05 gas age scale.
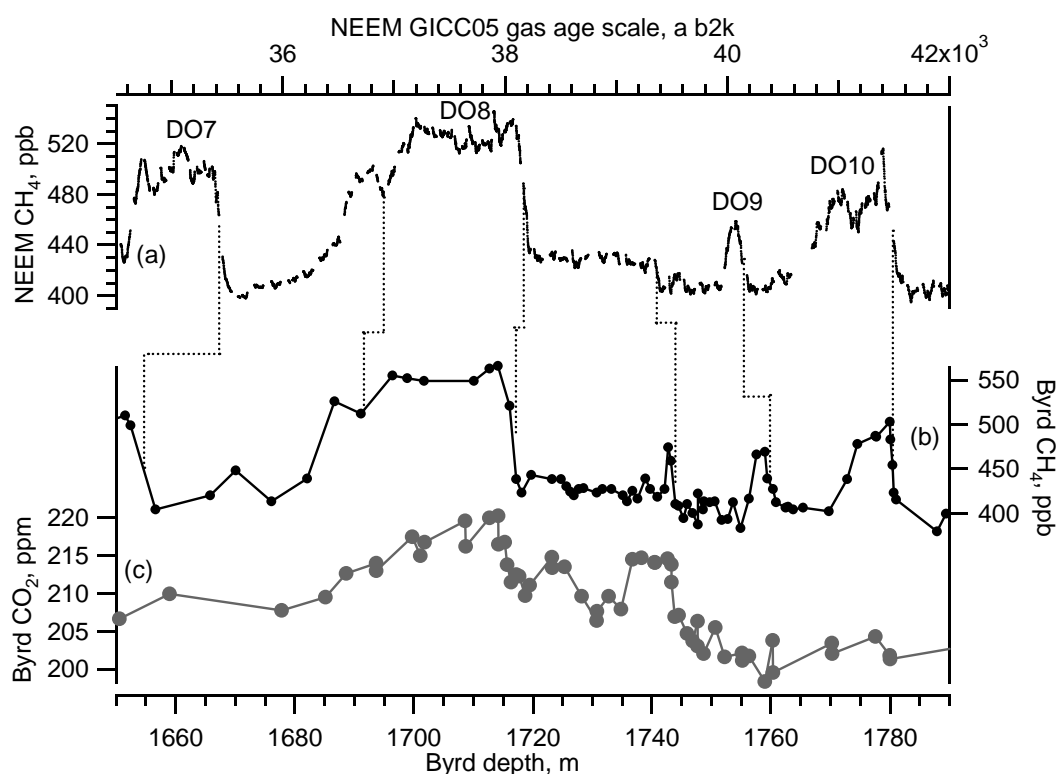
5.4.4   Heinrich event 5: a similar sequence of events compared to H4

Heinrich event 5 is an IRD layer originating from the LIS (Hemming, 2004), occurring during GS-13. Fig. 5.12 compiles published ice cores data of interest covering GS-13: NEEM $\delta^{18}O$, GISP2 MSA, NGRIP $\delta^{18}O_{atm}$, NEEM CH_4 together with CH_4 and CO_2 data from the Talos Dome (TALDICE) ice core, Antarctica. The NEEM water isotopes, in agreement with other Greenland ice cores, as well as Greenland d-excess data (Masson-Delmotte et al., 2005a; Jouzel et al., 2007b), show a stable GS-13 with constant $\delta^{18}O$ data. The GISP2 MSA concentration data (Saltzman et al., 1997) shows the same pattern of changes as during GS-9 marked by 3 phases. Phase 1 starts with the $\delta^{18}O$ decrease at the onset of GS-13 and ends by the MSA drop at 48,200 a b2k ±1,980 a (160±20 a after the onset of GS-13). The onset of phase 2 is accompanied by abrupt increases in the atmospheric concentration of methane (+40 ppb in NEEM, +45 ppb in TALDICE) and CO_2 (+5 ppm in TALDICE Chappellaz et al., 2013; Bereiter et al., 2012), as well as a gradual increase in the NGRIP $\delta^{18}O_{atm}$ (Huber et al., 2006). Phase 2 defined from low MSA levels lasts 860±40 a (~100 a longer than the cold phase following the onset of H4). Phase 3 starts by an increase in MSA prior to GI-12 and has an overall duration of 480±30 a, comparable to the duration of phase 3 of GS-9.

This brief inspection of GS-13 confirms the substructure (3 phases) sequence of events and durations observed for GS-9. If the same mechanisms are at play, we expect the following signals: a high [17]O excess during phases 1 and 3 and a low plateau during phase 2, and a high δD-CH_4 during phase 2 compared to lower δD-CH_4 during phases 1 and 3.
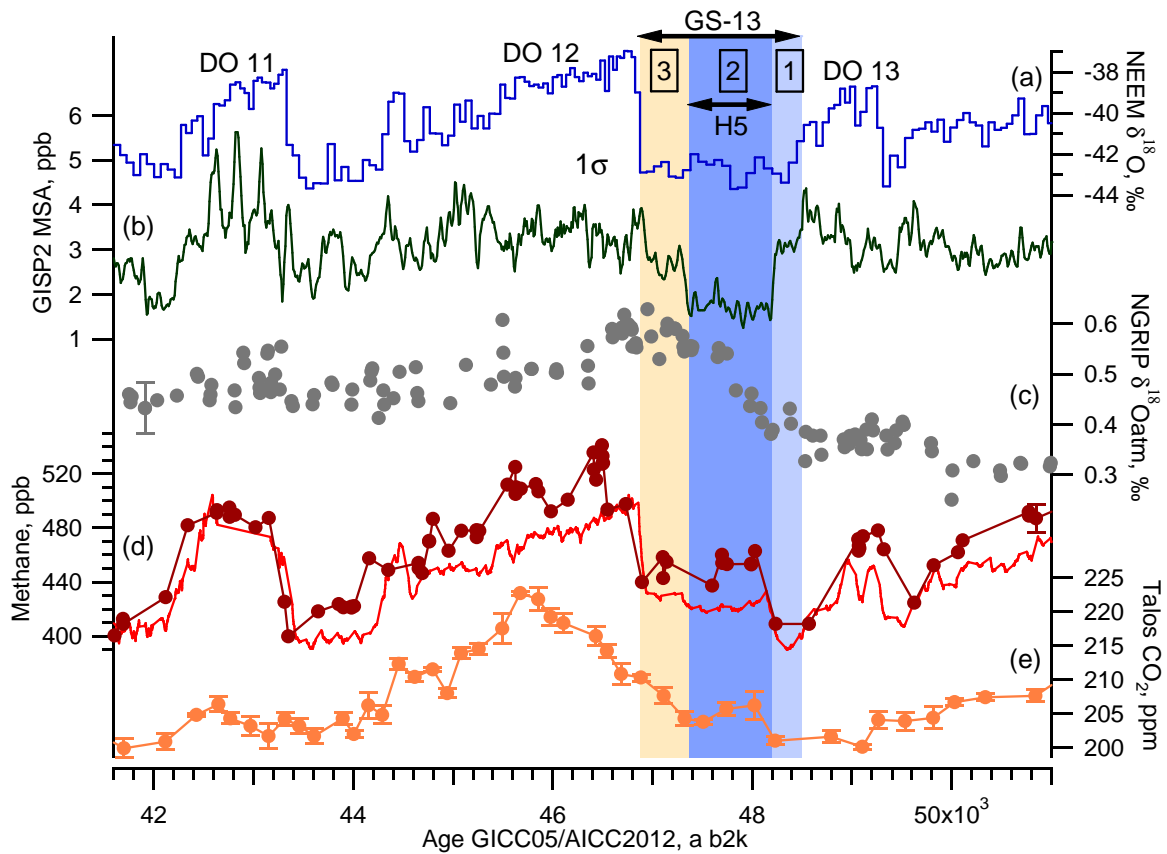
Figure 5.12: Sequence of events for Heinrich event 5 in multi-proxy ice core records. Light blue area, phase 1: 48,380-48,200 a b2k. Blue area, phase 2: 48,200-47,340 a b2k. Yellow area, phase 3: 47,340-46,880 a b2k. All records are reported on the GICC05 timescale (see Sect. 5.4.3). **(a)** NEEM δ^{18}O, ‰, this study. **(b)** GISP2 MSA concentration data, ppb (Saltzman et al., 1997), 50 a running average. **(c)** NGRIP δ^{18}O$_{atm}$, ‰(Huber et al., 2006). **(d)** red: NEEM methane mixing ratio (Chappellaz et al., 2013, we use here the record measured by the Picarro instrument). Dark red dots: TALDICE (Talos Dome, Antarctica Buiron et al., 2011), AICC2012 gas age scale (Veres et al., 2013; Bazin et al., 2013), compatible with GICC05 in this time period. **(e)** TALDICE CO_2, ppm (Bereiter et al., 2012), on the AICC2012 gas age scale.

Conclusion

This thesis was a combination of analytical development, experimental measurements, as well as simple modelling in order to study abrupt climatic events of the last glacial period registered in the northern hemisphere, the Dansgaard-Oeschger events and Heinrich events. This work was based on new and published data from Greenland ice cores, and especially from the NEEM ice core, NW Greenland. We summarise our main findings below.

Can we use ^{17}O excess from Greenland ice cores as a tracer for relative humidity at the oceanic vapour source? In Chapter 1, we have presented new measurements of ^{17}O excess from recent Greenland snow (years 2003-2005). These new data showed seasonal variations with amplitudes of 25 permeg, with a minimum in July leading the d-excess maximum level reached 3 months later. These observations are in agreement with our understanding of ^{17}O excess and d-excess variations in polar regions with minima in ^{17}O excess in phase with maxima in source relative humidity and maxima in d-excess largely influenced by source temperature increase. These findings therefore support the interpretation of present-day ^{17}O excess in Greenland snow as a tracer for oceanic vapour source relative humidity.

How to reference methane isotopes vs primary standards for carbon and hydrogen isotopes? In Chapter 2 in collaboration with P. Sperlich, we have developed a protocol for absolute referencing of methane gas isotopes, and making full air standard with known concentration and isotopic composition of methane. A combustion system was developed, enabling a complete combustion of pure methane into CO_2 and H_2O. These two products were then frozen at different temperatures to be separately trapped. The isotopic composition of the produced CO_2 was measured by dual inlet IRMS vs a reference pure CO_2 itself referenced vs VPDB. The same principle was applied to the produced water, measured vs a standard water referenced vs VSMOW. Based on the pooled standard deviation, we estimate the reproducibility of this offline combustion method to 0.04 ‰ for δ^{13}C and 0.7 ‰ for δ^2H. Referenced parental CH_4 gases were mixed to obtain pure CH_4 gases with precisely referenced isotopic composition of δ^{13}C near atmospheric values. Based on these CH_4 mixtures, we created synthetic isotope reference gases with present-day and glacial atmospheric CH_4 concentrations and δ^{13}C-CH_4 isotope values. Such standards are needed for intercomparison between different laboratories measuring methane isotopes.

What was the sensitivity of the water isotope δ^{18}O to temperature in Greenland during the last glacial period? In Chapter 3 and 4, we have used a method independent from water isotopes to reconstruct the past temperature in Greenland. Based on new and pub-

lished δ^{15}N and Δage data and two different firn models, the Goujon model (Goujon et al., 2003) and the Schwander model (Schwander et al., 1997), we have reconstructed scenarios of the lock-in depth, Δage history, temperature and accumulation rates for the GRIP, GISP2, NEEM and NGRIP ice cores.

Focusing on the NGRIP ice core, we have shown that these two firn models, while using different densification equations, produce very similar δ^{15}N and Δage scenarios for climatic conditions covering present and glacial NGRIP conditions. The only exception to this is the NGRIP last glacial maximum, where the warm bedrock temperature may have warmed up noticeably the bottom of the firn. This effect is taken into account in the Goujon model and it would be a useful development to include it in the Schwander model. We have proposed a methodology to estimate the uncertainty assigned to lock-in-depth, accumulation and temperature reconstruction linked to the firn modelling method, for periods where δ^{15}N data are available and where the Δage uncertainty is calculated. Such uncertainty estimation is necessary to compare the firn model-based temperature and accumulation rates with the output of other methods, such as ice flow models. We suggest that to better constrain firn model based reconstructions, it would be needed to measure δ^{40}Ar data in addition to δ^{15}N data in periods where Δage match points are missing. An alternative approach would be to combine a firn model, a borehole temperature model and an ice flow model, constrained by δ^{15}N data, present-day borehole temperature measurements and timescale, as currently developed by Lundin et al. (2012).

Our new δ^{15}N-based NGRIP temperature reconstruction from the Holocene to the Eemian shows that the amplitude of Greenland warming at the onset of DO events cannot be explained by the seesaw mechanism only and support local Arctic amplification mechanisms. At orbital timescales, our results suggest that the sensitivity of water isotopes to Greenland temperature increase with decreasing obliquity (qualitatively in agreement with the Rayleigh distillation) and with increasing northern hemisphere ice sheet size (possibly through changes in atmospheric circulation, influencing the vapour source location and its trajectory on the way to Greenland).

What was the spatial expression of the Greenland climate over a sequence of DO events?
In Chapter 4, focusing on a sequence of Dansgaard-Oeschger events during Marine Isotopic Stage 3, we have used δ^{15}N data and firn models to quantitatively reconstruct temperature and accumulation rates at NEEM, NGRIP, GRIP and GISP2. We have shown that at the onset of DO-8 and DO-10, the temperature and accumulation increases are smaller going north, while the water isotope increase is larger. These observations are in agreement with a study of spatial Greenland response to reduced sea-ice extent in the Nordic seas (Li et al., 2010). Our results therefore suggest that abrupt sea ice retreat in the Nordic Seas at the beginning of a DO event is likely to contribute to the warming and accumulation rate increase in Greenland.

During MIS3, the sensitivity of NEEM water isotopes to temperature is higher compared to NGRIP, GRIP and GISP2. This may be due to limited changes in precipitation seasonality at NEEM. The relatively high isotope–temperature relationship for NEEM will have implications for climate reconstructions based on NEEM water isotope data. To assess the stability of this observation, further paleoclimate reconstructions for different MIS would be needed.

Can we identify the fingerprint of Heinrich events in ice cores? Heinrich events were originally identified by layers of ice rafted debris in North Atlantic marine cores, deposited by icebergs melt. In Chapter 5, we have developed a multi-proxy approach to identify in polar ice cores the fingerprint of Heinrich Events. We propose that at 39 400 a b2k according to the GICC05 chronology, 540 a after the onset of GS-9, the ^{17}O excess decrease (attributed to a southward shift and more mixing of Greenland moisture source, without significant source temperature effect) and the methyl sulfonic acid decrease (North Atlantic sea ice expansion) correspond to the signature of the H4 iceberg delivery from the Laurentide ice sheet. These variations are accompanied by heavier $\delta^{18}O_{atm}$ and δD-CH$_4$ (probably reflecting heavier meteoric water in the northern tropics due to ITCZ southwards shift) and a small abrupt increase in methane (reflecting enhanced emissions in the southern tropics) and CO$_2$ measured in Antarctic ice cores (possibly caused by southwards westerlies shift and subsequent enhanced upwelling at the East coast of South America). These synchronous changes are interpreted as a polar ice core fingerprint of the climatic impacts associated with H4. Based on a reduced dataset, a similar fingerprint is observed for H5, also mostly due to the Laurentide collapse. Our findings obviously call for systematic investigations of the ice core multi-proxy fingerprints of other Heinrich events, and in particular H3 and H6 that are mainly due to European ice sheets and may have different signatures. Our results evidence a decoupling between the Greenland climate, stable during all GS-9, and the mid to low latitudes climate of the Northern hemisphere, impacted by H4. Our multi-proxy study therefore opens new paths for parallel investigations of different marine, terrestrial and ice core climate archives.

Bibliography

Abram, N. J., Wolff, E. W., and Curran, M. A. (2013). A review of sea ice proxy information from polar ice cores. *Quaternary Sci. Rev.*, 79:168–183.

Ahn, J., Brook, E., Schmittner, A., and Kreutz, K. (2012). Abrupt change in atmospheric CO_2 during the last ice age. *Geophys. Res. Lett.*, 39:L18711.

Ahn, J. and Brook, E. J. (2008). Atmospheric CO_2 and climate on millennial time scales during the last glacial period. *Science*, 322:83–85.

Alley, R. B. (1987). Firn densification by grain boundary sliding: a first model. *Journal de Physique*, C1(48):249–256.

Alvarez-Solas, J., Charbit, S., Ritz, C., Paillard, D., Ramstein, G., and Dumas, C. (2010). Links between ocean temperature and iceberg discharge during Heinrich events. *Nat. Geosci.*, 3:122 – 126.

Andersen, K. K., Svensson, A., Johnsen, S. J., Rasmussen, S. O., Bigler, M., Röthlisberger, R., Ruth, U., Siggaard-Andersen, M.-L., Steffensen, J. P., Dahl-Jensen, D., Vinther, B. M., and Clausen, H. B. (2006). The Greenland Ice Core Chronology 2005, 15–42 ka. Part 1: constructing the time scale. *Quaternary Sci. Rev.*, 25:3246–3257.

Anderson, R. F., Ali, S., Bradtmiller, L. I., Nielsen, S. H. H., Fleisher, M. Q., Anderson, B. E., and Burckle, L. H. (2009). Wind-driven upwelling in the Southern Ocean and the deglacial rise in atmospheric CO_2. *Science*, 323(5920):1443–1448.

Angert, A., Cappa, C. D., and Depaolo, D. J. (2004). Kinetic ^{17}O effects in the hydrologic cycle: indirect evidence and implications. *Geochim. Cosmochim. Ac.*, 68(17):3487–3495.

Arnaud, L., Barnola, J.-M., and Duval, P. (2000). *Physical modeling of of the densification of snow/firn and ice in the upper part of polar ice sheets*. Hokkaido University Press, Sapporo, Japan.

Arzel, O. and England, M. H. (2010). The impact of wind stress feedback on the stability of the Atlantic Meridional Overturning Circulation. *J. Climate*, 24:1965–1984.

Arzt, E. (1982). The influence of an increasing particle coordination on the densification of spherical powders. *Acta Metall.*, 30:1883–1890.

Arzt, E., Ashby, M. F., and Easterling, K. E. (1983). Practical applications of hot-isostatic pressing diagrams: four case studies. *Metall. Trans. A*, 14:211–221.

Auffret, G., Zaragosi, S., Dennielou, B., Cortijo, E., Rooij, D. V., Grousset, F., Pujol, C., Eynaud, F., and Siegert, M. (2002). Terrigenous fluxes at the celtic margin during the last glacial cycle. *Mar. Geol.*, 188(1–2):79 – 108.

Austin, W. E. and Hibbert, F. D. (2012). Tracing time in the ocean: a brief review of chronological constraints (60-8 kyr) on North Atlantic marine event-based stratigraphies. *Quaternary Sci. Rev.*, 36(0):28–37.

Bader, H. (1964). *Density of ice as a function of temperature and stress*. Special report (U.S. Army Cold Regions Research and Engineering Laboratory). Cold Regions Research and Engineering Laboratory, U.S. Army Material Command.

Baertschi, P. (1976). Absolute ^{18}O content of standard mean ocean water. *Earth Planet. Sc. Lett.*, 31:341–344.

Bard, E., Rostek, F., Turon, J.-L., and Gendreau, S. (2000). Hydrological impact of Heinrich event in the subtropical Northeast Atlantic. *Science*, 289(5483):1321–1324.

Barkan, E. and Luz, B. (2005). High precision measurements of $^{17}O/^{16}O$ and $^{18}O/^{16}O$ ratios in H_2O. *Rapid Commun. Mass Spectrom.*, 19:3737–3742.

Barkan, E. and Luz, B. (2007). Diffusivity fractionations of $H_2^{16}O/H_2^{17}O$ and $H_2^{16}O/H_2^{18}O$ in air and their implications for isotope hydrology. *Rapid Commun. Mass Spectrom.*, 21:2999–3005.

Barker, S., Cacho, I., Benway, H., and Tachikawa, K. (2005). Planktonic foraminiferal Mg/Ca as a proxy for past oceanic temperatures: a methodological overview and data compilation for the Last Glacial Maximum. *Quaternary Sci. Rev.*, 24:821–834.

Barkov, N. and Uvarov, N. (1973). Geophysical investigations of the borehole at Vostok Station in 1970. *Soviet Antarctic Expedition, Information Bulletin*, 8(7):389–383.

Barnola, J. M., Pimienta, P., Raynaud, D., and Korotkevich, Y. S. (1991). CO_2–climate relationship as deduced from the Vostok ice core: a re-examination based on new measurements and on a re-evaluation of the air dating. *Tellus*, 43B:83–90.

Battle, M., Bender, M., Sowers, T., Tans, P. P., Butler, J. H., Elkins, J. W., Ellis, J. T., Conway, T., Zhang, N., Lang, P., and Clarket, A. D. (1996). Atmospheric gas concentrations over the past century measured in air from firn at the South Pole. *Nature*, 383:231–235.

Baumgartner, M., Kindler, P., Eicher, O., Floch, G., Schilt, A., Schwander, J., Spahni, R., Capron, E., Chappellaz, J., Leuenberger, M., Fischer, H., and Stocker, T. F. (2013). NGRIP CH_4 concentration from 120 to 10 kyr before present and its relation to a $\delta^{15}N$ temperature reconstruction from the same ice core. *Clim. Past Discuss.*, 9(4):4655–4704.

Baumgartner, M., Schilt, A., Eicher, O., Schmitt, J., Schwander, J., Spahni, R., Fischer, H., and Stocker, T. F. (2012). High-resolution interpolar difference of atmospheric methane around the Last Glacial Maximum. *Biogeosciences*, 9(10):3961–3977.

Bazin, L., Landais, A., Lemieux-Dudon, B., Toyé Mahamadou Kele, H., Veres, D., Parrenin, F., Martinerie, P., Ritz, C., Capron, E., Lipenkov, V., Loutre, M.-F., Raynaud, D., Vinther, B., Svensson, A., Rasmussen, S. O., Severi, M., Blunier, T., Leuenberger, M., Fischer, H., Masson-Delmotte, V., Chappellaz, J., and Wolff, E. (2013). An optimized multi-proxy, multi-site Antarctic ice and gas orbital chronology (AICC2012): 120–800 ka. *Clim. Past*, 9:1715–1731.

Bender, M., Sowers, T., Barnola, J.-M., and Chappellaz, J. (1994a). Changes in the O_2/N_2 ratio of the atmosphere during recent decades reflected in the composition of air in the firn at Vostok Station, Antarctica. *Geophys. Res. Lett.*, 21(3):189 – 192.

Bender, M., Sowers, T., Dickinson, M., Orchado, J., Grootes, P., Mayewski, P., and Meese, D. (1994b). Climate correlations between Greenland and Antarctica during the past 100 000 years. *Nature*, 372:663 – 666.

Bereiter, B., Lüthi, D., Siegrist, M., Schüpbach, S., Stocker, T. F., and Fischer, H. (2012). Mode change of millennial CO_2 variability during the last glacial cycle associated with a bipolar marine carbon seesaw. *P. Natl. Acad. Sci. U.S.A.*, 109(25):9755 – 9760.

Bintanja, R., van de Wal, R. S. W., and Oerlemans, J. (2005). Modelled atmospheric temperatures and global sea levels over the past million years. *Nature*, 437:125–128.

Blunier, T. and Brook, E. J. (2001). Timing of millennial-scale climate change in Antarctica and Greenland during the last glacial period. *Science*, 291:109–112.

Blunier, T., Chappellaz, J., Schwander, J., Dällenbach, A., Stauffer, B., Stocker, T., Raynaud, D., Jouzel, J., Clausen, H., Hammer, C., and Johnsen, S. (1998). Asynchrony of Antarctic and Greenland climate change during the last glacial period. *Nature*, 394(6695):739–743.

Blunier, T., Chappellaz, J., Schwander, J., Stauffer, B., and Raynaud, D. (1995). Variations in atmospheric methane concentration during the Holocene epoch. *Nature*, 374:46–49.

Blunier, T. and Schwander, J. (2000). *Gas enclosure in ice: age difference and fractionation*. Hokkaido University Press, Sapporo, Japan.

Blunier, T., Spahni, R., Barnola, J.-M., Chappellaz, J., Loulergue, L., , and Schwander, J. (2007). Synchronization of ice core records via atmospheric gases. *Clim. Past*, 3:325–330.

Boch, R., Cheng, H., Spötl, C., Edwards, R. L., Wang, X., and Häuselmann, P. (2011). NALPS: a precisely dated European climate record 120–60 ka. *Clim. Past*, 7(4):1247–1259.

Bock, M., Schmitt, J., Möller, L., Spahni, R., Blunier, T., and Fischer, H. (2010). Hydrogen isotopes preclude marine hydrate CH_4 emissions at the onset of Dansgaard-Oeschger events. *Science*, 328(5986):1686–1689.

Bond, G., Broecher, W., Johnsen, S. J., MacManus, J., Laberie, L., Jouzel, J., and Bonani, G. (1993). Correlations between climate records from North Atlantic sediments and Greenland ice. *Nature*, 365:143–147.

Bond, G., Heinrich, H., Broecker, W., Labeyrie, L., McManus, J., Andrews, J., Huon, S., Jantschik, R., Clasen, S., Simet, C., Tedesco, K., Klas, M., Bonani, G., and Ivy, S. (1992). Evidence for massive discharges of icebergs into the North Atlantic ocean during the last glacial period. *Nature*, 360:245–249.

Bousquet, P., Ciais, P., Miller, J. B., Dlugokencky, E. J., Hauglustaine, D. A., Prigent, C., der Werf, G. R. V., Peylin, P., Brunke, E.-G., Carouge, C., Langenfelds, R. L., Lathière, J., Papa, F., Ramonet, M., Schmidt, M., Steele, L. P., Tyler, S. C., and White, J. (2006). Contribution of anthropogenic and natural sources to atmospheric methane variability. *Nature*, 443:439–443.

Bousquet, P., Ringeval, B., Pison1, I., Dlugokencky, E. J., Brunke, E.-G., Carouge, C., Chevallier, F., Fortems-Cheiney, A., Frankenberg, C., Hauglustaine, D. A., Krummel, P. B., Langenfelds, R. L., Ramonet, M., Schmidt, M., Steele, L. P., Szopa, S., Yver, C., Viovy, N., , and Ciais, P. (2011). Source attribution of the changes in atmospheric methane for 2006–2008. *Atmos. Chem. Phys.*, 11:3689–3700.

Boyle, E. A. (2000). Is ocean thermohaline circulation linked to abrupt stadial/interstadial transitions? *Quaternary Sci. Rev.*, 19:255–272.

Braun, H., Christl, M., Rahmstorf, S., Ganopolski, A., Mangini, A., Kubatzki, C., Roth, K., and Kromer, B. (2005). Possible solar origin of the 1,470-year glacial climate cycle demonstrated in a coupled model. *Nature*, 438(7065):208–211.

Braun, H., Ditlevsen, P., and Chialvo, D. R. (2008). Solar forced Dansgaard-Oeschger events and their phase relation with solar proxies. *Geophys. Res. Lett.*, 35(6).

Broecker, W. (1998). Paleocean circulation during the last deglaciation: A bipolar seesaw? *Paleoceanography*, 13(2):119–121.

Broecker, W., Bond, G., Klas, M., Clark, E., and McManus, J. (1992). Origin of the Northern Atlantic's Heinrich events. *Clim. Dynam.*, 6:265–273.

Broecker, W. and Denton, G. (1989). The role of ocean-atmosphere reorganizations in glacial cycles. *Geochim. Cosmochim. Ac.*, 53:2465–2501.

Broecker, W. and Denton, G. (1990). What drives glacial cycles? *Scientific American*, 262(1):48–56.

Bromwich, D., Toracinta, E. R., Wei, H., Oglesby, R. J., Fastook, J., and Hughes, T. (2004). Polar MM5 simulations of the winter climate of the Laurentide ice sheet at the LGM. *J. Climate*, 17:3415 – 3433.

Brook, E. J., Harder, S., Severinghaus, J. P., Steig, E. J., and Sucher, C. M. (2000). On the origin and timing of rapid changes in atmospheric methane during the last glacial period. *Global Biogeochem. Cy.*, 14(2):559–572.

Brook, E. J., White, J. W., Schilla, A. S., Bender, M. L., Barnett, B., Severinghaus, J. P., Taylor, K. C., Alley, R. B., and Steig, E. J. (2005). Timing of millennial-scale climate change at Siple Dome, West Antarctica, during the last glacial period. *Quaternary Sci. Rev.*, 24:1333–1343.

Bräunlich, M., Aballain, O., Marik, T., Jöckel, P., Brenninkmeijer, C. A. M., Chappellaz, J., amd R. Mulvaney, J.-M. B., and Sturges, W. T. (2001). Changes in the global atmospheric methane budget over the last decades inferred from ^{13}C and D isotopic analysis of Antarctic firn air. *J. Geophys. Res.*, 106(D17):20465–20481.

Brunnée, C. and Voshage, H. (1964). *Massenspektrometrie, Teil 1*. Verlag Karl Thiemig KG, München, 12 edition.

Buiron, D., Chappellaz, J., Stenni, B., Frezzotti, M., Baumgartner, M., Capron, E., Landais, A., Lemieux-Dudon, B., Masson-Delmotte, V., Montagnat, M., Parrenin, F., and Schilt, A. (2011). TALDICE-1 age scale of the Talos Dome deep ice core, East Antarctica. *Clim. Past*, 7(1):1–16.

Buizert, C., Martinerie, P., Petrenko, V. V., Severinghaus, J. P., Trudinger, C. M., E.Witrant, Rosen, J. L., Orsi, A. J., Rubino, M., Etheridge, D. M., Steele, L. P., Hogan, C., Laube, J. C., Sturges, W. T., Levchenko, V. A., Smith, A. M., Levin, I., Conway, T. J., Dlugokencky, E. J., Lang, P. M., Kawamura, K., Jenk, T. M., White, J. W. C., Sowers, T., Schwander, J., and Blunier, T. (2012). Gas transport in firn: multiple-tracer characterisation and model intercomparison for NEEM, northern Greenland. *Atmos. Chem. Phys.*, 12:4259–4277.

Cai, Y., An, Z., Cheng, H., Edwards, R. L., Kelly, M. J., Liu, W., Wang, X., and Shen, C.-C. (2006). High-resolution absolute-dated Indian Monsoon record between 53 and 36 ka from Xiaobailong Cave, southwestern China. *Geology*, 34(8):621–524.

Caillon, N. (2001). *Composition isotopique de l'air piégé dans les glaces polaires: outil de paléothermométrie*. PhD thesis, Université Pierre et Marie Curie Paris 6, France.

Capron, E. (2010). *L'air piégé dans les glaces polaires: contraintes chronologiques et charactérisation de la variabilité climatique rapide*. PhD thesis, Université de Versailles Saint Quentin en Yvelines, France.

Capron, E., Landais, A., Buiron, D., Cauquoin, A., Chappellaz, J., Debret, M., Jouzel, J., Leuenberger, M., Martinerie, P., Masson-Delmotte, V., Mulvaney, R., Parrenin, F., and Prié, F. (2013). Glacial–interglacial dynamics of Antarctic firn columns: comparison between simulations and ice core air-δ^{15}N measurements. *Clim. Past*, 9(3):983–999.

Capron, E., Landais, A., Chappellaz, J., Buiron, D., Fischer, H., Johnsen, S. J., Jouzel, J., Leuenberger, M., Masson-Delmotte, V., and Stocker, T. F. (2012). A global picture of the first abrupt climatic event occurring during the last glacial inception. *Geophys. Res. Lett.*, 39(15):L15703.

Capron, E., Landais, A., Chappellaz, J., Schilt, A., Buiron, D., Dahl-Jensen, D., Johnsen, S. J., Jouzel, J., Lemieux-Dudon, B., Loulergue, L., Leuenberger, M., Masson-Delmotte, V., Meyer, H., Oerter, H., and Stenni, B. (2010a). Millennial and sub-millennial scale climatic variations recorded in polar ice cores over the last glacial period. *Clim. Past*, 6:345–365.

Capron, E., Landais, A., Lemieux-Dudon, B., Schilt, A., Masson-Delmotte, V., Buiron, D., Chappellaz, J., Dahl-Jensen, D., Johnsen, S., Leuenberger, M., Loulergue, L., and Oerter, H. (2010b). Synchronising EDML and NorthGRIP ice cores using δ^{18}O of atmospheric oxygen ($\delta^{18}O_{atm}$) and CH_4 measurements over MIS5 (80–123 kyr). *Quaternary Sci. Rev.*, 29:222–234.

Chanton, J., Fields, D., and Hines, M. E. (2006). Controls on the hydrogen isotopic composition of biogenic

methane from high latitudes terrestrial wetlands. *J. Geophys. Res.*, 111:G04004.

Chapman, M. R. and Shackleton, N. J. (1998). Millennial-scale fluctuations in North Atlantic heat flux during the last 150,000 years. *Earth Planet. Sc. Lett.*, 159:57–70.

Chapman, M. R. and Shackleton, N. J. (1999). Global ice-volume fluctuations, North Atlantic ice-rafting events, and deep-ocean circulation changes between 130 and 70 ka. *Geology*, 27(9):795–798.

Chapman, S. and Cowling, T. G. (1970). *The mathematical theorie of non-uniform gases*. Cambridge University Press, New York.

Chappellaz, J., Blunier, T., Raynaud, D., Barnola, J., Schwander, J., and Stauffer, B. (1993). Synchronous changes in atmospheric CH_4 and Greenland climate between 40 and 8 kyr BP. *Nature*, 366:443–445.

Chappellaz, J., Stowasser, C., Blunier, T., Baslev-Clausen, D., Brook, E. J., Dallmayr, R., Faïn, X., Lee, J. E., Mitchell, L. E., Pascual, O., Romanini, D., Rosen, J., and Schüpbach, S. (2013). High-resolution glacial and deglacial record of atmospheric methane by continuous-flow and laser spectrometer analysis along the NEEM ice core. *Clim. Past*, 9(6):2579–2593.

Chiang, J. C. H., Cheng, W., and Bitz, C. M. (2008). Fast teleconnections to the tropical Atlantic sector from Atlantic thermohaline adjustment. *Geophys. Res. Lett.*, 35:L07704.

Ciais, P. and Jouzel, J. (1994). Deuterium and oxygen 18 in precipitation: isotopic model, including mixed cloud processes. *J. Geophys. Res.*, 99(D8):16793 – 16803.

Clement, A. C., Hall, A., and Broccoli, A. J. (2004). The importance of precessional signals in the tropical climate. *Clim. Dynam.*, 22:327–341.

Clement, A. C. and Peterson, L. C. (2008). Mechanisms of abrupt climate change of the last glacial period. *Rev. Geophys.*, 46(4).

Coplen, T. B. (2011). Guidelines and recommended terms for expression of stable-isotope-ratio and gas-ratio measurement results. *Rapid Commun. Mass Sp.*, 25(17):2538–2560.

Cortijo, E., Duplessy, J.-C., Labeyrie, L., Duprat, J., and Paillard, D. (2005). Heinrich events: hydrological impact. *CR Geosci.*, 337:897–907.

Cortijo, E., Labeyrie, L., Vidal, L., Vautravers, M., Chapman, M., Duplessy, J.-C., Elliot, M., Arnold, M., Turon, J.-L., and Auffret, G. (1997). Changes in sea surface hydrology associated with Heinrich event 4 in the North Atlantic Ocean between 40°N and 60°N. *Earth Planet. Sc. Lett.*, 146:39 – 45.

Craig, H. (1961). Isotopic variations in meteoric waters. *Science*, 133:1702–1703.

Craig, H. and Gordon, L. (1965). Deuterium and oxygen 18 variations in the ocean and the marine atmosphere. In *Symposium on Marine Geochemistry*, volume 3, pages 277–374. Narraganset Marine Laboratory, University of Rhode Island Publication.

Craig, H., Horibe, Y., and Sowers, T. (1988). Gravitational separation of gases and isotopes in polar ice caps. *Science*, 242:1675 – 1678.

Cuffey, K. M. and Clow, G. D. (1997). Temperature, accumulation, and ice sheet elevation in central Greenland through the last deglacial transition. *J. Geophys. Res.*, 102:26383–26396.

Cuffey, K. M. and Vimeux, F. (2001). Covariation of carbon dioxide and temperature from the Vostok ice core after deuterium-excess correction. *Nature*, 412:523–527.

Cvijanovic, I. and Chiang, J. (2013). Global energy budget changes to high latitude North Atlantic cooling and the tropical ITCZ response. *Climate Dyn.*, 40:1435–1452.

Dahl-Jensen, D., Gundestrup, N., Gorgineni, S., and Miller, H. (2003). Basal melt at NorthGRIP modeled from borehole, ice-core and radio-echo sounder observations. *Ann. Glaciol.*, 37:207–212.

Dahl-Jensen, D., Johnsen, S., Hammer, C., Clausen, H., and Jouzel, J. (1993). *Past accumulation rates derived from observed annual layers in the GRIP ice core from Summit, central Greenland, in Ice in the Climate System*. Berlin, Springer-Verlag edition.

Dahl-Jensen, D., Mosegaard, K., Gundestrup, N., Clow, G. D., Johnsen, S. J., Hansen, A. W., and Balling, N. (1998). Past temperatures directly from the Greenland ice sheet. *Science*, 282:268–271.

Dahl-Jensen, D. and NEEM community members (2013). Eemian interglacial reconstructed from a Greenland folded ice core. *Nature*, 493:489 – 494.

Dällenbach, A., Blunier, T., Flückiger, J., Stauffer, B., Chappellaz, J., and Raynaud, D. (2000). Changes in the atmospheric CH_4 gradient between Greenland and Antarctica during the last glacial and the transition to the Holocene. *Geophys. Res. Lett.*, 27(7):1005–1008.

Dansgaard, W. (1964). Stable isotopes in precipitation. *Tellus*, 16:436–468.

Dansgaard, W., Clausen, H., Gundestrup, N., Hammer, C., Johnsen, S., Kristinsdottir, P., and Reeh, N. (1982). A new Greenland deep ice core. *Science*, 218(4579):1273–1277.

Dansgaard, W., Johnsen, S., Mø ller, J., and Langway, C.C., J. (1969). One thousand centuries of climatic record

from Camp Century on the Greenland ice sheet. *Science*, 166(3903):377–381.

Dansgaard, W. and Johnsen, S. J. (1969). A flow model and a time scale for the ice core from Camp Century, Greenland. *J. Glaciol.*, 8:215–223.

de Abreu, L., Shackleton, N. J., Schönfeld, J., Hall, M., and Chapman, M. (2003). Millennial-scale oceanic climate variability off the Western Iberian margin during the last two glacial periods. *Mar. Geol.*, 196(1–2):1–20.

de Vernal, A., Eynaud, F., Henry, M., Hillaire-Marcel, C., Londeix, L., Mangin, S., Matthiessen, J., Marret, F., Radi, T., Rochon, A., Solignac, S., and Turon, J.-L. (2005). Reconstruction of sea-surface conditions at middle to high latitudes of the Northern Hemisphere during the last glacial maximum (LGM) based on dinoflagellate cyst assemblages. *Quaternary Sci. Rev.*, 24:897–924.

de Vernal, A., Rosell-Melé, A., Kucera, M., Hillaire-Marcel, C., Eynaud, F., Weinelt, M., Dokken, T., and Kageyama, M. (2006). Comparing proxies for the reconstruction of LGM sea-surface conditions in the northern North Atlantic. *Quaternary Sci. Rev.*, 25:2820–2834.

Delmas, R., Megie, G., and Peuch, V. H. (2005). *Physique et chimie de l'atmosphère*. Belin.

Denman, K. L., Brasseur, G., Chidthaisong, A., Ciais, P., Cox, P. M., Dickinson, R. E., Hauglustaine, D., Heinze, C., Holland, E., Jacob, D., Lohmann, U., Ramachandran, S., da Silva Dias, P. L., Wofsy, S. C., and Zhang, X. (2007). *Couplings between changes in the climate system and biogeochemistry, in: Climate change 2007: The physical science basis. Contribution of working group I to the fourth assessment report of the Intergovernmental Panel on Climate Change*. Cambridge University Press, Cambridge, UK and New York, NY, USA.

Deplazes, G., Lückge, A., Peterson, L. C., Timmermann, A., Hamann, Y., Hughen, K. A., Röhl, U., Laj, C., Cane, M. A., Sigman, D. M., and Haug, G. H. (2013). Links between tropical rainfall and North Atlantic climate during the last glacial period. *Nat. Geosci.*, 6:213–217.

Dickson, A. J., Austin, W. E. N., Hall, I. R., Maslin, M. A., and Kucera, M. (2008). Centennial-scale evolution of Dansgaard-Oeschger events in the northeast Atlantic Ocean between 39.5 and 56.5 ka B.P. *Paleoceanography*, 23(3).

Dlugokencky, E. J., Myers, R. C., Lang, P. M., Masarie, K. A., Crotwell, A. M., Thoning, K. W., Hall, B. D., Elkins, J. W., and Steele, L. P. (2005). Conversion of NOAA atmospheric dry air CH_4 mole fractions to a gravimetrically prepared standard scale. *J. Geophys. Res. Atmos.*, 110(D18):D18306.

Dokken, T. M., Nisancioglu, K. H., Li, C., Battisti, D. S., and Kissel, C. (2013). Dansgaard-Oeschger cycles: Interactions between ocean and sea ice intrinsic to the Nordic seas. *Paleoceanography*.

Ellehoj, M. D. (2011). *Ice-vapor equilibrium fractionation factor: experimental investigations and possible impacts on the understanding of the hydrological cycles on Earth and Mars*. PhD thesis, Niels Bohr Institute, Faculty of Science, University of Copenhagen, Denmark.

Elliot, M., Labeyrie, L., Bond, G., Cortijo, E., Turon, J.-L., Tisnerat, N., and Duplessy, J.-C. (1998). Millennial-scale iceberg discharges in the Irminger Basin during the last glacial period: Relationship with the Heinrich events and environmental settings. *Paleoceanography*, 13(5):433–446.

Elliot, M., Labeyrie, L., and Duplessy, J.-C. (2002). Changes in North Atlantic deep-water formation associated with the Dansgaard-Oeschger temperature oscillations (60–10 ka). *Quaternary Sci. Rev.*, 21:1153–1165.

EPICA community members (2004). Eight glacial cycles from an Antarctic ice core. *Nature*, 429(6992):623–628.

EPICA community members (2006). One-to-one coupling of glacial climate variability in Greenland and Antarctica. *Nature*, 444:195–198.

Eynaud, F., Malaizé, B., Zaragosi, S., de Vernal, A., Scourse, J., Pujol, C., Cortijo, E., Grousset, F. E., Penaud, A., Toucanne, S., Turon, J.-L., and Auffret, G. (2012). New constraints on European glacial freshwater releases to the North Atlantic Ocean. *Geophys. Res. Lett.*, 39:L15601.

Eynaud, F., Turon, J., Matthiessen, J., Kissel, C., Peypouquet, J., de Vernal, A., and Henry, M. (2002). Norwegian sea-surface palaeoenvironments of marine oxygen-isotope stage 3: the paradoxical response of dinoflagellate cysts. *J. Quaternary Sci.*, 17(4):349–359.

Fischer, H., Behrens, M., Bock, M., Richter, U., Schmitt, J., Loulergue, L., Chappellaz, J., Spahni, R., Blunier, T., Leuenberger, M., and Stocker, T. F. (2008). Changing boreal methane sources and constant biomass burning during the last termination. *Nature*, 452(7189):864–867.

Fisher, D. (1992). Stable isotope simulations using a regional stable isotope model coupled to a zonally averaged global model. *Cold Reg. Sci. Technol.*, 21:61–77.

Fisher, D., Koerner, R., and Reeh, N. (1995). Holocene climatic records from Agassiz Ice Cap, Ellesmere Island, NWT, Canada. *The Holocene*, 5(1):19–24.

Fleitmann, D., Cheng, H., Badertscher, S., Edwards, R. L., Mudelsee, M., Göktürk, O. M., Fankhauser, A., Pickering, R., Raible, C. C., Matter, A., Kramers, J., and Tüysüz, O. (2009). Timing and climatic impact of Greenland interstadials recorded in stalagmites from northern Turkey. *Geophys. Res. Lett.*, 36(19).

Flückinger, J., Blunier, T., Stauffer, B., Chappellaz, J., Spahni, R., Kawamura, K., Schwander, J., Stocker, T., and Dahl-Jensen, D. (2004). N_2O and CH_4 variations during the last epoch: insight into global processes. *Global Biogeochem. Cycles*, 18:GB1020.

Fourré, E., Jean-Baptiste, P., Dapoigny, A., Baumier, D., Petit, J.-R., and Jouzel, J. (2006). Past and recent tritium levels in Arctic and Antarctic polar caps. *Earth Planet. Sc. Lett.*, 245:56–64.

Francey, R. J., Allison, C. E., Etheridge, D. M., Trudinger, C. M., Enting, I. G., Leuenberger, M., Langenfelds, R. L., Michel, E., and Steele, L. P. (1999). A 1000-year high precision record of $\delta^{13}C$ in atmospheric CO_2. *Tellus*, 51(2):170–193.

Freitag, J., Kipfstuhl, S., and Laepple, T. (2013). Core-scale radioscopic imagine: a new method reveals density–calcium link in Antarctic firn. *J. Glaciol.*, 59:1009–1014.

Gallée, H. and Gorodestkaya, I. V. (2010). Validation of a limited area model over Dome C, Antarctic Plateau, during winter. *Clim. Dynam.*, 34(1):61–72.

Genty, D., Blamart, D., Ghaleb, B., Plagnes, V., Causse, C., Bakalowicz, M., Zouari, K., Chkir, N., Hellstrom, J., Wainer, K., and Bourges, F. (2006). Timing and dynamics of the last deglaciation from European and North African $\delta^{13}C$ stalagmite profiles—comparison with Chinese and South Hemisphere stalagmites. *Quaternary Sci. Rev.*, 25(17–18):2118 – 2142.

Genty, D., Combourieu-Nebout, N., Peyron, O., Blamart, D., Wainer, K., Mansuri, F., Ghaleb, B., Isabello, L., Dormoy, I., von Grafenstein, U., Bonelli, S., Landais, A., and Brauer, A. (2010). Isotopic characterization of rapid climatic events during OIS3 and OIS4 in Villars Cave stalagmites (SW-France) and correlation with Atlantic and Mediterranean pollen records. *Quaternary Sci. Rev.*, 29:2799–2820.

Gonfiantini, R. (1978). Standards for stable isotope measurements in natural compounds. *Nature*, 271:534.

Gonzalez, C., Dupont, L. M., Behling, H., and Wefer, G. (2008). Neotropical vegetation response to rapid climate changes during the last glacial period: Palynological evidence from the Cariaco Basin. *Quaternary Res.*, 69(2):217–230.

Goujon, C., Barnola, J.-M., and Ritz, C. (2003). Modeling the densification of polar firn including heat diffusion: application to close-off characteristics and gas isotopic fractionation for Antarctica and Greenland sites. *J. Geophys. Res.*, 108(D24):4792.

Gow, A. J. (1965). On the accumulation and seasonal stratification of snow at the South Pole. *J. Glaciol.*, 5:467–477.

Grachev, A. M., Brook, E. J., , and Severinghaus, J. P. (2007). Abrupt changes in atmospheric methane at the MIS 5b–5a transition. *Geophys. Res. Lett.*, 34:L20703.

Grachev, A. M. and Severinghaus, J. P. (2003a). Determining the thermal diffusion factor for $^{40}Ar/^{36}Ar$ in air to aid paleoreconstruction of abrupt climate change. *J. Phys. Chem.*, 107:4636–4642.

Grachev, A. M. and Severinghaus, J. P. (2003b). Laboratory determination of thermal diffusion constants for $^{29}N_2/^{28}N_2$ in air at temperatures from -60 to 0°C for reconstruction of magnitudes of abrupt climate changes using the ice core fossil–air paleothermometer. *Geochim. Cosmochim. Ac.*, 67:345–360.

Grachev, A. M. and Severinghaus, J. P. (2005). A revised +10±4°C magnitude of the abrupt change in Greenland temperature at the Younger Dryas termination using published GISP2 gas isotope data and air thermal diffusion constants. *Quaternary Sci. Rev.*, 24:513–519.

Grootes, P. M. and Stuiver, M. (1997). Oxygen 18/16 variability in Greenland snow and ice with 10^{-3} to 10^5-year time resolution. *J. Geophys. Res.*, 102:26455–26470.

Grootes, P. M., Stuiver, M., White, J. W. C., Johnsen, S. J., and Jouzel, J. (1993). Comparison of oxygen isotope records from the GISP2 and GRIP Greenland ice cores. *Nature*, 366:552–554.

Grousset, F., Cortijo, E., Huon, S., Hervé, L., Richter, T., Burdloff, D., Duprat, J., and Weber, O. (2001). Zooming in on Heinrich layers. *Paleoceanography*, 16(3):240 – 259.

Grousset, F., Labeyrie, L., Sinko, J., Cremer, M., Bond, G., Duprat, J., Cortijo, E., and Huon, S. (1993). Patterns of ice-rafted detritus in the glacial North Atlantic (40–55N). *Paleoceanography*, 8(2):175–192.

Grousset, F., Pujol, C., Labeyrie, L., Auffret, G., and Boelaert, A. (2000). Were the North Atlantic Heinrich events triggered by the behavior of the European ice sheets? *Geology*, 28:123 – 126.

Guillevic, M., Bazin, L., Landais, A., Kindler, P., Orsi, A., Masson-Delmotte, V., Blunier, T., Buchardt, S. L., Capron, E., Leuenberger, M., Martinerie, P., Prié, F., and Vinther, B. M. (2013). Spatial gradients of temperature, accumulation and $\delta^{18}O$-ice in Greenland over a series of Dansgaard–Oeschger events. *Clim. Past*, 9:1029–1051.

Gutjahr, M., Hoogakker, B., Frank, M., and McCave, I. (2010). Changes in North Atlantic Deep Water strength and bottom water masses during Marine Isotope Stage 3 (45–35 ka PB). *Quaternary Sci. Rev.*, 29:2451–2461.

Gwiazda, R., Hemming, S., and Broecker, W. (1996). Provenance of icebergs during Heinrich Event 3 and the

contrast to their sources during other Heinrich episodes. *Paleoceanography*, 11(4):371–378.

Haapaniemi, A. I., Scourse, C. P. J., Peck, V. L., Kennedy, H., Kennedy, P., Hemming, S., Furze, M., Pienkowski, A., Austin, W., Walden, J., Wadsworth, E., and Hall, I. (2010). Source, timing, frequency and flux of ice-rafted detritus to the Northeast Atlantic margin, 30-12 ka: testing the Heinrich precursor hypothesis. *Boreas*, 39(3):576–591.

Hammer, C. U., Andersen, K. K., Clausen, H. B., Dahl-Jensen, D., Hvidberg, C. S., and Iversen, P. (1997). The stratigraphic dating of the GRIP ice core. Special Report of the Geophysical Department, Niels Bohr Institute for Astronomy, Physics and Geophysics, University of Copenhagen.

Hattori, A. (1983). *Denitrification and dissimilatory nitrate reduction, in Nitrogen in the marine environment*. Academic Press, San Diego, Calofirnia.

Heinrich, H. (1988). Origin and consequences of cyclic ice rafting in the Northeast Atlantic Ocean during the past 130,000 years. *Quaternary Res.*, 29:142 – 152.

Hemming, S., Broecker, W., Sharp, W., Bond, G., Gwiazda, R., McManus, J., Klas, M., and Hajdas, I. (1998). Provenance of the Heinrich layers in core V28-82, northeastern Atlantic, ^{40}Ar-^{39}Ar ages of ice-rafted hornblende, Pb isotopes in feldspar grains, and Nd-Sr-Pb isotopes in the fine sediment fraction. *Earth Planet. Sc. Lett.*, 164(1-2):317–333.

Hemming, S. R. (2004). Heinrich events: massive Late Pleistocene detritus layers of the North Atlantic and their global climate imprint. *Rev. Geophys.*, 42:RG1005.

Hendricks, M. B., DePaolo, D. J., and R.C.Cohen (2000). Space and time variation of δ^{18}0 and δD in precipitation: Can paleotemperature be estimated from ice cores? *Global Geochem. Cycles*, 14(3):851–861.

Herron, M. M. and Langway, C. C. (1980). Firn densification: an empirical model. *J. Glaciol.*, 25:373–385.

Hoch, S. W., Calanta, P., Philipona, R., and Ohmura, A. (2007). Yearround observation of longwave radiative flux divergence in Greenland. *J. Appl. Meteorol. Climatol.*, 46:1469–1479.

Hoffmann, G., Jouzel, J., and Johnsen, S. (2001). Deuterium excess record from central Greenland over the last millennium: Hints of a North Atlantic signal during the Little Ice Age. *J. Geophys. Res.*, 106(D13):14265–14274.

Hoffmann, G., Stievenard, M., Jouzel, J., White, J., and Johnsen, S. (1998). Deuterium excess record from Central Greenland: Modelling and observations. *International Symposium on Isotope Techniques in the Study of Past and Current Environmental Changes in the Hydrosphere and the Atmosphere*, IAEA-SM-349/54:591–602.

Hopcroft, P. O., Valdes, P. J., and Beerling, D. J. (2011). Simulating idealized Dansgaard-Oeschger events and their potential impacts on the global methane cycle. *Quaternary Sci. Rev.*, 30(23–24):3258–3268.

Hörhold, M., Laepple, T., Freitag, J., Bigler, M., Fischer, H., and Kipfstuhl, S. (2012). On the impact of impurities on the densification of polar firn. *Earth Planet. Sc. Lett.*, 325–326:93–99.

Huber, C., Leuenberger, M., Spahni, R., Flückiger, J., Schwander, J., Stocker, T. F., Johnsen, S. J., Landais, A., and Jouzel, J. (2006). Isotope calibrated Greenland temperature record over Marine Isotope Stage 3 and its relation to CH$_4$. *Earth Planet. Sc. Lett.*, 243:504–519.

Johnsen, S. J. (1977). Stable isotope homogenization of polar firn and ice. In *Proc. of Symp. on Isotopes and Impurities in Snow and Ice, I.U.G.G. XVI, General Assembly, Grenoble Aug. Sept., 1975*, pages 210–219. Washington D.C.

Johnsen, S. J., Clausen, H. B., Cuffey, K. M., Hoffmann, G., Schwander, J., and Creyts, T. (2000). Diffusion of stable isotopes in polar firn and ice: The isotope effect in firn diffusion. In Hondoh, T., editor, *Physics of Ice Core Records*, pages 121–140. Hokkaido University Press, Sapporo.

Johnsen, S. J., Clausen, H. B., Dansgaard, W., Fuhrer, K., Gundestrup, N., Hammer, C. U., Iversen, P., Jouzel, J., Stauffer, B., and Steffensen, J. P. (1992). Irregular glacial interstadials recorded in a new Greenland ice core. *Nature*, 359:311–313.

Johnsen, S. J., Dahl-Jensen, D., Dansgaard, W., and Gundestrup, N. (1995). Greenland paleotemperatures derived from GRIP borehole temperature and ice core isotope profiles. *Tellus*, 47B:624 – 629.

Johnsen, S. J., Dahl-Jensen, D., Gundestrup, N., Steffensen, J. P., Clausen, H. B., Miller, H., Masson-Delmotte, V., Sveinbjörnsdóttir, A., and White, J. (2001). Oxygen isotope and palaeotemperature records from six Greenland ice-core stations: Camp Century, Dye-3, GRIP, GISP2, Renland and NorthGRIP. *J. Quaternary Sci.*, 16:299–307.

Johnsen, S. J., Dansgaard, W., and White, J. W. C. (1989). The origin of Arctic precipitation under present and glacial climate. *Tellus*, 41B:452–468.

Jongma, J. I., Renssen, H., and Roche, D. M. (2013). Simulating Heinrich event 1 with interactive icebergs. *Clim. Dynam.*, 40:1373–1385.

Jonkers, L., Moros, M., Prins, M. A., Dokken, T., Dahl, C. A., Dijkstra, N., Perner, K., and Brummer, G.-J. A. (2010). A reconstruction of sea surface warming in the northern North Atlantic during MIS 3 ice-rafting

events. *Quaternary Sci. Rev.*, 29(15–16):1791 – 1800.

Jouzel, J. (2013). A brief history of ice core science over the last 50 yr. *Clim. Past*, 9(6):2525–2547.

Jouzel, J., Masson-Delmotte, V., Cattani, O., Dreyfus, G., Falourd, S., Hoffmann, G., Minster, B., Nouet, J., Barnola, J. M., Chappellaz, J., Fischer, H., Gallet, J. C., Johnsen, S., Leuenberger, M., Loulergue, L., Luethi, D., Oerter, H., Parrenin, F., Raisbeck, G., Raynaud, D., Schilt, A., Schwander, J., Selmo, E., Souchez, R., Spahni, R., Stauffer, B., Steffensen, J. P., Stenni, B., Stocker, T. F., Tison, J. L., Werner, M., and Wolff, E. W. (2007a). Orbital and millennial Antarctic climate variability over the past 800,000 years. *Science*, 317(5839):793–796.

Jouzel, J. and Merlivat, L. (1984). Deuterium and oxygen 18 in precipitation: modeling of the isotopic effects during snow formation. *J. Geophys. Res.*, 89:11749–11757.

Jouzel, J., Merlivat, L., and Roth, E. (1975). Isotopic study of hail. *J. Geophys. Res.*, 80:5115–5030.

Jouzel, J., Stiévenard, N., Johnsen, S., Landais, A., Masson-Delmotte, V., Sveinbjörnsdóttir, A., Vimeux, F., von Grafenstein, U., and White, J. (2007b). The GRIP deuterium-excess record. *Quaternary Sci. Rev.*, 26:1–17.

Jouzel, J., Vimeux, F., Caillon, N., Delaygue, G., Hoffmann, G., Masson-Delmotte, V., and Parrenin, F. (2003). Magnitude of isotope/temperature scaling for interpretation of central Antarctic ice cores. *J. Geophys. Res.*, 108(D12):4361.

Jullien, E., Grousset, F. E., Hemming, S. R., Peck, V. L., Hall, I. R., Jeantet, C., and Billy, I. (2006). Contrasting conditions preceding MIS3 and MIS2 Heinrich events. *Global Planet. Change*, 54:225 – 238.

Kageyama, M., Merkel, U., Otto-Bliesner, B., Prange, M., Abe-Ouchi, A., Lohmann, G., Ohgaito, R., Roche, D. M., Singarayer, J., Swingedouw, D., and Zhang, X. (2013). Climatic impacts of fresh water hosing under Last Glacial Maximum conditions: a multi-model study. *Clim. Past*, 9(2):935–953.

Kageyama, M., Paul, A., Roche, D. M., and van Meerbeeck, C. J. (2010). Modelling glacial climatic millennial-scale variability related to changes in the Atlantic meridional overturning circulation: a review. *Quaternary Sci. Rev.*, 29:2931–2956.

Kaiser, J. and Röckmann, T. (2008). Correction of mass spectrometric isotope ratio measurements for isobaric isotopologues of O_2, CO, CO_2, N_2O and SO_2. *Rapid Commun. Mass Spectrom.*, 22(24):3997–4008.

Kalnay, E., Kanamltsu, M., Kistler, R., Collins, W., Deaven, D., Gandin, L., Iredell, M., Saha, S., White, G., Woolle, J., Zhu, Y., Chelliah, M., Ebisuzaki, W., Higgins, W., Janowiak, J., Mo, K. C., Ropelewski, C., Wang, J., Leetmaa, A., Reynolds, R., Jenne, R., and Joseph, D. (1996). The NCEP/NCAR 40-year reanalysis project. *Bulletin American Meteorological Society*, 77:437–471.

Kanner, L. C., Burns, S. J., Cheng, H., and Edwards, R. L. (2012). High-latitude forcing of the South American summer monsoon during the Last Glacial. *Science*, 335(6068):570–573.

Kaspi, Y., Sayag, R., and Tziperman, E. (2004). A "triple sea-ice state" mechanism for the abrupt warming and synchronous ice sheet collapses during heinrich events. *Paleoceanography*, 19(3):n/a–n/a.

Kavanaugh, J. and Cuffey, K. (2003). Space and time variation of $\delta^{18}O$ and δD in Antarctic precipitation revisited. *Global Geochem. Cycles*, 17(1):1017.

Kawamura, K., Parrenin, F., Lisiecki, L., Uemura, R., Vimeux, F., Severinghaus, J. P., Hutterli, M. A., Nakazawa, T., Aoki, S., Jouzel, J., Raymo, M. E., Matsumoto, K., Nakata, H., Motoyama, H., Fujita, S., Goto-Azuma, K., Fujii, Y., and Watanabe, O. (2007). Northern Hemisphere forcing of climatic cycles in Antarctica over the past 360,000 years. *Nature*, 448(7156):912–U4.

Kawamura, K., Severinghaus, J. P., Albert, M. R., Courville, Z. R., Fahnestock, M. A., Scambos, T., Shields, E., and Shuman, C. A. (2013). Kinetic fractionation of gases by deep air convection in polar firn. *Atmos. Chem. Phys. Discuss.*, 13(3):7021–7059.

Keigwin, L. and Lehman, S. (1994). Deep circulation change linked to Heinrich event 1 and Younger Dryas in a middepth North Atlantic core. *Paleoceanography*, 9(2):185–194.

Khalil, M. A. K. and Rasmussen, R. A. (1983). Sources, sinks, and seasonal cycles of atmospheric methane. *J. Geophys. Res.*, 88(C9):5131–5144.

Kindler, P., Guillevic, M., Baumgartner, M., Schwander, J., Landais, A., and Leuenberger, M. (2014). Temperature reconstruction from 10 to 120 kyr b2k from the NGRIP ice core. *Clim. Past*.

Kobashi, T., Kawamura, K., Severinghaus, J. P., Barnola, J.-M., Nakaegawa, T., Vinther, B. M., Johnsen, S. J., and Box, J. E. (2011). High variability of Greenland surface temperature over the past 4000 years estimated from trapped air in an ice core. *Geophys. Res. Lett.*, 38:L21501.

Kobashi, T., Severinghaus, J. P., Brook, E. J., Barnola, J.-M., and Grachev, A. M. (2007). Precise timing and characterization of abrupt climate change 8200 years ago from air trapped in polar ice. *Quaternary Sci. Rev.*, 26:1212–1222.

Kobashi, T., Severinghaus, J. P., and Kawamura, K. (2008). Argon and nitrogen isotopes of trapped air in the GISP2 ice core during the Holocene epoch (0–11,500 B.P.): Methodology and implications for gas loss

processes. *Geochim. Cosmochim. Ac.*, 72:4675–4686.

Kucera, M., A., R.-M., Schneider, R., Waelbroeck, C., and Weinelt, M. (2005). Multiproxy approach for the reconstruction of the glacial ocean surface (MARGO). *Quaternary Sci. Rev.*, 24:813–819.

Kurita, N. (2011). Origin of Arctic water vapor during the icegrowth season. *Geophys. Res. Lett.*, 38:L02709.

Lamy, F., Kaiser, J., Arz, H. W., Hebbeln, D., Ninnemann, U., Timm, O., Timmermann, A., and Toggweiler, J. (2007). Modulation of the bipolar seesaw in the Southeast Pacific during Termination 1. *Earth Planet. Sc. Lett.*, 259(3–4):400 – 413.

Landais, A., Barkan, E., and Luz, B. (2008a). Record of δ^{18}O and ^{17}O-excess in ice from Vostok Antarctica during the last 150,000 years. *Geophys. Res. Lett.*, 35(2).

Landais, A., Barkan, E., and Luz, B. (2008b). Reply to comment by Martin F. Miller on "Record of δ^{18}O and ^{17}O-excess in ice from Vostok Antarctica during the last 150,000 years". *Geophys. Res. Lett.*, 35(23).

Landais, A., Barnola, J., Kawamura, K., Caillon, N., Delmotte, M., Ommen, T. V., Dreyfus, G., Jouzel, J., Masson-Delmotte, V., Minster, B., Freitag, J., Leuenberger, M., Schwander, J., Huber, C., Etheridge, D., and Morgan, V. (2006). Firn-air δ^{15}N in modern polar sites and glacial–interglacial ice: a model-data mismatch during glacial periods in Antarctica? *Quaternary Sci. Rev.*, 25(1–2):49 – 62.

Landais, A., Barnola, J.-M., Masson-Delmotte, V., Jouzel, J., Chappellaz, J., Caillon, N., Huber, C., Leuenberger, M., and Johnsen, S. J. (2004a). A continuous record of temperature evolution over a sequence of Dansgaard-Oeschger events during Marine Isotopic Stage 4 (76 to 62 kyr BP). *Geophys. Res. Lett.*, 31:L22211.

Landais, A., Caillon, N., Goujon, C., Grachev, A. M., Barnola, J. M., Chappellaz, J., Jouzel, J., Masson-Delmotte, V., and Leuenberger, M. (2004b). Quantification of rapid temperature change during DO event 12 and phasing with methane inferred from air isotopic measurements. *Earth Planet. Sc. Lett.*, 225:221–232.

Landais, A., Caillon, N., Severinghaus, J., Barnola, J.-M., Goujon, C., Jouzel, J., and Masson-Delmotte, V. (2004c). Isotopic measurements of air trapped in ice to quantify temperature changes. *CR Geosci.*, 336:963–970.

Landais, A., Caillon, N., Severinghaus, J., Jouzel, J., and Masson-Delmotte, V. (2003a). Analyses isotopiques à haute précision de l'air piégé dans les glaces polaires pour la quantification des variations rapides de température : méthode et limites. *Notes des activités instrumentales de l'IPSL*, 39.

Landais, A., Chappellaz, J., Delmotte, M., Jouzel, J., Blunier, T., Bourg, C., Caillon, N., Cherrier, S., Malaize, B., Masson-Delmotte, V., Raynaud, D., Schwander, J., and Steffensen, J. P. (2003b). A tentative reconstruction of the last interglacial and glacial inception in Greenland based on new gas measurements in the Greenland Ice Core Project (GRIP) ice core. *J. Geophys. Res. Atmos.*, 108(D18).

Landais, A., Dreyfus, G., Capron, E., Masson-Delmotte, V., Sanchez-Goni, M., Desprat, S., Hoffmann, G., Jouzel, J., Leuenberger, M., and Johnsen, S. (2010). What drives the millennial and orbital variations of $\delta^{18}O_{atm}$? *Quaternary Sci. Rev.*, 29:235–246.

Landais, A., Ekaykin, A., Barkan, E., Winkler, R., and Luz, B. (2012a). Seasonal variations of ^{17}O-excess and d-excess in snow precipitation at the Vostok station (East Antarctica). *J. Glaciol.*, 58.

Landais, A., Masson-Delmotte, V., Jouzel, J., Raynaud, D., Johnsen, S. J., Huber, C., Leuenberger, M., Schwander, J., and Minster, B. (2005). The glacial inception as recorded in the NorthGRIP Greenland ice core: timing, structure and associated abrupt temperature changes. *Clim. Dynam.*, 26:273–284.

Landais, A., Steen-Larsen, H., Guillevic, M., Masson-Delmotte, V., Vinther, B., and Winkler, R. (2012b). Triple isotopic composition of oxygen in surface snow and water vapor at NEEM (Greenland). *Geochim. Cosmochim. Ac.*, 77(0):304 – 316.

Lang, C., Leuenberger, M., Schwander, J., and Johnsen, S. (1999). $16-30\,^{\circ}$C rapid temperature variation in central Greenland 70,000 years ago. *Science*, 286(5441):934–937.

Langen, P. L. and Vinther, B. M. (2009). Response in atmospheric circulation and sources of Greenland precipitation to glacial boundary conditions. *Clim. Dynam.*, 32(7-8):1035–1054.

Lee, K. (2004). Compilation of alkenone LGM SST data.

Leigh, S. N. B. (2006). A study of the dynamics of the British ice sheet during Marine Isotope Stages 2 and 3 focusing on Heinrich Events 2 and 4 and their relationship to the North Atlantic glaciological and climatological conditions. Master's thesis, Univ. of St. Andrews, St. Andrews, U.K.

Leuenberger, M., Lang, C., and Schwander, J. (1999). Delta^{15}N measurements as a calibration tool for the paleothermometer and gas-ice age differences: A case study for the 8200 B.P. event on GRIP ice. *J. Geophys. Res.*, 104(D18):22163–22170.

Lewis, S., LeGrande, A. N., Kelley, M., and Schmidt, G. A. (2010). Water vapour source impacts on oxygen isotope variability in tropical precipitation during Heinrich events. *Clim. Past*, 6:325–343.

Li, C., Battisti, D., and Bitz, C. (2010). Can North Atlantic sea ice anomalies account for Dansgaard-Oeschger climate signals? *J. Climate*, 23:5457 – 5475.

Li, C., Battisti, D. S., Schrag, D. P., , and Tziperman, E. (2005). Abrupt climate shifts in Greenland due to displacements of the sea ice edge. *Geophys. Res. Lett.*, 32:L19702.

Liu, Z., Carlson, A. E., He, F., Brady, E. C., Otto-Bliesner, B. L., Briegleb, B. P., Wehrenberg, M., Clark, P. U., Wu, S., Cheng, J., Zhang, J., Noone, D., and Zhua, J. (2012). Younger Dryas cooling and the Greenland climate response to CO_2. *P. Natl. Acad. Sci. U.S.A.*

Lliboutry, L. (1979). A critical review of analytical approximate solutions for steady stade velocities and temperature in cold ice-sheets. *Z. Gletscherkd. Glazialgeol.*, 15(2):135–148.

Loewe, F. (1936). The Greenland ice cap as seen by a meteorologist. *Quarterly Journal of the Royal Meteorological Society*, 62:359–377.

Loulergue, L., Schilt, A., Spahni, R., Masson-Delmotte, V., Blunier, T., Lemieux, B., Barnola, J. M., Raynaud, D., Stocker, T. F., and Chappellaz, J. (2008). Orbital and millennial-scale features of atmospheric CH_4 over the past 800,000 years. *Nature*, 453(7193):383–386.

Lundin, J., Waddington, E., Koutnik, M., and Conway, H. (2012). Self-consistent model of ice-sheet evolution and paleoclimate (poster presentation). In *International Partnership in Ice Cores Sciences*.

Luz, B. and Barkan, E. (2005). The isotopic ratios $^{17}O/^{16}O$ and $^{18}O/^{16}O$ in molecular oxygen and their significance in biogeochemistry. *Geochim. Cosmochim. Ac.*, 69:1099–1110.

Luz, B. and Barkan, E. (2010). Variations of $^{17}O/^{16}O$ and $^{18}O/^{16}O$ in meteoric waters. *Geochim. Cosmochim. Ac.*, 74(22):6276–6286.

Luz, B., Barkan, E., Yam, R., and Shemesh, A. (2009). Fractionation of oxygen and hydrogen isotopes in evaporating water. *Geochim. Cosmochim. Ac.*, 73(22):6697 – 6703.

Majoube, M. (1971). Fractionnement en ^{18}O entre la glace et la vapeur d'eau. *Journal de Chimie Physique*, 68(4):625–636.

Manabe, S. and Stouffer, R. J. (1995). Simulation of abrupt climate change induced by freshwater input to the North Atlantic Ocean. *Nature*, 378(6553):165–167.

Marcott, S. A., Clark, P. U., Padman, L., Klinkhammer, G. P., Springer, S. R., Liu, Z., Otto-Bliesner, B. L., Carlson, A. E., Ungerer, A., Padman, J., He, F., Cheng, J., and Schmittner, A. (2011). Ice-shelf collapse from subsurface warming as a trigger for Heinrich events. *P. Natl. Acad. Sci. U.S.A.*

Mariotti, A. (1983). Atmospheric nitrogen is a reliable standard for natural ^{15}N abundance measurements. *Nature*, 303:685–687.

Martinerie, P., Lipenkov, V., Raynaud, D., Chappellaz, J., Barkov, N., and Lorius, C. (1994). Air content paleo record in the Vostok ice core (Antarctica): A mixed record of climatic and glaciological parameters. *J. Geophys. Res.*, 99(D5):10565–10576.

Masson-Delmotte, V., Braconnot, P., Hoffmann, G., Jouzel, J., Kageyama, M., Landais, A., Lejeune, Q., Risi, C., Sime, L., Sjolte, J., Swingedouw, D., , and Vinther, B. (2011). Sensitivity of interglacial Greenland temperature and $\delta^{18}O$: ice core data, orbital and increased CO_2 climate simulations. *Clim. Past*, 7:1041–1059.

Masson-Delmotte, V., Hou, S., Ekaykin, A., Jouzel, J., Aristarain, A., Bernardo, R. T., Bromwich, D., Cattani, O., Delmotte, M., Falourd, S., Frezzotti, M., Gallée, H., Genoni, L., Isaksson, E., Landais, A., Helsen, M., Hoffmann, G., Lopez, J., Morgan, V., Motoyama, H., Noone, D., Oerter, H., Petit, J.-R., Royer, A., Uemura, R., Schmidt, G., Schlosser, E., Jefferson, S. C., Steig, E. J., Stenni, B., Stievenard, M., van den Broeke, M., van de Wal, R., van de Berg, W., Vimeux, F., and White, J. (2008). A review of Antarctic surface snow isotopic composition: observations, atmospheric circulation and isotopic modelling. *J. Climate*, 21(13):3359–3387.

Masson-Delmotte, V., Jouzel, J., Landais, A., Stiévenard, M., Johnsen, S. J., White, J. W. C., Werner, M., Sveinbjörnsdóttir, A., and Fuhrer, K. (2005a). GRIP deuterium excess reveals rapid and orbital-scale changes in Greenland moisture origin. *Science*, 309:118–121.

Masson-Delmotte, V., Landais, A., Stievenard, M., Cattani, O., Falourd, S., Jouzel, J., Johnsen, S. J., Jensen, D. D., Sveinsbjornsdottir, A., White, J. W. C., Popp, T., and Fischer, H. (2005b). Holocene climatic changes in Greenland: Different deuterium excess signals at Greenland Ice Core Project (GRIP) and NorthGRIP. *J. Geophys. Res-Atmos.*, 110(D14).

McManus, J., Oppo, D. W., D., K. L., Cullen, J. L., and Bond, G. C. (2002). Thermohaline circulation and prolonged interglacial warmth in the North Atlantic. *Quaternary Res.*, 58:17–21.

Meese, D. A., Gow, A. J., Alley, R. B., Zielinski, G. A., Grootes, P. M., Ram, M., Taylor, K. C., Mayewski, P. A., and Bolzan, J. F. (1997). The Greenland Ice Sheet Project 2 depth-age scale: methods and results. *J. Geophys. Res.*, 102:26411 – 26423.

Meijer, H. and Li, W. (1998). The use of electrolysis for accurate $\delta^{17}O$ and $\delta^{18}O$ isotope measurements in water. *Isotopes Environ. Health Stud.*, 34(4):349–369.

Merlivat, L. and Jouzel, J. (1979). Global climatic interpretation of the deuterium-oxygen 18 relationship for

precipitation. *J. Geophys. Res.*, 84(C8):5029 – 5033.

Merlivat, L. and Nief, G. (1967). Fractionnement isotopique lors des changements d'état solid-vapeur et liquide-vapeur de l'eau des tempéeratures inféerieures à 0 degrés C. *Tellus*, 1.

Miller, M. F. (2008). Comment on "Record of δ^{18}O and ^{17}O-excess in ice from Vostok Antarctica during the last 150,000 years" by Amaelle Landais et al. *Geophys. Res. Lett.*

Mohtadi, M., Rossel, P., Lange, C. B., Pantoja, S., Böning, P., Repeta, D. J., Grunwald, M., Lamy, F., Hebbeln, D., and Brumsack, H.-J. (2008). Deglacial pattern of circulation and marine productivity in the upwelling region off central-south Chile . *Earth Planet. Sc. Lett.*, 272(1–2):221 – 230.

Möller, L., Sowers, T., Bock, M., Spahni, R., Behrens, M., Schmitt, J., Miller, H., and Fischer, H. (2013). Independent variations of ch$_4$ emissions and isotopic composition over the past 160,000 years. *Nat. Geosci.*

Montade, V., Nebout, N. C., Kissel, C., Haberle, S. G., Siani, G., and Michel, E. (2013). Vegetation and climate changes during the last 22,000 yr from a marine core near Taitao Peninsula, southern Chile. *Palaeogeogr. Palaeocl.*, 369:335–348.

Mook, W. (2001). *Environmental isotopes in the hydrological cycle: principle and applications*, volume 1. International Atomic Energy Agency and United Nations Educational, Scientific and Cultural Organization. IHP-V Technical Documents in Hydrology, Nº 39.

Moreno, A., Cacho, I., Canals, M., Grimalt, J. O., ni, M. S.-G., Shackleton, N., and Sierro, F. J. (2005). Links between marine and atmospheric processes oscillating on a millennial time-scale. A multi-proxy study of the last 50,000 yr from the Alboran Sea (Western Mediterranean Sea). *Quaternary Sci. Rev.*, 24:1623–1636.

Moreno, E., Thouveny, N., Delanghe, D., McCave, I., and Shackleton, N. J. (2002). Climatic and oceanographic changes in the Northeast Atlantic reflected by magnetic properties of sediments deposited on the Portuguese Margin during the last 340 ka . *Earth Planet. Sc. Lett.*, 202(2):465–480.

Mosblech, N. A., Bush, M. B., Gosling, W. D., Hodell, D., Thomas, L., van Calsteren, P., Correa-Metrio, A., Valencia, B. G., Curtis, J., and van Woesik, R. (2012). North Atlantic forcing of Amazonian precipitation during the last ice age. *Nat. Geosci.*, 5:817–820.

Muscheler, R., Kromer, B., Björck, S., Svensson, A., Friedrich, M., Kaiser, K., and Southon, J. (2008). Tree rings and ice cores reveal ^{14}C calibration uncertainties during the Younger Dryas. *Nat. Geosci.*, 1(4):263–267.

Naughton, F., Goñi, M. S., Kageyama, M., Bard, E., Duprat, J., Cortijo, E., Desprat, S., Malaizé, B., Joly, C., Rostek, F., and Turon, J.-L. (2009). Wet to dry climatic trend in north-western Iberia within Heinrich events. *Earth Planet. Sc. Lett.*, 284:329 – 342.

NGRIP members (2004). High-resolution record of Northern Hemisphere climate extending into the last interglacial period. *Nature*, 431:147–151.

Noone, D. (2008). The influence of midlatitude and tropical overturning circulation on the isotopic composition of atmospheric water vapor and Antarctic precipitation. *J. Geophys. Res.*, 113:D04102, doi:10.1029/2007JD008892.

Orsi, A., Cornuelle, B., and Severinghaus, J. (2013). Magnitude and temporal evolution of interstadial 8 abrupt temperature change inferred from nitrogen and argon isotopes in GISP2 ice using a new least-squares inversion, submitted.

Otto-Bliesner, B. L. and Brady, E. C. (2010). The sensitivity of the climate response to the magnitude and location of freshwater forcing: last glacial maximum experiments. *Quaternary Sci. Rev.*, 29:56–73.

Paillard, D. and Cortijo, E. (1999). A simulation of the Atlantic meridional circulation during Heinrich event 4 using reconstructed sea surface temperatures and salinities. *Paleoceanography*, 14(6):716–724.

Pailler, D. and Bard, E. (2002). High frequency palaeoceanographic changes during the past 140 000 yr recorded by the organic matter in sediments of the Iberian Margin . *Palaeogeogr. Palaeocl.*, 181(4):431 – 452.

Paterson, W. (1994). *The Physics of Glaciers*. Pergamon, New York.

Pausata, F. S. R., Battisti, D. S., Nisancioglu, K. H., and Bitz, C. M. (2011a). Chinese stalagmite δ^{18}O controlled by changes in the Indian monsoon during a simulated Heinrich event. *Nat. Geosci.*, 4:474–480.

Pausata, F. S. R., Li, C., Wettstein, J. J., Kageyama, M., and Nisancioglu, K. H. (2011b). The key role of topography in altering North Atlantic atmospheric circulation during the last glacial period. *Clim. Past*, 7(4):1089–1101.

Peck, V. L., Hall, I. R., Zahn, R., Grousset, F., Hemming, S. R., and Scourse, J. D. (2007). The relationship of Heinrich events and their European precursors over the past 60 ka BP: a multi-proxy ice-rafted debris provenance study in the North East Atlantic. *Quaternary Sci. Rev.*, 26(7-8):862–875.

Pérez-Folgado, M., Sierro, F., Flores, J., Cacho, I., Grimalt, J., Zahn, R., and Shackleton, N. (2003). Western mediterranean planktonic foraminifera events and millennial climatic variability during the last 70 kyr. *Mar. Micropaleontol.*, 48(1–2):49–70.

Persson, A., Langen, P. L., Ditlevsen, P., , and Vinther, B. M. (2011). The influence of precipitation weighting on interannual variability of stable water isotopes in Greenland. *J. Geophys. Res.*, 116:D20120.

Peters, C., Walden, J., and Austin, W. E. N. (2008). Magnetic signature of European margin sediments: Provenance of ice-rafted debris and the climatic response of the British ice sheet during Marine Isotope Stages 2 and 3. *J. Geophys. Res.-Earth*, 113(F3).

Peterson, L. C., Haug, G. H., Hughen, K. A., and Röhl, U. (2000). Rapid changes in the hydrologic cycle of the tropical Atlantic during the Last Glacial. *Science*, 290:1947–1951.

Petrenko, V. V., Severinghaus, J. P., Brook, E. J., Reeh, N., and Schaefer, H. (2006). Gas records from the West Greenland ice margin covering the Last Glacial Termination: a horizontal ice core. *Quaternary Sci. Rev.*, 25(9–10):865 – 875.

Quay, P., Stutsman, J., Wilbur, D., Snover, A., Dlugokencky, E., and Brown, T. (1999). The isotopic composition of atmospheric methane. *Global Biogeochem. Cy.*, 13(2):445–461.

Rashid, H. and Grosjean, E. (2006). Detecting the source of Heinrich layers: An organic geochemical study. *Paleoceanography*, 21(3).

Rashid, H., Hesse, R., and Piper, D. (2003). Evidence for an additional Heinrich event between H5 and H6 in the Labrador Sea. *Paleoceanography*, 18(4).

Rasmussen, S. O., Abbott, P. M., Blunier, T., Bourne, A. J., Brook, E., Buchardt, S. L., Buizert, C., Chappellaz, J., Clausen, H. B., Cook, E., Dahl-Jensen, D., Davies, S. M., Guillevic, M., Kipfstuhl, S., Laepple, T., Seierstad, I. K., Severinghaus, J. P., Steffensen, J. P., Stowasser, C., Svensson, A., Vallelonga, P., Vinther, B. M., Wilhelms, F., and Winstrup, M. (2013). A first chronology for the North Greenland Eemian Ice Drilling (NEEM) ice core. *Clim. Past*, 9(6):2713–2730.

Rasmussen, S. O., Andersen, K. K., Svensson, A. M., Steffensen, J. P., Vinther, B. M., Clausen, H. B., Siggaard-Andersen, M.-L., Johnsen, S. J., Larsen, L. B., Dahl-Jensen, D., Bigler, M., Röthlisberger, R., Fischer, H., Goto-Azuma, K., Hansson, M. E., and Ruth, U. (2006). A new Greenland ice core chronology for the last glacial termination. *J. Geophys. Res.*, 111:D06102.

Rasmussen, S. O., Seierstad, I., Andersen, K., Bigler, M., Dahl-Jensen, D., and Johnsen, S. (2008). Synchronization of the NGRIP, GRIP, and GISP2 ice cores across MIS 2 and palaeoclimatic implications. *Quaternary Sci. Rev.*, 27:18 – 28.

Rasmussen, T., Oppo, D., Thomsen, E., and Lehman, S. (2003). Deep sea records from the southeast labrador sea: Ocean circulation changes and ice-rafting events during the last 160,000 years. *Paleoceanography*, 18(1):1018.

Rasmussen, T. L. and Thomsen, E. (2004). The role of the North Atlantic Drift in the millennial timescale glacial climate fluctuations. *Palaeogeogr. Palaeocl.*, 210(1):101–116.

Ringeval, B., de Noblet-Ducoudre, N., Ciais, P., Bousquet, P., Prigent, C., Papa, F., and Rossow, W. B. (2010). An attempt to quantify the impact of changes in wetland extenton methane emissions at the seasonal and interannual time scales. *Global Biogeochem. Cycles*, 24:GB2003.

Risi, C., Landais, A., Bony, S., Jouzel, J., Masson-Delmotte, V., and Vimeux, F. (2010). Understanding the ^{17}O excess glacial-interglacial variations in Vostok precipitation. *J. Geophys. Res.-Atmos.*, 115(D10).

Ritz, C. (1989). Interpretation of the temperature profile measured at Vostok, east Antarctica. *Ann. Glaciol.*, 12:138 – 144.

Roche, D., Paillard, D., and Cortijo, E. (2004). Constraints on the duration and freshwater release of Heinrich event 4 through isotope modelling. *Nature*, 432(7015):379–382.

Roche, D., Wiersma, A., and Renssen, H. (2010). A systematic study of the impact of freshwater pulses with respect to different geographical locations. *Climate Dyn.*, 34:997 – 1013.

Romero, O. E., Kim, J.-H., and Hebbeln, D. (2006). Paleoproductivity evolution off central Chile from the Last Glacial Maximum to the Early Holocene. *Quaternary Res.*, 65(3):519 – 525.

Salamatin, A., Lipenkov, V., and Blinov, K. (1994). Vostok (Antarctica) climate record time-scale deduced from the analysis of a borehole-temperature profile. *Ann. Glaciol.*, 20:207–214.

Saltzman, E., Whung, P.-Y., and Mayewski, P. (1997). Methanesulfonate in the Greenland Ice Sheet Project 2 Ice Core. *J. Geophys. Res.*, 102(C12):26649–26657.

Sánchez Goñi, M. and Harrison, S. (2010). Millennial-scale climate variability and vegetation changes during the Last Glacial: Concepts and terminology. *Quaternary Sci. Rev.*, 29:2823–2827.

Sánchez-Goñi, M., Landais, A., Fletcher, W. J., Naughton, F., Desprat, S., and Duprat, J. (2008). Contrasting impacts of Dansgaard–Oeschger events over a western European latitudinal transect modulated by orbital parameters. *Quaternary Sci. Rev.*, 27:1136–1151.

Sánchez-Goñi, M., Turon, J.-L., Eynaud, F., and Gendreau, S. (2000). European climatic response to millennial-scale changes in the atmosphere-ocean system during the Last Glacial Period. *Quaternary Res.*, 54:394–403.

Sapart, C. J., Martinerie, P., Chappellaz, J., van de Wal, R. S. W., Sperlich, P. van der Veen, C., Bernard, S., Sturges, W. T., Blunier, T., Witrant, E., Schwander, J., Etheridge, D., and Rockmann, T. (2012a). Reconstruction of the carbon isotopic composition of methane over the last 50 yr based on firn air measurements at 11 polar sites. *Atmos. Chem. Phys. Discuss.*, 12(12):9587–9619.

Sapart, C. J., Monteil, G., Prokopiou, M., van de Wal, R. S. W., Kaplan, J. O., Sperlich, P., Krumhardt, K. M., van der Veen, C., Houweling, S., Krol, M. C., Blunier, T., Sowers, T., Martinerie, P., Witrant, E., Dahl-Jensen, D., and Röckmann, T. (2012b). Natural and anthropogenic variations in methane sources during the past two millennia. *Nature*, 490:85–88.

Schaefer, H. and Whiticar, M. J. (2008). Potential glacial-interglacial changes in stable carbon isotope ratios of methane sources and sink fractionation. *Global Biogeochem. Cycles*, 22:GB1001.

Schmidt, G. A., LeGrande, A. N., and Hoffmann, G. (2007). Water isotope expressions of intrinsic and forced variability in a coupled ocean-atmosphere model. *J. Geophys. Res. Atmospheres*, 112(D10).

Schoenemann, S. W., Schauer, A. J., and Steig, E. J. (2013). Measurement of SLAP2 and GISP δ^{17}O and proposed VSMOW-SLAP normalization for δ^{17}O and $^{17}O_{excess}$. *Rapid Commun. Mass Sp.*, 27:582–590.

Schönfeld, J., Zahn, R., and de Abreu, L. (2003). Surface and deep water response to rapid climate changes at the Western Iberian Margin. *Global Planet. Change*, 36(4):237–264.

Schwander, J. (1989). *The transformation of snow to ice and the occlusion of gases*. J. Wiley and Sons Limited, New York.

Schwander, J., Barnola, J. M., Andrié, C., Leuenberger, M., Ludin, A., Raynaud, D., and Stauffer, B. (1993). The age of the air in the firn and the ice at Summit, Greenland. *J. Geophys. Res.*, 98:2831–2838.

Schwander, J., Sowers, T., Barnola, J.-M., Blunier, T., Fuchs, A., and Malaizé, B. (1997). Age scale of the air in the Summit ice: Implication for glacial-interglacial temperature change. *J. Geophys. Res.*, 102(D16):19483–19493.

Schwander, J. and Stauffer, B. (1984). Age difference between polar ice and the air trapped in its bubbles. *Nature*, 311:45–47.

Schwander, J., Stauffer, B., and Sigg, A. (1988). Air mixing in firn and the age of the air at pore close-off. *Ann. Glaciol.*, 10:141 – 145.

Scourse, J. D., Hall, I. R., McCave, I., Young, J. R., and Sugdon, C. (2000). The origin of Heinrich layers: evidence from H2 for European precursor events. *Earth Planet. Sc. Lett.*, 182(2):187–195.

Severinghaus, J., Beaudette, R., Headly, M. A., Taylor, K., and Brook, E. J. (2009). Oxygen-18 of O_2 records the impact of abrupt climate change on the terrestrial biosphere. *Science*, 324:1431–1434.

Severinghaus, J. and Brook, E. (1999). Abrupt climate change at the end of the Last Glacial Period inferred from trapped air in polar ice. *Science*, 286:930–934.

Severinghaus, J., Grachev, A., Luz, B., and Caillon, N. (2003). A method for precise measurement of argon 40/36 and krypton/argon ratios in trapped air in polar ice with applications to past firn thickness and abrupt climate change in Greenland and at Siple Dome, Antarctica. *Geochim. Cosmochim. Ac.*, 67:325–343.

Severinghaus, J., Sowers, T., Brook, E. J., Alley, R. B., and Bender, M. L. (1998). Timing of abrupt climate change at the end of the Younger Dryas interval from thermally fractionated gases in polar ice. *Nature*, 391:141–146.

Shackleton, N., Fairbanks, R. G., chien Chiu, T., and Parrenin, F. (2004). Absolute calibration of the Greenland time scale: implications for Antarctic time scales and for Δ^{14}C. *Quaternary Sci. Rev.*, 23(14–15):1513 – 1522.

Sime, L. C., Risi, C., Tindall, J. C., Sjolte, J., Wolff, E. W., Masson-Delmotte, V., and Capron, E. (2013). Warm climate isotopic simulations: what do we learn about interglacial signals in Greenland ice cores? . *Quaternary Sci. Rev.*, 67(0):59 – 80.

Singer, B. S., Guillou, H., Jicha, B. R., Laj, C., Kissel, C., Beard, B. L., and Johnson, C. M. (2009). Ar-40/Ar-39, K-Ar and Th-230-U-238 dating of the Laschamp excursion: A radioisotopic tie-point for ice core and climate chronologies. *Earth Planet. Sc. Lett.*, 286(1-2):80–88.

Sjolte, J., Hoffmann, G., Johnsen, S. J., Vinther, B. M., Masson-Delmotte, V., and Sturm, C. (2011). Modeling the water isotopes in greenland precipitation 1959–2001 with the meso-scale model remo-iso. *J. Geophys. Res.*, 116:D18105.

Skinner, L. C. (2008). Revisiting the absolute calibration of the Greenland ice core age-scales. *Clim. Past*, 4(4):295–302.

Smith, J. A. and Rodbell, D. T. (2010). Cross-cutting moraines reveal evidence for North Atlantic influence on glaciers in the tropical Andes. *J. Quaternary Sci.*, 25(3):243–248.

Snoeckx, H., Grousset, F., Revel, M., and Boelaert, A. (1999). European contribution of ice-rafted sand to Heinrich layers H3 and H4. *Mar. Geol.*, 158:197–208.

Sodemann, H., Masson-Delmotte, V., Schwierz, C., Vinther, B. M., and Wernli, H. (2008). Interannual variability of Greenland winter precipitation sources: 2. Effects of North Atlantic Oscillation variability on stable

isotopes in precipitation. *J. Geophys. Res.*, 113:D12111, doi:10.1029/2007JD009416.

Sowers, T. (2006). Late quaternary atmospheric CH_4 isotope record suggests marine clathrates are stable. *Science*, 311(5762):838–840.

Sowers, T. (2010). Atmospheric methane isotope records covering the holocene period. *Quaternary Sci. Rev.*, 29:213–221.

Sowers, T. and Bender, M. (1995). Climate records covering the last deglaciation. *Science*, 269:210–214.

Sowers, T., Bender, M., and Raynaud, D. (1989). Elemental and isotopic composition of occluded O_2 and N_2 in polar ice. *J. Geophys. Res.*, 94(D4):5137–5150.

Sowers, T., Bender, M., Raynaud, D., and Korotkevich, Y. (1992). $\delta^{15}N$ of N_2 in air trapped in polar ice: a tracer of gas transport in the firn and a possible constraint on ice age – gas age differences. *J. Geophys. Res.*, 97(D14):15683–15697.

Sowers, T., Brook, E., Etheridge, D., Blunier, T., Fuchs, A., Leuenberger, M., Chappellaz, J., Barnola, J. M., Wahlen, M., Deck, B., and Weyhenmeyer, C. (1997). An interlaboratory comparison of techniques for extracting and analysing trapped gases in ice cores. *J. Geophys. Res.*, 102(C12):26527–26538.

Spencer, M. K., Alley, R. B., and Creyts, T. (2001). Preliminary firn-densification model with 38-site datadet. *J. Glaciol.*, 47(159):671–676.

Sperlich, P., Buizert, C., Jenk, T. M., Sapart, C. J., Prokopiou, M., Röckmann, T., and Blunier, T. (2013). An automated GC-C-GC-IRMS setup to measure palaeoatmospheric $\delta^{13}C$-CH_4, $\delta^{15}N$-N_2O and $\delta^{18}O$-N_2O in one ice core sample. *Atmos. Meas. Tech.*, 6(8):2027–2041.

Sperlich, P., Guillevic, M., Buizert, C., Jenk, T. M., Sapart, C. J., Schaefer, H., Popp, T. J., and Blunier, T. (2012). A combustion setup to precisely reference $\delta^{13}C$ and δ^2H isotope ratios of pure CH_4 to produce isotope reference gases of $\delta^{13}C$-CH_4 in synthetic air. *Atmos. Meas. Tech.*, 5:2227–2236.

Stanford, J., Rohling, E., Bacon, S., Roberts, A., Grousset, F., and Bolshawa, M. (2011). A new concept for the paleoceanographic evolution of heinrich event 1 in the north atlantic. *Quaternary Sci. Rev.*, 30:1047 – 1066.

Steen-Larsen, H. C., Masson-Delmotte, V., Sjolte, J., Johnsen, S. J., Vinther, B. M., Bréon, F.-M., Clausen, H. B., Dahl-Jensen, D., Falourd, S., Fettweis, X., Gallée, H., Jouzel, J., Kageyama, M., Lerche, H., Minster, B., Picard, G., Punge, H. J., Risi, C., Salas, D., Schwander, J., Steffen, K., Sveinbjörnsdóttir, A. E., Svensson, A., and White, J. W. C. (2011). Understanding the climatic signal in the water stable isotope records from the NEEM shallow firn/ice cores in northwest Greenland. *J. Geophys. Res.*, 116:D06108.

Steffensen, J. P., Andersen, K. K., Bigler, M., Clausen, H. B., Dahl-Jensen, D., Fischer, H., Goto-Azuma, K., Hansson, M., Johnsen, S. J., Jouzel, J., Masson-Delmotte, V., Popp, T., Rasmussen, S. O., Röthlisberger, R., Ruth, U., Stauffer, B., Siggaard-Andersen, M.-L., Sveinbjörnsdóttir, A. E., Svensson, A., and White, J. W. C. (2008). High-resolution greenland ice core data show abrupt climate change happens in few years. *Science*, 321:680–684.

Stenni, B., Masson-Delmotte, V., Johnsen, S., Jouzel, J., Longinelli, A., Monnin, E., Röthlisberger, R., and Selmo, E. (2001). An oceanic cold reversal during the last deglaciation. *Science*, 293(5537):2074–2077.

Stenni, B., Masson-Delmotte, V., Selmo, E., Oerter, H., Meyer, H., Röthlisberger, R., Jouzel, J., Cattani, O., Falourd, S., Fischer, H., Hoffmann, G., Iacumin, P., Johnsen, S., Minster, B., and Udisti, R. (2010). The deuterium excess records of EPICA Dome C and Dronning Maud Land ice cores (East Antarctica). *Quaternary Sci. Rev.*, 29:146–159.

Stocker, T. F. (1998). The seesaw effect. *Science*, 282(5386):61–62.

Stocker, T. F. and Johnsen, S. J. (2003). A minimum thermodynamic model for the bipolar seesaw. *Paleoceanography*, 18(4):1087.

Svensson, A., Andersen, K., Bigler, M., Clausen, H., Dahl-Jensen, D., Davies, S., Johnsen, S., Muscheler, R., Rasmussen, S., Röthlisberger, R., Steffensen, J., and Vinther, B. (2006). The Greenland Ice Core Chronology 2005, 15-42 ka. Part 2: comparison to other records. *Quaternary Sci. Rev.*, 25:3258–3267.

Svensson, A., Andersen, K. K., Bigler, M., Clausen, H. B., Dahl-Jensen, D., Davies, S. M., Johnsen, S. J., Muscheler, R., Parrenin, F., Rasmussen, S. O., Röthlisberger, R., Seierstad, I., Steffensen, J. P., and Vinther, B. M. (2008). A 60 000 year Greenland stratigraphic ice core chronology. *Clim. Past*, 4:47–57.

Thiemens, M. H. (1999). Mass-independent isotope effects in planetary atmospheres and the early solar system. *Science*, 283:341–345.

Thouveny, N., Moreno, E., Delanghe, D., Candon, L., Lancelot, Y., and Shackleton, N. (2000). Rock magnetic detection of distal ice-rafted debries: clue for the identification of Heinrich layers on the Portuguese margin. *Earth Planet. Sci. Lett.*, 180(1–2):61–75.

Toggweiler, J., Russell, J., and Carson, S. (2006). Midlatitude westerlies, atmospheric CO_2, and climate change during the ice ages. *Paleoceanography*, 21(PA2005).

Trigo, I. (2006). Climatology and interannual variability of storm-tracks in the Euro-Atlantic sector: A comparison between ERA-40 and NCEP/NCAR reanalyses. *Clim. Dynam.*, 26:127–143.

Uemura, R., Barkan, E., Abe, O., and Luz, B. (2010). Triple isotope composition of oxygen in atmospheric water vapor. *Geophys. Res. Lett.*, 37(4).

Vallelonga, P., Bertagna, G., Blunier, T., Kjær, H. A., Popp, T. J., Rasmussen, S. O., Steffensen, J. P., Stowasser, C., Svensson, A. S., Warming, E., Winstrup, M., Bigler, M., and Kipfstuhl, S. (2012). Duration of Greenland Stadial 22 and ice-gas Δage from counting of annual layers in Greenland NGRIP ice core. *Clim. Past*, 8(6):1839–1847.

Van Hook, W. A. (1968). Vapor pressures of the isotopic waters and ices. *J. Phys. Chem.*, pages 1234–1244.

van Kreveld, S., Sarnhein, M., Erlenkeuser, H., Grootes, P., Jung, S., Nadeau, M., Pfaumann, U., and Voelker, A. (2000). Potential links between surging ice sheets, circulation changes, and the Dansgaard-Oeschger cycles in the Irminger Sea, 60-18 kyr. *Paleoceanography*, 15(4):425–442.

Vautravers, M. J., Shackleton, N. J., Lopez-Martinez, C., and Grimalt, J. O. (2004). Gulf Stream variability during marine isotope stage 3. *Paleoceanography*, 19(2):PA2011.

Veres, D., Bazin, L., Landais, A., Kele, H. T. M., Lemieux-Dudon, B., Parrenin, F., Martinerie, P., Blayo, E., Blunier, T., Capron, E., Chappellaz, J., Rasmussen, S. O., Severi, M., Svensson, A., Vinther, B., , and Wolff, E. W. (2013). The Antarctic ice core chronology (AICC2012): an optimized multi-parameter and multi-site dating approach for the last 120 thousand years. *Clim. Past*, 9:1733–1748.

Vidal, L., Labeyrie, L., Cortijo, E., Arnold, M., Duplessy, J., Michel, E., Becqué, S., and van Weering, T. (1997). Evidence for changes in the North Atlantic Deep Water linked to welt water surges during the Heinrich events. *Earth Planet. Sc. Lett.*, 146:13 – 27.

Vidal, L., Labeyrie, L., and van Weering, T. C. E. (1998). Benthic $\delta^{18}O$ records in the North Atlantic over the last glacial period (60–10 kyr): Evidence for brine formation. *Paleoceanography*, 13(3):245–251.

Vimeux, F., Cuffey, K. M., and Jouzel, J. (2002). New insights into Southern Hemisphere temperature changes from Vostok ice cores using deuterium excess correction. *Earth Planet. Sc. Lett.*, 203(3-4):829–843.

Vimeux, F., Masson, V., Jouzel, J., Stievenard, M., and Petit, J. (1999). Glacial-interglacial changes in ocean surface conditions in the Southern Hemisphere. *Nature*, 398:410–413.

Vinther, B. M., Clausen, H. B., Johnsen, S. J., Rasmussen, S. O., Andersen, K. K., Buchardt, S. L., Dahl-Jensen, D., Seierstad, I. K., Siggaard-Andersen, M.-L., Steffensen, J. P., and Svensson, A. (2006). A synchronized dating of three Greenland ice cores throughout the Holocene. *J. Geophys. Res.*, 111(D13):D13102.

Voelker, A. H. L. (2002). Global distribution of centennial-scale records for Marine Isotope Stage (MIS) 3: a database. *Quaternary Sci. Rev.*, 21:1185–1212.

Waelbroeck, C., Duplessy, J.-C., Michel, E., Labeyrie, L., Paillard, D., and Duprat, J. (2001). The timing of the last deglaciation in North Atlantic climate records. *Nature*, 412:724–727.

Walden, J., Wadsworth, E., Austin, W., Scourse, C. P. J., and Hall, I. (2007). Compositional variability of ice-rafted debris in Heinrich layers 1 and 2 on the northwest European continental slope identified by environmental magnetic analyses. *J. Quaternary Sci.*, 22(2):163–172.

Waldron, S., Hall, A. J., and Fallick, A. E. (1999). Enigmatic stable isotope dynamics of deep peat methane. *Global Biogeochem. Cy.*, 13(1):93–100.

Walter, B. P., Heimann, M., and Matthews, E. (2001). Modeling modern methane emissions from natural wetlands 2. interannual variations 1982–1993. *J. Geophys. Res.*, 106(D24):34207–34219.

Wang, X., Auler, A. S., Edwards, L., Cheng, H., Cristalli, P. S., Smart, P. L., Richards, D. A., and Shen, C.-C. (2004). Wet periods in northeastern Brazil over the past 210 kyr linked to distant climate anomalies. *Nature*, 432(7018):740–743.

Wang, X., Auler, A. S., Edwards, R. L., Cheng, H., Ito, E., Wang, Y., Kong, X., and Solheid, M. (2007). Millennial-scale precipitation changes in southern Brazil over the past 90,000 years. *Geophys. Res. Lett.*, 34(23).

Wang, Y. J., Cheng, H., Edwards, R. L., An, Z. S., Wu, J. Y., Shen, C. C., and Dorale, J. A. (2001). A high-resolution absolute-dated Late Pleistocene monsoon record from Hulu Cave, China. *Science*, 294(5550):2345–2348.

Weinelt, M. (2004). Compilation of global planktic foraminifera LGM SST data. *PANGAEA*.

Werner, M., Heimann, M., and Hoffmann, G. (2001). Isotopic composition and origin of polar precipitation in present and glacial climate simulations. *Tellus*, 53B:53–71.

Werner, M., Heimann, M., and Hoffmann, G. (2011). Isotopic composition and origin of polar precipitation in present and glacial climate simulations. *Tellus*, 53B(1):53–71.

Werner, M., Mikolajewicz, U., Heimann, M., and Hoffman, G. (2000). Borehole versus isotope temperatures on Greenland: seasonality does matter. *Geophys. Res. Lett.*, 27(5):723–725.

Whiticar, M. (1993). *Stable isotopes and global budgets, in: Atmospheric Methane: Sources, Sinks, and Role in Global*

Change, NATO ASI Series I, Global Environmental Change, volume 13. M. A. K. Khalil.

Whiticar, M. J., Faber, E., and Schoell, M. (1986). Biogenic methane formation in marine and freshwater environments: CO_2 reduction vs. acetate fermentation-isotope evidence. *Geochim. Cosmochim. Ac.*, 50:693–709.

Wilkinson, D. and Ashby, M. (1975). Pressure sintering by power law creep. *Acta Metallurgica*, 23(11):1277–1285.

Willamowski, C. and Zahn, R. (2000). Upper ocean circulation in the glacial North Atlantic from benthic foraminiferal isotope and trace element fingerprinting. *Paleoceanography*, 15(5):515–527.

Winkler, R. (2012). *Triple-oxygen isotopic composition of meteoric waters: ^{17}Oexcess a new tracer of the hydrological cycle*. PhD thesis, Université de Versailles Saint Quentin en Yvelines, France.

Winkler, R., Landais, A., Risi, C., Baroni, M., Ekaykin, A., Jouzel, J., Petit, J. R., Prie, F., Minster, B., and Falourd, S. (2013). Interannual variation of water isotopologues at Vostok indicates a contribution from stratospheric water vapor. *P. Natl. Acad. Sci. U.S.A.*

Winkler, R., Landais, A., Sodemann, H., Dümbgen, L., Prié, F., Masson-Delmotte, V., Stenni, B., and Jouzel, J. (2012). Deglaciation records of ^{17}O-excess in East Antarctica: reliable reconstruction of oceanic normalized relative humidity from coastal sites. *Clim. Past*, 8(1):1–16.

Witrant, E., Martinerie, P., Hogan, C., Laube, J. C., Kawamura, K., Capron, E., Montzka, S. A., Dlugokencky, E. J., Etheridge, D., Blunier, T., and Sturges, W. T. (2012). A new multi-gas constrained model of trace gas non-homogeneous transport in firn: evaluation and behaviour at eleven polar sites. *Atmos. Chem. Phys.*, 12:11465–11483.

Wolff, E., Chappellaz, J., Blunier, T., Rasmussen, S., and Svensson, A. (2010). Millennial-scale variability during the last glacial: The ice core record. *Quaternary Sci. Rev.*, 29(21–22):2828 –2838.

Wunsch, C. (2006). Abrupt climate change: An alternative view. *Quaternary Res.*, 65(2):191–203.

Yokoyama, Y., Esat, T., Lambeck, K., and Fifield, L. (2000). Last ice age millennial scale climate changes recorded in Huon Peninsula carals. *Radiocarbon*, 43(3):383–401.

Zahn, R., Shönfeld, J., Kudrass, H.-R., Park, M.-H., Erlenkeuser, H., , and Grootes, P. (1997). Thermohaline instability in the North Atlantic during meltwater events: Stable isotope and ice-rafted detritus records from core SO75-26KL, Portuguese margin. *Paleoceanography*, 12(5):696–710.

Zumaque, J., Eynaud, F., Zaragosi, S., Marret, F., Matsuzaki, K. M., Kissel, C., Roche, D. M., Malaizé, B., Michel, E., Billy, I., Richter, T., , and Palis, E. (2012). An ocean–ice coupled response during the last glacial: a view from a marine isotopic stage 3 record south of the Faeroe Shetland Gateway. *Clim. Past*, 8:1997 – 2017.

Acknowledgments

I have met ice core science about five years ago when I first met Amaëlle, who was happy to find a student to measure ^{17}O excess in vapor and snow samples from Greenland. The samples were from Hans Christian and I remember that all the bottles were labeled HC-i (i being a number). Since I broke nothing too expensive after these few months in her lab, Amaëlle recommended me to Thomas, and that's how I arrived in Denmark for my master project. I remember that I arrived in February and the sea was covered with small ice pieces, and all Copenhagen was under the snow. That was quite a change for me!

I first would like to thank my three wonderful supervisors: Thomas, Valérie, and especially Amaëlle. I have really enjoyed working with you and have definitely learned a lot, and not only about science (also about how to take care of an injured cat). I really hope we will work again together in the future.

This PhD was definitely not a lonely work and it started by a collaboration with Peter in the gaslab in Copenhagen. Peter, it was a great pleasure to work with you and become friends. You have always had good advices and ideas. I really hope to see you and Colleen and Palla again soon. Corentin, I really like discussing about so many different things with you, and sometimes realizing when we go deep in the details that we actually agree with each other's. It was also great to have Theo, Christo, David and Christopher as colleagues in the Gaslab, and recently Kirstin and Gabriela.

I really enjoyed working at CIC in general and I'm very happy to have met the great friends and colleagues you are. I really enjoyed walking, cooking and discussing with Mai and Ivana. HC, thank you very much for inviting me to spend Christmas with you and your family. Now that you are in France you should definitely visit my family! Sune thank you for your support. Nanna and Henning for taking care of my harp when I was away. Bo for the fireworks on New Year's Eve (actually quite dangerous). Ernesto it was great not to be alone working over the weekend, thank you for your help with latex and all our tea breaks. Iben, thank you very much to make me feel at home in Denmark. In France at LSCE I really enjoyed sharing an office with Lucie and Alexandre and working with Fred, you are wonderful colleagues (and Alex thank you so much for hiding this coffee machine!). And I had the chance to have Bérangère and Nadia as roommates for a few months in Gif sur Yvette, and we had to face together the house falling into pieces. And finally, it seems that we are at least two people happy that the NEEM preliminary gas age scale was quite off around DO 10. Philippe, thank you for the chocolate, and being who you are.

I had the great chance to go to NEEM twice during this PhD and this was quite an experience (JP thank you for putting me on the list!). Last summer with Alex, AK, Lisbeth and Bo S.M. I could experience once in a while how wrong my English was but at least it made you laugh, so that was good in the end (no I don't want to taste it!). Sarah, thank you for your useful advices and for sharing recipes.

And then I would really like to thank my family, so now I switch to French: Aurore, Maman, Papa, merci d'être toujours là.